Constraining the exchange of carbon dioxide over the Amazon

New insights from stable isotopes, remote sensing and inverse modeling

Gerbrand Koren

Propositions

1. The discrimination formulation is not suitable for leaf exchange of oxygen isotopes (this thesis).

2. There are no normal years in the Amazon (this thesis).

3. Every scientist working with numerical methods should spend some time doing measurements.

4. Ownership of scientific data should have an expiration date.

5. Efficiency and people management are more important than intelligence for a successful scientific career.

6. The urgency of climate change is not effectively communicated by climate scientists.

7. A name that is difficult to pronounce, such as 'Gerbrand', hurts a scientific career.

Propositions belonging to the thesis, entitled

Constraining the exchange of carbon dioxide over the Amazon: New insights from stable isotopes, remote sensing and inverse modeling

Gerbrand Koren
Wageningen, 18 September 2020

Constraining the exchange of carbon dioxide over the Amazon

New insights from stable isotopes, remote sensing and inverse modeling

Gerbrand Koren

Thesis committee

Promotors:
Prof. Dr Wouter Peters
Personal chair, Air Quality and Atmospheric Chemistry
Wageningen University & Research
Professor of Atmospheric Composition Modeling
University of Groningen

Prof. Dr Thomas Röckmann
Professor, Atmospheric Physics and Chemistry Group
Utrecht University

Co-promotor:
Dr Ingrid T. Luijkx
Assistant professor, Meteorology and Air Quality Group
Wageningen University & Research

Other members:
Prof. Dr P.A. Zuidema, Wageningen University & Research
Dr P. Peylin, Laboratoire des Sciences du Climat et de l'Environnement, Gif-sur-Yvette, France
Prof. Dr S. Houweling, VU University Amsterdam
Prof. Dr H.A.J. Meijer, University of Groningen

This research was conducted under the auspices of the Graduate School for Socio Economic and Natural Sciences of the Environment (SENSE)

Constraining the exchange of carbon dioxide over the Amazon

New insights from stable isotopes, remote sensing and inverse modeling

Gerbrand Koren

Thesis

submitted in fulfilment of the requirements for the degree of doctor
at Wageningen University
by the authority of the Rector Magnificus
Prof. Dr A.P.J. Mol,
in the presence of the
Thesis Committee appointed by the Academic Board
to be defended in public
on Friday 18 September 2020
at 11 a.m. in the Aula.

Gerbrand Koren
Constraining the exchange of carbon dioxide over the Amazon
New insights from stable isotopes, remote sensing and inverse modeling
259 pages

PhD thesis, Wageningen University, Wageningen, The Netherlands (2020)
With references, with summary in English

ISBN 978-94-6395-438-9
DOI https://doi.org/10.18174/524771

Contents

1

Introduction

1.1 Atmospheric CO_2

The level of carbon dioxide (CO_2) in the atmosphere has increased substantially since the start of the industrial revolution. Around 1850, the global average dry air mole fraction (i.e. the moles of CO_2 per mole of air in the absence of water) was around 280 μmole/mole (*Etheridge et al.*, 1996). Often, the mole fraction for CO_2 is expressed in the unit 'parts per million', which we abbreviate as 'ppm'. Nowadays the global mean CO_2 mole fraction has surpassed the level of 400 ppm (*Betts et al.*, 2016).

One of the first measurement series of atmospheric CO_2 was started in 1958 by Charles D. Keeling from the Scripps Institution of Oceanography (SIO) at the top of the volcano Mauna Loa in Hawaii (*Keeling et al.*, 1976). Because of its location on an island far away from land masses, and with relatively small local sources and sinks of CO_2, air sampled at Mauna Loa is considered to be representative for the Northern Hemisphere. From 1974 onward, measurements at Mauna Loa were also conducted by the National Oceanic and Atmospheric Administration (NOAA) Earth System Research Laboratory (ESRL) as described by *Thoning et al.* (1989). The combined CO_2 record from Scripps and NOAA

is shown in Fig. 1.1.

The CO_2 time series from Mauna Loa in Fig. 1.1 shows a long-term increasing trend, which reflects that the sources of CO_2 dominate the sinks of CO_2 on the annual time scale for the contemporary carbon cycle. On top of this long-term increase, there is a distinct 'wiggle', which is related to the growth cycle of vegetation, that will be addressed in more detail in Sect. 1.3. The interannual variability in the CO_2 growth rate, and its relation to large-scale droughts, will be discussed in Sect. 1.4.

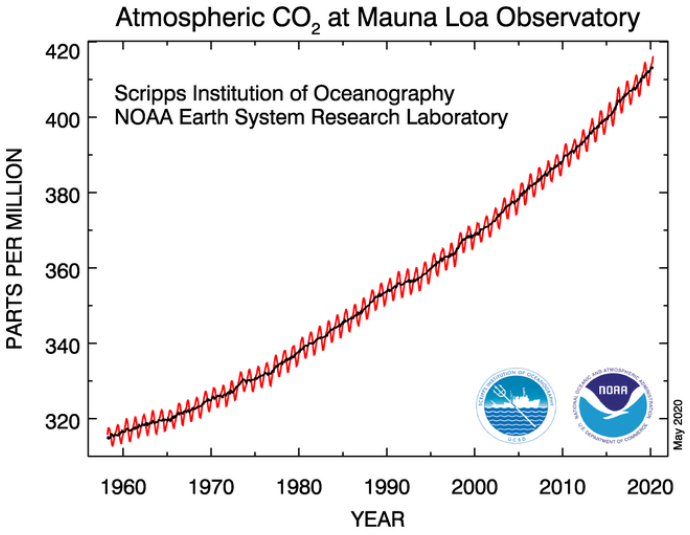

Figure 1.1: Dry air mole fraction of CO_2 measured at the Mauna Loa Observatory by the Scripps Institution of Oceanography (SIO) and the NOAA Earth System Research Laboratory (ESRL). The red curve represents the monthly average values and the black curve is the deseasonalized CO_2 mole fraction. Figure retrieved from `https://www.esrl.noaa.gov/gmd/ccgg/trends/` in May 2020.

At the end of the 19$^{\text{th}}$ century Svante Arrhenius (1859-1927) described that atmospheric CO_2 can trap heat in the climate system and thus increase global temperatures (*Arrhenius*, 1896), which is often referred to as the 'greenhouse effect'. Increased temperatures can have many consequences, an example that receives a lot attention in popular media is sea water level rise, which is a threat for many coastal areas that are essential for the lives of a large number of people (*IPCC*, 2014).

The climate system is complex and there are many positive and negative feedbacks. Examples of both are respectively the ice-albedo feedback (less ice leads to a reduction of surface reflection, which results in more heat from solar radiation being trapped in the Earth system) and the cloud-albedo feedback (more heat means more evaporation and thus more cloud cover, however a larger cloud cover results in more refection of sun light).

The interplay of these different feedbacks in the climate system remains an area of active research (*IPCC*, 2013).

In addition, there are also consequences to the higher concentrations of atmospheric CO_2 that are related to its chemical properties. Increased levels of atmospheric CO_2 lead to higher concentrations of dissolved CO_2 in ocean water. Dissolved CO_2 can dissociate into bicarbonate (HCO_3^-) or carbonate (CO_3^{2-}) and as such increase the acidity of ocean water, which is often referred to as 'ocean acidification'. Decrease of ocean pH is a threat for small organisms living in oceans that are an essential part of the food chain for many organisms (*IPCC*, 2011).

The Mauna Loa measurements started at a time when there was little awareness or concern about increased levels of CO_2 in the atmosphere and its negative consequences, but were mostly driven by scientific curiosity. A systematic measurement series spanning a period of roughly 60 years is unique, especially considering the short time window that is usually considered for funding of scientific research. Even though the rise of atmospheric CO_2 is now a major concern in politics and mainstream media, it is a struggle to maintain funding for the Mauna Loa measurements as described by *Houweling et al.* (2012).

1.2 Global carbon cycle

The change of the atmospheric CO_2 mass over time dM_{CO_2}/dt follows from a simple mass balance of the different sources (fossil fuel combustion F_{ff} and land-use change F_{luc}) and sinks of CO_2 (net uptake by vegetation F_{bio} and oceans F_{oce})

$$\frac{d}{dt}M_{CO_2} = F_{\text{ff}} + F_{\text{luc}} + F_{\text{bio}} + F_{\text{oce}}. \tag{1.1}$$

An estimate of these numbers is annually reported by the Global Carbon Project (GCP) initiative, which is used as input for the Intergovernmental Panel on Climate Change (IPCC). Fig. 1.2 is taken from *Le Quéré et al.* (2016) and summarizes the global carbon budget for the decade 2006-2015.

Fig. 1.2 shows that the main source of CO_2 is the combustion of fossil fuels and industry emissions, while the contribution from land-use change is an order of magnitude smaller. The relative uncertainty in the emission from fossil fuel combustion is small compared to the other sources and sinks, which reflects the fact that the production and consumption

of fossil fuels is well documented by the different statistical government agencies (*Andres et al.*, 2012).

According to the numbers in Fig. 1.2, roughly half of the carbon emitted stays in the atmosphere as CO_2. The fraction of emitted CO_2 that remains in the atmosphere is often referred to as the 'airborne fraction' (*Keeling*, 1973; *Gloor et al.*, 2010). The uncertainty on the reported growth rate is small, because the CO_2 concentration can be measured accurately (as e.g. shown for Mauna Loa in Fig. 1.1) from which the global growth rate of CO_2 can be estimated well.

The CO_2 that does not end up in the atmosphere must have a different destination. We now know that roughly half of it is taken up by the biosphere and the other half by oceans (Fig. 1.2). Uptake of CO_2 by oceans is predicted by Henry's law that describes the equilibrium between CO_2 in the gas phase and dissolved CO_2. Contrary to this, the uptake of CO_2 by the biosphere was not so obvious and establishing this 'missing sink' has been one of the major topics in the carbon cycle community (*Siegenthaler and Sarmiento*, 1993) .

The estimate for the land sink reported in Fig. 1.2 was obtained by estimating all other terms and closing the budget given in Eq. (1.1). More recent versions of the GCP estimates use a direct method to estimate biosphere fluxes (*Le Quéré et al.*, 2018a,b; *Friedlingstein et al.*, 2019) and also report the 'budget imbalance', which is the difference between the left-hand-side and right-hand-side of Eq. (1.1).

The relative magnitude of the ocean and biosphere sinks can also be estimated from the change in atmospheric oxygen (O_2). The uptake of CO_2 by oceans does not affect O_2, whereas the uptake of CO_2 by the biosphere (described in more detail in Sect. 1.3) is a source of O_2 in a $\sim$1:1 ratio. *Keeling et al.* (1996) showed how the uptake of CO_2 by oceans and the biosphere can be distinguished using precise measurements of CO_2 and O_2. The use of a specific compound, usually referred to as a 'tracer', to disentangle different processes is an often used method in studying the carbon cycle and we will encounter more examples in the following sections.

1.3 Biosphere-atmosphere exchange

The uptake of CO_2 by vegetation is driven by light (with a wavelength in the range of 400-700 nm) through the photosynthesis process that occurs in chloroplasts inside leaves.

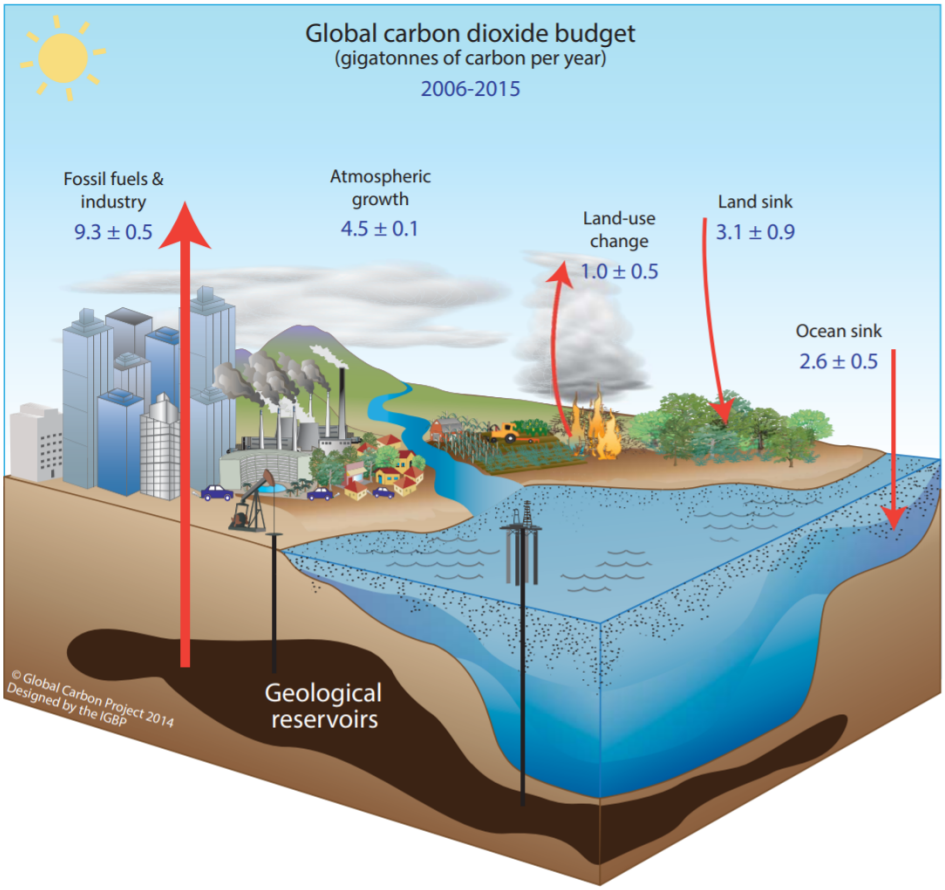

Figure 1.2: Schematic representation of the carbon cycle for the years 2006-2015. The reported numbers are the fluxes and their uncertainty given in petagrams (10^{15}g) of carbon per year (PgC/yr, which is equal to the often used non-SI unit GtC/yr). Note that the land sink and ocean sink are reported here as positive numbers, these should be multiplied with -1 according to our sign convention. Figure taken from *Le Quéré et al.* (2016).

Photosynthesis converts CO_2 into sugars while producing O_2 and consuming H_2O.

$$6\ CO_2 + 6\ H_2O \xrightarrow{\text{light}} C_6H_{12}O_6 + 6\ O_2 \tag{1.2}$$

The CO_2 required for photosynthesis enters the leaf through small openings called 'stomates'. Plants also loose water through these stomates through transpiration. To avoid the loss of too much water, plants can (partly) close the stomates, as we will discuss in more detail in Sect. 1.4.

Plants also consume sugars and respire CO_2 that is produced through the opposite reaction of Eq. (1.2) for growth and maintenance. Respiration by plants is referred to as 'autotrophic respiration'. The decomposition of organic material (e.g. the decomposition

of shedded leaves by micro organisms) is also a biospheric source of CO_2, that is referred to as 'heterotrophic respiration'.

The total exchange of CO_2 is often referred to as Net Ecosystem Exchange (NEE). The photosynthetic CO_2 flux is called Gross Primary Production (GPP) and the sum of autotrophic and heterotrophic is termed Terrestrial Ecosystem Respiration (TER), and these fluxes are related as follows

$$\mathrm{NEE} = \mathrm{GPP} + \mathrm{TER} \tag{1.3}$$

For convenience we use the the 'atmospheric' sign convention, which means that GPP is negative or zero, TER is positive or zero, and the sign of NEE, which varies strongly with space and time across the globe, determines the net effect of photosynthesis and respiration.

The seasonal variation on top of the increasing long-term trend in Fig. 1.1 is related to the seasonality of vegetation. During the Northern Hemisphere spring and summer, CO_2 is taken up by the biosphere (i.e. $\mathrm{NEE} < 0$), whereas it is released during the autumn and winter (i.e. $\mathrm{NEE} > 0$). At the global scale, the seasonal cycle of the Northern Hemisphere dominates that of the Southern Hemisphere since it contains more vegetation.

Measurements of CO_2 fluxes over a forest, grassland or other ecosystem can be obtained using the eddy covariance (EC) technique (*Baldocchi et al.*, 1988). In this method, the concentration of CO_2 (or a different gas) is measured simultaneously with the vertical wind velocity at a point above the surface with a sufficiently high frequency ($\sim$1 Hz). Due to turbulence, both the concentration and vertical velocity will fluctuate over time. The net flux can then be determined by correlating the velocity fluctuations with concentration fluctuations, typically averaged over a period of half an hour.

Using the EC technique the net flux of CO_2 can be measured directly, but not the individual contributions of GPP and TER. A popular method for partitioning the fluxes makes use of the fact that photosynthesis cannot occur at night and that nighttime EC measurements thus only represent respiration (*Reichstein et al.*, 2005). Since nighttime EC measurement are less reliable, alternative methods are available for partitioning photosynthesis and respiration from daytime EC observations using additional measurements of incoming light and humidity (*Lasslop et al.*, 2010). A large compilation of CO_2 flux measurements from different ecosystems partitioned using the nighttime and daytime method is made available by the FLUXNET community (*Baldocchi et al.*, 2001; *Pastorello et al.*,

2017).

Partitioning CO_2 fluxes into GPP and TER using the EC technique is only feasible for areas of $\sim$1 km^2, so this cannot be used to quantify GPP for large ecosystems. To estimate GPP at the global scale, *Beer et al.* (2010) applied machine learning methods to the FLUXNET database to derive patterns between GPP and environmental conditions. Using these relations, the magnitude of global GPP was estimated to be 123$\pm$8 PgC/yr. Using the net land uptake from Fig. 1.2 and Eq. (1.3), this estimate implies that global TER is approximately 120 PgC/yr.

Another estimate of global GPP was made by *Welp et al.* (2011) based on the ^{18}O isotopic composition of CO_2 measured at atmospheric stations following large El Niño events. El Niño is a large scale climate event that has a strong effect on the global distribution of precipitation and that perturbs the oxygen isotopic composition of CO_2. The exponential recovery of the isotopic composition observed at atmospheric stations is a measure for the magnitude of exchange between CO_2 and terrestrial water in leaves (discussed in more detail in Sect. 1.5.1), from which global GPP was estimated to be 150-175 PgC/yr.

The large range of the current estimates of global GPP reflects the difficulty in estimating this number. The magnitude of GPP (and thus also TER) is much larger than that of the net fluxes described in Fig. 1.2. Climate feedbacks act on these individual processes, and a small perturbation of either GPP or TER could result in a large shift of the global CO_2 budget (*Booth et al.*, 2012). Improved estimates of GPP and its feedbacks are thus essential for more accurate predictions of future climate and carbon cycling.

A promising tracer for GPP is carbonyl sulfide (COS), which is an atmospheric compound with a mole fraction of about 400 ppt (i.e. $400 \cdot 10^{-6}$ ppm). Similar to CO_2, COS can diffuse through stomates and is taken up inside leaves. Unlike CO_2, COS does not have a source in vegetation and can therefore give more direct information on the uptake of CO_2 by vegetation. *Montzka et al.* (2007) were the first to recognize the similarities in the seasonal cycles of CO_2 and COS. Shortly after that, *Campbell et al.* (2008) were the first to use COS fluxes to constrain GPP during the growing season over North America. Recently, *Kooijmans et al.* (2019) studied the influence of light and humidity on CO_2 and COS uptake in a boreal forest, and their findings can improve COS-based GPP estimates.

1.4 The Amazon and drought sensitivity

We briefly discussed feedbacks between increasing CO_2 levels and the climate system in Sect. 1.1. There are also feedbacks between climate and the carbon cycle. One of the mechanisms is 'CO_2 fertilization', which describes that due to higher atmospheric CO_2 levels, plants can take up more carbon. Based on the increasing amplitude of the seasonal cycles of CO_2 observed at measurement station Barrow, *Graven et al.* (2013) concluded that the magnitude of GPP on the Northern Hemisphere is indeed increasing.

In addition to CO_2 fertilization, there are also possible feedback mechanisms that negatively impact the uptake of CO_2 by vegetation. Higher temperatures could trigger more fires and the frequency of large scale droughts could increase. In fact, *Langenfelds et al.* (2002) showed that the interannual variability (IAV) in the CO_2 growth rate is strongly coupled to the tropical terrestrial biosphere. A better understanding of the response of tropical ecosystems to changing climatic conditions is therefore crucial.

Beer et al. (2010) estimates that the tropical biomes represent ∼60% of global GPP and from all tropical biomes the Amazon is by far the largest, containing nearly 50% of the above ground biomass (*Saatchi et al.*, 2011). In 2005 and 2010 the Amazon was affected by large scale droughts that were both characterized as a 1 in a 100 year event (*Lewis et al.*, 2011). These events and the more recent 2015/2016 drought indeed correspond to years with large peaks in the global CO_2 growth rate reported by NOAA.

Gatti et al. (2014) analyzed the effect of the 2010 drought on the Amazon carbon cycle based on air samples collected over the Amazon with small aircraft. Measurements of CO and CO_2 were used to estimate CO_2 emissions from fires and net biome exchange. It was concluded that during the drought of 2010 the Amazon became a net source of CO_2 to the atmosphere (including the CO_2 emissions from fires), whereas the forest is a sink of CO_2 in the 'normal' year 2011. *van der Laan-Luijkx et al.* (2015) repeated this analysis in a full atmospheric inversion, described in more detail in Sect. 1.5.3.

An interesting tracer that carries information on the uptake of carbon and the loss of water by vegetation is the ^{13}C isotopic composition of CO_2. Plants prefer to take up the lighter $^{12}CO_2$ rather than the heavier $^{13}CO_2$. This effect is caused by faster diffusion of $^{12}CO_2$ through stomates, but is even stronger for the assimilation rates by the Rubisco enzyme that is part of the photosynthetic pathway. During droughts plants reduce their stomatal conductance to avoid excessive loss of water, such that the 'discrimination' by the Rubisco enzyme becomes less dominant and the overall discrimination between $^{12}CO_2$

and $^{13}CO_2$ reduces. Recently it was demonstrated that the increase of water use efficiency during droughts has a measurable impact on the ^{13}C isotopic composition of atmospheric CO_2 (*Peters et al.*, 2018).

Also, *Keeling et al.* (2017) demonstrated that the increase of CO_2 over the last decades has resulted in an increase of discrimination by vegetation that is apparent in the ^{13}C isotopic composition of CO_2 over the past decades. They describe that plants are able to operate at lower stomatal conductance, thus being able to grow more efficiently. The increase of water-use efficiency for tropical ecosystems was also demonstrated from $\delta^{13}C$ measurements of tree rings (*van der Sleen et al.*, 2015). These examples illustrate that ^{13}C is a versatile tracer of the terrestrial carbon cycle for drought events that occur at time scales of months, but also contains information on processes that occur at time scales of decades.

1.5 Novel monitoring methods

1.5.1 Triple oxygen isotope signature

There are three stable isotopes of oxygen: ^{16}O, ^{17}O and ^{18}O. Since these are oxygen atoms, they all consist of a nucleus with 8 protons, complemented with 8, 9 and 10 neutrons, respectively. The relative abundance of 'normal' CO_2 in the atmosphere is 99.5%, while the abundances of $C^{17}OO$ and $C^{18}OO$ are only 0.077% and 0.41%, respectively (e.g. *Eiler and Schauble*, 2004).

We can express the oxygen isotopic composition of a sample using 'delta notation' relative to an international reference (e.g. Vienna Standard Mean Ocean Water (VSMOW) for oxygen isotopes)

$$\delta^n O = \frac{[^nO/^{16}O]_{\text{sample}}}{[^nO/^{16}O]_{\text{reference}}} - 1 \quad \text{for} \quad n = 17 \text{ or } 18 \tag{1.4}$$

Because variations in the isotopic composition are usually small, the δ values are expressed in per mill (i.e. per thousand) denoted by the symbol '‰' (e.g. *Meijer and Li*, 1998).

The isotopic composition of a sample can change when a certain process affects the isotopes differently, which is called 'fractionation'. An example is the diffusion of molecules

through a narrow opening (e.g. the leaf stomates described in Sect. 1.3), which occurs faster for lighter molecules. This is an example of a mass dependent process, where the fractionation for $C^{18}OO$ is roughly twice as much as for $C^{17}OO$ (since ^{17}O has one additional neutron relative to ^{16}O, whereas ^{18}O has two additional neutrons).

There are also some processes known where the fractionation is not mass dependent, which is called mass-independent fractionation (MIF). An example of this is the production of ozone (O_3) from molecular oxygen (O_2), for which the enrichments in ^{17}O and ^{18}O are roughly equal (*Heidenreich and Thiemens*, 1983). This can be expressed by the '^{17}O-excess' or the 'triple oxygen isotope ratio', that is defined as

$$\Delta^{17}O = \ln(\delta^{17}O + 1) - \lambda_{RL} \cdot \ln(\delta^{18}O + 1) \tag{1.5}$$

Using the Taylor series expansion $\ln(x+1) \approx x$ for x close to 1, we can approximate this to the following more intuitive equation

$$\Delta^{17}O \approx \delta^{17}O - \lambda_{RL} \cdot \delta^{18}O \tag{1.6}$$

Here λ_{RL} is referred to as the 'slope of the reference line' and it has a value close to 0.5. Different values are used in different fields of study and also the logarithmic and linear definitions in Eqs. (1.5) and (1.6) are both used in different studies which should be taken into account when interpreting reported $\Delta^{17}O$ signatures.

The oxygen isotopes in stratospheric ozone can be transferred to stratospheric CO_2 through the highly energetic $O(^1D)$ oxygen radicals (*Yung et al.*, 1991), which leads to positive $\Delta^{17}O$ signatures in stratospheric CO_2 as observed by *Thiemens et al.* (1995a) and several others later. Through atmospheric mixing, CO_2 with positive $\Delta^{17}O$ signature gets into the troposphere where CO_2 can come into contact with liquid water. When CO_2 dissolves into water, it can exchange oxygen isotopes with water molecules, which has a $\Delta^{17}O$ signature close to 0 (*Luz et al.*, 1999). One would expect that most exchange between CO_2 would occur between the air-sea interface or in clouds, however it turns out that the exchange between CO_2 and water occurs mostly inside leaves due to the presence of the enzyme carbonic anhydrase, which speeds up the dissolution of CO_2 in water by several orders of magnitude (*Francey and Tans*, 1987).

The $\Delta^{17}O$ signature of atmospheric CO_2 is thus a dynamic balance between stratospheric production ($\Delta^{17}O \gg 0$) and exchange with leaf water ($\Delta^{17}O \approx 0$). Since the exchange

with leaf water scales with GPP, the tropospheric $\Delta^{17}O$ is a potential tracer of GPP, as was first recognized by *Hoag et al.* (2005). The mechanisms behind the application of $\Delta^{17}O$ in CO_2 as a tracer for GPP are summarized in Fig. 1.3. They also noted that a major advantage of $\Delta^{17}O$ over $\delta^{18}O$ is that the former is less sensitive to hydrological processes (e.g. evaporation), since these processes are mass-dependent and therefore have a limited effect on the $\Delta^{17}O$ signature of the leaf water.

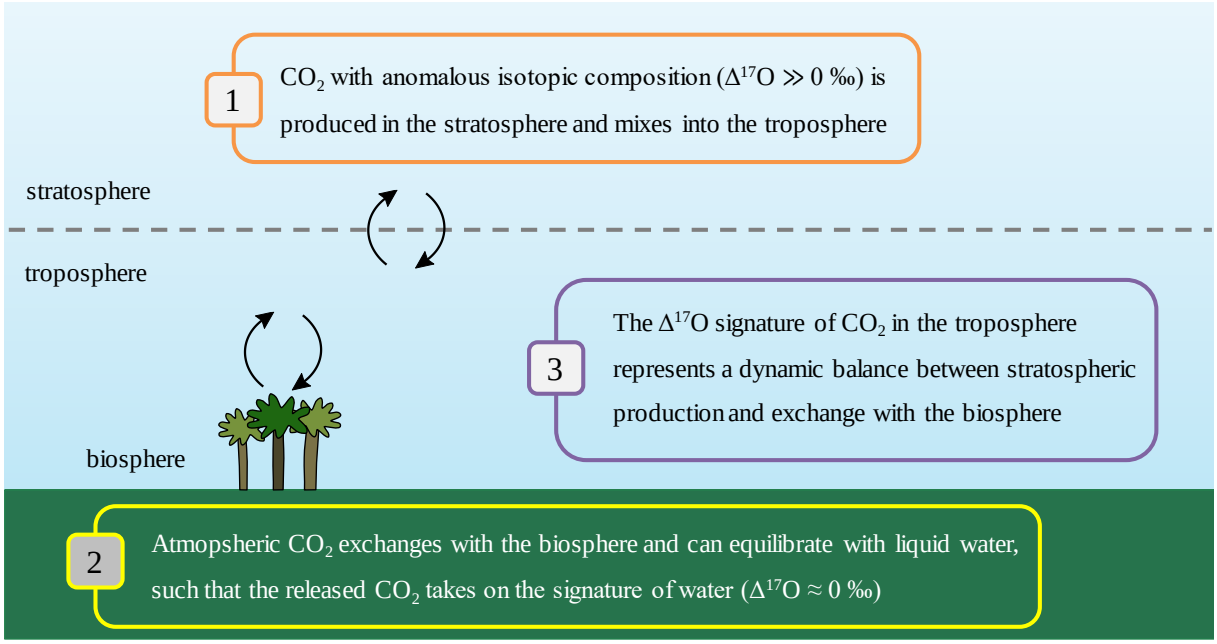

Figure 1.3: Simplified balance for $\Delta^{17}O$ in atmospheric CO_2. The numbered items correspond to processes that are essential for the application of $\Delta^{17}O$ in CO_2 as a tracer for GPP. A more detailed version of this conceptual figure is provided later in this thesis (Fig. 2.1).

1.5.2 Sun-induced fluorescence and near-infrared reflection from vegetation

Sun-induced fluorescence (SIF) is the release of light by plants during photosynthesis. A schematic illustration of the incoming radiation and the photons released through fluorescence is shown in Fig. 1.4. The amount of photons re-emitted as fluorescence is ~1% of the incoming radiation, and has smooth spectral distribution in the range 650-850 nm with a 'red peak' at ~680 nm and a 'far-red peak' at ~740 nm (*Frankenberg and Berry*, 2018).

Frankenberg et al. (2011) showed that SIF can be detected from the Japanese Greenhouse Gases Observing Satellite (GOSAT) and that the spatial and temporal patterns correlate

strongly with those in the machine learned GPP product from *Beer et al.* (2010).

Lee et al. (2013) studied SIF from GOSAT over the Amazon for the years 2009 and 2010 and found that SIF was lower in the dry year 2010, suggesting that GPP was reduced during the drought. More recently, *Liu et al.* (2017) used GOSAT SIF to estimate a reduction of 0.9 PgC for the Amazon during the 2015 El Niño drought. Drawbacks of GOSAT are the relatively coarse spatial and temporal resolution, thus limiting the possibility to study differences across the Amazon basin.

SIF is also retrieved from the Global Ozone Monitoring Experiment 2 (GOME-2) instrument onboard the MetOp satellites. A popular SIF product from this platform was produced by *Joiner et al.* (2013, 2016). However, recently a new SIF retrieval algorithm was developed at the Royal Netherlands Meteorological Institute (KNMI) and Wageningen University & Research (WUR), that is particularly suited for humid tropical environments (*Kooreman et al.*, 2018; *van Schaik et al.*, 2020).

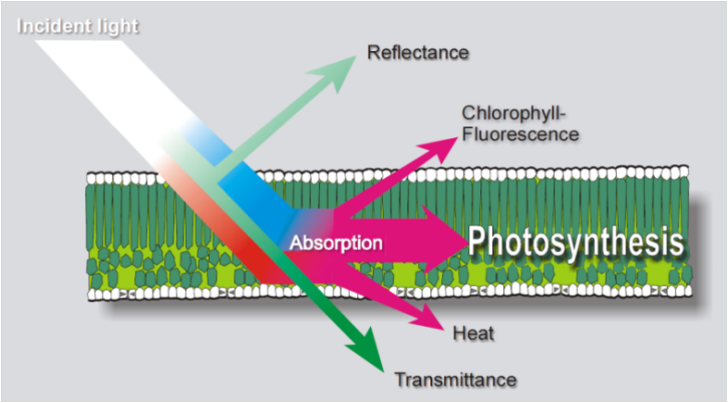

Figure 1.4: Schematic representation of a chloroplast with incident light and possible follow-up pathways for the redistribution of the energy from the incoming photon. Figure taken from *Davidson et al.* (2003).

Another proxy for photosynthesis from satellites is near infrared reflectance from vegetation (NIRv), that was recently introduced by *Badgley et al.* (2017). NIRv is defined as the product of (soil corrected) normalized difference vegetation index (NDVI) with near infrared reflectance (NIR)

$$\text{NIRv} = (\text{NDVI} - c) \cdot \text{NIR} \quad \text{with} \quad \text{NDVI} = \frac{\text{NIR} - \text{red light}}{\text{NIR} + \text{red light}} \tag{1.7}$$

Here c is a soil correction variable, for which a value of 0.08 was proposed by *Badgley et al.* (2017). For a given pixel, soil corrected NDVI represents the amount of vegetation

in that pixel and NIR represents the amount of reflected radiation (also shown in Fig. 1.4) in that pixel. NIRv is determined by the orientation of the leaf and the structure of the canopy, which in turn has a high correlation with the photosynthetic uptake. Annual mean SIF and NIRv over part of South America is shown in Fig. 1.5.

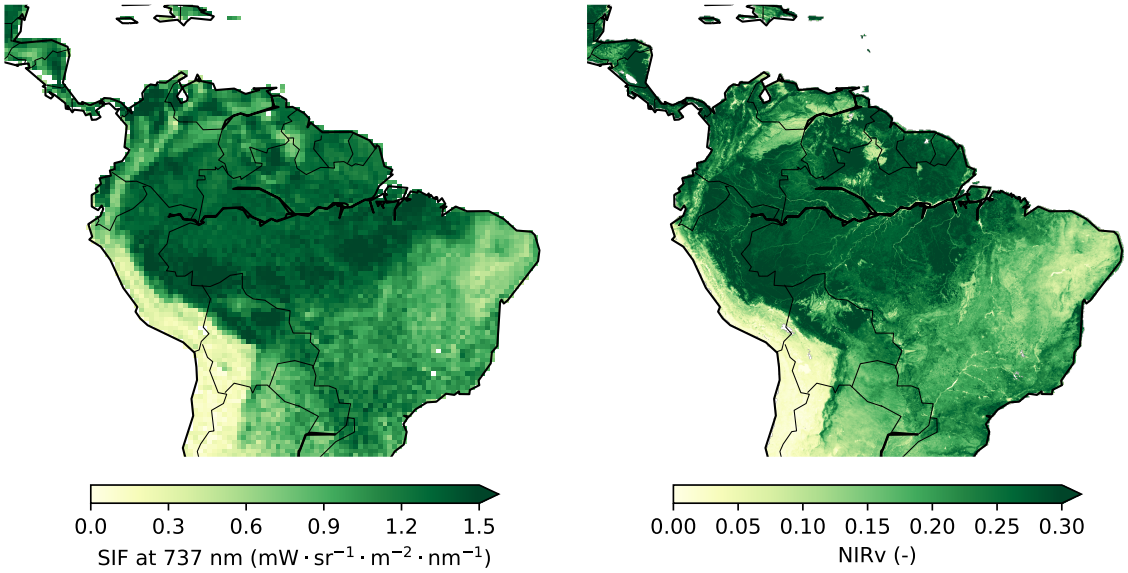

Figure 1.5: Annual mean GOME-2 SIF from *van Schaik et al.* (2020) at a 0.5°×0.5° spatial resolution (left) and NIRv calculated from MODIS surface reflectance at a 0.05°×0.05° spatial resolution (right). Regions with high SIF and NIRv correspond to regions with high GPP.

1.5.3 Inverse modelling

The general goal of inverse modelling in atmospheric sciences, is to estimate surface emissions based on atmospheric observations and prior information. More specifically, a state vector $\boldsymbol{x}$ representing surface emissions is adjusted such that the value of a cost function $J(\boldsymbol{x})$ is minimal.

$$J(\boldsymbol{x}) = (\boldsymbol{y}^{\mathrm{o}} - \mathcal{H}(\boldsymbol{x}))^{\mathrm{T}}\mathbf{R}^{-1}(\boldsymbol{y}^{\mathrm{o}} - \mathcal{H}(\boldsymbol{x})) + (\boldsymbol{x} - \boldsymbol{x}^{\mathrm{b}})^{\mathrm{T}}\mathbf{P}^{-1}(\boldsymbol{x} - \boldsymbol{x}^{\mathrm{b}}) \tag{1.8}$$

The cost function $J(\boldsymbol{x})$ contains the prior fluxes $\boldsymbol{x}^{\mathrm{b}}$, atmospheric observations $\boldsymbol{y}^{\mathrm{o}}$ and an observation operator $\mathcal{H}$. In the case of atmospheric inversions, the observation operator is usually an atmospheric transport model (e.g. TM5, *Krol et al.*, 2005) that simulates atmospheric concentrations for a given set of fluxes. The matrices $\mathbf{R}$ and $\mathbf{P}$ are respectively the error covariance matrices for the observations and the prior fluxes. The fluxes

that result in a minimal cost function are referred to as 'optimized' fluxes or 'posterior' fluxes.

There exist several methods to obtain an optimal solution, including variational methods (e.g. the TM5-4DVAR system), in which the derivative of the cost function is approximated and ensemble methods (e.g. the ensemble Kalman filter used in CarbonTracker, *Peters et al.*, 2005). Advantages of the ensemble data assimilation methods are, that they (1) do not require an adjoint model or other linearization of the observation operator; and (2) also produce an uncertainty estimate for the optimized fluxes. A version of CarbonTracker dedicated to South-America was used by *van der Laan-Luijkx et al.* (2015) to estimate CO_2 fluxes over the Amazon during the drought year 2010 and the 'normal' year 2011.

1.6 Thesis outline

Here we describe the research questions that are central in this thesis.

RQ1: What are the expected spatiotemporal patterns of $\Delta^{17}O$ in tropospheric CO_2 and are these within the detectable range for currently available instruments?

This question is addressed in Chapter 2. We describe a model framework based on the terrestrial biosphere model SiBCASA (*Schaefer et al.*, 2008) and the transport model TM5 (*Krol et al.*, 2005). The seasonal variations and spatial patterns of simulated $\Delta^{17}O$ in CO_2 are shown and for several locations these variations are within the detectable range of currently available instruments. In addition, we report the sensitivity of the simulated $\Delta^{17}O$ to changes in the stratospheric source strength, the magnitude of soil invasion, variations in the $\Delta^{17}O$ signature in water soil and leaf water, and the contribution of atmospheric CO oxidation.

RQ2: How large is the observed diurnal cycle of $\Delta^{17}O$ in CO_2 in a forest, and which processes are needed to simulate this diurnal cycle?

In Chapter 3 we study the diurnal variations of $\Delta^{17}O$ at the ecosystem level. We implemented a 'tracer tagging' technique in our 3-D model and simulated the contribution of different processes to the diurnal cycle of $\Delta^{17}O$ in CO_2. In addition, we implemented $\Delta^{17}O$ in the MXL model that already included $\delta^{13}C$ and $\delta^{18}O$ (*Vilà-Guerau de Arellano et al.*, 2019). This model simulates tracer budgets in the convective boundary layer and was shown to be able to represent the isotopic composition and fluxes for Harvard Forest

(*Wehr et al.*, 2013). Finally, we compared our model simulations with an observed diurnal cycle of $\delta^{13}C$, $\delta^{18}O$, $\Delta^{17}O$ obtained from a 25-m tower and close to the surface in the mid-latitude pine forest Loobos (*Dolman et al.*, 2002; *Elbers et al.*, 2011).

RQ3: What is the GPP response of the Amazon forest to the 2015/2016 El Niño, as diagnosed from sun-induced fluorescence?

In Chapter 4 we use SIF to analyze the development of the drought in the Amazon following the 2015 El Niño and the subsequent recovery. In our analysis we separate the Amazon forest into three different sub-regions based on the Köppen climate zones. In addition, we translate the SIF anomalies into GPP anomalies and quantify the reduction of photosynthesis during the drought.

RQ4: What is the variability in CO_2 exchange over the Amazon for the years 2010-2017, and how does this relate to environmental drivers?

In Chapter 5 we use the inverse modelling system CarbonTracker to estimate the net ecosystem exchange for the Amazon region over the period 2010-2017 with a focus on the legacy effect of the 2015/2016 El Niño drought. In addition, we use both SIF and NIRv to attribute changes in the inverted NEE fluxes to changes in GPP or TER.

2

Global 3-D simulations of the triple oxygen isotope signature $\Delta^{17}O$ in atmospheric CO_2

The triple oxygen isotope signature $\Delta^{17}O$ in atmospheric CO_2, also known as its '^{17}O-excess', has been proposed as a tracer for Gross Primary Production (GPP; the gross uptake of CO_2 by vegetation through photosynthesis). We present the first global 3D model simulations for $\Delta^{17}O$ in atmospheric CO_2 together with a detailed model description and sensitivity analyses. In our 3D model framework we include the stratospheric source of $\Delta^{17}O$ in CO_2 and the surface sinks from vegetation, soils, ocean, biomass burning and fossil fuel combustion. The effect of oxidation of atmospheric CO on $\Delta^{17}O$ in CO_2 is also included in our model. We estimate that the global mean $\Delta^{17}O$ (defined as $\Delta^{17}O = \ln(\delta^{17}O+1) - \lambda_{RL} \cdot \ln(\delta^{18}O+1)$ with $\lambda_{RL} = 0.5229$) of CO_2 in the lowest 500 m of the atmosphere is 39.6 per meg, which is ∼20 per meg lower than estimates from existing

This chapter is published as: Koren, G., Schneider, L., van der Velde, I.R., van Schaik, E., Gromov, S.S., Adnew, G.A., Mrozek Martino, D.J., Hofmann, M.E.G., Liang, M.-C., Mahata, S., Bergamaschi, P., van der Laan-Luijkx, I.T., Krol, M.C., Röckmann, T, and Peters, W. (2019). Global 3-D simulations of the triple oxygen isotope signature $\Delta^{17}O$ in atmospheric CO_2. Journal of Geophysical Research: Atmospheres, 124, 8808– 8836. https://doi.org/10.1029/2019JD030387.

box models. We compare our model results with a measured stratospheric $\Delta^{17}O$ in CO_2 profile from Sodankylä (Finland), which shows good agreement. In addition, we compare our model results with tropospheric measurements of $\Delta^{17}O$ in CO_2 from Göttingen (Germany) and Taipei (Taiwan), which shows some agreement but we also find substantial discrepancies that are subsequently discussed. Finally, we show model results for Zotino (Russia), Mauna Loa (United States), Manaus (Brazil) and South Pole, which we propose as possible locations for future measurements of $\Delta^{17}O$ in tropospheric CO_2 that can help to further increase our understanding of the global budget of $\Delta^{17}O$ in atmospheric CO_2.

2.1 Introduction

Oxygen has three naturally occurring stable isotopes ^{16}O, ^{17}O and ^{18}O, of which ^{16}O is by far the most abundant on Earth. For atmospheric CO_2, the relative abundances of $C^{16}O^{16}O$, $C^{17}O^{16}O$ and $C^{18}O^{16}O$ are 99.5%, 0.077% and 0.41%, respectively (see e.g. *Eiler and Schauble*, 2004). We can quantify the oxygen isotopic composition of a sample as

$$\delta^n = \frac{\left[{}^nO/{}^{16}O\right]_{\text{sample}}}{\left[{}^nO/{}^{16}O\right]_{\text{VSMOW}}} - 1, \tag{2.1}$$

where n refers to the rare oxygen isotope (i.e. $n = 17$ or 18), Vienna Standard Mean Ocean Water (VSMOW) is used as the reference standard and δ values are usually expressed in per mill (‰). The isotopic composition of oxygen-containing molecules on Earth, like CO_2 or H_2O, is affected by processes such as diffusion, evaporation and condensation. These processes depend on the mass of the molecules and therefore result in a mass-dependent fractionation of the oxygen isotopes. As a consequence, the variations in $\delta^{17}O$ and $\delta^{18}O$ of oxygen-containing substances on Earth are strongly correlated.

A deviation from the mass-dependent fractionation can be expressed by the $\Delta^{17}O$ signature ('triple oxygen isotope' or '^{17}O-excess'). In this study we consistently use the logarithmic definition for $\Delta^{17}O$ (see Sect. S2.1 for an overview of alternative definitions that are commonly used)

$$\Delta^{17}O = \ln(\delta^{17}O + 1) - \lambda_{\text{RL}} \cdot \ln(\delta^{18}O + 1), \tag{2.2}$$

which is usually expressed in per mill (‰) or per meg (0.001‰), depending on the mag-

nitude of the $\Delta^{17}O$ signature, where λ_{RL} is the reference line. We selected $\lambda_{RL} = 0.5229$, which is equal to the isotopic equilibration constant of CO_2 and water $\lambda_{CO_2-H_2O}$ (*Barkan and Luz*, 2012), since equilibration of CO_2 with water is a key process in our study. As a consequence, the $\Delta^{17}O$ signature of CO_2 that equilibrates with a large amount of water will be reset to the $\Delta^{17}O$ signature of the water reservoir. Relative to this selected reference line λ_{RL}, other mass-dependent processes (e.g. diffusion) result in a minor fractionation of oxygen isotopes (fractionation of $\Delta^{17}O$ due to diffusion is described in Sect. 2.2.3.1).

Stratospheric CO_2 was shown to be anomalously enriched in oxygen isotopes with $\Delta^{17}O \gg 0‰$ in measurement campaigns performed with rockets (*Thiemens et al.*, 1995a), aircraft (*Thiemens et al.*, 1995b; *Boering et al.*, 2004), balloons (*Alexander et al.*, 2001; *Lämmerzahl et al.*, 2002; *Kawagucci et al.*, 2008; *Mrozek et al.*, 2016) or using aircraft and balloons (*Yeung et al.*, 2009; *Wiegel et al.*, 2013). The anomalous isotopic composition of stratospheric CO_2 has been linked to oxygen exchange with stratospheric O_3, which has a positive $\Delta^{17}O$ signature, by *Yung et al.* (1991). Photolysis of O_3 produces the highly reactive radical $O(^1D)$

$$O_3 + h\nu \rightarrow O_2 + O(^1D), \tag{2.3}$$

which can form the unstable CO_3^* when colliding with CO_2, which dissociates into CO_2 and an oxygen radical

$$O(^1D) + CO_2 \rightarrow CO_3^* \rightarrow CO_2 + O(^3P). \tag{2.4}$$

The oxygen atom that is removed by disintegration of CO_3^* is random (except for the small fractionation of a few per mill favoring ^{18}O remaining in the CO_2 product, *Mebel et al.*, 2004), such that there is a $\sim 2/3$ probability that the reactions in Eqs. (2.3) and (2.4) will result in the substitution of an oxygen atom in CO_2 with an oxygen atom that was originally present in O_3. This exchange of oxygen atoms from stratospheric O_3 to CO_2 is responsible for the transfer of the ^{17}O anomaly (i.e. $\Delta^{17}O \gg 0‰$) from stratospheric O_3 to stratospheric CO_2.

In the upper troposphere, there is an influx of stratospheric CO_2 with $\Delta^{17}O \gg 0‰$. Following transport to the troposphere, the CO_2 is mixed and can come into contact with liquid water in vegetation, soils or oceans. When CO_2 dissolves in liquid H_2O, exchange of oxygen atoms occurs, such that the CO_2 that is released back to the atmosphere has

a signature of $\Delta^{17}O \approx 0‰$. The exchange between CO_2 and H_2O in vegetation is highly effective due to the presence of the enzyme carbonic anhydrase, whereas the exchange of oxygen isotopes between CO_2 and cloud droplets is negligible due to the absence of carbonic anhydrase in the atmosphere (*Francey and Tans*, 1987). The resulting $\Delta^{17}O$ signature in tropospheric CO_2 reflects a dynamic balance of highly enriched stratospheric CO_2 and equilibration that occurs in vegetation and other water reservoirs. Tropospheric measurements of $\Delta^{17}O$ in CO_2 have previously been performed in Jerusalem, Israel (*Barkan and Luz*, 2012); La Jolla, United States (*Thiemens et al.*, 2014); Taipei, Taiwan (*Liang and Mahata*, 2015; *Mahata et al.*, 2016b; *Liang et al.*, 2017a,b), Göttingen, Germany (*Hofmann et al.*, 2017) and Palos Verdes, United States (*Liang et al.*, 2017b).

Gross Primary Production (GPP; the gross uptake of CO_2 by vegetation through photosynthesis) is a key process in the carbon cycle which is currently poorly constrained. Increasing our understanding of the terrestrial carbon cycle is essential for predicting future climate and atmospheric CO_2 concentrations (*Booth et al.*, 2012). An estimate of 120 $PgC \cdot yr^{-1}$ for global GPP was provided by *Beer et al.* (2010) by using machine learning techniques to extrapolate a database of eddy-covariance measurements of CO_2 to the global domain. An estimate of 150-175 $PgC \cdot yr^{-1}$ for global GPP was derived by *Welp et al.* (2011) based on the response of $\delta^{18}O$ in atmospheric CO_2 after El Niño/Southern Oscillation events. The large spread in estimates of global GPP clearly indicates our current lack of understanding of the biospheric domain in the global carbon cycle.

Because the $\Delta^{17}O$ signature of tropospheric CO_2 strongly depends on the magnitude of the exchange of CO_2 with liquid water in leaves, it is a potential tracer for GPP, as was first proposed by *Hoag et al.* (2005). Similarly, the $\delta^{18}O$ signature of tropospheric CO_2 has been explored to constrain terrestrial carbon fluxes by *Ciais et al.* (1997a,b), *Peylin et al.* (1997, 1999) and *Cuntz et al.* (2003a,b). The main advantage of using $\Delta^{17}O$ instead of $\delta^{18}O$ is that the signal is less affected by processes in the hydrological cycle (e.g. evaporation and condensation), since these are largely mass-dependent (*Hoag et al.*, 2005). Besides constraining gross terrestrial CO_2 fluxes, other possible applications of $\Delta^{17}O$ in atmospheric CO_2 have been suggested, such as constraining stratospheric circulation and constraining the abundance and variability of $O(^1D)$ (e.g. *Alexander et al.*, 2001).

The first 2-box model for $\Delta^{17}O$ in tropospheric CO_2 for the Northern and Southern Hemisphere was developed by *Hoag et al.* (2005). This conceptual box model takes into account the exchange fluxes of CO_2 between the troposphere and the stratosphere, vegetation and oceans. In addition, the supply of CO_2 from fossil fuel combustion and land-use change is incorporated in the box model. All these CO_2 fluxes are associated with a reservoir-

specific $\Delta^{17}O$ signature. The resulting $\Delta^{17}O$ for tropospheric CO_2 was calculated using a mass balance. Results from *Hoag et al.* (2005) can be converted into our reference frame, as defined in Eq. (2.2), assuming a global $\delta^{18}O$ signature of 41.5‰ (observations from *Francey and Tans* (1987) show that the global mean $\delta^{18}O$ in CO_2 is ∼0‰ PDB-CO_2, which can be converted using Eq. (5) from *Brenninkmeijer et al.* (1983) into 41.5‰ VSMOW), which yields $\Delta^{17}O = 0.066$‰ for tropospheric CO_2.

A more sophisticated global 1-box model was developed by *Hofmann et al.* (2017). This model takes into account that certain processes (e.g. diffusion of CO_2 from the atmosphere into leaf stomata) can fractionate oxygen isotopes and influence the $\Delta^{17}O$ signature of CO_2. Another significant difference with the model from *Hoag et al.* (2005) are the soil invasion fluxes that are taken into account. Also, both models differ in the magnitude of the CO_2 fluxes and the $\Delta^{17}O$ reservoir signatures. Based on a Monte Carlo simulation where the uncertainty in the input variables is considered, *Hofmann et al.* (2017) predict $\Delta^{17}O = 0.061 \pm 0.033$‰ for tropospheric CO_2.

In recent years, there have been developments in the available measurement techniques for $\Delta^{17}O$ in CO_2. *Mahata et al.* (2013, 2016a) developed a measurement technique based on the equilibration between CO_2 and O_2 catalyzed by hot platinum, followed by measurement of the $\Delta^{17}O$ signature of O_2, from which the initial $\Delta^{17}O$ signature of CO_2 can be inferred with a precision of 8 per meg. *Barkan and Luz* (2012) developed a high precision measurement technique based on equilibration of CO_2 and H_2O, resulting in a precision of 5 per meg for $\Delta^{17}O$ in CO_2. Using laser-based techniques, *Stoltmann et al.* (2017) were able to reach a precision for $\Delta^{17}O$ in CO_2 of better than 10 per meg. The quantum cascade laser developed by Aerodyne Research is also able to measure $\Delta^{17}O$ in CO_2 with high precision (*Nelson et al.*, 2008; *McManus et al.*, 2015). In addition, a recently developed ion fragment method allows to measure $\delta^{17}O$ and $\delta^{18}O$ directly on CO_2 without the need of chemical conversion (*Adnew et al.*, 2019). The recent developments in the measurement techniques for $\Delta^{17}O$ in CO_2 are essential for its application as tracer for the terrestrial carbon cycle.

Because of the recent advancements in measurement techniques for $\Delta^{17}O$ in CO_2, it is now possible to observe spatial and temporal gradients of $\Delta^{17}O$ more accurately. To simulate the spatial and temporal variability of the $\Delta^{17}O$ signal in atmospheric CO_2, the available box models are not suitable and a 3D model framework is required. For this purpose, an oxygen isotope module for atmospheric CO_2 was implemented in the atmospheric transport model TM5 (*Krol et al.*, 2005; *Huijnen et al.*, 2010). Results from an early version of our 3D model were compared with the $\Delta^{17}O$ measurement series from

Göttingen, Germany (*Hofmann et al.*, 2017). A detailed description of our updated $\Delta^{17}O$ model is given in Sect. 2.2 and the changes in our current model with respect to the earlier version used by *Hofmann et al.* (2017) are summarized in Sect. S2.2. The model results are reported in Sect. 2.3, followed by the discussion and conclusion in Sects. 2.4 and 2.5.

2.2 Methods

2.2.1 General model description

Our model framework for $\Delta^{17}O$ in atmospheric CO_2 is based on the atmospheric transport model TM5 (*Krol et al.*, 2005), which is driven by ERA-Interim meteorological fields (*Dee et al.*, 2011) provided by the European Centre for Medium-Range Weather Forecasts (ECMWF). TM5 uses a longitude-latitude grid of 6°×4°, 3°×2°, or 1°×1° resolution, depending on the chosen setup. Also, TM5 allows the use of two-way nested zoom regions to simulate with a higher horizontal resolution for specific regions. For the vertical coordinate TM5 uses 25, 34 or 60 hybrid sigma-pressure levels, such that the lowest model levels follow the surface elevation and the higher levels are (almost completely) isobaric. For this study, we performed simulations with the coarsest resolution (i.e. a horizontal resolution of 6°×4° and 25 vertical levels with the highest model level at 47.8 Pa).

In our model we apply two-way CO_2 fluxes, exchanging between the stratosphere, biosphere, soil, ocean and the troposphere and one-way CO_2 fluxes from fossil fuel combustion, biomass burning and oxidation of CO into the troposphere, as illustrated in Fig. 2.1. Modeling the gross two-way exchange fluxes for some reservoirs is necessary to estimate the resulting $\Delta^{17}O$ signature of tropospheric CO_2. The CO_2 fluxes in our model are time and space dependent and can originate from the stratosphere (described in Sect. 2.2.2), the Earth surface (Sect 2.2.3) or are present within the troposphere itself in the case of oxidation of atmospheric CO (Sect. 2.2.4). Also, the $\Delta^{17}O$ signatures of the different reservoirs are indicated in Fig. 2.1. The $\Delta^{17}O$ signatures for stratospheric CO_2, soil water, leaf water and atmospheric CO are time and space dependent in our model. Note that for the exchange fluxes between the atmosphere and biosphere, kinetic fractionation affects the $\Delta^{17}O$ signature (described in Sects. 2.2.3.1 and 2.2.3.2) and that the oxidation of CO by OH is not a mass-dependent process, such that the $\Delta^{17}O$ signature of atmospheric CO is not directly transfered to CO_2 (described in more detail in Sect. 2.2.4).

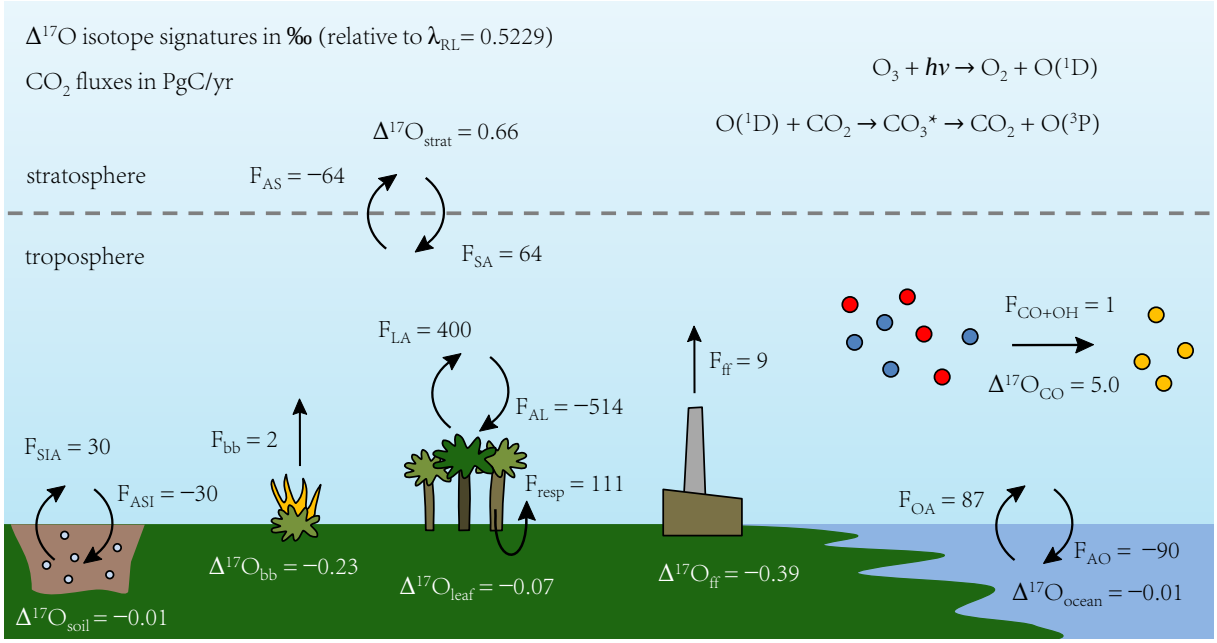

Figure 2.1: Conceptual overview of processes affecting the $\Delta^{17}O$ signature of atmospheric CO_2 in our model. The CO_2 mass fluxes, indicated with symbol F, are given in units of $PgC{\cdot}yr^{-1}$ and $\Delta^{17}O$ signatures are given in ‰ as defined in Eq. (2.2) relative to a reference line $\lambda_{RL} = 0.5229$. The reported values for CO_2 mass fluxes are integrated over the global domain, averaged over the years 2012/2013 (as reported in Table S2.2) and rounded to integer values. As a sign convention, the CO_2 mass fluxes that tend to increase the tropospheric CO_2 mass are expressed as positive numbers. The main source of $\Delta^{17}O$ in tropospheric CO_2 is exchange with the stratosphere (F_{SA} and F_{AS}), as described in Sect. 2.2.2. The stratospheric signature $\Delta^{17}O_{strat}$ in our model is time and space dependent and the indicated value of 0.66‰ is the effective signature that is associated with stratosphere-troposphere exchange (determined from the stratosphere-troposphere CO_2 mass flux and $\Delta^{17}O$ isoflux as reported in Table S2.2). The main sink for $\Delta^{17}O$ in tropospheric CO_2 is the exchange with leaves (F_{AL} and F_{LA}), which is associated with a large uncertainty. Also, the magnitude of the exchange fluxes between the soil and atmosphere (F_{ASI} and F_{SIA}) is uncertain. The implementation of the surface sources and sinks of CO_2 is described in Sect. 2.2.3. Note that the high $\Delta^{17}O_{CO}$ signature is not directly transferred to CO_2 because of fractionation of oxygen isotopes that occurs during the oxidation of CO, as described in Sect. 2.2.4.

In our model framework we implemented CO_2 and $C^{17}OO$ as independent tracers, while assuming a fixed atmospheric signature of $\delta^{18}O = 41.5‰$ VSMOW. With the fixed $\delta^{18}O$, we can translate the imposed boundary conditions (i.e. sources and sinks) of $\Delta^{17}O$ into an equivalent boundary condition for the $\delta^{17}O$ signature, based on Eq. (2.2). Subsequently, the $C^{17}OO$ tracer mass can be determined from the local tracer mass of CO_2 and $\delta^{17}O$ using Eq. (2.1). The $C^{17}OO$ tracer mass can then be transported in our atmospheric model. By again using $\delta^{18}O = 41.5‰$ VSMOW we can 'translate' the simulated $C^{17}OO$ tracer mass back into $\Delta^{17}O$ for analysis. By using a fixed $\delta^{18}O$ signature we are able

to simulate the transport of the $\Delta^{17}O$ signature in CO_2, without the need of explicitly modeling the variations in $\delta^{18}O$ that are strongly related to the water cycle (*Ciais et al.*, 1997a,b; *Peylin et al.*, 1997, 1999; *Cuntz et al.*, 2003a,b). The consequence of this approach is that our model simulated $\delta^{17}O$ can not be directly compared to $\delta^{17}O$ observations. Model output becomes meaningful after converting the simulated $\delta^{17}O$ fields using the fixed $\delta^{18}O$ signature into $\Delta^{17}O$ fields. To convert isotopic signatures to isotope ratios we use $[^{18}O/^{16}O]_{VSMOW} = 2005.20 \cdot 10^{-6}$ (*Baertschi*, 1976) and $[^{17}O/^{16}O]_{VSMOW} = 379.9 \cdot 10^{-6}$ (*Li et al.*, 1988). Note that more recent studies estimate the latter to be slightly higher, $386.7 \cdot 10^{-6}$ and $382.7 \cdot 10^{-6}$ according to *Assonov and Brenninkmeijer* (2003) and *Kaiser* (2008) respectively, but the effect on our simulated $\Delta^{17}O$ is negligible.

We have defined several model parameters that can be set to user-specified values. The motivation for this implementation is that many of the model parameters are uncertain (e.g. the magnitude of the soil invasion flux, as discussed in Sect. 2.2.3.2) and this flexibility allows us to efficiently investigate the sensitivity to these model parameters. An overview of the most important model parameters and the available settings is given in Table 2.1. A more detailed explanation of the model parameters and available settings is given in Sects. 2.2.2-2.2.4. A summary of the model simulations that were conducted in this research is provided in Table 2.2.

2.2.2 Stratospheric source of $\Delta^{17}O$ in CO_2

2.2.2.1 N_2O–$\Delta^{17}O(CO_2)$ correlation

The production of isotopically anomalously enriched CO_2 in the stratosphere has been linked to the exchange of oxygen atoms between O_3 and CO_2 via $O(^1D)$ as described in Sect. 2.1 and shown in Eqs. (2.3) and (2.4). Since the initial discovery of stratospheric CO_2 with $\Delta^{17}O \gg 0‰$, a number of research groups were able to produce anomalously enriched CO_2 from UV-irradiated O_2 or O_3 and CO_2 in controlled laboratory environments (*Wen and Thiemens*, 1993; *Johnston et al.*, 2000; *Chakraborty and Bhattacharya*, 2003; *Shaheen et al.*, 2007; *Wiegel et al.*, 2013). Despite the knowledge gained through these studies, there are currently still many questions remaining regarding the dependence on temperature, pressure, photolysis wavelength and concentrations of O_2, O_3 and CO_2 in the stratosphere. Considering the uncertainties associated with explicitly modeling the production of $\Delta^{17}O$ in CO_2 based on the reactions in Eqs. (2.3) and (2.4), we decided to impose $\Delta^{17}O$ in stratospheric CO_2 based on its observed correlation with N_2O, which we expect to be a more robust approach.

Table 2.1: Overview of the main model parameters and available settings for our $\Delta^{17}O$ model. Note that the soil water signature $\Delta^{17}O_{soil}$ is listed here under the vegetation reservoir but it also affects the soil invasion fluxes. The model results with base settings are described in Sects. 2.3.1.1 and 2.3.1.2. The effect of some of the alternative settings on the model predictions is discussed in Sect. 2.3.1.3.

Reservoir	Section	Model parameter	Base setting	Alternative settings
Stratosphere	2.2.2	$\Delta^{17}O$–N_2O fit	least squares fit	upper/lower 95% confidence limit fit
		$[N_2O]$ fit threshold	240 ppb level	zero or positive value
		relaxation time scale	0 hr (i.e. no relaxation)	zero or positive value
Vegetation	2.2.3.1	soil water $\Delta^{17}O$	distributed from precipitation	constant $\Delta^{17}O_{soil}$
		leaf water $\Delta^{17}O$	dynamic from rel. humidity	constant λ_{transp}
Soil	2.2.3.2	invasion flux magnitude	30 $PgC \cdot yr^{-1}$ globally	zero or positive value
		invasion flux distribution	scaled from CO_2 respiration flux	scaled from H_2 deposition velocity
Ocean	2.2.3.3	CO_2 fluxes	dynamically coupled to $[CO_2]$	calculated from predefined $[CO_2]$
		$C^{17}OO$ fluxes	dynamically coupled to $[C^{17}OO]$	calculated from predefined $[C^{17}OO]$
Atmospheric CO	2.2.4	setting	not included	included with non-zero ϵ_{CO+OH}

Table 2.2: Overview of performed simulations for sensitivity analysis including the base model run. The resulting $\Delta^{17}O$ signature of atmospheric CO_2 and the $\Delta^{17}O$ isofluxes for the base model run are discussed in Sects. 2.3.1.1 and 2.3.1.2. The results of the sensitivity analyses are given in Sect. 2.3.1.3.

Name	Description
`BASE`	Base model run
`ST_LOWER`	95% conf. interval lower limit fit
`ST_UPPER`	95% conf. interval upper limit fit
`SOIL_CONST`	$\Delta^{17}O_{\text{soil}} = -5$ per meg
`LEAF_CONST`	$\lambda_{\text{transp}} = 0.5156$
`RESP_240`	Respiration scaling; glob. magnitude 240 $PgC{\cdot}yr^{-1}$
`RESP_450`	Respiration scaling; glob. magnitude 450 $PgC{\cdot}yr^{-1}$
`HYD_240`	H_2 deposition scaling; glob. magnitude 240 $PgC{\cdot}yr^{-1}$
`HYD_450`	H_2 deposition scaling; glob. magnitude 450 $PgC{\cdot}yr^{-1}$
`CO_ROCK`	$\epsilon_{\text{CO+OH}}$ from *Röckmann et al.* (1998b)
`CO_FEIL`	$\epsilon_{\text{CO+OH}}$ from *Feilberg et al.* (2005)

The correlation between N_2O and $\Delta^{17}O$ in CO_2 was first used by *Luz et al.* (1999) to estimate the stratospheric influx of $\Delta^{17}O$ for CO_2 and O_2 into the troposphere. *Boering et al.* (2004) describe that atmospheric transport is the physical mechanism behind the N_2O–$\Delta^{17}O(CO_2)$ correlation, as both N_2O and $\Delta^{17}O$ in CO_2 are long-lived tracers (the lifetime of N_2O is approx. 120 years; *Volk et al.*, 1997). The negative slope of the N_2O–$\Delta^{17}O(CO_2)$ correlation is explained by the opposite effect of stratospheric photochemistry on N_2O and $\Delta^{17}O$ in CO_2 ($\Delta^{17}O$ in CO_2 is produced from $O(^1D)$ originating from O_3 photolysis, as described in Sect. 2.1, and N_2O is removed by photolysis and $O(^1D)$, as described in Sect. 2.2.2.2).

Experimental datasets for stratospheric N_2O and $\Delta^{17}O$ in CO_2 from *Thiemens et al.* (1995a), *Boering et al.* (2004), *Kawagucci et al.* (2008) and *Wiegel et al.* (2013) were examined to test the robustness of the N_2O–$\Delta^{17}O(CO_2)$ correlation. The $\Delta^{17}O$ values for these studies were recalculated from the reported $\delta^{17}O$ and $\delta^{18}O$ signatures using the definition of $\Delta^{17}O$ as given in Eq. (2.2). The N_2O mole fractions were detrended to account for the atmospheric growth rate of N_2O and the difference in date of sample collection, according to the detrending procedure described in Sect. 2.2.2.2. The reader is referred to the original works for details on experimental techniques and the associated uncertainties. Despite the difference in date and location of sample collection there is a strong correlation between the N_2O mole fraction and the $\Delta^{17}O$ signature of CO_2, that is linear for N_2O in the range of 50 ppb to 320 ppb as shown in Fig. 2.2b. In the

mesosphere the correlation between N_2O and $\Delta^{17}O$ in CO_2 breaks down as discussed in detail by *Mrozek* (2017).

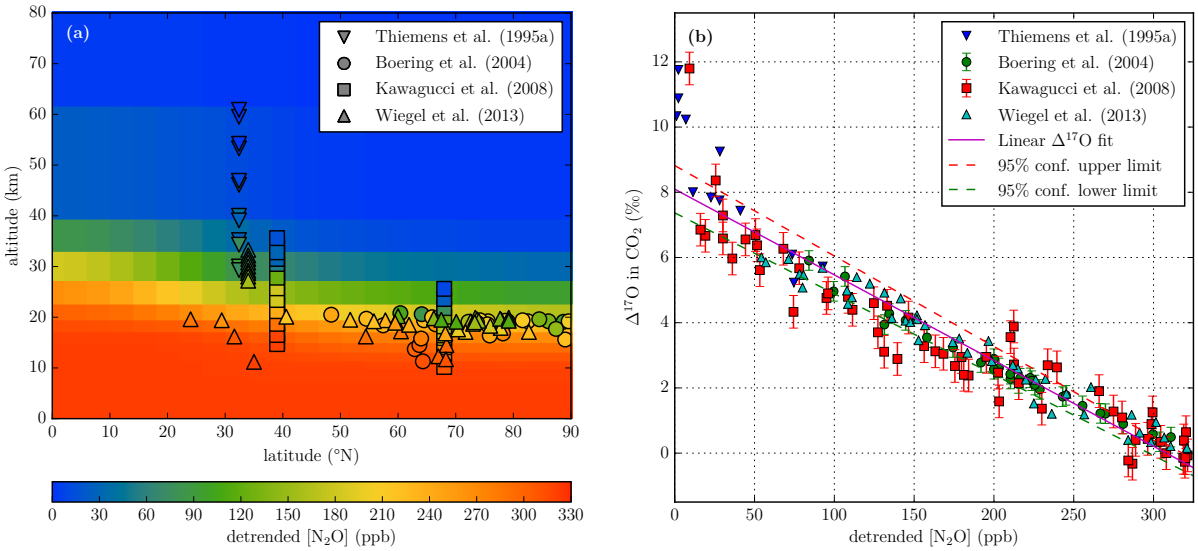

Figure 2.2: Overview of simulated and measured stratospheric N_2O mole fraction and $\Delta^{17}O$ signature in CO_2. **(a)** Annual mean, zonal mean TM5 model predictions of detrended N_2O mole fractions using a horizontal resolution of 6°×4° and 25 vertical levels compared to detrended measurements of N_2O mole fractions from *Thiemens et al.* (1995a), *Boering et al.* (2004), *Kawagucci et al.* (2008) and *Wiegel et al.* (2013) for stratospheric air in Northern Hemisphere. The background color indicates the value of the TM5 model prediction and the color of the symbols indicates the measured value. **(b)** $\Delta^{17}O$ signatures of stratospheric CO_2 versus detrended N_2O mole fraction, constructed from measurements by *Thiemens et al.* (1995a), *Boering et al.* (2004), *Kawagucci et al.* (2008) and *Wiegel et al.* (2013) and linear least squares fit with its corresponding 95% confidence interval. The error bars from *Thiemens et al.* (1995a) and *Wiegel et al.* (2013) are omitted from the figure to improve visibility.

We derived a linear fit for the detrended N_2O mole fraction and $\Delta^{17}O$ in CO_2 using a least squares approach with equal weights assigned to each individual measurement (data for $[N_2O] < 50$ ppb was excluded), based on the formulation

$$\Delta^{17}O_{\text{fit}} = a \cdot ([N_2O]_{\text{dtd}} - 320.84) + b, \tag{2.5}$$

where $[N_2O]_{\text{dtd}}$ is the detrended N_2O mole fraction. In addition to the least squares solution for the coefficients a and b in Eq. (2.5), we also constructed a 95% confidence interval, as shown in Fig. 2.2b. The effect of the N_2O–$\Delta^{17}O$ fit on the resulting distribution of $\Delta^{17}O$ in CO_2 is tested by performing different simulations (`BASE`, `ST_UPPER` and `ST_LOWER` as defined in Table 2.2), the results of which are discussed in Sect. 2.3.1.3.

In our model framework, the fit in Eq. (2.5) is implemented with a cut-off at 0‰, to prevent negative $\Delta^{17}O$ values in the stratosphere. Also, a relaxation time can be specified in the model that determines the strength of the coupling between $\Delta^{17}O$ for stratospheric CO_2 and N_2O mole fractions, such that

$$\Delta^{17}O_{new} = \Delta^{17}O_{fit} + e^{-\Delta t/\tau_{relax}}(\Delta^{17}O_{old} - \Delta^{17}O_{fit}), \tag{2.6}$$

where Δt is the model time step, τ_{relax} is a user-specified time scale; $\Delta^{17}O_{new}$ and $\Delta^{17}O_{old}$ refer to $\Delta^{17}O$ signature for the new and old time step respectively. In our model, we can apply the fit based on the vertical level (e.g. for cells with atmospheric pressure below 100 hPa) or depending on the local N_2O mole fraction (e.g. for cells with N_2O mole fractions below 280 ppb). The values used for these parameters in the base model run are summarized in Table 2.1.

2.2.2.2 N_2O

We simulated N_2O based on stratospheric sinks and optimized surface fluxes from *Corazza et al.* (2011) and *Bergamaschi et al.* (2015). The 2D surface fluxes have a time resolution of 1 month and a horizontal resolution of 6°×4°. The 3D sink fields have the same time resolution and same horizontal resolution and consist of 25 vertical levels. The N_2O surface fluxes are optimized for the years 2006 and 2007 by *Corazza et al.* (2011) and *Bergamaschi et al.* (2015), and we extrapolate the N_2O sources for years outside of this range. The N_2O sinks are climatological fields derived from the ECHAM5/MESSy1 model (*Brühl et al.*, 2007). The sink fields distinguish between N_2O loss caused by $O(^1D)$ (roughly 10% of total loss) and photolysis (roughly 90% of N_2O loss) and have a strong seasonal cycle due to the changing orientation of the Earth with respect to the sun. The sum of the yearly emissions is on average: ∼16 $TgN{\cdot}yr^{-1}$, and the imbalance between the sources and sinks is ∼3.5 $TgN{\cdot}yr^{-1}$, resulting in an increase of the N_2O mass in our model. The global N_2O emission and growth rate are in good agreement with results from *Hirsch et al.* (2006).

In this study, we are not interested in the atmospheric increase of the N_2O mole fraction over time, but its correlation with $\Delta^{17}O$ in CO_2. *Assonov et al.* (2013) have encountered the same issue and constructed a detrending method based on measured N_2O at Mauna Loa. This detrending method assumes a constant growth rate for N_2O mole fractions of $\alpha_{ref} = 0.844 \pm 0.001$ $ppb{\cdot}yr^{-1}$, which is representative of tropospheric air but not suitable to the (upper) stratospheric air that we also consider in this study (e.g. upper stratospheric

air samples from *Thiemens et al.* (1995a) with N_2O mole fractions of less than 10 ppb). We modified the detrending method from *Assonov et al.* (2013) as described in Sect. S2.3 to arrive at

$$X_{\mathrm{dtd}} = X_{\mathrm{obs}} \cdot \left[1 - \frac{\alpha_{\mathrm{ref}}}{X_{\mathrm{ref}}} \cdot (t_{\mathrm{ref}} - t_{\mathrm{obs}})\right]^{-1}, \tag{2.7}$$

where X_{obs} and X_{dtd} refer to the observed and detrended mole fractions; and where t_{obs} and t_{ref} are respectively the time of observation and the reference time (January 1$^{\mathrm{st}}$, 2007) on which the N_2O mole fractions are projected. This detrending scheme is applied for: (1) the validation of the N_2O simulation against N_2O observations; (2) the derivation of the N_2O–$\Delta^{17}O$ fit; (3) the detrending of simulated stratospheric N_2O before applying the correlation in TM5.

The modeled tropospheric N_2O mole fraction is nearly constant (well mixed) at ∼320 ppb (for January 1$^{\mathrm{st}}$, 2007) and the NH mole fraction is roughly 0.7-1 ppb higher than for the SH, which agrees well with the results from *Hirsch et al.* (2006). To test the uncertainty that is associated with our modeled N_2O, we compare our model predictions for N_2O with stratospheric measurements of N_2O. Fig. 2.2a shows a comparison of modeled zonal mean, yearly mean N_2O with detrended experimental data from *Thiemens et al.* (1995a), *Boering et al.* (2004), *Kawagucci et al.* (2008) and *Wiegel et al.* (2013). For the measurements from *Thiemens et al.* (1995a), we assume that the latitude of measurements is equal to latitude of the launching site of the rocket. Our model prediction agrees well with the vertical profile from *Kawagucci et al.* (2008) at 39°N, but overestimates the N_2O mole fractions in the upper part of the vertical profile at 68°N. In Fig. S2.1 we provide similar plots for each season.

2.2.2.3 Stratosphere-troposphere exchange

The transport of air masses in our model, including stratosphere-troposphere exchange (STE), is fully driven by ECMWF ERA-Interim meteorological fields (*Dee et al.*, 2011). Since STE is essential in this study, both for the transport of N_2O and for CO_2 with anomalous $\Delta^{17}O$, we aim to diagnose the magnitude and variability of STE. The diagnosed spatiotemporal variation of STE could help to explain variations in predicted $\Delta^{17}O$ in the troposphere.

To diagnose the STE of CO_2 in TM5, two artificial tracers were defined: `CO2_trop` and

`CO2_strat`, that have the same properties as the normal tracer `CO2`, but do not have any sources or sinks at the surface. For each time step, the tracer mass and tracer mass slopes of `CO2_trop` in tropospheric cells are copied from `CO2`, whereas the tracer mass and slopes of `CO2_trop` are set equal to zero for all stratospheric cells. The opposite procedure is performed each time step for the tracer `CO2_strat` after which all tracers in the model are transported. By diagnosing the tracer mass of `CO2_trop` that was transported into the stratosphere, we can determine for each time step a 2D field of the transport across the user-defined tropopause. By combining the two gross exchange fluxes from `CO2_trop` and `CO2_strat` we can calculate the net STE flux. This method allows the use of a static flat 'tropopause' or a dynamic tropopause derived from the local temperature profile or the local N_2O mole fraction. The transport of $C^{17}OO$ is tracked in a similar fashion, which allows for the calculation of the $\Delta^{17}O$ stratospheric isoflux. Finally, we can determine the troposphere-stratosphere flux F_{AS} by integrating over the tropical region (30°S-30°N) and the stratosphere-troposphere flux F_{SA} by integrating over the extratropical regions (outside the range 30°S-30°N).

It is known that meteorological fields from data assimilation systems have the tendency to overestimate the Brewer-Dobson circulation (*van Noije et al.*, 2004; *Bregman et al.*, 2006). The ERA-Interim reanalysis performs better at simulating the Brewer-Dobson circulation than its predecessor ERA-40 (*Monge-Sanz et al.*, 2007), but upward transport is still too large compared to observations (*Schoeberl et al.*, 2008). Also, the advection scheme for transport of tracer mass has an effect on the STE. *Bönisch et al.* (2008) showed that the 'second order moments' scheme (*Prather*, 1986) is more accurate for stratospheric transport than the 'slopes' scheme by *Russell and Lerner* (1981) that is used in our current model framework.

Given the importance of STE for our purposes and the difficulty of accurately modeling STE, we compared our diagnosed STE with data from *Appenzeller et al.* (1996) and *Holton* (1990). These studies were also used by *Luz et al.* (1999) to calculate the stratospheric source of $\Delta^{17}O$ for tropospheric CO_2 and O_2 and in the box models by *Hoag et al.* (2005) and *Hofmann et al.* (2017). In order to determine the air mass flux crossing the tropopause, we switched off the CO_2 sources and sinks at the surface and initialized the CO_2 tracer with a constant mixing ratio throughout the entire domain. Using our method to track the STE of CO_2 and the imposed constant CO_2 mixing ratio, we inferred the air mass STE. The comparison of our derived STE and data from *Appenzeller et al.* (1996) and *Holton* (1990) is shown in Fig. 2.3. It should be noted that the pressure levels for which the fluxes are given are not equal and also the years are different (as indicated in the legend). Still, some general conclusions about the STE in TM5 can be made.

The magnitude of the STE from TM5 is for most months in between the estimates from *Appenzeller et al.* (1996) and *Holton* (1990) and the timing of the seasonality in STE agrees well. Despite the agreement, it should be noted that the range of reported values by *Appenzeller et al.* (1996) and *Holton* (1990) is large, and hence considerable uncertainty is associated with our model derived STE. The implications of the large uncertainty in STE on the potential application of $\Delta^{17}O$ in CO_2 as tracer of GPP are further discussed in Sect. 2.4.3.

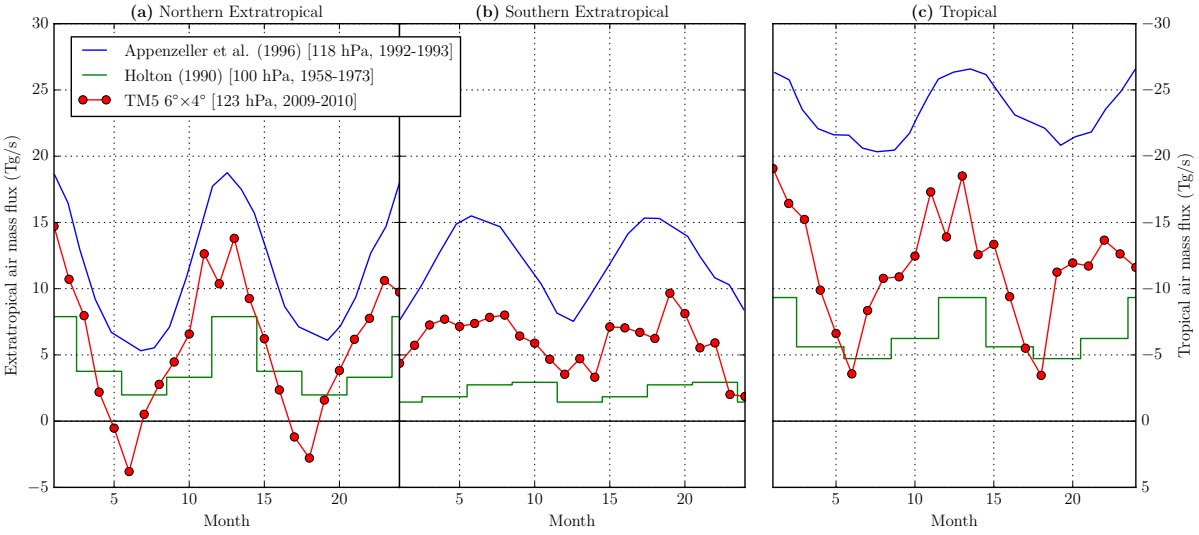

Figure 2.3: Net air mass flux through ∼100 hPa pressure levels from TM5 model simulation and from literature for 2 consecutive years. Mass fluxes from *Appenzeller et al.* (1996) for years 1992-1993 are given for the 118 hPa surface. Mass fluxes from *Holton* (1990) are averaged over years 1958-1973; this averaged data is shown for the first years and is repeated for the second year. Monthly output was taken from our TM5 model simulation; the predicted mass flux is given for 123 hPa for years 2009 and 2010. **(a)** Fluxes for northern extratropical region (latitudes above 30°N). **(b)** Fluxes for southern extratropical region (latitudes below 30°S). **(c)** Fluxes for tropical region (latitudes between 30°N and 30°S). Note that for the tropical mass flux the vertical axis is shown on the right-hand side of the figure and is reversed to facilitate easy visual comparison with the extratropical regions.

The mass fluxes from *Appenzeller et al.* (1996) are derived from a United Kingdom Meteorological Office (UKMO) dataset (*Swinbank and O'Neill*, 1994) with a resolution of 3.75° longitude by 2.5° latitude and with a vertical resolution of ∼50 hPa in the lowermost stratosphere. We reproduced the STE graph by carefully extracting data points from the graphs in *Appenzeller et al.* (1996). STE mass fluxes by *Holton* (1990) are derived from climatological data of *Oort* (1983) specified on 5° latitude intervals and aggregated for the different seasons. Our TM5 simulation was performed with a horizontal resolution of 6°×4° and for 25 vertical levels. The TM5 model uses hybrid sigma-pressure levels, for the level at which the mass flux is diagnosed, the levels are almost completely isobaric.

2.2.3 Surface Sinks of $\Delta^{17}O$ in CO_2

2.2.3.1 Atmosphere-leaf exchange

The atmosphere-leaf exchange of CO_2 is modeled using the Simple Biosphere/Carnegie-Ames-Stanford Approach (SiBCASA) model (*Schaefer et al.*, 2008). To calculate photosynthesis, SiBCASA combines the C_3 and C_4 assimilation models (*Farquhar et al.*, 1980; *Collatz et al.*, 1992) with the Ball-Berry-Collatz stomatal conductance model (*Collatz et al.*, 1991), from which the internal leaf CO_2 concentration c_i can be calculated. SiBCASA is driven by ERA-Interim meteorology with 3 hourly time resolution and a spatial resolution of 1°×1°. Furthermore, the spatial distribution of C_3 and C_4 vegetation is taken from *Still et al.* (2003) and SiBCASA uses a climatological mean seasonal leaf phenology based on satellite derived Normalized Difference Vegetation Index (NDVI). SiBCASA results are first stored in full resolution in files that are subsequently read by our atmospheric transport model TM5.

The gross atmosphere-leaf exchange fluxes can be derived from the ratio of leaf internal to atmospheric CO_2 concentration c_i/c_a and the assimilation flux F_A (which we obtain by scaling GPP with a factor 0.88, to take out the component that is released through autotrophic leaf respiration, similar to *Ciais et al.*, 1997a), according to

$$F_{AL} = F_A \frac{c_a}{c_a - c_i}, \tag{2.8}$$

$$F_{LA} = -F_A \frac{c_i}{c_a - c_i}. \tag{2.9}$$

We have used monthly averaged GPP-weighted c_i/c_a ratios, similar to *Ciais et al.* (1997a,b) and *Peylin et al.* (1997, 1999). Furthermore our assimilation flux has 3-hourly time resolution, whereas we assume that leaf respiration is a constant fraction of GPP. In future studies we recommend to include c_i/c_a and leaf respiration at the same temporal resolution as GPP, similar to the model by *Cuntz et al.* (2003a,b) for $\delta^{18}O$ in CO_2, as is also discussed in Sect. 2.4.1.

In our model framework, we use the sign convention that positive fluxes increase the CO_2 mass in the troposphere. The magnitude of global GPP in our model is taken from SiBCASA and is -133 PgC·yr^{-1} for 2011. This represents a larger uptake than the values of -100 PgC·yr^{-1} and -120 PgC·yr^{-1} as used in the box models by *Hoag et al.* (2005) and *Hofmann et al.* (2017), respectively.

The average distribution of GPP weighted c_i/c_a for 2011 and the resulting gross atmosphere-leaf flux F_{AL} are shown in Fig. 2.4. The presence of C_4 vegetation in tropical Africa can be recognized clearly by the band of relatively low c_i/c_a ratios near the equator. Our c_i/c_a ratios are higher than what was used in the box models by *Hofmann et al.* (2017) (a fixed ratio of 0.7) and *Hoag et al.* (2005) ($\frac{2}{3}$ and $\frac{1}{3}$ for C_3 and C_4 vegetation respectively based on a study by *Pearcy and Ehleringer*, 1984). To prevent excessive atmosphere leaf fluxes in our model, we have imposed an upper limit such that $c_i/c_a \leq 0.9$ for all grid cells in the domain during all months of the simulation. Our global gross atmosphere-leaf fluxes in Fig. 2.4b exhibit a clear seasonal signal, peaking during the NH summer months. During the entire year, our atmosphere-leaf flux is larger than the estimated -352 PgC·yr^{-1} from the box model by *Hofmann et al.* (2017), which can be explained by our higher c_i/c_a ratios and the larger magnitude of our assimilation flux F_{A}.

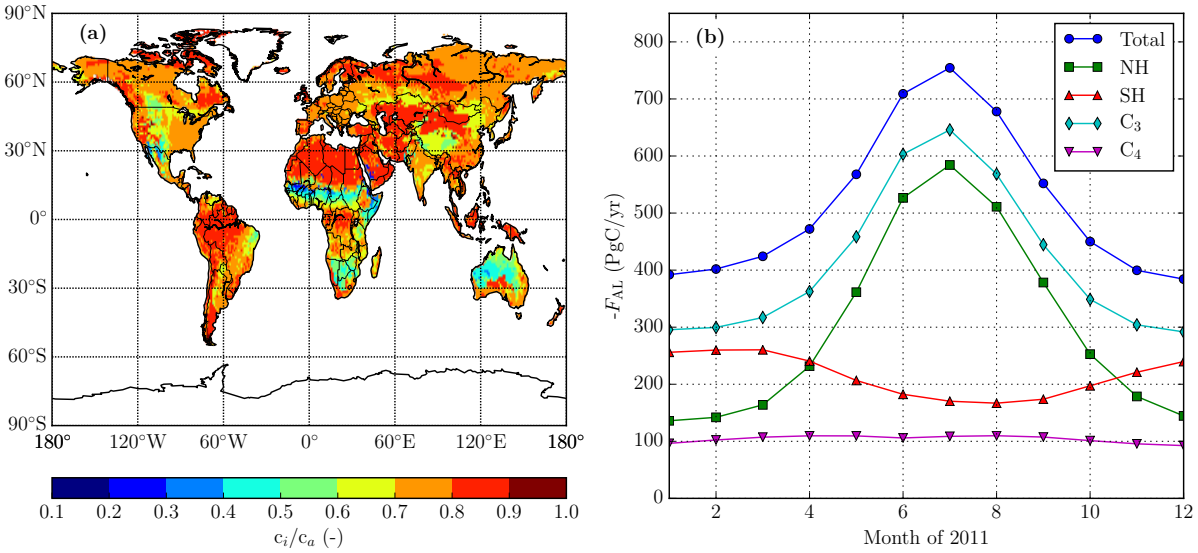

Figure 2.4: Vegetation parameters as predicted by SiBCASA. **(a)** Spatial distribution of GPP weighted c_i/c_a over the Earth surface averaged over the year 2011. **(b)** Temporal variation of global atmosphere-leaf flux F_{AL} as predicted by SiBCASA, partitioned over Northern/Southern Hemisphere and for C_3/C_4 vegetation.

A fraction of the CO_2 that diffuses out of the leaf, has equilibrated with leaf water inside the leaf. This can be expressed by dividing the gross leaf-atmosphere flux F_{AL} into an equilibrated and non-equilibrated part

$$F_{\mathrm{LAeq}} = (f_{C_3} \cdot \theta_{C_3} + f_{C_4} \cdot \theta_{C_4}) \cdot F_{\mathrm{LA}}, \tag{2.10}$$

$$F_{\mathrm{LAnoneq}} = (f_{C_3} \cdot [1 - \theta_{C_3}] + f_{C_4} \cdot [1 - \theta_{C_4}]) \cdot F_{\mathrm{LA}}, \tag{2.11}$$

where f_{C_i} refers to the fraction of a vegetation type and θ_{C_i} is the vegetation type specific equilibration constant. In our model we use $\theta_{C_3} = 0.93$ and $\theta_{C_4} = 0.38$ (*Gillon and Yakir*, 2000, 2001).

The isotopic signature associated with the gross atmosphere-leaf exchange fluxes is determined by the signature of the source (atmospheric CO_2 for F_{AL} and $F_{LAnoneq}$ and leaf water for F_{LAeq}) and kinetic fractionation during inflow and outflow of CO_2 through the leaf stomata

$$\Delta^{17}O_{AL} = \Delta^{17}O_A + (\lambda_{kinetic} - \lambda_{RL}) \cdot \ln(\alpha_{leaf}), \quad (2.12)$$

$$\Delta^{17}O_{LAeq} = \Delta^{17}O_{leaf} + (\lambda_{kinetic} - \lambda_{RL}) \cdot \ln(\alpha_{leaf}), \quad (2.13)$$

$$\Delta^{17}O_{LAnoneq} = \Delta^{17}O_A + (\lambda_{kinetic} - \lambda_{RL}) \cdot \ln(\alpha_{leaf}), \quad (2.14)$$

where $\Delta^{17}O_A$ and $\Delta^{17}O_{leaf}$ are the $\Delta^{17}O$ signatures for atmospheric CO_2 and for CO_2 that has equilibrated with leaf water, $\alpha_{leaf} = 0.9926$ is the fractionation factor for diffusion of $C^{18}OO$ relative to CO_2 through leaf stomata (*Farquhar et al.*, 1993) and $\lambda_{kinetic} = 0.509$ is the coefficient associated with kinetic fractionation of $C^{17}OO$ relative to $C^{18}OO$ (*Young et al.*, 2002). A derivation and process-based interpretation of Eq. (2.12) is given in Sect. S2.4. An alternative derivation for Eqs. (2.12)-(2.14) is given in Sect. S2.5.

To calculate $\Delta^{17}O_{leaf}$, we first need to determine the isotopic signature of soil water $\Delta^{17}O_{soil}$. We derive the $\delta^{18}O$ signature of soil water from the $\delta^{18}O$ signature of precipitation water, which we obtained from *Bowen and Revenaugh* (2003) through the portal `http://www.waterisotopes.org`. We use the yearly average precipitation water signatures, since the amplitude in the seasonal signal of soil water is weaker than for precipitation water and the phase of the seasonal signal can be shifted depending on the depth of the soil water in the soil layer (e.g. *Affolter et al.*, 2015). Similar to *Hofmann et al.* (2017), we derive the $\Delta^{17}O$ signature of soil water from its $\delta^{18}O$ signature by assuming that soil water falls on the Global Meteoric Water Line, i.e.

$$\ln(\delta^{17}O_{soil} + 1) = \lambda_{GMWL} \cdot \ln(\delta^{18}O_{soil} + 1) + \gamma_{GMWL}, \quad (2.15)$$

with $\lambda_{GMWL} = 0.528$ and $\gamma_{GMWL} = 0.033‰$ (*Luz and Barkan*, 2010). The resulting distribution of the $\Delta^{17}O_{soil}$ has a maximum value near the equator and drops to its minimum close to the North Pole, see Fig. 2.5b.

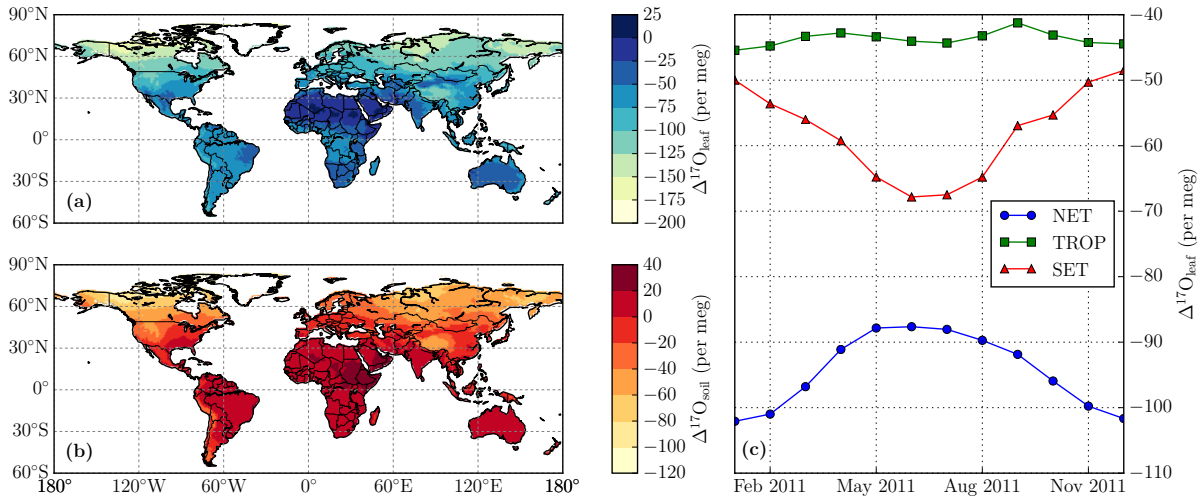

Figure 2.5: Δ^{17}O signature of soil water and leaf water. **(a)** Annual mean distribution of $\Delta^{17}O_{leaf}$ for 2011. **(b)** Annual mean distribution of $\Delta^{17}O_{soil}$ for 2011. **(c)** Temporal variation of $\Delta^{17}O_{leaf}$ for northern extratropical region (NET; latitudes above 30°N), tropical region (TROP; latitudes between 30°S and 30°N) and southern extratropical region (SET; latitudes below 30°S) during 2011.

The isotopic signature of leaf water $\Delta^{17}O_{leaf}$ is determined from the isotopic signature of soil water $\Delta^{17}O_{soil}$ and the fractionation occurring due to the transpiration of water

$$\Delta^{17}O_{leaf} = \Delta^{17}O_{soil} + (\lambda_{transp} - \lambda_{RL}) \cdot \ln(\alpha_{transp}), \tag{2.16}$$

where $\alpha_{transp} = 1/0.9917$ (*West et al.*, 2008) is the fractionation factor of transpiration of $H_2{}^{18}O$ relative to $H_2{}^{16}O$ and λ_{transp} is the exponent relating fractionation of $H_2{}^{17}O$ to transpiration of $H_2{}^{18}O$

$$\lambda_{transp} = 0.522 - 0.008 \cdot h, \text{for } 0.3 \leq h \leq 1, \tag{2.17}$$

where h is the relative humidity as was demonstrated by *Landais et al.* (2006). The resulting spatial distribution and temporal variation of $\Delta^{17}O_{leaf}$ is shown in Fig. 2.5, where we used relative humidity data from ERA-Interim. The isotopic signature $\Delta^{17}O_{leaf}$ attains its maximum in the African Sahara, where relative humidity is low and has low values in the arctic region. The leaf signature for the northern and southern extratropical regions (NET and SET) exhibits a seasonal cycle of opposite phase with a peak-to-peak amplitude of ∼20 per meg. The $\Delta^{17}O_{leaf}$ in the tropical region has hardly any seasonality.

To test the effect of the soil water signature $\Delta^{17}O_{soil}$ and the leaf water signature $\Delta^{17}O_{leaf}$

on $\Delta^{17}O$ in CO_2, we performed simulations with a spatially distributed $\Delta^{17}O_{soil}$ and temporally and spatially distributed $\Delta^{17}O_{leaf}$ (`BASE` in Table 2.2) as well as a simulation with a constant soil water signature of -5 per meg (`SOIL_CONST`) and a simulation with a constant relative humidity of 0.8, which can be converted using Eq. (2.17) to $\lambda_{transp} = 0.5156$ (`LEAF_CONST`). The results of these simulations are given in Sect. 2.3.1.3.

2.2.3.2 Respiration and soil invasion

The CO_2 respiration flux is calculated in SiBCASA from multiple above and below ground carbon pools with different turn-over rates, depending on temperature and moisture (*Schaefer et al.*, 2008). The calculated respiration flux from SiBCASA is aggregated over a period of 1 month for each 1°×1° grid cell. From the monthly respiration fluxes and the ERA-Interim 2 m temperature, the coefficient R_0 is determined (see Eq. (2.18) for its definition) and stored in a file. In our TM5 model, the CO_2 respiration flux depends on temperature (and thus also on time) according to the following Q_{10} relation (*Potter et al.*, 1993)

$$F_{resp} = R_0 \cdot Q_{10}^{\frac{T-T_{ref}}{10}}, \tag{2.18}$$

with $Q_{10} = 1.5$ and $T_{ref} = 273.5$ K. For T we used the 2 m temperature from ERA-Interim, which has a spatial resolution of 1°×1° and a 3 hourly time resolution, which allows us to simulate a diurnal cycle in the respiration flux. The coefficient R_0 is read from the SiBCASA output file and assures that the aggregated monthly respiration flux calculated according to Eq. (2.18) agrees with the monthly respiration flux for each cell from SiBCASA. The global respiration flux that we determine with SiBCASA for 2011 is 129 PgC·yr^{-1} (total respiration, including autotrophic leaf respiration).

The isotopic signature of respired CO_2 (excluding the autotrophic leaf respired component, calculated similar to the net assimilation flux as described in Sect. 2.2.3.1) is determined by equilibration with soil water, followed by kinetic fractionation due to diffusion through the soil column into the atmosphere

$$\Delta^{17}O_{resp} = \Delta^{17}O_{soil} + (\lambda_{kinetic} - \lambda_{RL}) \cdot \ln(\alpha_{soil}), \tag{2.19}$$

where $\alpha_{soil} = 0.9928$ is the kinetic fractionation factor of $C^{18}OO$ relative to CO_2 for diffusion out of the soil column into the atmosphere (*Miller et al.*, 1999).

The reported magnitudes of the global soil invasion flux cover a wide range: from 30 PgC·yr^{-1} (*Stern et al.*, 2001) to 450 PgC·yr^{-1} (*Wingate et al.*, 2009). The high soil invasion flux estimate is explained by the presence of the enzyme carbonic anhydrase in soils (*Wingate et al.*, 2009). Similar to CO_2, soil invasion fluxes of carbonyl sulfide (COS) are also affected by carbonic anhydrase (*Ogée et al.*, 2016). The soil uptake of COS has been modeled by *Launois et al.* (2015) assuming that COS uptake scales linearly with v_{dep}, the deposition velocity of molecular hydrogen to soils (based on the assumption that both processes are affected by similar soil microorganisms).

In this study, the global magnitude of the soil invasion flux is set to 30 PgC·yr^{-1} by default (normalized for years 2012-2013) but can be changed to any user-specified value. Also, the spatial distribution of the soil invasion flux can be scaled with the biosphere CO_2 respiration flux (i.e. $F_{\mathrm{SIA}} \propto F_{\mathrm{resp}}$) or alternatively the hydrogen deposition velocity (i.e. $F_{\mathrm{SIA}} \propto v_{\mathrm{dep}}$). See Table 2.1 for an overview of the available model settings for the soil invasion flux. To test the sensitivity of the $\Delta^{17}O$ signature of atmospheric CO_2 on the magnitude and spatial distribution of the soil invasion flux, we performed 4 additional simulations (`RESP_240`, `RESP_450`, `HYD_240` and `HYD_450` that are summarized in Table 2.2), for which the results are discussed in Sect. 2.3.1.3.

The isotopic signature of CO_2 that diffuses into soils ('ASI') is determined from the local atmospheric $\Delta^{17}O$ as predicted by our model. The $\Delta^{17}O$ signature of CO_2 released from the soil ('SIA') is set equal to the signature of soil water $\Delta^{17}O_{\mathrm{soil}}$ described in Sect. 2.2.3.1. Isotopic fractionation is not taken into account for the soil invasion fluxes, since the ingoing and outgoing fluxes have equal magnitude in our model (i.e. $F_{\mathrm{SIA}} = -F_{\mathrm{ASI}}$), and therefore the kinetic fractionation effect on the atmospheric $\Delta^{17}O$ budget cancels out.

2.2.3.3 Ocean exchange

The exchange of CO_2 between the atmosphere and the ocean is based on the relationship between wind speed and gas exchange over the ocean as reported by *Wanninkhof* (1992). The gas transfer coefficient k, in cm·hr^{-1}, is calculated from

$$k = 0.31 \cdot u^2 \cdot \left[\frac{\mathrm{Sc}}{660}\right]^{-0.5}, \tag{2.20}$$

where u is the wind speed in m·s^{-1} and Sc is the dimensionless Schmidt number. Note that the coefficient 0.31 in Eq. (2.20) is not dimensionless. Now, the two-way CO_2 exchange

fluxes can be determined from

$$F_{AO} = k \cdot s \cdot p_{CO_2}, \quad (2.21)$$

$$F_{OA} = k \cdot s \cdot (p_{CO_2} + \Delta p_{CO_2}), \quad (2.22)$$

where s is the solubility of CO_2 in ocean water expressed in $mol \cdot m^{-3} \cdot atm^{-1}$, p_{CO_2} is the partial pressure of CO_2 in the atmosphere in μatm ($\approx$0.1 Pa) and Δp_{CO_2} is the CO_2 partial pressure difference between the ocean and the atmosphere in μatm. When we express k in $m \cdot s^{-1}$, the CO_2 fluxes have units of $mol \cdot m^{-2} \cdot s^{-1}$. For cells that are covered with sea ice, the exchange fluxes are set to zero. The sea ice cover and wind speed data are taken from the ERA-Interim dataset (*Dee et al.*, 2011), with a time resolution of 3 hours and a horizontal resolution of 1°×1°. Data for solubility, CO_2 partial pressure difference and the Schmidt number are taken from *Jacobson et al.* (2007) with a horizontal resolution of 5°×4° and a temporal resolution of 1 month.

The isotopic signature of ocean water is taken as $\Delta^{17}O_{ocean} = -0.005‰$ (*Luz and Barkan*, 2010). Note that equilibration between CO_2 and H_2O does not result in a fractionation of our $\Delta^{17}O$ signal, because we have taken the CO_2–H_2O equilibration constant as our reference line (i.e. $\lambda_{RL} = \lambda_{CO_2-H_2O}$). We have neglected the kinetic fractionation effect for diffusion across the ocean-atmosphere interface, since the associated fractionation factor for $C^{18}OO$ relative to CO_2 is close to 1 ($\alpha_{ocean} \approx 0.9992$ according to *Vogel et al.*, 1970) and the gross ocean fluxes largely cancel out (with a difference of $\sim$3 $PgC \cdot yr^{-1}$ on the global scale, see Fig. 2.1).

In our model, the ocean sink for the CO_2 and $C^{17}OO$ tracers can be determined from predefined constant CO_2 and $C^{17}OO$ concentrations, or dynamically coupled to the local concentrations of CO_2 and $C^{17}OO$ above the ocean surface that the model calculates each time step (see Table 2.1 for an overview of the available model settings). For the results that we include in this paper, we always used the dynamic coupling between the ocean sink and the local atmospheric concentration.

2.2.3.4 Fossil fuel combustion and biomass burning

The CO_2 fluxes from fossil combustion in our model are based on the Emissions Database for Global Atmospheric Research version 4.2 (EDGAR 4.2) from the Joint Research Centre (JRC) of the European Union. The temporal resolution of this dataset was improved by

coupling to country and sector specific time profiles by the Institute for Energy Economics and the Rational Use of Energy (IER) from the University of Stuttgart. For our model we use the CO_2 fluxes with a monthly time resolution and a horizontal resolution of 1°×1°. We assign a signature of $\Delta^{17}O_{ff} = -0.386‰$ to the CO_2 that is released by fossil fuel combustion, which is largely determined by the $\Delta^{17}O$ signature of ambient O_2 (*Horváth et al.*, 2012). *Laskar et al.* (2016) reconstructed the same $\Delta^{17}O$ signature for CO_2 from car exhausts measured in a tunnel.

The CO_2 released to the atmosphere by biomass burning is taken from the Global Fire Emissions Database version 4 (GFED4) (*Giglio et al.*, 2013). This dataset is comprised by combining remotely sensed burned areas with modeled carbon pools from SiBCASA (*van der Werf et al.*, 2010; *van der Velde et al.*, 2014). The SiBCASA biomass burning emissions are available with a monthly time resolution and a spatial resolution of 1°×1°. The isotopic signature of CO_2 released by biomass burning is determined by the isotopic signature of ambient O_2 and the wood intrinsic oxygen, resulting in an average signature of $\Delta^{17}O_{bb} = -0.230‰$ for released CO_2 (*Horváth et al.*, 2012).

2.2.4 Tropospheric source of $\Delta^{17}O$ in CO_2

2.2.4.1 Tropospheric CO and $\Delta^{17}O$(CO) budget

Most of the atmospheric CO_2 originates from the Earth surface, where it is released directly in the form of CO_2 through one of the processes as described in Sect. 2.2.3. In addition, CO_2 can be produced in the atmosphere through oxidation of atmospheric CO by the hydroxyl radical OH,

$$CO + OH \rightarrow CO_2 + H. \tag{2.23}$$

In this section we describe observed spatiotemporal patterns in $\Delta^{17}O(CO)$; the processes driving $\Delta^{17}O(CO)$ and the implications for the production of CO_2 isotopologues. Subsequently we describe in Sect. 2.2.4.2 how the production of CO_2 isotopologues from CO oxidation is implemented in our 3D atmospheric transport model.

Measurements have revealed a large positive $\Delta^{17}O$ signature in atmospheric CO varying with season and location (measured at the per mill scale, similar to stratospheric CO_2 shown in Fig. 2.2). *Huff and Thiemens* (1998) report that $\Delta^{17}O(CO)$ increases from a

minimum of ∼0.3‰ during winter to a maximum of ∼2.7‰ during summer months in San Diego, California. *Röckmann et al.* (2002) measured a $\Delta^{17}O(CO)$ winter minimum of ∼2‰ and summer maximum of ∼8‰ at high northern latitude stations in Alert, Canada and Spitsbergen, Norway. At the tropical station Izaña, Tenerife, the seasonal cycle of $\Delta^{17}O(CO)$ is much lower (∼1‰) but the annual average value is rather similar at about 5‰ (*Röckmann et al.*, 1998b).

The most important source of the large $\Delta^{17}O$ signature of CO is the oxidation of CO by OH (*Röckmann et al.*, 1998b), which is not a mass-dependent process (the rate coefficients for oxidation of $C^{16}O$ and $C^{17}O$ are approximately equal, whereas the rate coefficient for $C^{18}O$ is substantially higher than for $C^{17}O$). This explains the observed seasonal cycle of $\Delta^{17}O(CO)$, since OH levels are higher during the summer months than during winter months, which is more pronounced at higher latitudes. Besides this main oxidation sink with a global magnitude of ∼1 $PgC \cdot yr^{-1}$ (*Holloway et al.*, 2000), CO is also taken up by soils at a global rate of 0.05-0.1 $PgC \cdot yr^{-1}$ (*Sanhueza et al.*, 1998) which is a mass-dependent process and thus not affecting $\Delta^{17}O(CO)$.

Another contribution to the positive $\Delta^{17}O$ in CO is the ozonolysis of non-methane hydrocarbons (NMHC) (*Röckmann et al.*, 1998a), but its effect on the $\Delta^{17}O(CO)$ budget is less strong than the effect of the oxidation reaction. The main sources of CO (i.e. fossil fuel combustion, biomass burning and oxidation of atmospheric hydrocarbons) are considered to have a negligible contribution to the $\Delta^{17}O(CO)$ budget (*Brenninkmeijer et al.*, 1999).

The sources and sinks of CO and their isotopic composition are uncertain and characterized by strong spatial and temporal variability, but allow us to describe the following implications for the production of $\Delta^{17}O$ in CO_2. As the OH levels increase after winter, the mass-independent OH sink in Eq. (2.23) results in the production of CO_2 with a negative $\Delta^{17}O$ signature and the simultaneous increase in $\Delta^{17}O$ of the remaining CO. Due to the increasing enrichment of the substrate $C^{17}O$ and depletion of the substrate $C^{18}O$, the $\Delta^{17}O$ isoflux from CO to CO_2 will increase (i.e. become more positive or less negative) during the summer months. Since the sources of CO are largely mass-dependent (i.e. with $\Delta^{17}O(CO) \approx 0$) and nearly all CO is removed through OH oxidation, we infer from mass conservation that the annual mean contribution of CO oxidation to the global budget of Δ^{17} in CO_2 is minor (as will be confirmed in Sect. 2.3.1.3.)

2.2.4.2 Production of CO_2 isotopologues

To simulate the production of $\Delta^{17}O$ in CO_2 from CO oxidation, we use climatological fields for $C^{16}O$, $C^{17}O$ and $C^{18}O$ from *Gromov* (2013) with a global mean $\Delta^{17}O(CO)$ signature of 5.0‰ and climatological OH fields from *Spivakovsky et al.* (2000). The OH fields are available for each month on a native TM5 resolution of 1°×1° horizontally and 60 vertical sigma-pressure levels. The climatological CO isotopologue fields are provided with a 5-day time resolution on a T42 spectral resolution and a vertical grid of 19 hybrid sigma-pressure levels and are regridded to match the temporal and spatial resolution of the OH fields.

We use a pressure dependent relation for the rate of oxidation of CO from *DeMore et al.* (1997)

$$k_{\mathrm{CO+OH}} = 1.5 \cdot 10^{-13} \cdot (1 + 0.6 \cdot p), \tag{2.24}$$

where p is the atmospheric pressure in atm and the unit of the rate coefficient $k_{\mathrm{CO+OH}}$ is $\mathrm{cm^3 \cdot molecules^{-1} \cdot s^{-1}}$. In our model this rate coefficient is based on climatological pressure fields derived from the orography of the Earth surface. The rate coefficients for the oxidation of the isotopologues $C^{17}O$ and $C^{18}O$ are determined with respect to the overall rate coefficient from

$$\epsilon_n = k_{\mathrm{CO+OH}} / k_{\mathrm{C^nO+OH}} - 1, \tag{2.25}$$

for $n = 17$ or 18. The enrichment ϵ_n was measured in a controlled lab environment by *Röckmann et al.* (1998b) as $\epsilon_{17} = -0.21 \pm 1.30$‰ and $\epsilon_{18} = -9.29 \pm 1.52$‰ (for atmospheric pressure, according to Table 3.6 in *Gromov*, 2013). In a different lab study by *Feilberg et al.* (2002, 2005) enrichments of $\epsilon_{17} = 0 \pm 4$‰ and $\epsilon_{18} = -15 \pm 5$‰ were found. To test the consequences of applying the different rate coefficients, we have performed simulations for both lab results (simulations `CO_ROCK` and `CO_FEIL`, as summarized in Table 2.2).

The oxygen in atmospheric OH likely does not have an anomalous $\Delta^{17}O$ signature, since it equilibrates rapidly with atmospheric water vapor (*Dubey et al.*, 1997; *Lyons*, 2001) and the $\Delta^{17}O$ signature of water vapor is negligible compared to that of CO (*Uemura et al.*, 2010). To calculate the production of CO_2 isotopologues in our model we assumed that $\Delta^{17}O(OH) = 0$‰, such that the temporal and spatial variation in the CO_2 production fields is determined fully by that of the CO isotopologues, the OH concentration and the

rate coefficients in Eqs. (2.24) and (2.25). To prevent interference with the stratospheric model described in Sect 2.2.2, we only apply the chemical production of $\Delta^{17}O$ between the Earth surface and the 100 hPa level.

From the derived $C^{16}OO$, $C^{17}OO$ and $C^{18}OO$ production fields we calculated the associated $\Delta^{17}O$ 'flux' field. Subsequently we scaled the $C^{18}OO$ fluxes such that the $\delta^{18}O$ fields for produced CO_2 equals our assumed fixed value of 41.5‰ (see Sect. 2.2.1). Finally, we scaled the $C^{17}OO$ flux fields to re-obtain the $\Delta^{17}O$ 'flux' field . As mentioned in Sect. 2.2.1, the motivation for using a fixed $\delta^{18}O$ for atmospheric CO_2 is that this considerably simplifies the coupling with the hydrological cycle. This method implies that the simulated $\Delta^{17}O$ signature is fully carried by the $C^{17}OO$ tracer in our atmospheric transport model.

Note that the contribution of mass-independent CO_2 through oxidation of atmospheric CO was not considered in the previous box models from *Hoag et al.* (2005) and *Hofmann et al.* (2017). Likewise, oxidation of CO is not included in our model runs with base settings (`BASE`), as summarized in Table 2.1. The resulting $\Delta^{17}O$ in atmospheric CO_2 for the simulations `CO_ROCK` and `CO_FEIL` (see Table 2.2) are presented and discussed in Sect. 2.3.1.3.

2.3 Results

2.3.1 Global model simulations

2.3.1.1 $\Delta^{17}O$ in tropospheric CO_2 for base model

In this section we show the results from the TM5 simulation with the base settings as summarized in Table 2.1 at a horizontal resolution of 6°×4° and with 25 vertical levels. We started a simulation with an initial CO_2 distribution from data assimilation system CarbonTracker (*Peters et al.*, 2007, 2010; *van der Laan-Luijkx et al.*, 2017) and with $\Delta^{17}O = 0$ for each cell. After running the model for ∼10 years we obtained a steady state (no further increase in the mean annual $\Delta^{17}O$ signature) for the years 2012 and 2013 for which we show the results. We provide insight into the temporal and spatial patterns of modeled $\Delta^{17}O$ in CO_2 for the lowest ∼500 m of the atmosphere (lowest 4 model levels). The CO_2 mass fluxes and corresponding $\Delta^{17}O$ isofluxes between the different reservoirs are discussed in Sect. 2.3.1.2.

In Fig. 2.6, we show the temporal variation of monthly average $\Delta^{17}O$ in CO_2. The Hovmöller diagram in Fig. 2.6a shows that the Northern Hemisphere experiences the largest seasonal variation and that the decrease in $\Delta^{17}O$ occurs during the summer months for both hemispheres. Fig. 2.6b shows the temporal variation of $\Delta^{17}O$ in CO_2 integrated over both hemispheres and for the global domain compared to box model predictions from *Hoag et al.* (2005) and *Hofmann et al.* (2017). Our 3D model predicts an average $\Delta^{17}O$ signature of 39.6 per meg for CO_2 in the lowest 500 m of the atmosphere, which is roughly 20 per meg lower than the prediction from the box model by *Hofmann et al.* (2017). This is an expected result since the exchange of CO_2 with the biosphere, which represents the main sink of $\Delta^{17}O$, is higher in our model than for the box models. For the NH and SH we predict a mean $\Delta^{17}O$ signature of 31.6 and 47.6 per meg and a seasonal cycle with a peak-to-peak amplitude of 17.7 per meg and 5.1 per meg, respectively. The spatial and temporal patterns in simulated $\Delta^{17}O$ confirm the potential of $\Delta^{17}O$ as a tracer of GPP.

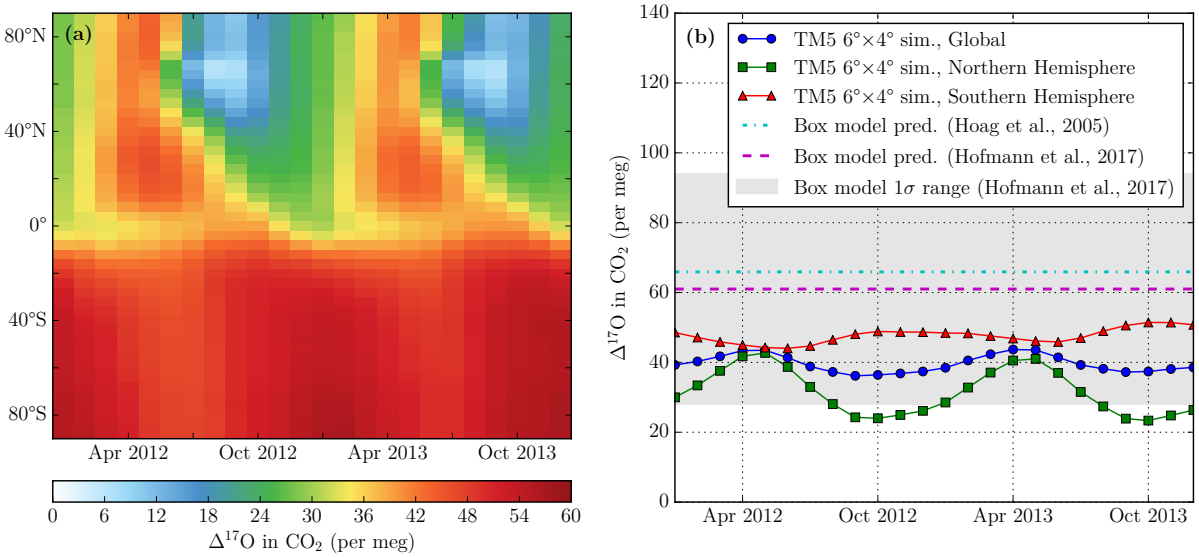

Figure 2.6: Monthly average of simulated $\Delta^{17}O$ in CO_2 for the lowest 500 m of the atmosphere using TM5 model with base settings and a 6°×4° horizontal resolution and 25 vertical levels. **(a)** Hovmöller diagram of $\Delta^{17}O$ in CO_2. **(b)** Time series of $\Delta^{17}O$ in CO_2 for TM5 integrated over NH, SH and global domain, compared with predictions from box models by *Hoag et al.* (2005) and *Hofmann et al.* (2017).

The spatial distribution of $\Delta^{17}O$ for the different seasons in 2013 is shown in Fig. 2.7. Besides the North-South gradient that was already visible in Fig. 2.6, we can see that the $\Delta^{17}O$ signature over oceans exceeds the $\Delta^{17}O$ above land, which can be explained by the strong effect of the biosphere on atmospheric $\Delta^{17}O$. In addition, the tropical regions in South America and Africa have low $\Delta^{17}O$ values during the entire year, with large zonal gradients, especially during DJF and SON. Although the exchange of CO_2 between the

biosphere and atmosphere is highest for the tropical regions, the lowest $\Delta^{17}O$ occurs in the northern extratropical region (NET). This is a direct consequence of the low $\Delta^{17}O$ signatures of soil water and leaf water (see Fig. 2.5c) in the NET compared to the tropics. Note also that fossil fuel combustion can have a strong effect on the local $\Delta^{17}O$ signal, which explains the low $\Delta^{17}O$ in CO_2 simulated over parts of China.

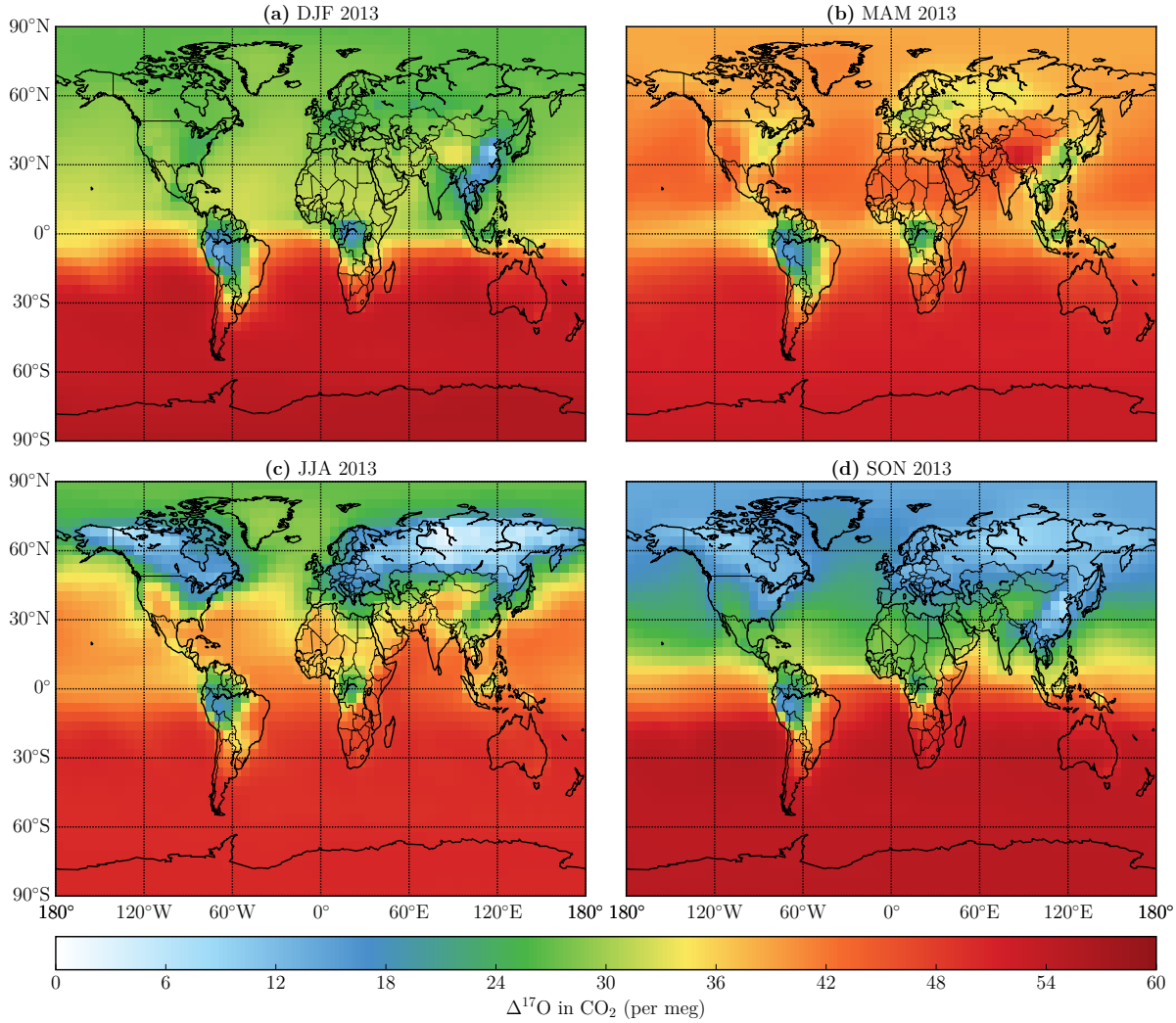

Figure 2.7: Seasonal average distributions of simulated $\Delta^{17}O$ in CO_2 for lowest 500 m of atmosphere from TM5 model with base settings using a 6°×4° horizontal resolution and 25 vertical levels. **(a)** Seasonal average for December, January and February (DJF) 2013. **(b)** Seasonal average for March, April and May (MAM) 2013. **(c)** Seasonal average for June, July and August (JJA) 2013. **(d)** Seasonal average for September, October and November (SON) 2013.

2.3.1.2 CO_2 mass fluxes and $\Delta^{17}O$ isofluxes for base model

To better understand the $\Delta^{17}O$ budget, we analyzed the magnitudes and spatiotemporal variations of the simulated CO_2 mass fluxes and $\Delta^{17}O$ isofluxes. The definition of the $\Delta^{17}O$ isoflux is

$$IF_{ij} = F_{ij} \cdot (\Delta^{17}O_i - \Delta^{17}O_{\text{trop}}), \tag{2.26}$$

where IF_{ij} and F_{ij} are respectively the $\Delta^{17}O$ isoflux and CO_2 mass flux from reservoir i to reservoir j. Furthermore, $\Delta^{17}O_{\text{trop}}$ and $\Delta^{17}O_i$ are the signatures for the troposphere and for the source reservoir (which can also be the troposphere, for instance for the isoflux from the atmosphere to the ocean IF_{AO}). In this study we have used a reference level of $\Delta^{17}O_{\text{trop}} = 40$ per meg, which is representative for the lowest ∼500 m of the atmosphere as described in Sect 2.3.1.1. The globally averaged yearly averaged CO_2 mass fluxes and $\Delta^{17}O$ isofluxes simulated by our TM5 model and the fluxes from the box models by *Hofmann et al.* (2017) and *Hoag et al.* (2005) are summarized in Table S2.2.

In Fig. 2.8 we show the global time series of the main biospheric and stratospheric $\Delta^{17}O$ isofluxes from the model simulation with base settings for the years 2012-2013. For the global biospheric $\Delta^{17}O$ isofluxes shown in Fig. 2.8a, the atmosphere-leaf isoflux IF_{AL} has the largest seasonal variation with a peak-to-peak amplitude of ∼25 ‰PgC·yr^{-1}. IF_{AL} attains its peak (i.e. the most negative value) during the summer months in the Northern Hemisphere, similar to the seasonality in global carbon uptake by vegetation. The global equilibrated leaf-atmosphere isoflux IF_{LAeq} has a seasonal cycle with peak-to-peak amplitude of ∼10 ‰PgC·yr^{-1} and is changing sign during the course of the year. The sign change in IF_{LAeq} is related to the change in the isotopic signature of leaf water (see Sect. 2.2.3.1) and the selected reference level $\Delta^{17}O_{\text{trop}}$. Finally, we see that global mean non-equilibrated leaf-atmosphere isoflux IF_{LAnoneq}, is nearly constant during the year. Note that for all biospheric fluxes shown in Fig. 2.8a the average value (and hence also the occurrence of sign changes for IF_{LAeq}) is sensitive to the reference level $\Delta^{17}O_{\text{trop}}$.

The global net stratospheric $\Delta^{17}O$ isoflux in Fig. 2.8b has a mean value of ∼40 ‰PgC·yr^{-1}, which agrees well with the estimates from *Boering et al.* (2004) and *Kawagucci et al.* (2008) that were derived from the observed N_2O–$\Delta^{17}O$ correlation and the estimated stratospheric N_2O loss rate. The simulated stratospheric $\Delta^{17}O$ isoflux has a seasonal cycle with a peak-to-peak amplitude of ∼40 ‰PgC·yr^{-1}. On top of this, a relatively large day-to-day variability is associated with the stratospheric $\Delta^{17}O$ isoflux. The average value of the

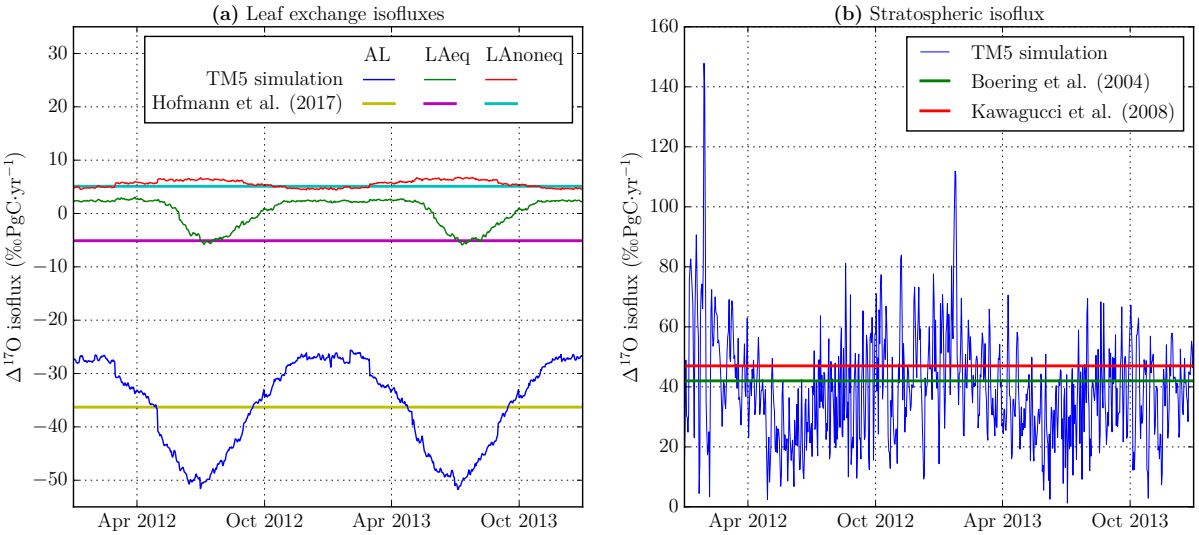

Figure 2.8: Daily time series of main $\Delta^{17}O$ isofluxes for TM5 simulation using base settings with 6°×4° horizontal resolution and 25 vertical levels compared with 1D global estimates. **(a)** Leaf-exchange isofluxes from TM5 compared with predictions from the box model from *Hofmann et al.* (2017). **(b)** Net stratosphere-troposphere $\Delta^{17}O$ isoflux simulated with TM5 model compared with global estimates from *Boering et al.* (2004) and *Kawagucci et al.* (2008) based on observed N_2O–$\Delta^{17}O$ correlation and the stratospheric N_2O loss rate.

stratospheric isoflux is not sensitive (compared to biospheric isofluxes) to small changes in the reference level, since $\Delta^{17}O_{strat} \gg \Delta^{17}O_{trop}$ whereas $\Delta^{17}O_{leaf} \approx \Delta^{17}O_{trop}$. During the Northern Hemispheric winter months, the global stratospheric influx of $\Delta^{17}O$ is relatively high, while at the same time the biospheric sink of $\Delta^{17}O$ is relatively weak, resulting in an increase of $\Delta^{17}O$ in atmospheric CO_2 on the global scale (which is visible in Fig. 2.6) An overview of the temporal variation of all global CO_2 mass fluxes and $\Delta^{17}O$ isofluxes during the years 2012-2013 is given in Figs. S2.2 and S2.3.

The latitudinal distribution of the annual mean net CO_2 mass fluxes and $\Delta^{17}O$ isofluxes for 2012-2013 are shown in Fig. 2.9 for different surface processes. Fig. 2.9a clearly shows the dominance of fossil fuel combustion ('ff') in the CO_2 budget. In the warm tropics, the ocean is a source of CO_2 to the atmosphere ($F_{OA} > F_{AO}$), whereas the ocean is a net sink of CO_2 in the extratropics. Across all latitudes, vegetation exchange and biomass burning act as a net sink and source respectively, and both processes peak in the tropical region. Soil invasion has no net contribution to the CO_2 budget, since we assume that the uptake is equal to the release for each grid cell. The $\Delta^{17}O$ isofluxes in Fig. 2.9b are negative for all latitudinal bands for each surface process. The $\Delta^{17}O$ isofluxes are dominated by the vegetation fluxes, although the contribution of fossil fuel combustion is significant in the Northern Hemisphere. Soil invasion $\Delta^{17}O$ isofluxes are relatively small, for this

simulation with base settings. More details for the contribution of different processes (e.g. the ingoing and outgoing leaf fluxes) as a function of latitude are presented in Figs. S2.4 and S2.5.

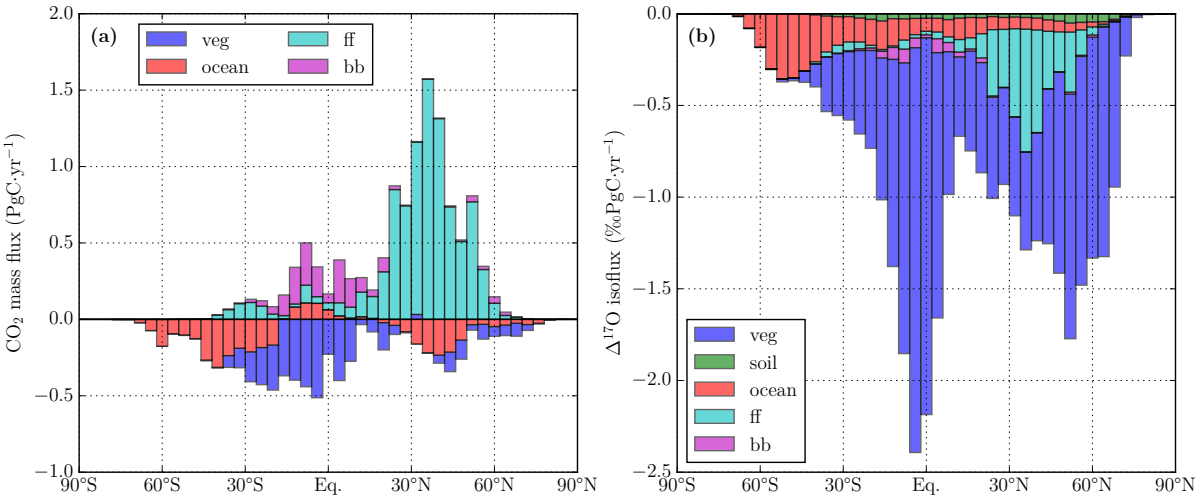

Figure 2.9: Net CO_2 mass fluxes **(a)** and net $\Delta^{17}O$ isofluxes **(b)** as function of latitude resulting from vegetation exchange ('veg'), soil invasion, ocean exchange, fossil fuel combustion ('ff') and biomass burning ('bb') for TM5 simulation with base settings, 6°×4° horizontal resolution and 25 vertical levels.

2.3.1.3 Model sensitivity analysis

Here we discuss the results of a sensitivity analysis for $\Delta^{17}O$ in CO_2. We have changed input values for the stratospheric N_2O–$\Delta^{17}O$ fit coefficients, the soil water and leaf water $\Delta^{17}O$ signatures, the soil invasion fluxes and the oxidation of atmospheric CO, as summarized in Table 2.2. In Table 2.3 we report the mean value and the peak-to-peak amplitude for $\Delta^{17}O$ in CO_2 for the lowest 500 m of the atmosphere for a selection of simulations with modified input settings. The peak-to-peak amplitude of global $\Delta^{17}O$ was determined by fitting a sine function on the monthly values for global $\Delta^{17}O$ for the years 2012 and 2013.

According to Table 2.3, the change in the stratospheric N_2O–$\Delta^{17}O$ fit coefficients results in a change of roughly +20 per meg and −20 per meg for the 95% upper (`ST_UPPER`) and lower limit (`ST_LOWER`) fits respectively (see Fig. 2.2b for the slope and offset of the fits) relative to the base model run (`BASE`). Clearly, the selected stratospheric fit is a key parameter for the resulting $\Delta^{17}O$ in tropospheric CO_2. Also, we see that the SH-NH difference and the amplitude of global $\Delta^{17}O$ increases when using the 95% upper limit confidence interval fit. As expected, the changes in these characteristics of the $\Delta^{17}O$

Table 2.3: Overview of the mean value and the peak-to-peak amplitude of the seasonal cycle of $\Delta^{17}O$ in CO_2 for the lowest 500 m of the atmosphere for different TM5 model simulations with horizontal resolution of 6°×4° and with 25 vertical levels. The input settings for each simulation are summarized in Table 2.2. The global and hemispheric results are discussed in Sect. 2.3.1.3 and the results for Zotino (60.80°N, 89.35°E), Mauna Loa (19.54°N, 155.58°W), Manaus (2.15°S, 59.00°W) and South Pole (90°S) are discussed in Sect. 2.3.2.2.

	Mean $\Delta^{17}O$ value (first column) [per meg] Peak-to-peak $\Delta^{17}O$ amplitude (second column, enclosed in parentheses) [per meg]						
Simulation	Global	NH	SH	Zotino	Mauna Loa	Manaus	South Pole
BASE	39.6 (6.5)	31.6 (17.7)	47.6 (5.1)	19.0 (36.1)	36.2 (19.5)	23.2 (2.9)	52.5 (7.4)
ST_LOWER	19.6 (5.4)	12.6 (14.4)	26.6 (3.9)	1.5 (31.4)	16.3 (15.5)	8.2 (2.9)	30.4 (5.5)
ST_UPPER	59.6 (7.7)	50.6 (21.1)	68.7 (6.3)	36.4 (40.9)	56.1 (23.5)	38.1 (2.9)	74.5 (9.2)
SOIL_CONST	40.5 (4.7)	34.7 (14.3)	46.3 (5.3)	27.8 (23.9)	38.7 (16.8)	18.5 (1.3)	51.1 (7.5)
LEAF_CONST	34.5 (6.7)	26.2 (17.8)	42.8 (4.9)	13.8 (36.1)	30.8 (19.7)	20.0 (2.3)	47.7 (7.1)
RESP_240	32.1 (6.4)	23.5 (17.4)	40.8 (4.9)	9.1 (35.3)	28.3 (19.2)	17.6 (3.0)	45.7 (7.2)
RESP_450	27.6 (6.3)	18.5 (17.1)	36.7 (4.8)	2.7 (34.5)	23.5 (18.9)	14.8 (3.0)	41.7 (7.0)
HYD_240	30.4 (6.6)	21.9 (17.7)	39.0 (4.9)	9.5 (35.6)	26.6 (19.3)	16.4 (3.1)	43.9 (7.1)
HYD_450	25.5 (6.6)	16.6 (17.5)	34.3 (4.7)	4.0 (35.5)	21.4 (19.0)	13.0 (3.1)	39.2 (6.9)
CO_ROCK	40.0 (6.5)	32.0 (17.6)	48.0 (5.1)	19.4 (36.0)	36.6 (19.4)	23.5 (2.9)	52.8 (7.4)
CO_FEIL	37.7 (6.4)	29.8 (17.5)	45.6 (5.1)	17.4 (35.5)	34.2 (19.3)	21.6 (3.1)	50.4 (7.3)

distribution are reversed when using the 95% lower limit confidence interval fit. On annual basis, the effect of changing the stratospheric fit coefficients is smallest for the tropical forests in the Amazon and in Central Africa, as shown in Fig. S2.6, which is caused by the rapid exchange between the atmosphere and biosphere in these regions.

In the base model run, we use a spatial distribution for the soil water signature $\Delta^{17}O_{soil}$ and spatial and temporal variation in the leaf water signature $\Delta^{17}O_{leaf}$ based on the local relative humidity, according to Eqs. (2.16) and (2.17). We performed TM5 simulations with a constant soil water signature $\Delta^{17}O_{soil} = -5$ per meg (`SOIL_CONST`) and with a constant transpiration exponent $\lambda_{transp} = 0.5156$ (`LEAF_CONST`) (values that are also used in the box model from *Hofmann et al.*, 2017). It should be noted that in this analysis we are not only changing the time and/or space dependency of $\Delta^{17}O_{soil}$ and $\Delta^{17}O_{leaf}$, but also their global average value. In the base model run the global mean values are $\Delta^{17}O_{soil} = -10.2$ per meg and $\lambda_{transp} = 0.5160$. Table 2.3 shows that changing to a constant $\Delta^{17}O_{soil} = -5$ per meg has a small effect on global mean $\Delta^{17}O$ in atmospheric CO_2, whereas using a constant $\lambda_{transp} = 0.5160$ results in a decrease of 5.1 per meg in global mean $\Delta^{17}O$. Finally, we see that changing the soil water signature to $\Delta^{17}O_{soil} = -5$ per meg leads to decreases in both the North-South difference and the amplitude of global $\Delta^{17}O$. In Fig. S2.7 we show the annual mean difference of $\Delta^{17}O$ for the TM5 simulations with modifications in the water signatures relative to the base model run.

The effect of a change in the global magnitude and the spatial distribution of the soil invasion flux can also be seen in Table 2.3. An increase from the base value of 30 PgC·yr^{-1} to 240 PgC·yr^{-1} or even 450 PgC·yr^{-1} leads to a decrease in the global mean $\Delta^{17}O$ signature of atmospheric CO_2, where the magnitude of the $\Delta^{17}O$ drop also depends on the spatial distribution of the soil invasion flux. For respiration scaling (`BASE`, `RESP_240` and `RESP_450`) the soil invasion fluxes are mostly present in the tropical region, whereas for hydrogen scaling (`HYD_240` and `HYD_450`) the soil invasion fluxes extend to higher latitudes, which have a lower $\Delta^{17}O_{soil}$ signature and hence result in a lower $\Delta^{17}O$ for atmospheric CO_2. Also, we see in Table 2.3 that increasing the soil invasion fluxes leads to a small decrease in the amplitude of global and hemispheric $\Delta^{17}O$. In Fig. S2.8 we show the global mean $\Delta^{17}O$ distribution for changes in the soil invasion fluxes.

Finally, we show in Table 2.3 that incorporating the CO + OH reaction with the enrichment ϵ_{CO+OH} from *Röckmann et al.* (1998b) (`CO_ROCK`) has a small positive effect on the resulting $\Delta^{17}O$ of atmospheric CO_2, whereas a larger negative effect was found for the fractionation factors from *Feilberg et al.* (2005) (`CO_FEIL`). Based on the enrichment coefficients given in Sect. 2.2.4.2 we expect that more ^{18}O enriched CO_2 is produced in `CO_FEIL`

than for CO_ROCK, which explains its lower resulting $\Delta^{17}O$ signature in atmospheric CO_2. Because the coefficients from *Röckmann et al.* (1998b) were also used to produce the CO isotopologue fields by *Gromov* (2013), we consider the results for CO_ROCK to be most representative. In Fig. S2.9 we show the distribution of the annual mean anomalies for the calculated $\Delta^{17}O$ relative to the base model run.

2.3.2 Local model simulations

2.3.2.1 Model-measurement comparisons

To test the ability of our model to simulate $\Delta^{17}O$ in atmospheric CO_2 we compare our model results with a stratospheric profile measured above Sodankylä, Finland (*Mrozek et al.*, 2016) and with tropospheric measurement series for Göttingen, Germany (*Hofmann et al.*, 2017) and Taipei, Taiwan (*Liang et al.*, 2017b). We selected these two data sets, because the measurement periods overlap (partially) with our model output for years 2010-2014. It should be noted that we are using a relatively coarse resolution for our model (a 6°×4° horizontal resolution and 25 vertical levels) and that the model output are daily averages and therefore not fully representative for the observations.

In Fig. 2.10, our TM5 model results are shown alongside the N_2O mole fraction and $\Delta^{17}O$ in CO_2 profiles that were obtained from an AirCore with Stratospheric Air Subsampler (SAS) by *Mrozek et al.* (2016) above Sodankylä, Finland (67.35°N, 26.93°E) on 5 November, 2014. Note that the N_2O mole fractions that are reported by *Mrozek et al.* (2016) are not directly measured, but inferred from measurements of CH_4. The profile of N_2O mole fractions from our simulation agrees reasonably well with the 'measured' N_2O profile. Contrary to the measured $\Delta^{17}O$ in CO_2 signatures, the simulated profile shows a monotonic increase with altitude. For the two observations at highest altitudes (at 24 and 39 hPa) we find that the simulated N_2O is too low and that the simulated $\Delta^{17}O$ in CO_2 is too high, which suggests that the sampled air is younger than simulated in the transport model for these altitudes. The opposite is found for two of the three lowest observations (at 87 and 151 hPa) indicating that the sampled air was older than the simulated air. Note that the comparison of our model results with the data from *Mrozek et al.* (2016) is independent, since the experimental data from *Mrozek et al.* (2016) was not used as input for the N_2O–$\Delta^{17}O$ fit.

In *Hofmann et al.* (2017), model predictions from an early version of our model (see Sect. S2.2 for an overview of the differences with our current model) were compared

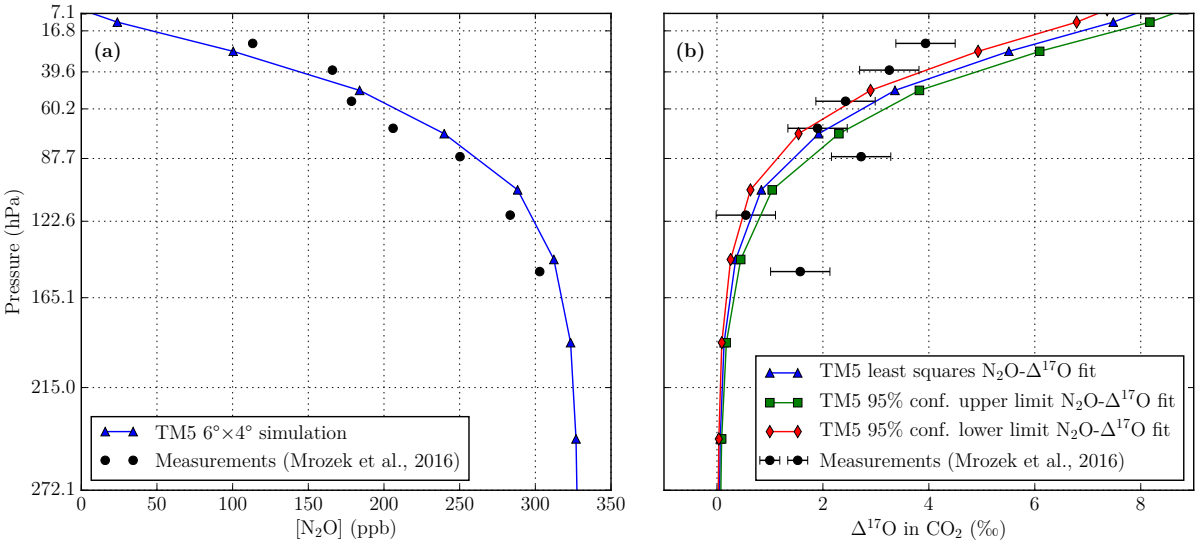

Figure 2.10: Comparison of vertical profiles measured over Sodankylä (67.35°N, 26.93°E) (*Mrozek et al.*, 2016) with TM5 model simulations with horizontal resolution of 6°×4° and with 25 vertical levels. The ticks on the vertical axis coincide with the cell boundaries in the TM5 model with 25 vertical levels. **(a)** Stratospheric profile of N_2O mole fraction. **(b)** Stratospheric profile of $\Delta^{17}O$ in CO_2 compared with TM5 least squares N_2O–$\Delta^{17}O$ fit simulation (`BASE`), 95% confidence upper limit fit simulation (`ST_UPPER`) and 95% confidence lower limit fit simulation (`ST_LOWER`).

with measurements of $\Delta^{17}O$ in CO_2 for Göttingen (51.56°N, 9.95°E) and Mt. Brocken (51.80°N, 10.62°E). We have repeated the analysis with our updated model and again find that there is a seasonal cycle in $\Delta^{17}O$ that is driven by the biosphere. Also, we again find that our model does not show the significant drop in $\Delta^{17}O$ that is reported based on observations (respectively a mean $\Delta^{17}O$ of -12.8 per meg and -108.2 per meg before and after July 1st, 2011). This unexplained, large drop in the reported observations is discussed in more detail in Sect. 6.2 of *Hofmann et al.* (2017). A comparison of the measured CO_2 mole fraction and its $\Delta^{17}O$ signature for Göttingen (51.56°N, 9.95°E) and Mt. Brocken (51.80°N, 10.62°E) with model predictions for the lowest level in TM5 (lowest ∼35 m), is given in Fig. S2.10.

We also compare our model predictions for $\Delta^{17}O$ in tropospheric CO_2 with measurement data obtained at the Academia Sinica campus (25.04°N, 121.61°E) and the National Taiwan University (25.01°N, 121.54°E) in Taipei, Taiwan from *Liang et al.* (2017b). In Fig. 2.11 we compare the measured and simulated CO_2 mole fractions and the $\Delta^{17}O$ signature. The uncertainty bar that is associated with the measured CO_2 mole fractions is determined from the deviation between measurements taken at different times on the same day, showing the importance of local contributions and the development of the atmospheric

boundary layer. The shading in Fig. 2.11b indicates the spread related to the 95% confidence interval for the N_2O–$\Delta^{17}O(CO_2)$ coefficients (slope and offset) that is used in the stratospheric module. The spread in model predictions for the different representations of the stratospheric source is substantial (∼40 per meg range), but cannot fully explain the model-measurement discrepancy for this location. Compared to Göttingen, there is a smaller contribution of the biospheric fluxes since Taipei is surrounded by ocean. In addition, we expect a lower seasonality of the biosphere at the latitude of Taipei compared to Göttingen. Contrary to measurement series from Göttingen, our model predictions are lower (mean value of 31.1 per meg) than the $\Delta^{17}O$ measurements from Taipei (mean value of 58.7 per meg).

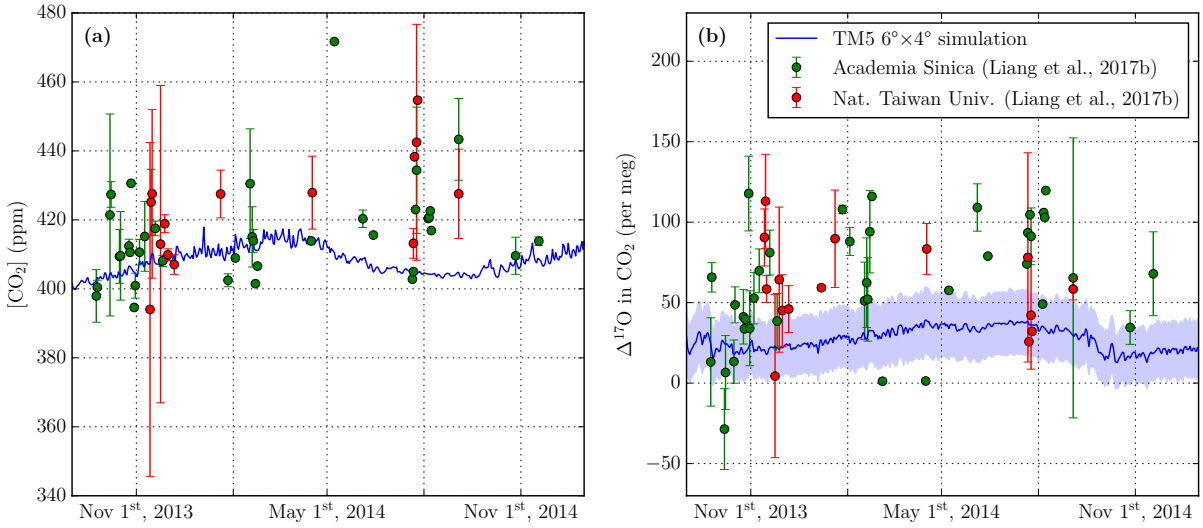

Figure 2.11: Comparison of tropospheric measurements for the Academia Sinica campus (25.04°N, 121.61°E) and the National Taiwan University (25.01°N, 121.54°E) in Taipei, Taiwan from *Liang et al.* (2017b) with daily model predictions for the lowest 35 m from TM5 with horizontal resolution of 6°×4° and 25 vertical levels. **(a)** CO_2 mixing ratios. **(b)** $\Delta^{17}O$ in CO_2. The shading indicates the spread in model estimates for the 95% confidence interval for the N_2O–$\Delta^{17}O$ fit for stratospheric CO_2 (obtained from simulations `ST_LOWER` and `ST_UPPER`).

2.3.2.2 Future measurements

The currently available measurement series for $\Delta^{17}O$ of tropospheric CO_2 have in common that the air was collected in the vicinity of the research groups that performed the measurements. Our objective here is to make use of our 3D model predictions to identify locations for which measurements of $\Delta^{17}O$ in CO_2 would be valuable for a better understanding of the global budget of $\Delta^{17}O$ in CO_2 and further model development. A global map of the peak-to-peak amplitude of simulated $\Delta^{17}O$ in CO_2 is shown in Fig. S2.11a.

We have selected four locations for which we describe the simulated patterns of $\Delta^{17}O$ in CO_2 in more detail.

Fig. 2.12a shows the $\Delta^{17}O$ signature for CO_2 in the lowest 500 m of the atmosphere for a selection of locations. Zotino (60.80°N, 89.35°E) is the location of the Zotino Tall Tower Observatory (ZOTTO) (*Heimann et al.*, 2014), where we expect a seasonal cycle of 36.1 per meg (see also Table 2.3), which is substantially larger than the measurement uncertainty of currently available measurement techniques (see also Sect. 2.1). Also, the mean value of $\Delta^{17}O$ at Zotino can be used to better constrain the magnitude of soil invasion fluxes (see Table 2.3). This site was also used in a study of the $\delta^{18}O$ in CO_2 signal by *Cuntz et al.* (2002).

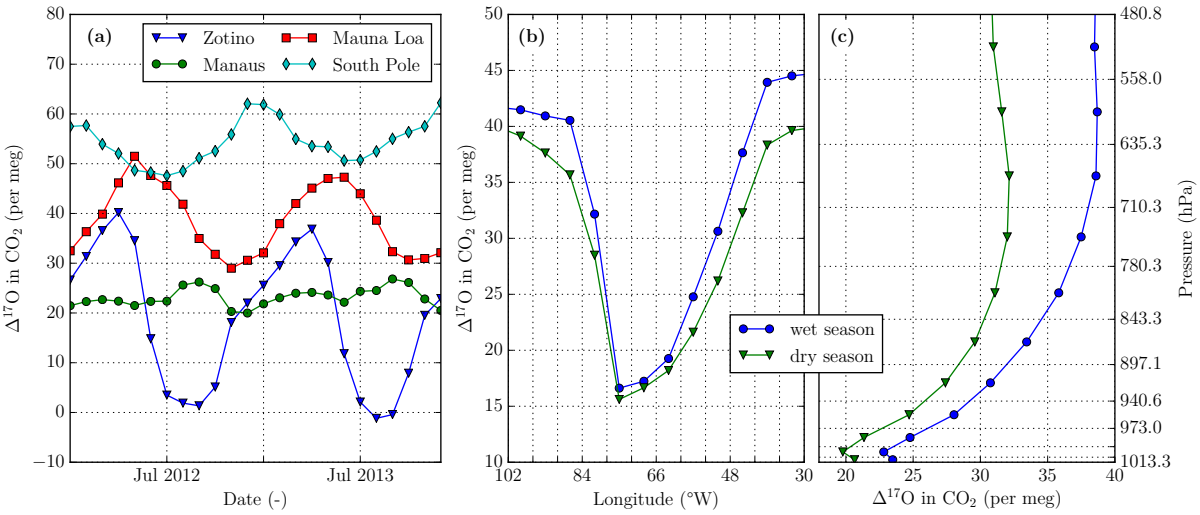

Figure 2.12: TM5 model predictions for $\Delta^{17}O$ in atmospheric CO_2 using base model settings with a horizontal resolution of 6°×4° and with 25 vertical levels for selected locations. **(a)** Time series of $\Delta^{17}O$ in CO_2 for the lowest 500 m of the atmosphere for Zotino (60.80°N, 89.35°E), Mauna Loa (19.54°N, 155.58°W), Manaus (2.15°S, 59.00°W) and South Pole (90°S). **(b)** Longitudinal cross-section through Manaus of $\Delta^{17}O$ in CO_2 for the lowest 500 m of the atmosphere in the dry season (defined here as months in the range July to October) and wet season; the vertical grid lines correspond to the longitudinal boundaries of the TM5 grid. **(c)** Vertical profile over Manaus of $\Delta^{17}O$ in CO_2 in the dry and wet seasons; the horizontal grid lines correspond to the vertical TM5 hybrid sigma pressure levels.

Mauna Loa (19.54°N, 155.58°W) and South Pole (90°S) are background stations that are famous for their long-standing CO_2 records that are operated by the National Oceanic and Atmospheric Administration (NOAA) and the Scripps Institution of Oceanography (SIO). The time series of $\Delta^{17}O$ for CO_2 in the lowest 500 m of the atmosphere (above the local surface) for Mauna Loa and South Pole in Fig. 2.12a exhibit a seasonal cycle in anti-phase with each other. Also, South Pole is an interesting location because we expect a

high annual mean $\Delta^{17}O$ signature. Dry air samples from the South Pole (British Antarctic Survey station) were collected in 2017, and are currently being analyzed for their $\Delta^{17}O$ in CO_2 signatures by the Centre for Isotope Research in Groningen, the Netherlands.

Also, we included model predictions of $\Delta^{17}O$ in CO_2 for Manaus (2.15°S, 59.00°W), the location of the Amazon Tall Tower Observatory (ATTO) (*Andreae et al.*, 2015). Although the annual variation of $\Delta^{17}O$ in CO_2 is small in the lowest 500 m of the atmosphere for Manaus, there is a relatively strong gradient for $\Delta^{17}O$ in the longitudinal direction across Manaus (Fig. 2.12b) and a strong vertical gradient above Manaus (Fig. 2.12c). Measurements in and around the Amazon region that are ongoing since February 2018 and analyzed at the LaGEE lab in Brazil could show whether these predicted features in the $\Delta^{17}O$ distribution can be observed. The zonal mean annual mean vertical profile for $\Delta^{17}O$ in CO_2 as a function of latitude can be seen in Fig. S2.11b.

2.4 Discussion

2.4.1 Possible improvements of model for $\Delta^{17}O$ in CO_2

In this section we discuss some model features that could be added to or improved with respect to our current 3D model for $\Delta^{17}O$ in CO_2. In our current model we represent the stratospheric source of $\Delta^{17}O$ by simulating N_2O and converting stratospheric N_2O mole fractions into $\Delta^{17}O$ signatures based on their observed correlation as described in Sect. 2.2.2.1. Although we feel that this is a robust and straightforward approach, we generally prefer to simulate the actual physical processes. As more details of the production process are unfolded by the scientific community, we foresee that it becomes more feasible to implement an explicit description of the production of $\Delta^{17}O$ in CO_2 in future model versions.

To calculate the atmosphere leaf fluxes F_{AL} and F_{LA} we use GPP from SiBCASA at a 3 hourly temporal resolution and GPP-weighted c_i/c_a values from SiBCASA at a monthly temporal resolution as described in Sect. 2.2.3.1. Also, we assume in our current model that leaf respiration is a constant fraction of 12% of GPP, similar to *Ciais et al.* (1997a). In future studies we intend to use c_i/c_a values and leaf respiration from SiBCASA at a 3 hourly temporal resolution to be fully consistent with the temporal resolution of GPP. In the comprehensive $\delta^{18}O$ model from *Cuntz et al.* (2003a,b) these components are also simulated at the same temporal resolution.

For some input fields we use year-specific data, such as the meteorological data ERA-Interim (*Dee et al.*, 2011) that drives the atmospheric transport in TM5. Also the vegetation-atmosphere fluxes from the SiBCASA model are calculated using the ERA-Interim meteorology. For other input fields, we resort to annually repeating fields, such as for the CO isotopologue fields (*Gromov*, 2013) and the OH fields (*Spivakovsky et al.*, 2000). In general we preferably use year-specific input data to capture interannual variability of the different processes. Especially for CO oxidation we expect some interannual variability to $\Delta^{17}O$ in CO_2 due to the irregular occurrence of wildfires (which is major source of CO, *Holloway et al.*, 2000) that we are now not able to simulate.

Another possible improvement is the resolution of the transport model for the performed simulations, which is relatively coarse (a horizontal resolution of $6°\times4°$ and a vertical resolution of 25 layers). A finer horizontal resolution could lead to better agreement with local surface measurements and a finer vertical resolution could be more representative for the stratosphere-troposphere exchange, which is of importance to the $\Delta^{17}O$ in CO_2 budget and its ability to be used as tracer of GPP, as discussed in Sect. 2.4.3. For follow-up studies focusing on specific regions, we intend to use finer spatial resolutions.

Finally, a valuable extension of this model would be to implement a 'tracer tagging' method that allows to disentangle the contributions of different processes (e.g. biosphere exchange or fossil fuel combustion) on the resulting $\Delta^{17}O$ signature of CO_2. This would allow to effectively attribute the seasonal patters, interannual variability or local disturbances that appear in the simulated $\Delta^{17}O$ signature to these processes. Such a 'tracer tagging' technique was also also used in the $\delta^{18}O$ studies from *Ciais et al.* (1997a,b), *Peylin et al.* (1997, 1999) and *Cuntz et al.* (2003a,b) to quantify the contribution of different processes to the simulated $\delta^{18}O$ signature for atmospheric CO_2.

2.4.2 Required measurements of $\Delta^{17}O$ in CO_2

In this section we discuss issues related to the measurements of $\Delta^{17}O$ in CO_2. For $\delta^{18}O$ in CO_2 there is a vast network of well characterized measurement stations operated by NOAA and collaborating organizations that measure $\delta^{18}O$ in CO_2 at a regular basis in addition to other atmospheric compounds and meteorological variables. These flasks are typically already collected with dried air, and with new measurement techniques for $\Delta^{17}O$ in CO_2 the air in these flasks is sufficient for a high-precision ($\pm$ 20 per meg) analysis. The opportunity to start a global characterization of actual signatures, followed by a monitoring effort across a subset of most interesting sites thus could be seized. In Sect

2.3.2.2, we describe in more detail four locations where measurements have, or could be, started using existing resources.

Besides these observations of $\Delta^{17}O$ on the global scale that can help to understand the budget of $\Delta^{17}O$ in CO_2, there is also a need to measure the individual processes that affect $\Delta^{17}O$ in CO_2. The value of experiments that unravel the remaining uncertainties about the stratospheric production of $\Delta^{17}O$ was already mentioned in Sect. 2.4.1. Also, controlled laboratory measurements on the effect of plant assimilation on the $\Delta^{17}O$ signature of atmospheric CO_2 could be valuable to test the assumptions used in our current model that are for a large part based on earlier works on $\delta^{18}O$ in CO_2 (e.g. *Gillon and Yakir*, 2000, 2001).

2.4.3 Potential of $\Delta^{17}O$ in CO_2 as tracer of GPP

In this final discussion section we reflect on the potential of $\Delta^{17}O$ in CO_2 to function as a tracer of GPP. One of the main requirements for its use as tracer of GPP is that the stratospheric influx of $\Delta^{17}O$ in CO_2 can be quantified accurately. However, as described in Sect. 2.2.2.3, estimates for the stratosphere-troposphere exchange vary considerably. Combination with other tracers (e.g. ^7Be, as described by *Dutkiewicz and Husain*, 1985) might be necessary to reduce the uncertainty in stratosphere-troposphere exchange.

One of the key variables in the budget of $\Delta^{17}O$ in CO_2 is the c_i/c_a ratio that relates the gross exchange fluxes between atmosphere and leaf to GPP as described in Sect. 2.2.3.1. *Cuntz* (2011) pointed out in a commentary about the GPP estimate by *Welp et al.* (2011) that uncertainty in the c_i/c_a ratio (or the percentage of the CO_2 that diffuses into a leaf that is fixed) can have significant effects on the inferred GPP. This exemplifies the necessity to better constrain c_i/c_a, which might be achieved with $\delta^{13}C$ observations (*Peters et al.*, 2018).

Similarly, the large uncertainty in the magnitude of soil invasion fluxes that was reported by *Wingate et al.* (2009), has implications for the potential use of $\Delta^{17}O$ in CO_2 as a tracer of GPP. If the soil invasion fluxes are underestimated, this could lead to overestimating GPP since these processes have a similar effect on $\Delta^{17}O$ in CO_2. The ongoing research on carbonic anhydrase in soils from the carbonyl sulfide (COS) community might also lead to better quantification of the CO_2 soil invasion fluxes and as such benefit the use of $\Delta^{17}O$ in CO_2 as tracer of GPP.

Finally, we address the effect of the hydrological cycle on the budget of $\Delta^{17}O$ in atmo-

spheric CO_2. The main reason to explore the use of $\Delta^{17}O$ as tracer for GPP instead of $\delta^{18}O$, was that $\Delta^{17}O$ is hardly sensitive to the hydrological cycle which greatly simplifies its interpretation and modeling according to *Hoag et al.* (2005). Still, we have put much effort in calculating the $\Delta^{17}O$ isotopic composition of different water reservoirs (e.g. soil water and leaf water, as discussed in Sect. 2.2.3.1) and we find that changing these values can have significant effect at high northern latitudes, as described in Sect. 2.3.1.3. Also, a recent study by *Tian et al.* (2018) shows that $\Delta^{17}O$ of precipitation collected at Indianapolis, Indiana, USA, can vary considerably within months. As such, the use of $\Delta^{17}O$ in CO_2 could be more involved than originally envisioned by *Hoag et al.* (2005) depending on the specifics of the application.

2.5 Conclusions

We developed a 3D model framework for $\Delta^{17}O$ (defined as $\Delta^{17}O = \ln(\delta^{17}O + 1) - \lambda_{RL} \cdot \ln(\delta^{18}O + 1)$, with $\lambda_{RL} = 0.5229$) in atmospheric CO_2, using the terrestrial biosphere model SiBCASA and atmospheric transport model TM5. In our model framework, the stratospheric source of $\Delta^{17}O$ in CO_2 is based on the observed N_2O–$\Delta^{17}O$ correlation using available stratospheric data. We included the CO_2 exchange fluxes from biosphere, oceans and soils with the atmosphere. Also, we added the release of CO_2 to the atmosphere from fossil fuel combustion and biomass burning and the production of CO_2 through the oxidation of atmospheric CO.

Our 3D model (with base model settings) predicts an average $\Delta^{17}O$ signature of 39.6 per meg for CO_2 in the lowest 500 m of the atmosphere, which is roughly 20 per meg lower than the prediction from the box model by *Hofmann et al.* (2017). This difference can be attributed mostly to the larger biosphere-atmosphere exchange in the 3D model (global mean $F_{AL} = -514.5$ PgC·yr^{-1} for 2012/2013) compared to the box model ($F_{AL} = -352$ PgC·yr^{-1}) by *Hofmann et al.* (2017). For the NH and SH we predict a mean $\Delta^{17}O$ signature of 31.6 and 47.6 per meg respectively. In addition, the $\Delta^{17}O$ signature exhibits a seasonal cycle with a peak-to-peak amplitude of 17.7 for the NH and 5.1 per meg for the SH, showing the largest drop in $\Delta^{17}O$ during the respective summer months for both hemispheres.

We showed that $\Delta^{17}O$ model predictions are sensitive to changes in the coefficients describing the N_2O–$\Delta^{17}O$ correlation for stratospheric CO_2. Also, the magnitude and spatial distribution of the soil invasion fluxes have a significant effect on $\Delta^{17}O$ in atmospheric

CO_2. Furthermore, it was found that using a spatially explicit soil water signature $\Delta^{17}O_{soil}$ and time and space dependent leaf water signature $\Delta^{17}O_{leaf}$ has a limited effect on the resulting $\Delta^{17}O$ in atmospheric CO_2 and that the oxidation of CO has a minor effect on $\Delta^{17}O$ in atmospheric CO_2.

We compared our model predictions with a stratospheric profile of $\Delta^{17}O$ in CO_2 measured above Sodankylä, Finland (*Mrozek et al.*, 2016), which showed good agreement indicating that our 3D model is able to simulate these large scale features of $\Delta^{17}O$ in atmospheric CO_2. Comparisons of model predictions with currently available tropospheric measurements of $\Delta^{17}O$ in CO_2 remain inconclusive due to the unexpected interannual variability for measurements from Göttingen, Germany (*Hofmann et al.*, 2017) and the influence of local disturbances that can not be resolved in our global model for Taipei, Taiwan (*Liang and Mahata*, 2015).

We identified Zotino, Russia (60.80°N, 89.35°E) as a suitable location to detect a large seasonal cycle of $\Delta^{17}O$ in CO_2 of 36.1 per meg, which is substantially larger than the uncertainty of several recently developed measurement techniques for $\Delta^{17}O$ in CO_2. Mauna Loa, U.S. (19.54°N, 155.58°W) and South Pole (90°S) are suitable background locations for which we predict a mean $\Delta^{17}O$ in CO_2 of 36.2 and 52.5 per meg respectively. For Manaus, Brazil (2.15°S, 59.00°W) we predict a small seasonal cycle in $\Delta^{17}O$ in CO_2 of 2.9 per meg, but a strong vertical and longitudinal gradient. Measurements at the suggested locations or at comparable sites could help to further increase our understanding of the global $\Delta^{17}O$ budget for tropospheric CO_2.

Acknowledgments

We thank Thomas Launois for providing H_2 deposition maps. The European Research Council (ERC) is acknowledged for funding this research (649087) as part of the ASICA (Airborne Stable Isotopes of Carbon from the Amazon) project. The model simulations in this work have been performed using a grant for computing time (SH-312-14) from the Netherlands Organization for Scientific Research (NWO). We thank Kristie Boering and two anonymous reviewers for their constructive suggestions.

Data availability

The model output data that are used to produce the figures and tables in this chapter are hosted by the ICOS Carbon Portal and are accessible online (`https://doi.org/10.18160/3D4N-5YMF`).

Supplemental information

S2.1 Overview of $\Delta^{17}O$ definitions

For historical reasons there are different definitions that are used to express the oxygen isotope anomaly $\Delta^{17}O$. Here we give an overview of the most commonly used definitions for $\Delta^{17}O$ and describe relations for converting $\Delta^{17}O$ values between different definitions. Our starting point is the mass-dependent relation between oxygen isotopes (see e.g. *Meijer and Li*, 1998)

$$\delta^{17}O + 1 = (\delta^{18}O + 1)^{\lambda}, \tag{S2.1}$$

which can be rewritten as

$$\frac{\delta^{17}O + 1}{(\delta^{18}O + 1)^{\lambda}} - 1 = 0. \tag{S2.2}$$

The deviation from this mass-dependent relation is the basis for the 'exponential definition' $\Delta^{17}O_{exp}$ that is used in e.g. *Assonov and Brenninkmeijer* (2005)

$$\Delta^{17}O_{exp} = \frac{\delta^{17}O + 1}{(\delta^{18}O + 1)^{\lambda}} - 1. \tag{S2.3}$$

An alternative definition for $\Delta^{17}O$ can be obtained by first taking the natural logarithm of Eq. (S2.1) to arrive at

$$\ln(\delta^{17}O + 1) = \ln\left((\delta^{18}O + 1)^{\lambda}\right), \tag{S2.4}$$

which can be rewritten as

$$\ln(\delta^{17}O + 1) - \lambda \cdot \ln(\delta^{18}O + 1) = 0. \tag{S2.5}$$

The deviation from this mass-dependent relation is the 'logarithmic definition' $\Delta^{17}O_{log}$ that we use consistently in our study and is used by the majority of the recent studies on $\Delta^{17}O$ in CO_2 (e.g. *Hofmann et al.*, 2017)

$$\Delta^{17}O_{log} = \ln(\delta^{17}O + 1) - \lambda \cdot \ln(\delta^{18}O + 1). \tag{S2.6}$$

The right-hand side of this equation can be approximated by using the Taylor series expansion for $\ln(x + 1) \approx x$ (for x close to 0), which results in the 'linear definition' $\Delta^{17}O_{lin}$ that is used in most of the older studies on $\Delta^{17}O$ (e.g. *Hoag et al.*, 2005)

$$\Delta^{17}O_{lin} = \delta^{17}O - \lambda \cdot \delta^{18}O. \tag{S2.7}$$

For $\delta^{17}O$ and $\delta^{18}O$ close to 0, the 'logarithmic' and 'linear' $\Delta^{17}O$ values are approximately equal, i.e.

$$\Delta^{17}O_{log} \approx \Delta^{17}O_{lin}. \tag{S2.8}$$

By adding 1 to both sides of Eq. (S2.3), taking the natural logarithm and rearranging the resulting terms, we get

$$\ln(\Delta^{17}O_{exp} + 1) = \ln(\delta^{17}O + 1) - \lambda \cdot \ln(\delta^{18}O + 1). \tag{S2.9}$$

We can rewrite this result further using Eq. (S2.6), to arrive at a conversion relation between the 'logarithmic definition' and 'exponential definition' for $\Delta^{17}O$

$$\Delta^{17}O_{log} = \ln(\Delta^{17}O_{exp} + 1) \approx \Delta^{17}O_{exp}, \tag{S2.10}$$

where the approximation is again based on the Taylor series expansion of $\ln(x+1) \approx x$ for x close to 0. Besides the difference in mathematical form (i.e. the 'linear', 'exponential'

or 'logarithmic' definition) of $\Delta^{17}O$, many studies use different values for the reference line (e.g. $\lambda = 0.516$ is used by *Hoag et al.* (2005); and $\lambda = 0.5229$ is used by *Hofmann et al.* (2017)). Conversion between different $\Delta^{17}O$ scales can then be performed by first reconstructing the $\delta^{17}O$ and $\delta^{18}O$ signatures.

S2.2 Updates to the 3-D model for $\Delta^{17}O$ in CO_2

Several updates were made in the latest model version (r5558) with respect to a previous version (r5337) that was described by *Schneider* (2015) and that was used in the study by *Hofmann et al.* (2017) to simulate $\Delta^{17}O$ in CO_2 for Göttingen and Mt. Brocken, Germany. A brief overview of the changes for the different reservoirs of the $\Delta^{17}O$ model is presented in Table S2.1. For a more detailed description of the latest model implementation (r5558), the reader is referred to Sect. 2.2.

S2.3 Derivation of N_2O detrending method

Here we give the derivation for our N_2O detrending method, which is a modification of the detrending method described by *Assonov et al.* (2013). The N_2O detrending method from *Assonov et al.* (2013) uses a constant atmospheric growth rate of $\alpha_{\mathrm{ref}} = 0.844 \pm 0.001$ ppb·yr^{-1} (based on observations of N_2O at Mauna Loa over the time period January 2007 to December 2011) to relate observed N_2O mole fractions X_{obs} to detrended N_2O mole fractions X_{dtd}

$$X_{\mathrm{dtd}} = X_{\mathrm{obs}} + \alpha_{\mathrm{ref}} \cdot (t_{\mathrm{ref}} - t_{\mathrm{obs}}), \tag{S2.11}$$

where t_{obs} is the time of observation and t_{ref} the reference time (in this case January 1$^{\mathrm{st}}$, 2007) on which the observations are projected. In our method we replace the constant atmospheric growth rate α_{ref} with an observation-specific growth rate α^*

$$X_{\mathrm{dtd}} = X_{\mathrm{obs}} + \alpha^* \cdot (t_{\mathrm{ref}} - t_{\mathrm{obs}}). \tag{S2.12}$$

We want the observation-specific growth rate α^* to satisfy the following two properties (1) that α^* scales linearly with the detrended mole fraction X_{dtd} (such that the growth rate

for N_2O at the 100 ppb level is 3 times lower than at the 300 ppb level) and (2) that for Mauna Loa the growth rate α^* is equal to the growth rate α_{ref} from *Assonov et al.* (2013). These desired properties are satisfied if we calculate the observation-specific growth rate α^* according to

$$\alpha^* = \alpha_{\mathrm{ref}} \cdot \frac{X_{\mathrm{dtd}}}{X_{\mathrm{ref}}}, \tag{S2.13}$$

where $X_{\mathrm{ref}} = 320.84$ ppb is the observed mole fraction at Mauna Loa for the reference date (*Assonov et al.*, 2013). Inserting the expression for α^* from Eq. (S2.13) into Eq. (S2.12) yields

$$X_{\mathrm{dtd}} = X_{\mathrm{obs}} + \alpha_{\mathrm{ref}} \cdot \frac{X_{\mathrm{dtd}}}{X_{\mathrm{ref}}} \cdot (t_{\mathrm{ref}} - t_{\mathrm{obs}}), \tag{S2.14}$$

which can be rewritten as

$$X_{\mathrm{dtd}} = X_{\mathrm{obs}} \cdot \left[1 - \frac{\alpha_{\mathrm{ref}}}{X_{\mathrm{ref}}} \cdot (t_{\mathrm{ref}} - t_{\mathrm{obs}})\right]^{-1}. \tag{S2.15}$$

By replacing the constant atmospheric growth rate α_{ref} with an observation-specific growth rate α^*, we have constructed a detrending method for N_2O that is not only suitable for tropospheric air, but also for stratospheric air.

S2.4 Derivation of $\Delta^{17}O$ atmosphere-leaf fractionation

Here we derive the fractionation of the $\Delta^{17}O$ signature that occurs when atmospheric CO_2 diffuses from the atmosphere into leaf stomata. First we give the definitions of $\Delta^{17}O_A$ and $\Delta^{17}O_{AL}$, which are the signatures for atmospheric CO_2 and for CO_2 that is diffused into leaf stomata

$$\Delta^{17}O_A = \ln(\delta^{17}O_A + 1) - \lambda_{\mathrm{RL}} \cdot \ln(\delta^{18}O_A + 1), \tag{S2.16}$$

$$\Delta^{17}O_{AL} = \ln(\delta^{17}O_{AL} + 1) - \lambda_{\mathrm{RL}} \cdot \ln(\delta^{18}O_{AL} + 1), \tag{S2.17}$$

where λ_{RL} is the selected reference line (in this study we use $\lambda_{\mathrm{RL}} = 0.5229$, which is the triple oxygen isotope fractionation exponent for CO_2–H_2O equilibration according to *Barkan and Luz*, 2012) and where $\delta^{17}O_A$ and $\delta^{18}O_A$ refer to the isotope signatures of atmospheric CO_2 and $\delta^{17}O_{AL}$ and $\delta^{18}O_{AL}$ refer to the isotope signatures of CO_2 that is diffused into the leaf stomata. The $\delta^{18}O$ signature for CO_2 diffused into the leaf can be related to the atmospheric $\delta^{18}O$ signature according to

$$\delta^{18}O_{AL} = \alpha_{\mathrm{leaf}} \cdot (\delta^{18}O_A + 1) - 1, \tag{S2.18}$$

where, α_{leaf} is the fractionation factor of $C^{18}OO$ relative to CO_2 for diffusion through the leaf stomate. Similarly, the fractionation in $\delta^{17}O$ during diffusion from the atmosphere into the leaf stomata is given by

$$\delta^{17}O_{AL} = {\alpha_{\mathrm{leaf}}}^{\lambda_{\mathrm{kinetic}}} \cdot (\delta^{17}O_A + 1) - 1, \tag{S2.19}$$

where $\lambda_{\mathrm{kinetic}}$ is the exponent that relates the fractionation of the isotopologue $C^{17}OO$ to the fractionation of the isotopologue $C^{18}OO$. Next, we insert Eqs. (S2.19) and (S2.18) for $\delta^{17}O$ and $\delta^{18}O$ into Eq. (S2.17) to arrive at

$$\Delta^{17}O_{AL} = \ln({\alpha_{\mathrm{leaf}}}^{\lambda_{\mathrm{kinetic}}} \cdot (\delta^{17}O_A + 1)) - \lambda_{\mathrm{RL}} \cdot \ln(\alpha_{\mathrm{leaf}} \cdot (\delta^{18}O_A + 1)), \tag{S2.20}$$

which can be rewritten as

$$\Delta^{17}O_{AL} = \lambda_{\mathrm{kinetic}} \cdot \ln(\alpha_{\mathrm{leaf}}) + \ln(\delta^{17}O_A + 1) - \lambda_{\mathrm{RL}} \cdot \left[\ln(\alpha_{\mathrm{leaf}}) + \ln(\delta^{18}O_A + 1)\right]. \tag{S2.21}$$

We can rewrite this by using the definition of $\Delta^{17}O_A$ from Eq. (S2.16) to arrive at

$$\Delta^{17}O_{AL} = \Delta^{17}O_A + (\lambda_{\mathrm{kinetic}} - \lambda_{\mathrm{RL}}) \cdot \ln(\alpha_{\mathrm{leaf}}). \tag{S2.22}$$

The fractionation of $\Delta^{17}O$ for other processes (e.g. evaporation or condensation) can be described by similar equations. Note that if the chosen reference line λ_{RL} is equal to the fractionation exponent for a given process, then this process will not affect the $\Delta^{17}O$ signature (if we take $\lambda_{\mathrm{RL}} = \lambda_{\mathrm{kinetic}}$, then the $\Delta^{17}O$ signature of CO_2 will be unaffected by diffusion through stomata, which follows directly from Eq. (S2.22)).

S2.5 Derivation of $\Delta^{17}O$ source signatures for atmosphere-leaf exchange

In this section we derive the $\Delta^{17}O$ source signature for atmosphere-leaf exchange as given in Eqs. (2.12)-(2.14). We start the derivation from Eq. (4.12) in *Hofmann et al.* (2017)

$$\begin{aligned} F_A \cdot \Delta_A^{17} &= \ln(\alpha_{leaf}) \cdot (\lambda_{kinetic} - \lambda_{RL}) \cdot (F_{AL} + F_{LAnoneq}) \\ &\quad + (\Delta^{17}O_{leaf} + (\lambda_{kinetic} - \lambda_{RL}) \cdot \ln(\alpha_{leaf}) - \Delta^{17}O_A) \cdot F_{LAeq}, \end{aligned} \tag{S2.23}$$

where Δ_A^{17} is the $\Delta^{17}O$ isotope discrimination due to assimilation and the other symbols are defined in Sect. 2.2.3.1. This equation can be re-ordered as follows

$$\begin{aligned} F_A \cdot \Delta_A^{17} &= \ln(\alpha_{leaf}) \cdot (\lambda_{kinetic} - \lambda_{RL}) \cdot F_{AL} \\ &\quad + (\Delta^{17}O_{leaf} + (\lambda_{kinetic} - \lambda_{RL}) \cdot \ln(\alpha_{leaf}) - \Delta^{17}O_A) \cdot F_{LAeq} \\ &\quad + \ln(\alpha_{leaf}) \cdot (\lambda_{kinetic} - \lambda_{RL}) \cdot F_{LAnoneq}. \end{aligned} \tag{S2.24}$$

This equation can be rewritten in the general form of a source signature minus the atmospheric signature, multiplied by the CO_2 flux (this form was also used in Eq. (4.3) of *Hofmann et al.* (2017) for the other contributions to the $\Delta^{17}O$ in CO_2 budget).

$$\begin{aligned} F_A \cdot \Delta_A^{17} &= (\Delta^{17}O_{AL} - \Delta^{17}O_A) \cdot F_{AL} \\ &\quad + (\Delta^{17}O_{LAeq} - \Delta^{17}O_A) \cdot F_{LAeq} \\ &\quad + (\Delta^{17}O_{LAnoneq} - \Delta^{17}O_A) \cdot F_{LAnoneq}. \end{aligned} \tag{S2.25}$$

Combining Eqs. (S2.24) and (S2.25) results in the following sources signatures

$$\Delta^{17}O_{AL} = \Delta^{17}O_A + (\lambda_{kinetic} - \lambda_{RL}) \cdot \ln(\alpha_{leaf}), \tag{S2.26}$$

$$\Delta^{17}O_{LAeq} = \Delta^{17}O_{leaf} + (\lambda_{kinetic} - \lambda_{RL}) \cdot \ln(\alpha_{leaf}), \tag{S2.27}$$

$$\Delta^{17}O_{LAnoneq} = \Delta^{17}O_A + (\lambda_{kinetic} - \lambda_{RL}) \cdot \ln(\alpha_{leaf}), \tag{S2.28}$$

These expressions are identical to Eqs. (2.12)-(2.14), thus showing the equivalence of the isotope discrimination due to assimilation used by *Hofmann et al.* (2017) and the source signatures for atmosphere-leaf exchange used in Chapter 2.

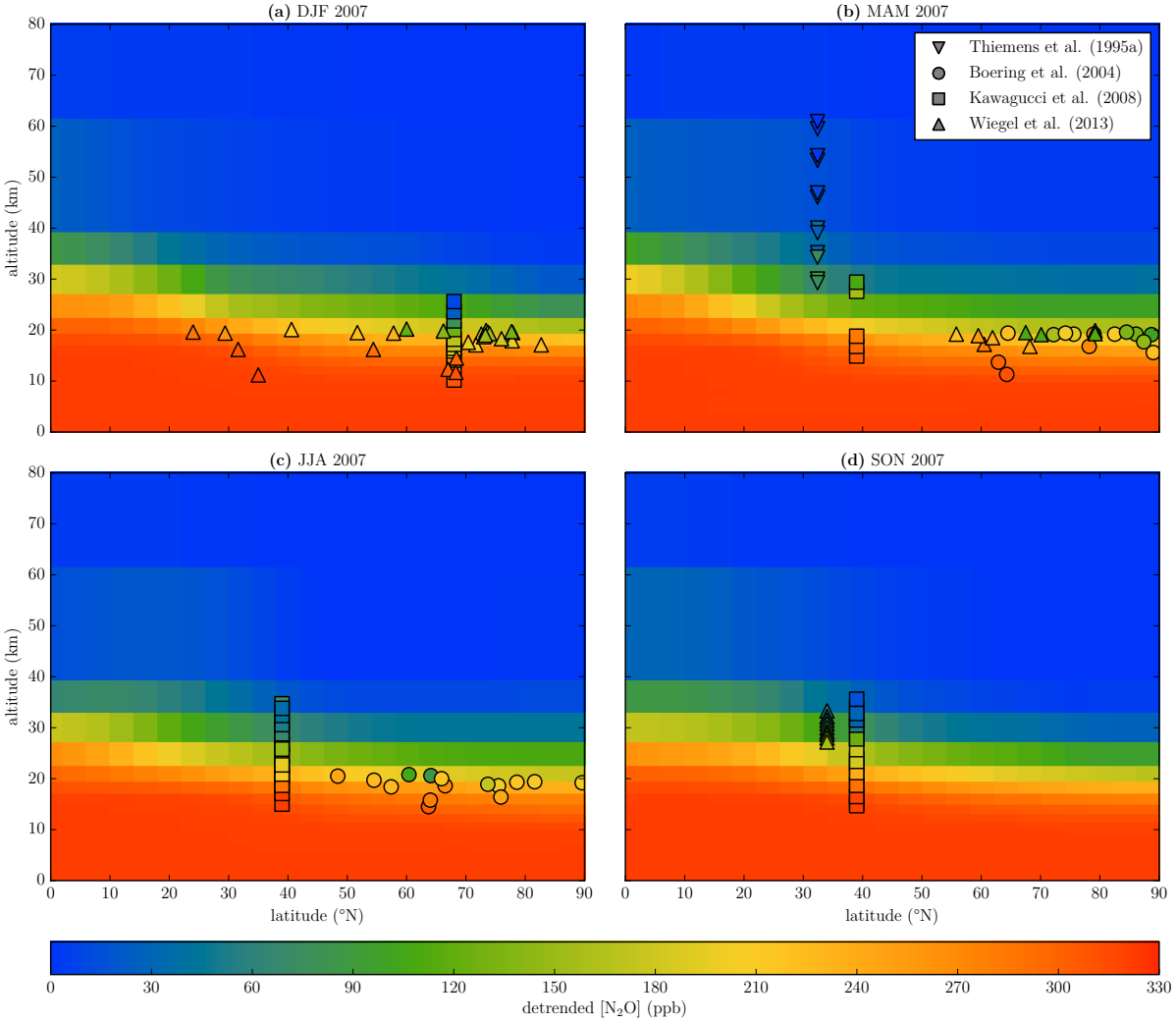

Figure S2.1: Zonal mean, yearly mean TM5 model predictions of detrended N_2O mixing ratios compared to detrended measurements of N_2O mixing ratios from *Thiemens et al.* (1995a), *Boering et al.* (2004), *Kawagucci et al.* (2008) and *Wiegel et al.* (2013) for stratospheric and upper tropospheric air in the Northern Hemisphere. The background color indicates the value of the TM5 model prediction with horizontal resolution of 6°×4° and 25 vertical levels, the color of the symbols indicate the measurement value. **(a)** Results for December, January and February (DJF) 2007. **(b)** Results for March, April and May (MAM) 2007. **(c)** Results for June, July and August (JJA) 2007. **(d)** Results for September, October and November (SON) 2007.

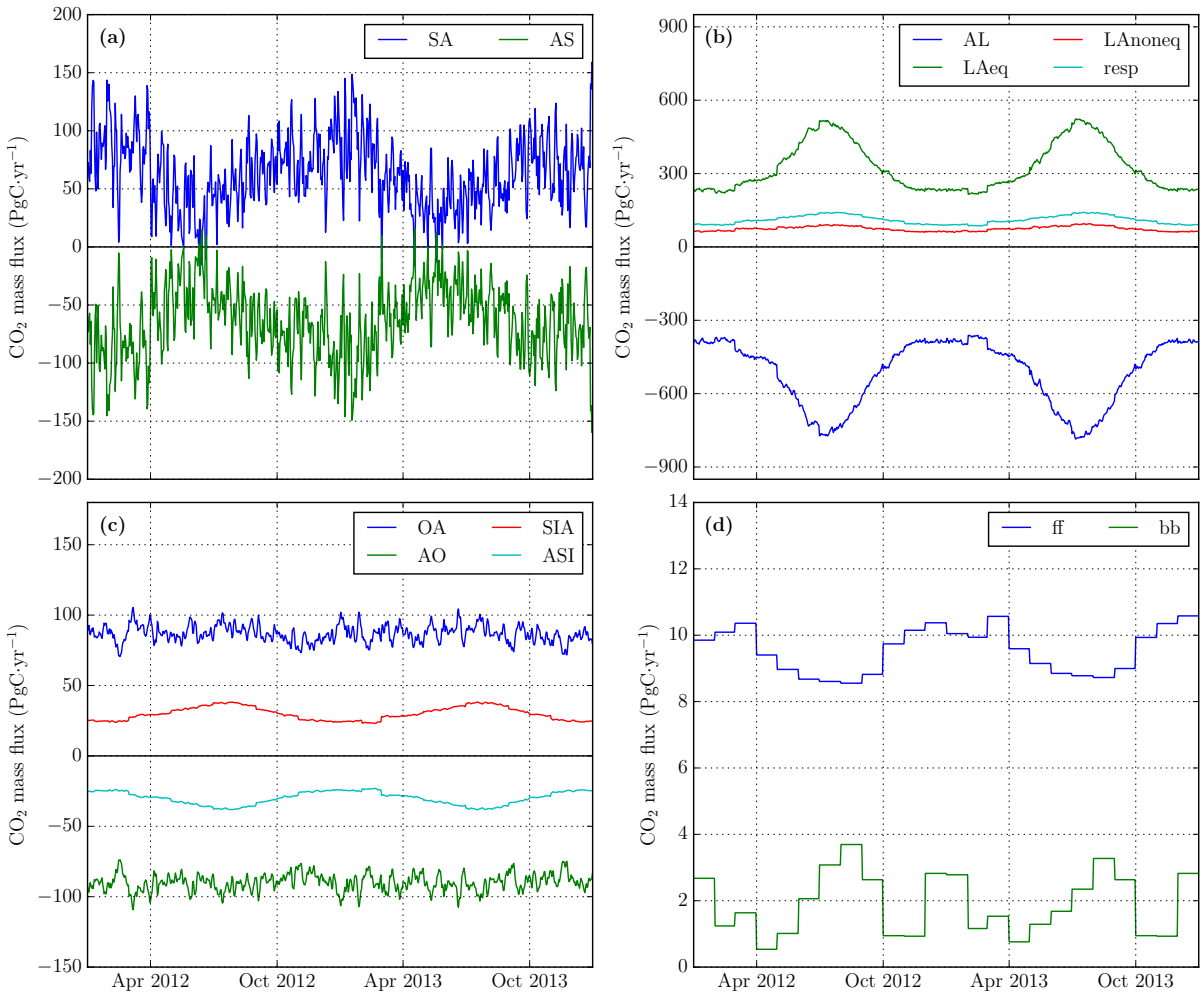

Figure S2.2: Daily time series of CO_2 fluxes for TM5 simulation with horizontal resolution of 6°×4° and 25 vertical levels. **(a)** Stratosphere-troposphere exchange fluxes. **(b)** Vegetation-atmosphere exchange fluxes. **(c)** Ocean-atmosphere and soil-atmosphere exchange fluxes. **(d)** Fossil fuel combustion and biomass burning fluxes.

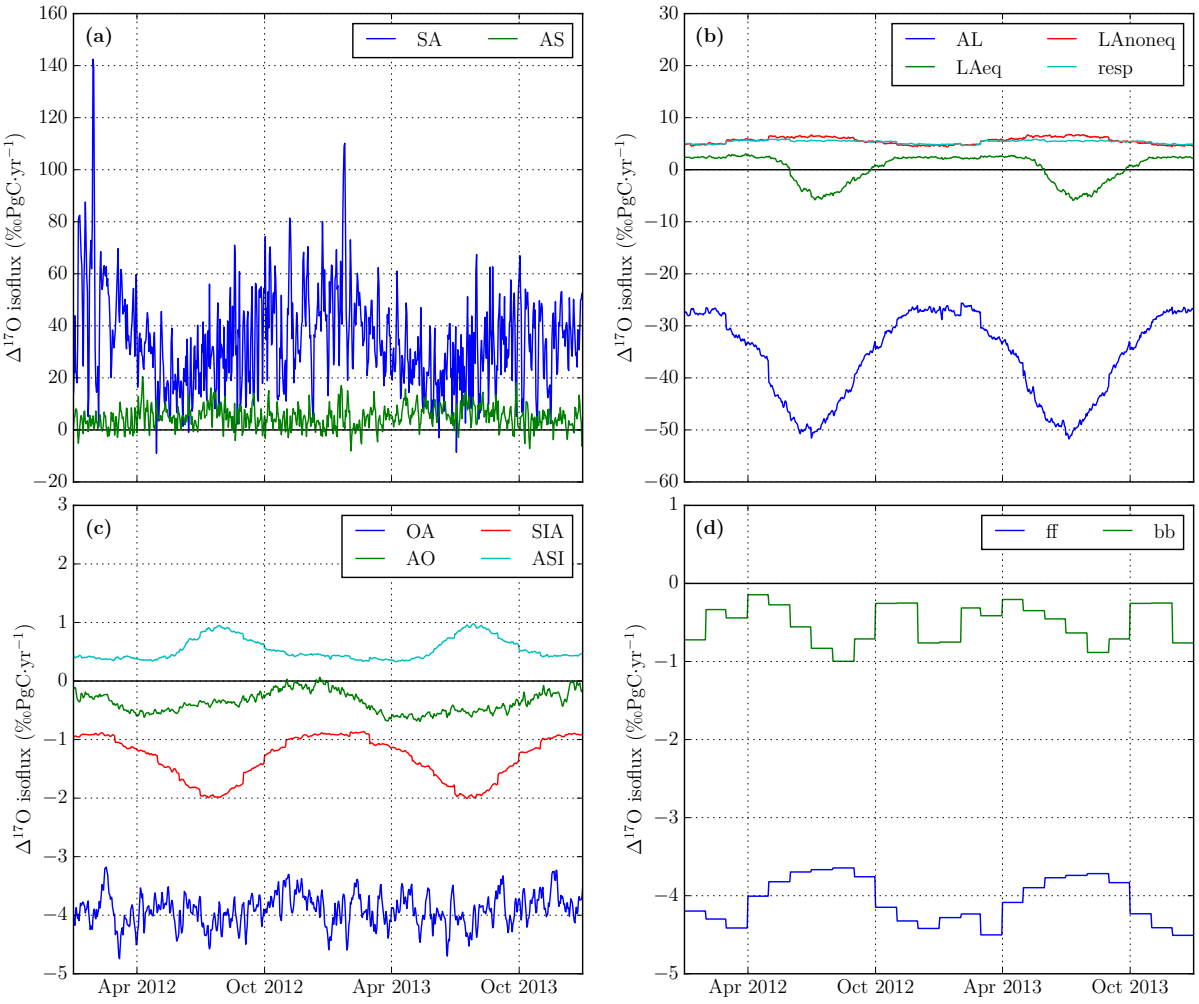

Figure S2.3: Daily time series of $\Delta^{17}O$ isofluxes relative to a reference level of $\Delta^{17}O_{trop}$ = 0.04 ‰ for TM5 simulation with horizontal resolution of 6°×4° and 25 vertical levels. **(a)** Stratosphere-troposphere exchange fluxes. **(b)** Vegetation-atmosphere exchange fluxes. **(c)** Ocean-atmosphere and soil-atmosphere exchange fluxes. **(d)** Fossil fuel combustion and biomass burning fluxes.

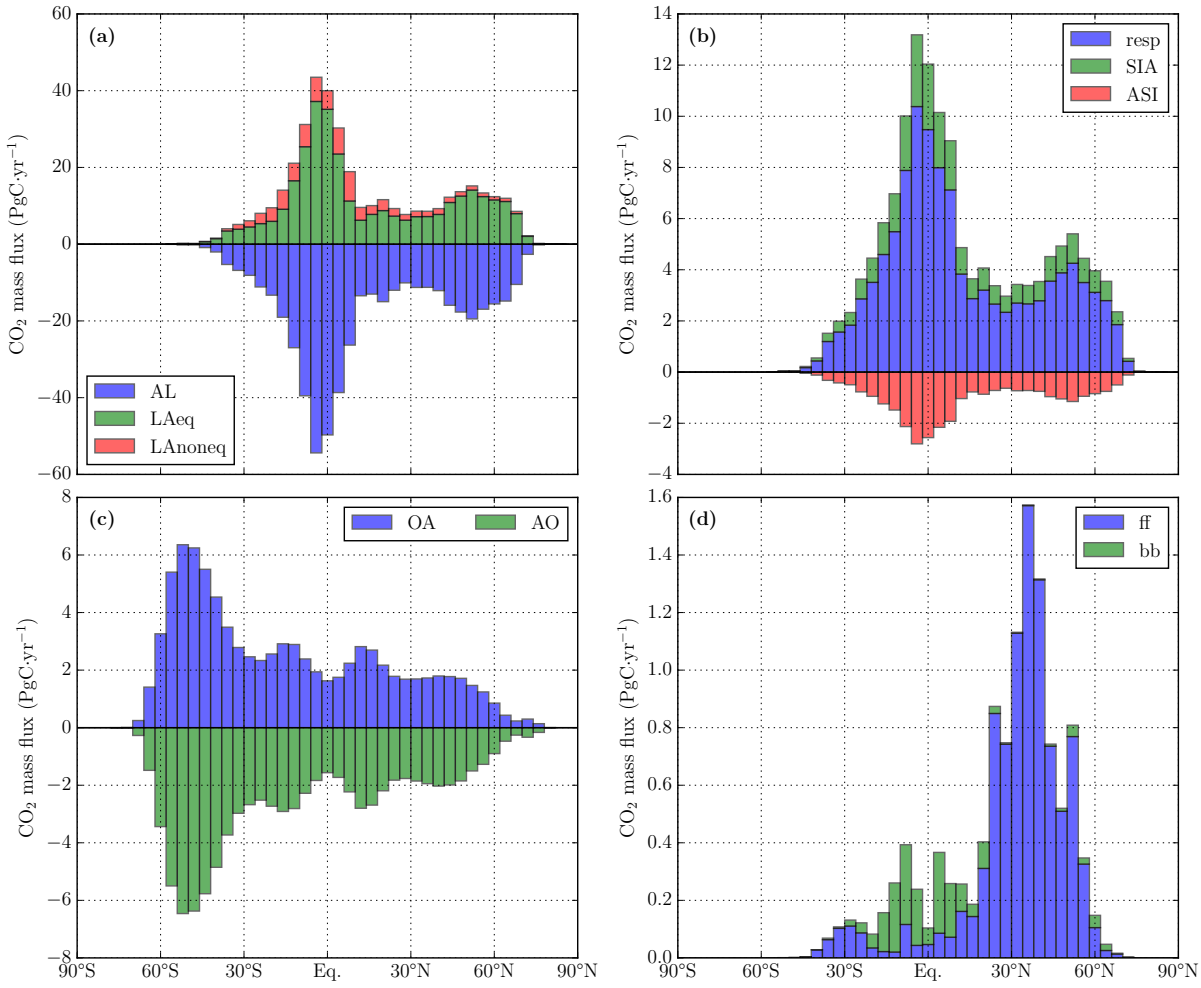

Figure S2.4: CO_2 mass fluxes as a function of latitude resulting from **(a)** leaf exchange; **(b)** respiration and soil invasion; **(c)** ocean exchange; and **(d)** fossil fuel combustion and biomass burning for TM5 simulation with base settings, 6°×4° horizontal resolution and 25 vertical levels.

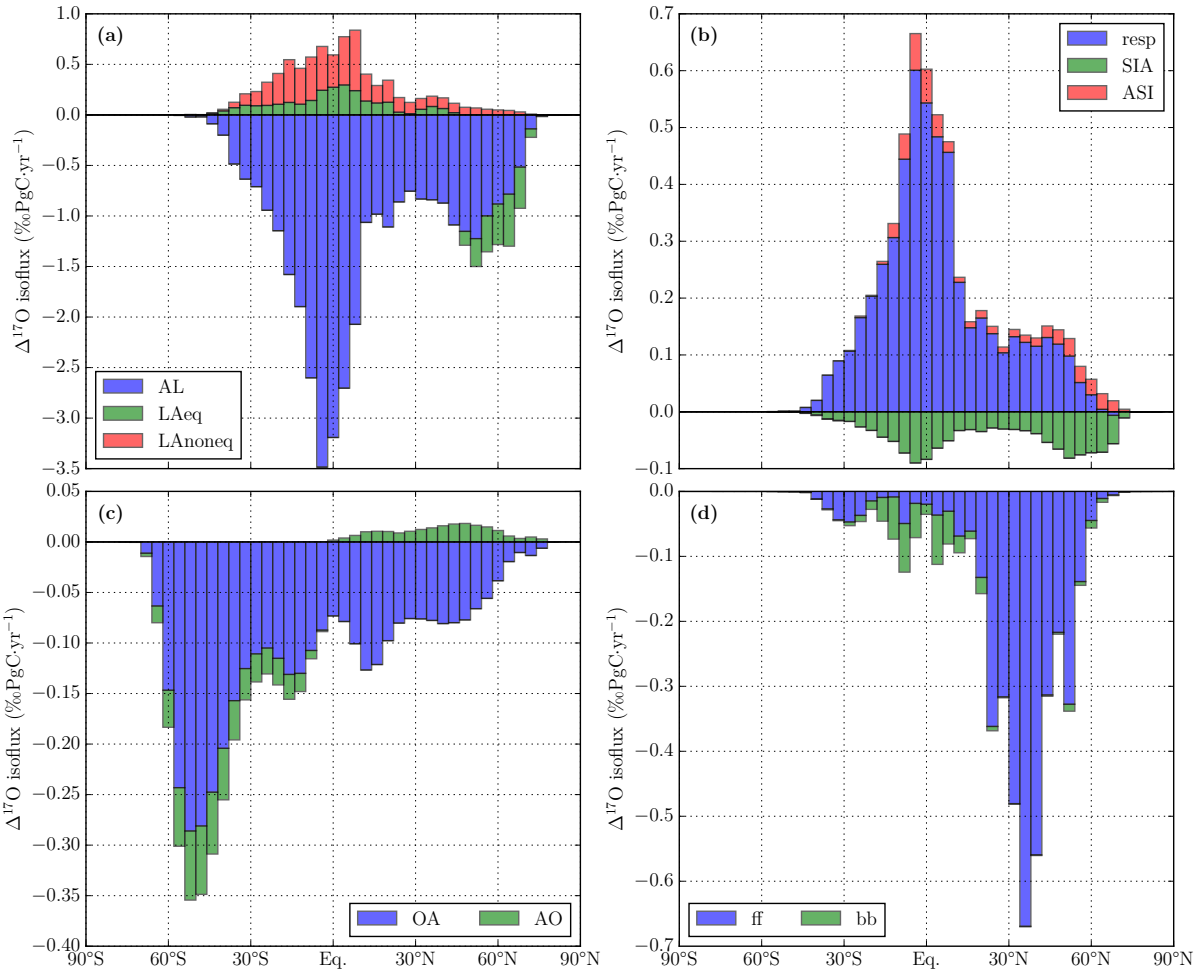

Figure S2.5: $\Delta^{17}O$ isofluxes as a function of latitude resulting from **(a)** leaf exchange; **(b)** respiration and soil invasion; **(c)** ocean exchange; and **(d)** fossil fuel combustion and biomass burning for TM5 simulation with base settings, 6°×4° horizontal resolution and 25 vertical levels.

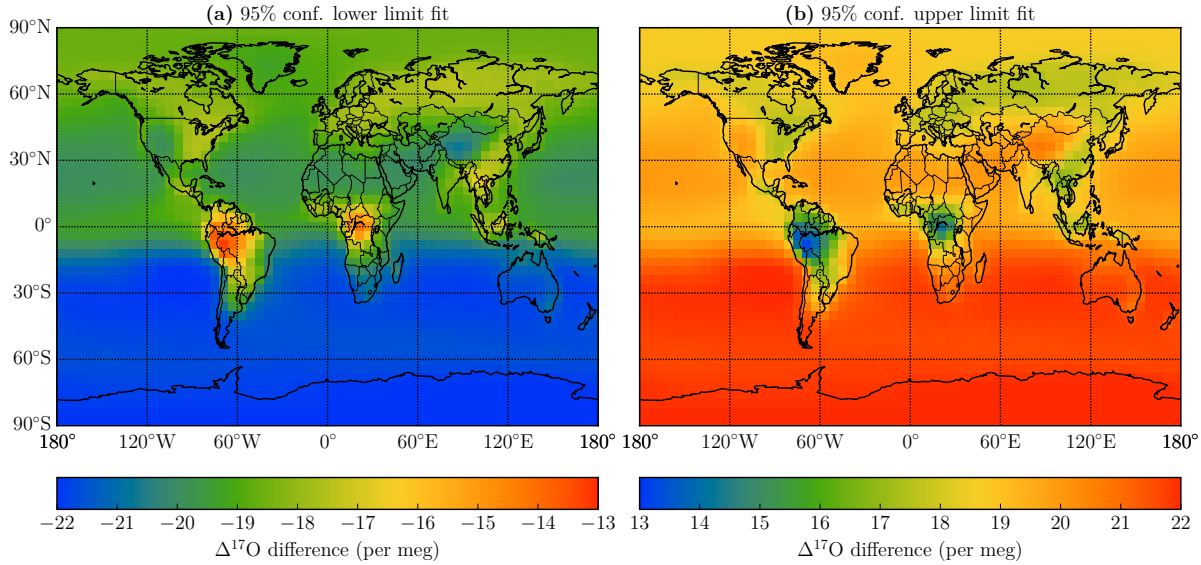

Figure S2.6: Annual mean difference in $\Delta^{17}O$ for TM5 simulation with modified input parameters relative to the TM5 base model run (`BASE`) for the lowest 500 m of the atmosphere. **(a)** TM5 simulation with 95% lower limit of confidence interval for stratospheric N_2O–$\Delta^{17}O$ fit (`ST_LOWER`). **(b)** TM5 simulation with 95% upper limit of confidence interval for stratospheric N_2O–$\Delta^{17}O$ fit (`ST_UPPER`).

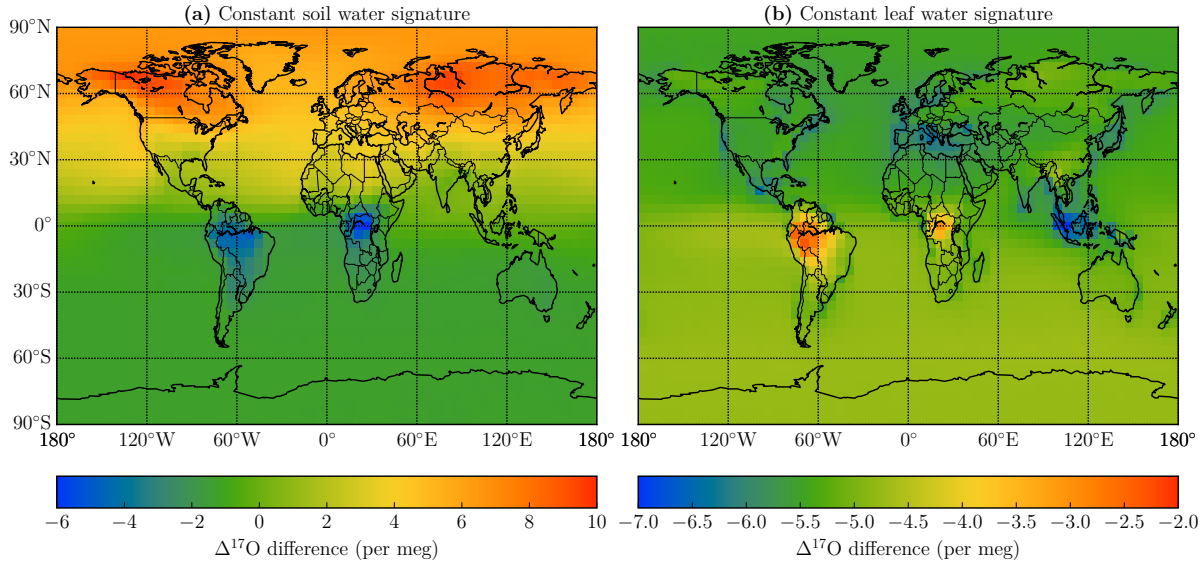

Figure S2.7: Annual mean difference in $\Delta^{17}O$ for TM5 simulation with modified input parameters relative to the TM5 base model run (`BASE`) for the lowest 500 m of the atmosphere. **(a)** TM5 simulation with constant soil water signature $\Delta^{17}O_{soil}$ = -5 per meg (`SOIL_CONST`). **(b)** TM5 simulation with constant leaf water fractionation exponent $\lambda_{transp} = 0.5156$ (`LEAF_CONST`).

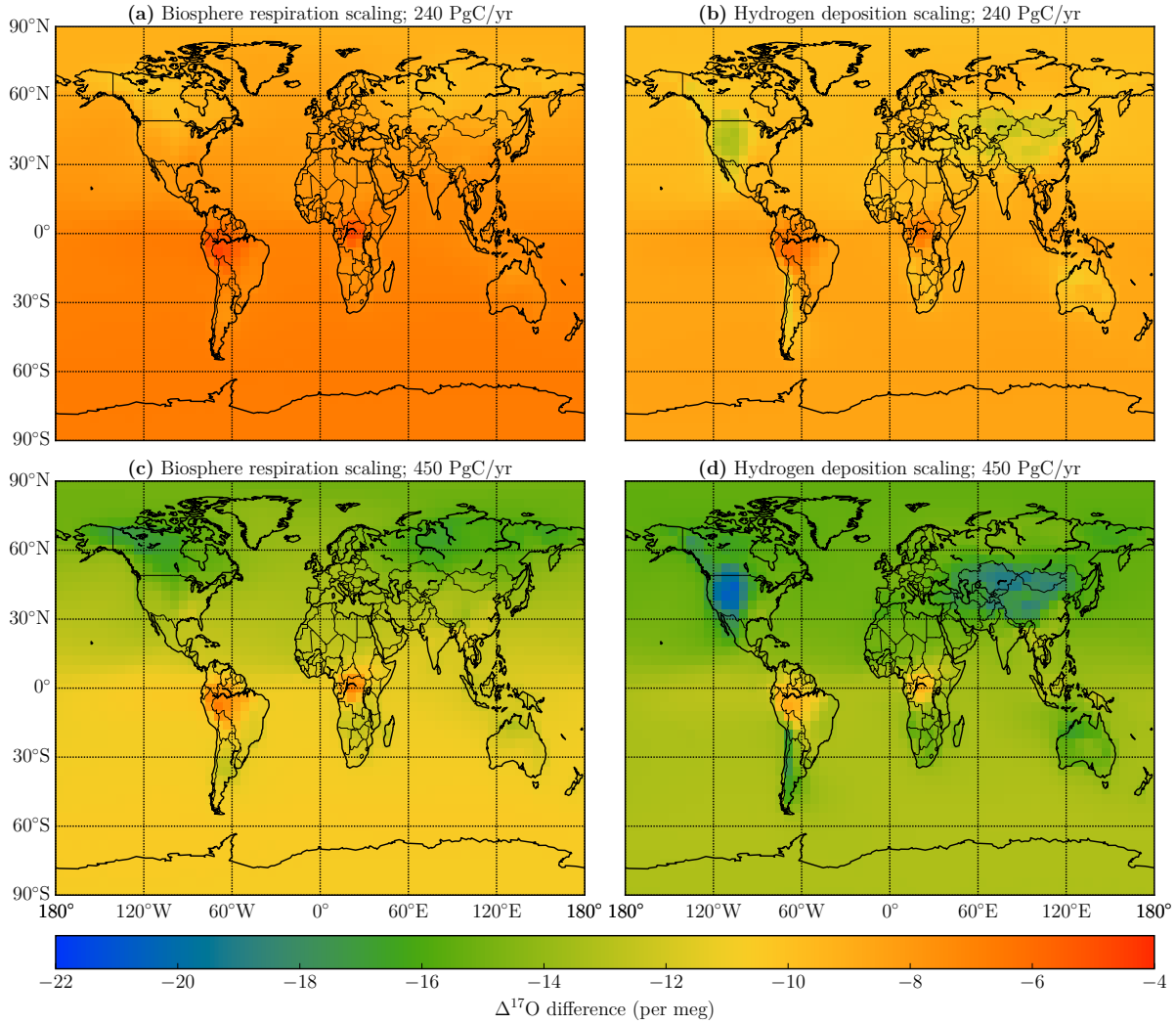

Figure S2.8: Annual mean difference in $\Delta^{17}O$ for TM5 simulation with modified input parameters relative to the TM5 base model run (`BASE`) for the lowest 500 m of the atmosphere. **(a,c)** TM5 simulations with soil invasion flux distributed according to the respiration flux (`RESP_*`). **(b,d)** TM5 simulations with soil invasion flux distributed according to the hydrogen deposition velocity (`HYD_*`). **(a,b)** TM5 simulations with soil invasion fluxes with global magnitude of 240 PgC·yr^{-1} (`*_240`). **(c,d)** TM5 simulations with soil invasion fluxes with global magnitude of 450 PgC·yr^{-1} (`*_450`).

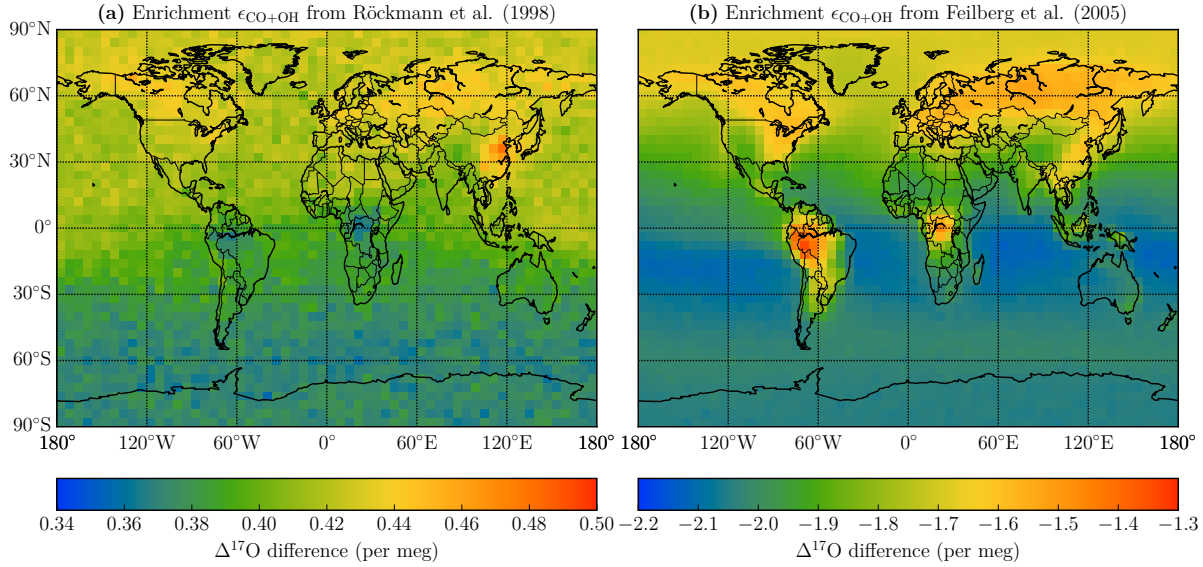

Figure S2.9: Annual mean difference in Δ^{17}O for TM5 simulation with modified input parameters relative to the TM5 base model run (`BASE`) for the lowest 500 m of the atmosphere. **(a)** TM5 simulation with enrichment ϵ_{CO+OH} according to *Röckmann et al.* (1998b) (`CO_ROCK`). **(b)** TM5 simulation with enrichment ϵ_{CO+OH} according to *Feilberg et al.* (2005) (`CO_FEIL`).

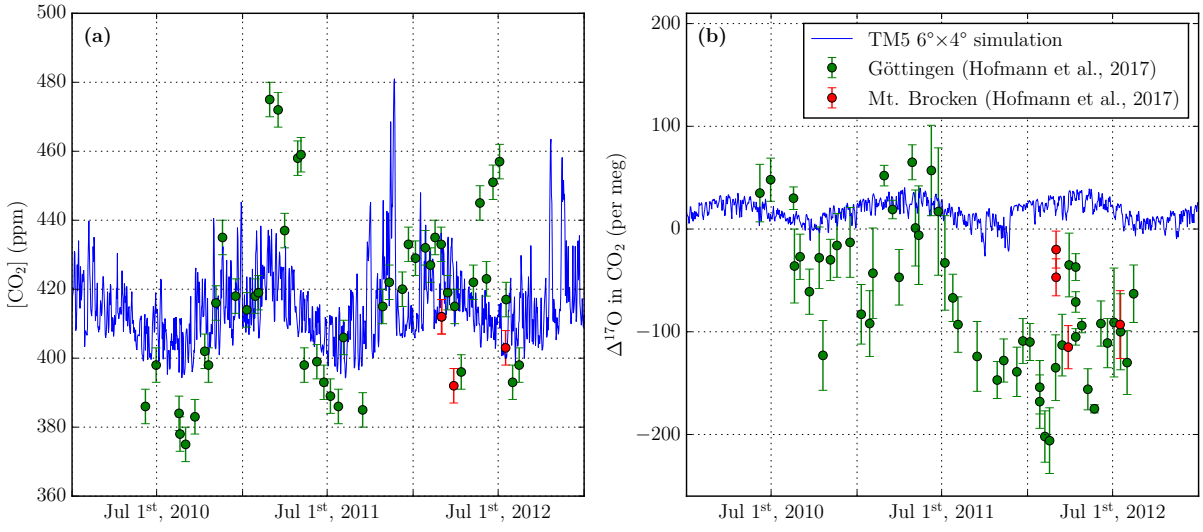

Figure S2.10: Comparison of tropospheric measurements for Göttingen (51.56°N, 9.95°E) and Mt. Brocken (51.80°N, 10.62°E) in Germany from *Hofmann et al.* (2017) with daily model predictions for the lowest 35 m from TM5 with horizontal resolution of 6°×4° and 25 vertical levels. **(a)** CO_2 mixing ratios. **(b)** Δ^{17}O in CO_2.

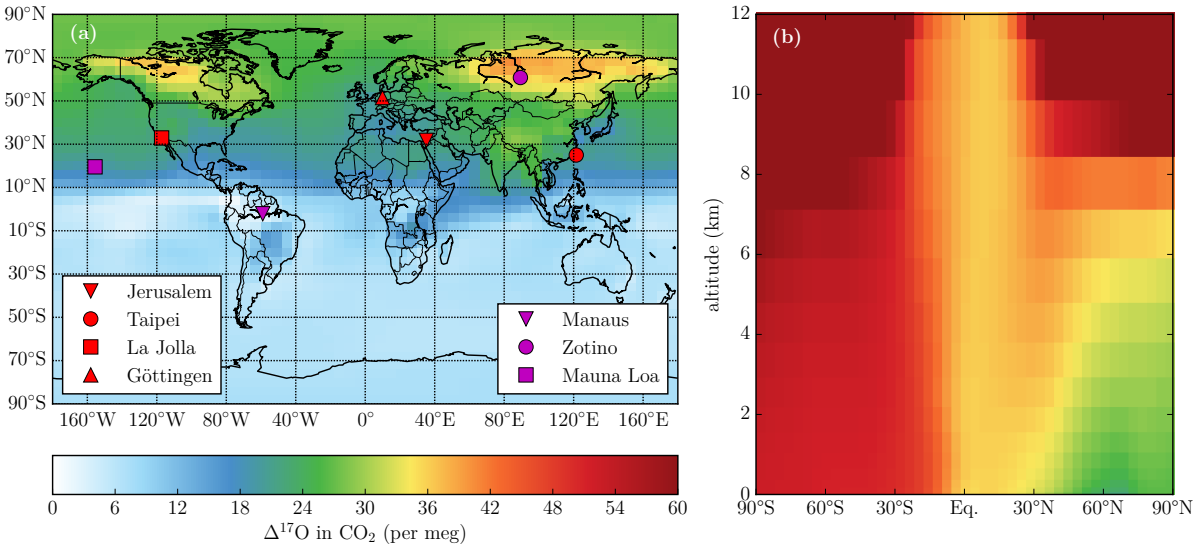

Figure S2.11: Simulated $\Delta^{17}O$ in CO_2 using TM5 model with 6°×4° horizontal resolution and 25 vertical levels. **(a)** Fitted peak-to-peak amplitude of $\Delta^{17}O$ in CO_2 for the lowest 500 m of the atmosphere. Locations for which measurements of $\Delta^{17}O$ in CO_2 are published are indicated with red symbols. Locations suggested for future measurements (Sect. 2.3.2.2) of $\Delta^{17}O$ in CO_2 are indicated with magenta symbols. **(b)** Zonal mean annual mean vertical profiles of $\Delta^{17}O$ in CO_2.

Table S2.1: Overview of the differences between the version of the model (r5558) that is described in Chapter 2 and a previous model version (r5337) that was described by *Schneider* (2015).

Model version r5558	**Model version r5337**
Stratosphere	
The stratospheric source of $\Delta^{17}O(CO_2)$ is derived from the simulated detrended N_2O mole fractions. The user can select different coefficients that describe the $\Delta^{17}O$–N_2O fit. Also, the user can select the region for which the fit is applied (e.g. based on the N_2O mole fractions or the height above the tropopause derived from the vertical temperature gradient). Finally, the user has the possibility to specify a relaxation constant to further tune the stratospheric source of $\Delta^{17}O$ in CO_2. A full description of the stratospheric module and the selected settings for the different simulations is given in Sect. 2.2.2.	The stratospheric source of $\Delta^{17}O$ in CO_2 is represented by assigning a fixed value of 2.76‰ for CO_2 in the 5 highest model layers (corresponding to altitudes of approx. 20-50 km).
Vegetation	
The signature of leaf water $\Delta^{17}O_{leaf}$ is calculated from the soil water signature $\Delta^{17}O_{soil}$ and the λ_{transp} which is a function of relative humidity according to *Landais et al.* (2006). The soil water signature field is derived from the annual mean $\delta^{18}O$ field of precipitation from *Bowen and Revenaugh* (2003) and relative humidity inside in the canopy that is calculated with SiBCASA at a 3 hourly temporal resolution. See Sect. 2.2.3.1 for more details about the implementation of leaf fluxes.	A constant value of -0.07‰ was used for the leaf water signature $\Delta^{17}O_{leaf}$.

Model version r5558	**Model version r5337**
Soil	
The distribution of the soil invasion fluxes is derived by scaling the CO_2 respiration flux fields calculated by SiBCASA or by scaling H_2 deposition velocity fields. The soil water signature $\Delta^{17}O_{soil}$ is derived from $\delta^{18}O$ of precipitation from *Bowen and Revenaugh* (2003) assuming that soil water is on the global meteoric water line (GMWL). The user can select values based on the annual mean $\delta^{18}O$ signature of precipitation or from its monthly climatology. More details about the implementation of soil invasion fluxes are given in Sect. 2.2.3.2	The soil invasion fluxes were modeled by scaling the CO_2 respiration flux fields from SiBCASA. The signature of soil water $\Delta^{17}O_{soil}$ was set to a constant value of $-0.01‰$.
Ocean	
The atmosphere-ocean flux F_{AO} for CO_2 and $C^{17}OO$ are dynamically coupled to the concentrations of CO_2 and $C^{17}OO$ as calculated each time step for the lowest level in the atmospheric transport model TM5. See Sect. 2.2.3.3 for more details about the ocean module.	The atmosphere-ocean exchange was calculated from a 375 ppm CO_2 mole fraction and $\Delta^{17}O$ signature of $-0.01‰$ above the ocean surface.
Atmospheric CO	
The production of CO_2 and $C^{17}OO$ from atmospheric CO oxidation is calculated using CO isotopologue fields from *Gromov* (2013) and OH fields from *Spivakovsky et al.* (2000). The user can decide not to include the effects of CO oxidation (this was done for our `BASE` simulation) or to include the effects based on the enrichments ϵ_{CO+OH} measured by *Röckmann et al.* (1998b) or those reported by *Feilberg et al.* (2002, 2005). More details are given in Sect. 2.2.4.	Not included.

Table S2.2: Overview of global CO_2 mass fluxes and $\Delta^{17}O$ isofluxes as predicted by our TM5 model using base settings with horizontal resolution of 6°×4° and 25 vertical levels averaged over years 2012 and 2013 compared with results from the box model by *Hofmann et al.* (2017), denoted by 'Hofmann17', and the box model from *Hoag et al.* (2005), denoted by 'Hoag05'. Positive CO_2 mass fluxes and $\Delta^{17}O$ isofluxes represent sources for the tropospheric CO_2 mass and $\Delta^{17}O$ signature, respectively.

		CO_2 mass flux [PgC·yr^{-1}]			$\Delta^{17}O$ isoflux [‰PgC·yr^{-1}]		
Reservoir	Flux	TM5 model	Hofmann17	Hoag05	TM5 model	Hofmann17	Hoag05
stratosphere	F_{SA}	63.4	100	104.3	34.6	44.5	43.8
	F_{AS}	−63.9	−100	−104.3	4.9	—	—
vegetation	F_{AL}	−514.5	−352	−240.5	−35.9	−36.3	—
	F_{LAeq}	324.6	197	122.5	0.4	−5.1	−18.4
	$F_{LAnoneq}$	74.3	49	30.0	5.6	5.1	—
	F_{resp}	111.0	103	85.6	5.3	3.3	−12.8
soil	F_{SIA}	30.0	30	—	−1.3	−2.1	—
	F_{ASI}	−30.0	−30	—	0.5	—	—
ocean	F_{OA}	86.9	90	88.0	−3.9	−6.1	−13.2
	F_{AO}	−90.0	−92	−90.0	−0.4	—	—
fossil fuel	F_{ff}	9.5	8	6.0	−4.1	−3.6	−1.8
biomass	F_{bb}	1.9	1	1.6	−0.5	−0.3	−0.2
total	F_{net}	3.2	4	3.2	5.2	−0.6	−2.6

3

Resolving the diurnal cycle of $\Delta^{17}O$ in CO_2 at the ecosystem level: Simulations and observations at a mid-latitude pine forest

The triple oxygen isotope signature $\Delta^{17}O$ in atmospheric CO_2 is a potential tracer for gross primary production (GPP). However, interpretation of $\Delta^{17}O$ in atmospheric CO_2 is complicated by the contributions from respired CO_2, isotopic exchange with soil and ocean water, and the release of CO_2 by fossil fuel combustion and biomass burning. Here we study $\Delta^{17}O$ in CO_2 at the ecosystem level, which is the domain that integrates the contributions from vegetation and soil to the atmospheric signal. We report for the first time an observed diurnal cycle of $\Delta^{17}O$ in CO_2, measured from air samples collected on 15-16 August 2019 at the mid-latitude pine forest Loobos (FLUXNET site NL-Loo). Also, we report observations of $\delta^{13}C$ and $\delta^{18}O$ in CO_2 for flasks collected close to the surface (at 0.5 m height, inside the canopy) and from the top of the tower (1–2 m above

This chapter by Koren, G., Adnew, G.A., Vilà-Guerau de Arellano, J., van der Molen, M K., Kruijt, B., Röckmann, T, and Peters, W., is in preparation for submission

the canopy). To support interpretation of observations, we simulated $\delta^{13}C$, $\delta^{18}O$, $\Delta^{17}O$ in CO_2 in the atmospheric boundary layer (ABL) during daytime for Loobos using the mixed layer model MXL. Furthermore, we used the MXL model to systematically explore the sensitivity of $\delta^{18}O$ and $\Delta^{17}O$ in CO_2 to the cloud cover, humidity of entrained air and degree of isotopic equilibration inside leaves. Finally, we used the global atmospheric transport model TM5 to (1) quantify the contribution of different sources that affect $\Delta^{17}O$ in CO_2 at Loobos; and (2) extend our analysis of the diurnal cycle to the global scale.

3.1 Introduction

Gross primary production (GPP; the uptake of CO_2 through photosynthesis) is the largest flux of the terrestrial carbon cycle. GPP can not be measured directly at large scales (> 1 km^2) and the magnitude of global GPP is currently poorly constrained (with estimates ranging from 120 PgC/yr (*Beer et al.*, 2010) up to 175 PgC/yr (*Welp et al.*, 2011)). Several tracers for GPP have been proposed, including carbonyl sulfide (COS) which is effectively taken up by vegetation in leaves (*Montzka et al.*, 2007; *Campbell et al.*, 2008) and the isotopic composition ($\delta^{18}O$, $\Delta^{17}O$, Δ_{47}) of CO_2 that is strongly coupled to isotopic exchange with leaf water (*Farquhar et al.*, 1993; *Hoag et al.*, 2005; *Eiler and Schauble*, 2004; *Koren et al.*, 2019). In addition, sun-induced fluorescence (SIF) from satellites (*Frankenberg et al.*, 2011) and near-infrared reflectance from vegetation (NIRv) that was first introduced by *Badgley et al.* (2017), have recently gained more interest to study the seasonal dynamics (*Luus et al.*, 2017; *Doughty et al.*, 2019; *Mengistu et al.*, in review) and drought response (Chapter 5, *Buitink et al.*, in review; *Smith et al.*, 2020) of GPP.

Hoag et al. (2005) first proposed $\Delta^{17}O$ of CO_2 (also known as its '^{17}O-excess', or the 'triple oxygen isotope ratio') as a tracer for GPP. First, we define what $\Delta^{17}O$ is, and subsequently we describe how it is related to the terrestrial carbon cycle. In this study we consistently use the 'logarithmic definition' (see Sect. S1 in the supplemental material of *Koren et al.*, 2019, for an overview of alternative definitions) for $\Delta^{17}O$:

$$\Delta^{17}O = \ln(\delta^{17}O + 1) - \lambda_{RL} \cdot \ln(\delta^{18}O + 1), \tag{3.1}$$

where $\delta^n O$ (for $n = 17, 18$) is the isotopic signature relative to the Vienna Standard Mean Ocean Water (VSMOW) reference

$$\delta^n O = \frac{[^nO/^{16}O]_{sample}}{[^nO/^{16}O]_{VSMOW}} - 1. \tag{3.2}$$

The isotopic signatures $\delta^n O$ are usually expressed in per mill, denoted by the symbol '‰', and the $\Delta^{17}O$ signature is expressed in 'per meg' (0.001 ‰). Both 'per meg' and 'ppm' are

acceptable terminology for isotopic composition according to *Coplen* (2011). However, we prefer the unit 'per meg' since (1) it is consistent with *Koren et al.* (2019); (2) it avoids confusion with the 'ppm' unit used for CO_2 mole fractions and (3) it is consistent with conventions used for $\delta(O_2/N_2)$, another tracer of the carbon cycle (*Keeling et al.*, 1998). Following *Hofmann et al.* (2017) and *Koren et al.* (2019), we use a reference line of $\lambda_{RL} = 0.5229$, which is equal to the three-isotope slope of the CO_2-H_2O equilibration line that was found by *Barkan and Luz* (2012).

CO_2 with high $\Delta^{17}O$ signatures (on the order of several per mill as observed by e.g. *Thiemens et al.*, 1995a; *Lämmerzahl et al.*, 2002; *Boering et al.*, 2004; *Wiegel et al.*, 2013) is produced in the stratosphere because of mass-independent isotopic effects occurring in ozone photo-chemistry (*Yung et al.*, 1991). This high $\Delta^{17}O$ signature in CO_2 can be transported into the upper troposphere (*Laskar et al.*, 2019) and further towards the Earth's surface (e.g. *Thiemens et al.*, 2014; *Hofmann et al.*, 2017). When the CO_2 dissolves in liquid water, the oxygen isotopes in CO_2 exchange with H_2O and the $\Delta^{17}O$ value of CO_2 will be 'reset' to a value close to 0, which is representative for terrestrial water reservoirs. Most of the exchange between CO_2 and water occurs inside leaves due to the presence of the enzyme carbonic anhydrase which increases the rate of dissolution by several orders of magnitude (*Francey and Tans*, 1987). The $\Delta^{17}O$ signature of atmospheric CO_2 is thus a dynamic balance between stratospheric production and exchange with leaf water, and it therefore carries information on the magnitude of the CO_2 flux into leaves. The advantage of using $\Delta^{17}O$ as a tracer for GPP over the more traditional $\delta^{18}O$ is that it is less dependent on the hydrological cycle as described in more detail by *Hoag et al.* (2005).

The focus of this study is the effect of vegetation on the $\Delta^{17}O$ signature of atmospheric CO_2. Recently, leaf-scale measurements of the effect of photosynthesis on $\Delta^{17}O$ in CO_2 were performed for two C_3 plants (sunflower and ivy) and a C_4 plant (maize) in a controlled lab environment (*Adnew et al.*, 2020, in review). These experiments confirmed that equilibration of CO_2 with water inside the leaf, followed by retro-diffusion of this CO_2 out of the leaf, exerts a strong control on the atmospheric $\Delta^{17}O$ signature. These detailed experiments at the leaf level (scales of $\sim cm^2$ and seconds) result in a better understanding of the contribution of vegetation to $\Delta^{17}O$ in atmospheric CO_2 (with simulated gradients that are detectable at $\sim$1000 km^2 and months). However, measurements at the ecosystem level ($\sim km^2$ and hours) are required to better understand processes that occur at intermediate scales.

Koren et al. (2019) developed a global 3-D model for $\Delta^{17}O$ in CO_2 and reported simulated large scale gradients (e.g. the mean seasonal cycle of $\Delta^{17}O$ for the Northern Hemisphere

and the Southern Hemisphere), that generally agree with the expected spatiotemporal patterns for this tracer (i.e. a decline of $\Delta^{17}O$ values for regions and periods with high GPP). However, it is not clear whether this relatively coarse model (6°×4°, 3°×2° or 1°×1°, longitude by latitude) can reproduce a diurnal cycle for a specific location. Recently, *Vilà-Guerau de Arellano et al.* (2019) developed a model to simulate isotopologues of CO_2 and H_2O in the atmospheric boundary layer, which was carefully validated against measurements ($\delta^{13}C$ and $\delta^{18}O$ in CO_2) from Harvard Forest (*Wehr et al.*, 2013). We developed this mixed layer model further by implementing the carbon cycle tracers COS, O_2, Δ_{47} and $\Delta^{17}O$ in CO_2.

Our goal is to observe and report for the first time a full diurnal cycle (day time and night time) of $\Delta^{17}O$ in CO_2 above a forest (the mid-latitude pine forest Loobos, the Netherlands). Furthermore, we aim to simulate the diurnal cycle of the newly implemented tracer $\Delta^{17}O$ in CO_2 with the mixed layer model (*Vilà-Guerau de Arellano et al.*, 2019). Given its cheap computational costs, the mixed layer model is an ideal tool to test parameterizations and systematically explore the sensitivity of $\Delta^{17}O$ in CO_2 to model parameters. Furthermore, we use the new tracer tagging routine in our global 3-D model for $\Delta^{17}O$ in CO_2 (documented in *Koren et al.*, 2019) to quantify the contributions of different processes to the diurnal cycle of $\Delta^{17}O$ in CO_2 at Loobos. Finally, we use the global model to extend our analysis to other ecosystems across the globe.

3.2 Methods

3.2.1 Sampling and measurements

We selected the Loobos site (NL-Loo) that is operated by Wageningen University & Research (WUR) as our study site for measuring the diurnal cycle of $\Delta^{17}O$ in CO_2. The Loobos site is well established in literature with its data being used in over 100 scientific publications, since the start of its operation in 1994. Loobos is a pine forest on sandy soil (*Dolman et al.*, 2002; *Elbers et al.*, 2011) and is situated in the eastern part of the Netherlands (at 52.17°N, 5.74°E), see Fig. 3.1. The Loobos tower has a height of 25 m, which reaches 1–2 m above the canopy. At Loobos CO_2 fluxes are measured using the eddy-covariance technique (*Moncrieff et al.*, 1997; *Aubinet et al.*, 1999). Concentrations of CO_2 and H_2O are also measured at five different levels ranging from 0.4 m just above the surface to 24.4 m at the top of the tower. The incoming and outgoing shortwave and longwave radiation are measured close to the top, at an elevation of 21.4 m. In addition,

basic meteorological parameters such as the air temperature, relative humidity, wind speed and wind direction are measured at the top of the tower. Finally, also measurements of the soil moisture and soil temperature at different soil depths are performed (see `https://www.climatexchange.nl` for more details).

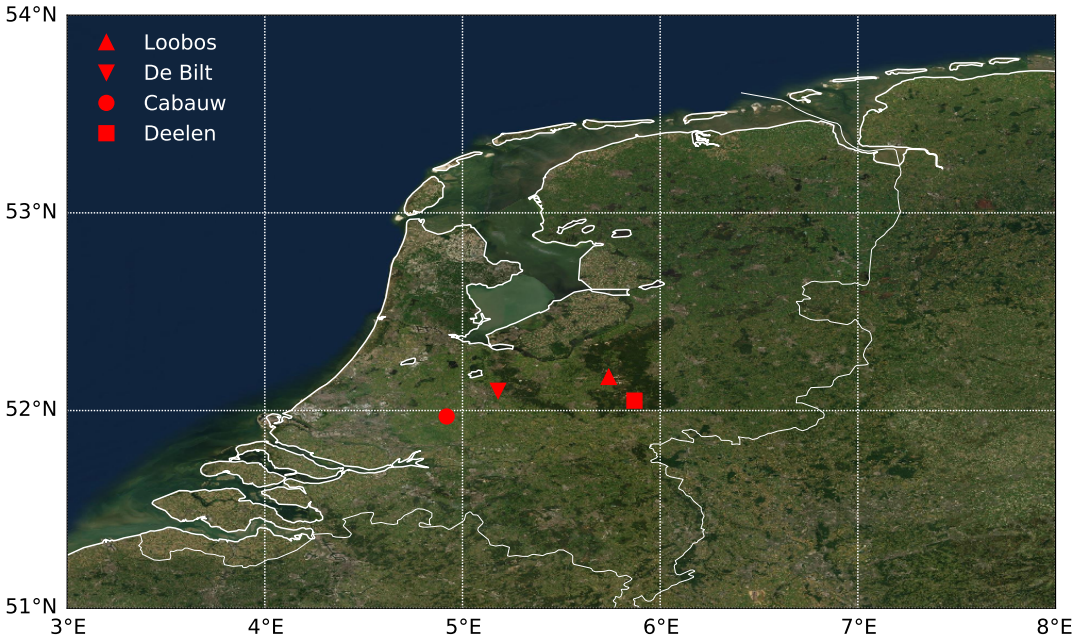

Figure 3.1: Locations of the Loobos flux tower, the KNMI ceilometer sites Cabauw and Deelen, and the launch site of the KNMI weather balloon at De Bilt are indicated by the different markers. The grid lines represent the 1°×1° grid boxes of the TM5 model.

To collect air from the tower, we installed a temporary inlet at the top of the tower using a metal-coated EATON Synflex® tube with 12 mm outer diameter that was connected to a portable drier and pump at the surface. In addition, the system had a switch that allowed to sample air from within the canopy (∼0.5 m above the surface). The air was dried using magnesium perchlorate $Mg(ClO_4)_2$ before sampling, which is necessary to avoid isotopic equilibration between CO_2 and H_2O in the flask. A 7 micron filter was used to prevent dust from entering the flasks. Before sampling air, the inlet line (for the tower samples) and the flasks were flushed for a period of ∼10 minutes at a flow rate of 5 L/minute to avoid contamination of the sample. The samples were collected in 2-L flasks at 1.5 bar. The flasks had been pre-filled in the lab with compressed air at 1.5 bar for conditioning.

The isotopic composition of the CO_2 from the flask samples ($\delta^{13}C$, $\delta^{18}O$ and $\Delta^{17}O$) was measured at Institute for Marine and Atmospheric research Utrecht (IMAU). To measure the isotopic composition, CO_2 was cryogenically extracted from the air using four traps. The first two traps were kept at a dry ice temperature to freeze moisture and some

organics and the second two traps were at liquid nitrogen temperature to collect the CO_2. (the procedure is described in more detial in *Adnew et al.*, 2019, 2020). The $\delta^{13}C$ and $\delta^{18}O$ signatures of the extracted CO_2 were measured on the dual inlet Thermo Scientific™ DELTA V™ isotope ratio mass spectrometer.

The $\Delta^{17}O$ was measured by establishing isotopic equilibration (catalyzed by hot platinum) of the sampled CO_2 with O_2 that has a known initial $\Delta^{17}O$ signature. After measuring the final $\Delta^{17}O$ signature of O_2 on the Finnigan™ DELTA^{plus} XL isotope ratio mass spectrometer, the isotopic composition of CO_2 can be inferred with a precision of 8 per meg (*Mahata et al.*, 2013, 2016a; *Adnew et al.*, 2019). The IMAU lab also has the possibility to measure $\Delta^{17}O$ directly on CO_2 using the fragment method (*Adnew et al.*, 2019), but this technique is less precise and was not available for this study. In addition, a Picarro gas concentration analyzer was used to measure the CO_2 mole fractions from the flasks (only for the flasks collected close to the surface).

The boundary layer height is not measured at Loobos directly, but was estimated from the CHM15K ceilometers (*De Haij et al.*, 2016) that are operated at the KNMI stations Cabauw (51.97°, 4.92°E) and Deelen (52.05°N, 5.87°E). The CHM15K ceilometers measure the cloud base every 5 minutes and the difference between the two stations provides an estimate of the spatial variation across the Netherlands. In addition, radiosondes released by KNMI from De Bilt (52.10°N, 5.18°E) were used to estimate the boundary layer height from the measured potential temperature profile. The locations of the ceilometer sites and the balloon launch site are indicated in Fig. 3.1.

3.2.2 Mixed layer model

We implemented $\Delta^{17}O$ in CO_2 as a new tracer in the mixed layer model MXL (`https://classmodel.github.io`), in a version that already included $\delta^{13}C$ and $\delta^{18}O$ for CO_2 and $\delta^{18}O$ for H_2O (*Vilà-Guerau de Arellano et al.*, 2019). The MXL model simulates the isotopic signatures in the atmospheric boundary layer above the canopy top and is limited to convective conditions. The exchange of CO_2 in the model is based on the A-gs formulation (Appendix E of *Vilà-Guerau de Arellano et al.*, 2015) that describes photosynthesis as a function of plant physiological parameters and environmental conditions (such as the available photosynthetically active radiation and the vapor pressure deficit). Finally, the CO_2 respiration flux is implemented as a function of temperature and soil water content (following the approach described in Appendix F of *Vilà-Guerau de Arellano et al.*, 2015).

Similar to $\delta^{18}O$, the $\Delta^{17}O$ signature of CO_2 is tightly linked to the isotopic composition of leaf water. To simulate the $\Delta^{17}O$ composition of leaf water, we used the empirical relationship found by *Landais et al.* (2006)

$$\lambda_{\text{transp}} = 0.522 - 0.008 \cdot \text{RH} \quad \text{for} \quad 0.3 < \text{RH} < 1, \tag{3.3}$$

that describes the isotopic enrichment of leaf water $\Delta^{17}O_{\text{lw}}$ relative to that in xylem water $\Delta^{17}O_{\text{x}}$ as a function of the relative humidity (RH). The isotopic signature of leaf water $\Delta^{17}O_{\text{lw}}$ can then be calculated as

$$\Delta^{17}O_{\text{lw}} = \Delta^{17}O_{\text{x}} + (\lambda_{\text{transp}} - \lambda_{\text{RL}}) \cdot \ln(\alpha_{\text{transp}}). \tag{3.4}$$

A complete description of the implementation of the leaf and soil exchange processes for $\Delta^{17}O$ in the MXL model is given in Sect. S3.1. An overview of all selected parameter values is given in Table S3.3.

One of the attractive features of the mixed layer model is that simulations are relatively fast (it takes roughly 1 minute computer time to simulate one full diurnal cycle), which makes it feasible to perform systematic sensitivity tests for some of the uncertain model parameters. Here we investigated the sensitivity of $\Delta^{17}O$ in CO_2 to the cloud cover, the humidity of entraining air and the degree of isotopic equilibration θ inside leaves. The cloud cover directly affects the radiation budget and therefore the development of the boundary layer and photosynthesis. The humidity also has an effect on the boundary layer development, but additionally controls the $\Delta^{17}O$ signature of leaf water through Eq. (3.3). Finally, the degree of isotopic equilibration inside leaves has no effect on meteorological variables and CO_2 fluxes, but only on $\delta^{18}O$ and $\Delta^{17}O$ in CO_2.

3.2.3 Global 3-D model

We also used a global 3-D model for $\Delta^{17}O$ in CO_2. The global 3-D model is fully documented by *Koren et al.* (2019) and we only provide a brief summary here. The atmospheric transport is simulated by TM5 (*Krol et al.*, 2005) which is driven by meteorological fields from ERA-Interim (*Dee et al.*, 2011). The stratospheric production of $\Delta^{17}O$ in CO_2 is parameterized by imposing the observed correlation (see e.g *Boering et al.*, 2004) between stratospheric N_2O mole fractions and $\Delta^{17}O$ in stratospheric CO_2. Finally, the effect of the vegetation is based on the CO_2 fluxes calculated from the terrestrial biosphere model SiB-CASA (*Schaefer et al.*, 2008). A comparison between the isotopic exchange formulation used in the TM5 model and the MXL model is given in Sect. S3.2.

For this study, we implemented a 'tracer tagging' routine which allows us to attribute variations in the $\Delta^{17}O$ signature of atmospheric CO_2 to its different sources. This technique is also used for CO_2 in the forward mode of the CarbonTracker model (*Peters et al.*, 2005, 2007, 2010). For CO_2, the total mole fraction (c_{total}) in each grid cell is the sum of the mole fractions from the individual processes (c_i, where i refers to the different sources and sinks; e.g. leaf uptake or fossil fuel combustion) in that grid cell.

$$c_{\text{total}}(x, y, z, t) = \sum_i c_i(x, y, z, t) \tag{3.5}$$

For the isotopic composition this is not so straightforward, because isotopic signatures are not additive (i.e., the δ-values of the different sources do not add up to the total δ in the atmosphere). To attribute the simulated atmospheric signature to the different processes, we follow the method first introduced by *Heimann and Keeling* (1989) for $\delta^{13}C$ in CO_2 and later adopted by *Peylin et al.* (1999) and *Cuntz et al.* (2003a) for $\delta^{18}O$ in CO_2. They refer to this as the 'δ-anomaly' and we generalize this to a 'Δ-anomaly'.

$$\Delta_i^* = \frac{c_i(\Delta_i - \Delta_{\text{bg}})}{\Sigma_i c_i} \tag{3.6}$$

Here, Δ_i^* is the Δ-anomaly for a specific process for a grid cell in the model, and Δ_{bg} is the background level (we used $\Delta_{\text{bg}} = 0$ per meg). One of the attractive features of this definition is its additivity, meaning that the sum of all Δ-anomalies results in the overall Δ signature (this is true for the linear definition of $\Delta^{17}O$ and by approximation also for the logarithmic definition of $\Delta^{17}O$, an overview of the definitions is provided in Sect. S1 of *Koren et al.*, 2019). The Δ-anomaly represents the contribution of a specific process to the overall $\Delta^{17}O$ signature.

We have performed simulations with the global 3-D model and extracted CO_2 mole fractions and its $\Delta^{17}O$ signatures for the Loobos location. This allows us to inspect the contribution from different sources and to investigate how well the relatively coarse global model (spatial resolution ranging from 6°×4° to 1°×1°, longitude by latitude) can simulate the Loobos observation site. Finally, we use the global model to simulate the diurnal cycle of $\Delta^{17}O$ in CO_2 for different sites across the globe, including tropical and boreal forests.

3.3 Results

3.3.1 Meteorological conditions and CO_2 fluxes

We performed a 24-hour measurement campaign on August 15-16, 2019, at the Loobos flux tower site (Fig. 3.1). Before reporting on the isotope budget, we first describe here the meteorological conditions and CO_2 fluxes for the Loobos site. During the campaign, the atmosphere was partially clouded (a snapshot of the cloud cover for August 15 and 16, 2019, is shown in Fig. S3.1), which affected incoming radiation and thus temperature, humidity, boundary layer height and CO_2 fluxes. The effect of these clouds on the isotopic composition of CO_2 is further explored in Sect. 3.3.3.

Observations of radiative fluxes for the Loobos site in August 2019 were not available, and we therefore calculated the climatological radiation for August at Loobos determined from the years 2013-2017 (we excluded the anomalous summer of 2018, *Buitink et al.*, in review; *Smith et al.*, 2020). Fig. S3.2 shows that the radiation in the MXL model, with an assigned cloud cover of 0.5, agrees reasonably well with the climatological Loobos radiation. We also show the net radiation, as measured at 10 minute time interval by KNMI at Cabauw, in Fig. S3.3. Since the cloud cover is mostly driven by synoptic conditions, we consider this representative for Loobos, and our comparison in Fig. S3.3 suggests that the net radiation in our MXL simulation is too high. For August 16 of 2019, a comparison of observed and simulated meteorological variables (sensible heat flux, latent heat flux, relative humidity and temperature) is shown in Fig. S3.4. In general there is a good agreement between the observations and the MXL model.

The development of the boundary layer height is important for the interpretation of the ecosystem measurements. Fig. 3.2 shows the cloud base measurements for August 16, 2019 from ceilometers at Cabauw and Deelen (Fig. 3.1) that are in close proximity (resp. 50 to 20 km) to Loobos. The cloud base usually coincides with the top of the boundary layer. Also, we included an estimate for the boundary layer height determined from a weather balloon launched by KNMI from De Bilt on the previous day, around 11:30. For completeness we show in Fig. S3.5 the potential temperature profile measured by this weather balloon and for two balloons that where launched around midnight. In addition, the boundary layer height simulated by the MXL model and used in the TM5 model (ERA-interim meteorology) are also included in Fig. 3.2. In general there is good agreement between the different estimates.

Fig. S3.6 shows the net ecosystem exchange (NEE) observed at Loobos with the eddy

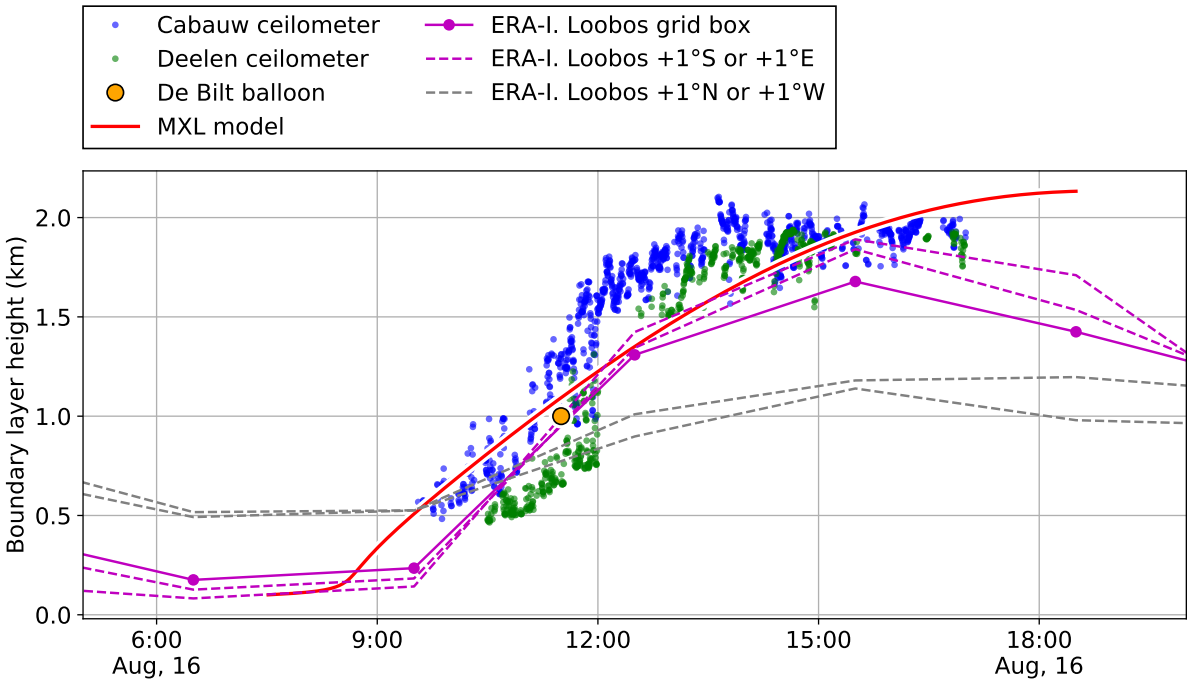

Figure 3.2: Temporal variation of atmospheric boundary layer height for August 16, 2019, reconstructed from (1) the 5-minute ceilometer observations from Cabauw and Deelen; (2) a weather balloon launched from De Bilt on the previous day at 11:30;(3) as simulated by the mixed layer model for the Loobos site; and (4) from ERA-Interim data used in the 3-D model for the 1°×1° grid box containing the Loobos flux tower site. Results from the four neighbouring grid cells are also included. Time is specified in local time (UTC+2).

covariance system. Due to a failure of the profile system, it was not possible to partition the NEE into GPP and terrestrial ecosystem (TER) in the usual way. Also, due to issues with the power supply, the nighttime NEE was not captured by the system. Therefore, we show the climatological range of NEE, GPP and TER as determined from Loobos observations for August of the years 2013-2017. We also included the NEE, GPP and TER simulated by the A-gs vegetation module of the MXL model. Although the fluxes represent different time periods, they are nonetheless in reasonable agreement.

3.3.2 CO_2 mole fraction and isotopic composition

During the 24-hour campaign, we collected air samples from the top of the Loobos tower, approximately 1–2 m above the canopy (15 samples) and from 0.5 m above the surface (15 samples). Isotopic measurements were performed afterwards in the IMAU lab. The observations of the CO_2 mole fraction and the isotopic composition ($\delta^{13}C$, $\delta^{18}O$ and $\Delta^{17}O$) from the top of the tower and near the surface are shown in Fig. 3.3, alongside simulations

from the MXL model and TM5 model. The isotopic measurement data (δ^{13}C, δ^{17}O and δ^{18}O) for CO_2 extracted from the tower and near-surface samples are reported in Tables S3.1 and S3.2, respectively.

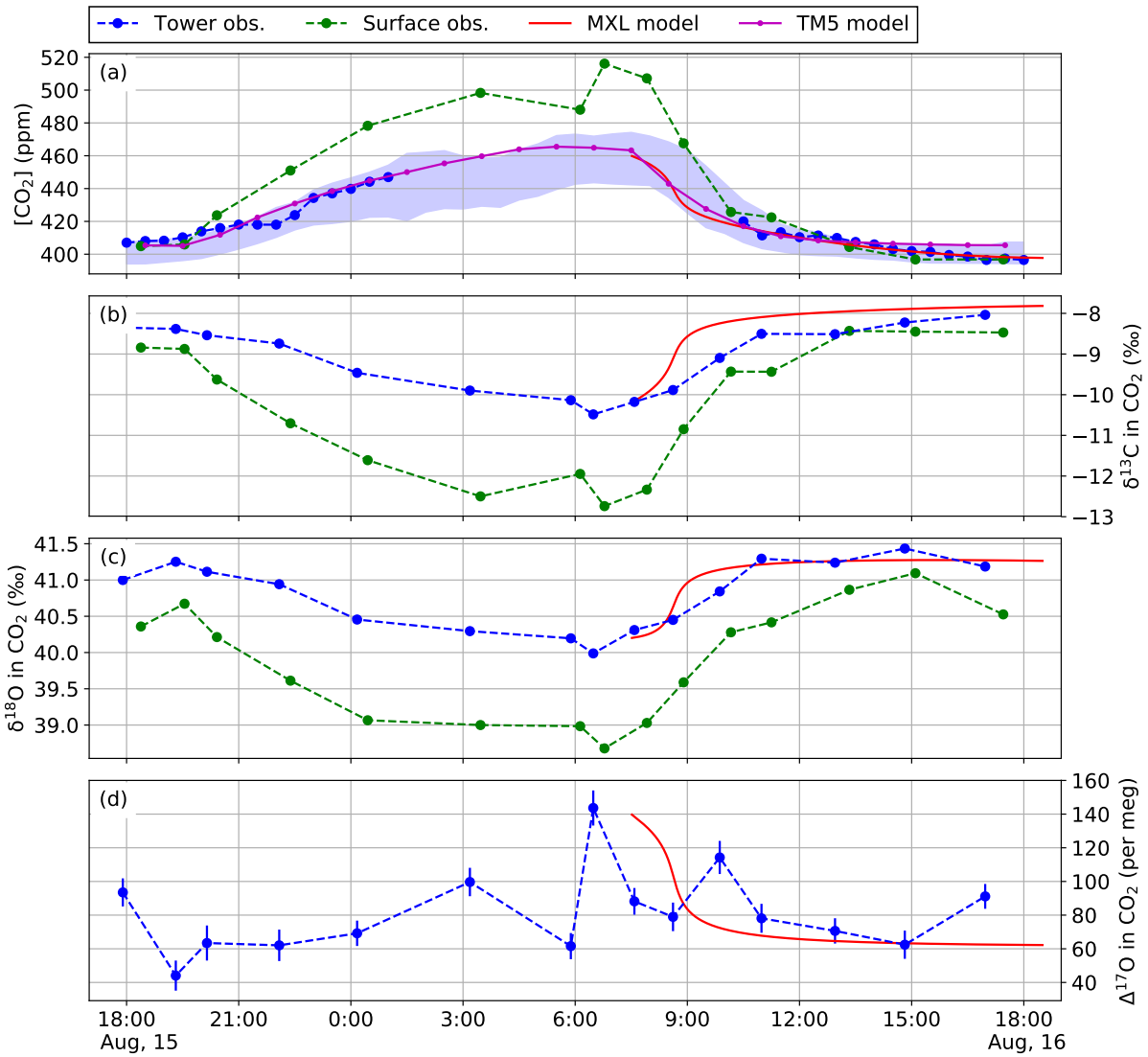

Figure 3.3: Temporal variation of (a) CO_2 mole fraction; (b) δ^{13}C in CO_2; (c) δ^{18}O in CO_2; and (d) Δ^{17}O in CO_2 for August 15-16, 2019, as observed at the Loobos site and simulated with the mixed layer model MXL and global transport model TM5. Note that the tower CO_2 mole fractions were not measured from the sampled flasks, but measured by the tower system (the shading indicates the standard deviation around the mean of the observations for August 2019). The global transport model TM5 model simulates CO_2, which is included here, and Δ^{17}O in CO_2, which falls outside of the range shown here and is described further in Sect. 3.3.4. Time is specified in local time (UTC+2) and the error bar for Δ^{17}O in CO_2 represents the standard error.

We first consider the observations of CO_2 mole fraction and its isotopic composition in

Fig. 3.3. During the stable nighttime conditions, the CO_2 mole fraction increases rapidly (panel a). The increase of CO_2 is largest for the observations near the surface, which is closer to respiration sources in the soils. Both $\delta^{13}C$ and $\delta^{18}O$ become depleted during the nighttime (panels b and c). As for the CO_2 mole fraction, the largest excursion occurs close to the surface. For $\Delta^{17}O$ in CO_2, the high value just after 6:00 in the morning is most notable (panel d). The other isotope signatures and the CO_2 mole fraction for the tower and surface samples are also somewhat anomalous at this time. This is possibly caused by the entrainment of residual air masses. Currently, the $\Delta^{17}O$ in CO_2 for the surface samples is not yet determined.

The MXL model only simulates the boundary layer under convective conditions, and therefore does not capture the nighttime build up of CO_2 and depletion of $\delta^{13}C$ and $\delta^{18}O$. However, the reduction of CO_2 and the enrichment of $\delta^{13}C$ and $\delta^{18}O$ during the day are well resolved. Currently the lapse rate for $\delta^{13}C$ and $\delta^{18}O$ are zero (Table S3.3), but a more gradual difference between the signatures in the boundary layer and the free troposphere will likely further improve the match between the MXL simulations and the observations. For $\Delta^{17}O$ in CO_2, the MXL model agrees reasonably with the observations, although the high $\Delta^{17}O$ value at $\sim$10:00 is not captured.

The CO_2 mole fractions simulated by the TM5 model agree well with the tower observations (the grid cells of the TM5 model are included in Fig. 3.1). We started the TM5 simulation with initial CO_2 fields from CarbonTracker (*Peters et al.*, 2005, 2007, 2010, see for more information also `https://www.carbontracker.eu`) for December 2008 and propagated this in time for five years (i.e. to December 2013). Finally, we extracted the August 2013 values for Loobos, and added an offset for the additional CO_2 released between 2013 and 2019 (determined from the NOAA Mauna Loa record for August 2019). Note that $\delta^{13}C$ and $\delta^{18}O$ are not simulated by the TM5 model. The $\Delta^{17}O$ signature simulated by TM5 is not included here, but is discussed further in Sect. 3.3.4.

In Fig. 3.4 we show Keeling plots for the samples collected from the tower and near the surface. The y-intercepts are an estimate of the source signature and can thus be used to reconstruct the relative contributions of CO_2 respired from soils and diffused out of leaves. The source signatures (including its standard deviation) and the R^2 coefficient are reported in Table 3.1. Note that the CO_2 mole fractions for the tower are not measured from the collected flasks, but from the CO_2 system at the Loobos tower. To perform the Keeling analysis, these CO_2 observations were first interpolated to the exact times that the flasks were sampled. Unfortunately, these tower CO_2 observations do not cover the nighttime (which has the most extreme variations in CO_2, $\delta^{13}C$ and $\delta^{18}O$). We also

included correlation plots between the different isotope signatures (see Fig. S3.7), which is not affected by the gap in CO_2 data during nighttime.

The $\delta^{13}C$ observations from the tower and surface have distinctly different source estimates (Table 3.1). This reflects that different processes are dominating the $\delta^{13}C$ isotope budget, depending on the sampling height and the time period that is considered. For $\delta^{18}O$ in CO_2, the estimated source signatures for the tower and surface observations are not so different, and in the range of the signatures associated with soil water equilibration (35–40‰ for CO_2 equilibrated with soil water for the Netherlands in August according to *Bowen and Revenaugh*, 2003, and obtained through the data portal `http://www.waterisotopes.org`), leaf water equilibration (some per mill higher than for soil water equilibration due to evaporative enrichment) and fossil fuel combustion (∼25‰, *Horváth et al.*, 2012; *Laskar et al.*, 2016). For the tower $\delta^{18}O$ the R^2 is somewhat lower, which suggests that multiple sources or sinks affect $\delta^{18}O$ at the height of the tower. Finally, the Keeling analysis for $\Delta^{17}O$ in CO_2 does not yield a reliable source signature, as reflected in the high uncertainty and low R^2 value. This suggests that the budget for $\Delta^{17}O$ is more complex, possibly involving multiple sources and sinks that are varying in strength during the day.

Table 3.1: Overview of parameters determined from the Keeling analysis for tower and surface observations. The y-intercept represents the source signature of the released CO_2 (its standard deviation is also reported) and the R^2 describes how well variations in the CO_2 mole fraction are related to changes in the isotopic composition. Note that for the tower observations we used CO_2 from the tower system (not from flasks) and that nighttime data (which have low $1/[CO_2]$) are not available for the tower observations.

Tracer	y-intercept	Std. dev.	R^2
Tower observations			
$\delta^{13}C$	-22.11 ‰	0.551 ‰	0.989
$\delta^{18}O$	32.93 ‰	1.936 ‰	0.718
$\Delta^{17}O$	-72.66 per meg	189.44 per meg	0.075
Surface observations			
$\delta^{13}C$	-27.25 ‰	0.5139 ‰	0.988
$\delta^{18}O$	31.68 ‰	0.530 ‰	0.949

3.3.3 Sensitivity study with MXL model

A practical advantage of the MXL mixed layer model is that it is computationally efficient. Here we exploit this feature by performing systematic sensitivity tests for (1) the cloud

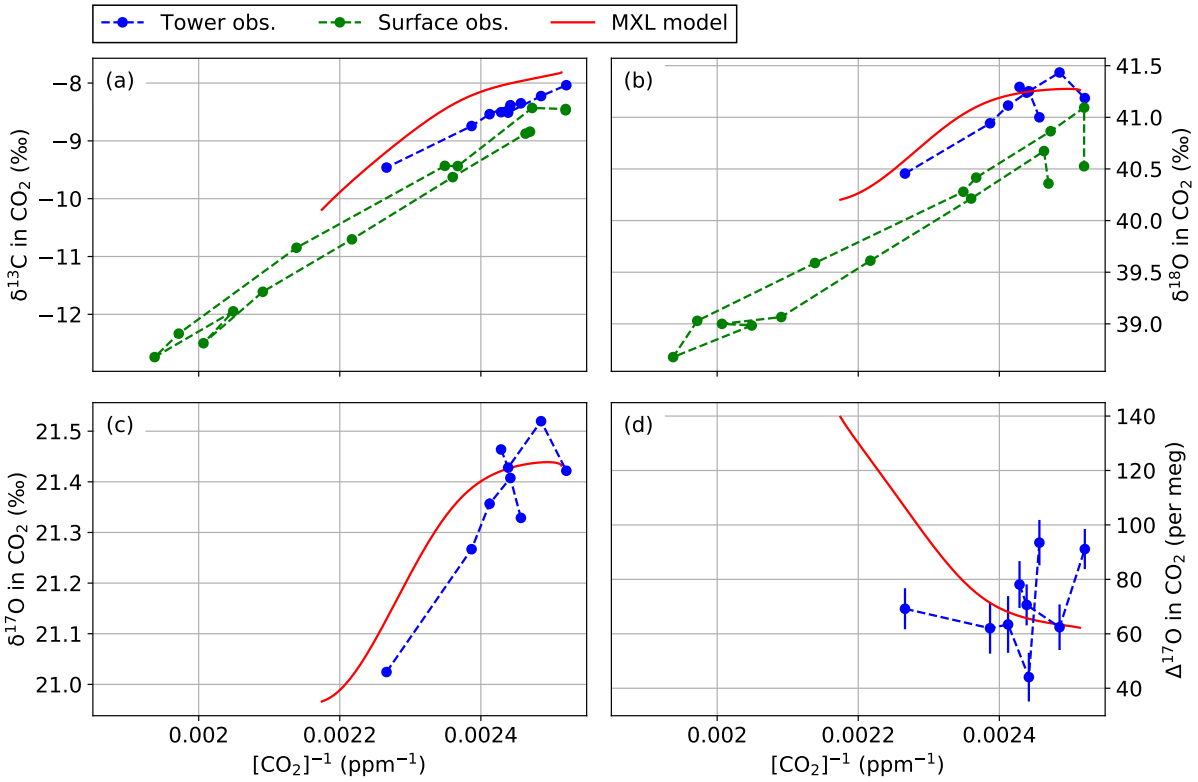

Figure 3.4: Keeling plots for (a) $\delta^{13}C$ in CO_2; (b) $\delta^{18}O$ in CO_2; (c) $\delta^{17}O$ in CO_2; and (d) $\Delta^{17}O$ in CO_2 of the samples collected at the Loobos site on August 15 and 16, 2019 and simulated with the MXL model. The y-intercept is an estimate of the source signatures. Note that the CO_2 data for the tower observations is obtained from the tower system (not from flasks) and that nighttime data (which have low $1/[CO_2]$) are not available for the tower observations.

cover; (2) the humidity of entraining air; and (3) the degree of isotopic equilibration inside leaves θ. As described in Sect. 3.2.2, the first and second variable interact with the meteorological conditions in the boundary layer, whereas the third parameter only affects the oxygen isotopes in CO_2.

First we consider the effect of changing the cloud cover, while using the default values for the initial humidity of air from the free troposphere and the degree of equilibration (Table S3.3). A decrease in the cloud cover results in more incoming radiation and in our case in a more rapid growth of the atmospheric boundary layer (Fig. S3.8a). In addition, more available light increases GPP (Fig. S3.8c) and higher temperatures increases TER (Fig. S3.8d). Since the response of GPP is stronger, the magnitude of NEE increases (i.e. more uptake, Fig. S3.8b) due to a decrease in the cloud cover.

The cloud cover will also affect the $\delta^{18}O$ signature of leaf water (Fig. S3.9a) through the

relative humidity (the relative humidity is one of the terms that appears in the Craig-Gordon model that relates $\delta^{18}O$ of water vapor to $\delta^{18}O$ in leaf water, see Eq. (A.26) in *Vilà-Guerau de Arellano et al.*, 2019). In addition, the triple isotope exponent λ_{transp} also depends on the relative humdity (Eq. (3.3), Fig. S3.9). Through Eq. (3.4), these variables control the $\Delta^{17}O$ signature of leaf water (Fig. S3.9).

The changes in the meteorological variables have an effect on the CO_2 mole fraction and its isotopic composition (Fig. S3.10). In addition, the oxygen isotope signatures ($\delta^{18}O$ and $\Delta^{17}O$) are affected by the isotopic composition of the leaf water described previously. It can be noted that the variation of the isotopic composition for the different simulations is most pronounced in the morning, when the boundary layer grows rapidly and when stomatal conductance increases, and that the differences become smaller in the afternoon.

In Fig. 3.5 we show the sensitivity of $\delta^{18}O$ and $\Delta^{17}O$ in CO_2 at two time instances: at 9:00 in the morning (panels a and b) and at 15:00 in the afternoon (panels c and d). For panels a and b, we varied the cloud cover and the initial humidity of the free troposphere (qFT0) while keeping the initial humidity in the boundary layer fixed at 9.0 g/kg. In the default setup we used a value of qFT0 = 8.9 g/kg, and thus a difference of dq0 = -0.1 g/kg, which is indicated by the star symbol in Fig. 3.5a,b. A higher cloud cover results in depletion of $\delta^{18}O$, especially when the free tropospheric or residual air is humid (dq0 > 0). The opposite pattern is found for $\Delta^{17}O$ in CO_2. As can be seen from the solid and dashed lines, the boundary layer is still quite shallow and GPP at a moderate level.

The isotopic composition ($\delta^{18}O$ and $\Delta^{17}O$) at 15:00 in the afternoon is shown in Fig. 3.5c,d. Here we manipulated the cloud cover and degree of isotopic equilibration θ and used the default value for the initial humidity (i.e., dq0 = -0.1 g/kg). An increase in the cloud cover and a reduction of θ both result in depletion of $\delta^{18}O$ and the opposite occurs for $\Delta^{17}O$ in CO_2. Also, it can be seen that at 15:00 (panels c and d) the variation between the different simulations is much smaller than at 9:00 (panels a and b). Although the variation in the isotopic composition of the boundary layer is small, there is still a substantial difference in the isofluxes (not shown here).

3.3.4 Source attribution using tagged tracers

In Fig. 3.6 we show the simulated diurnal cycles for the tagged CO_2 tracer and its $\Delta^{17}O$ signature. Note that we do not show the absolute values, but the variation around the daily mean value. The different categories are represented by colored areas and the total

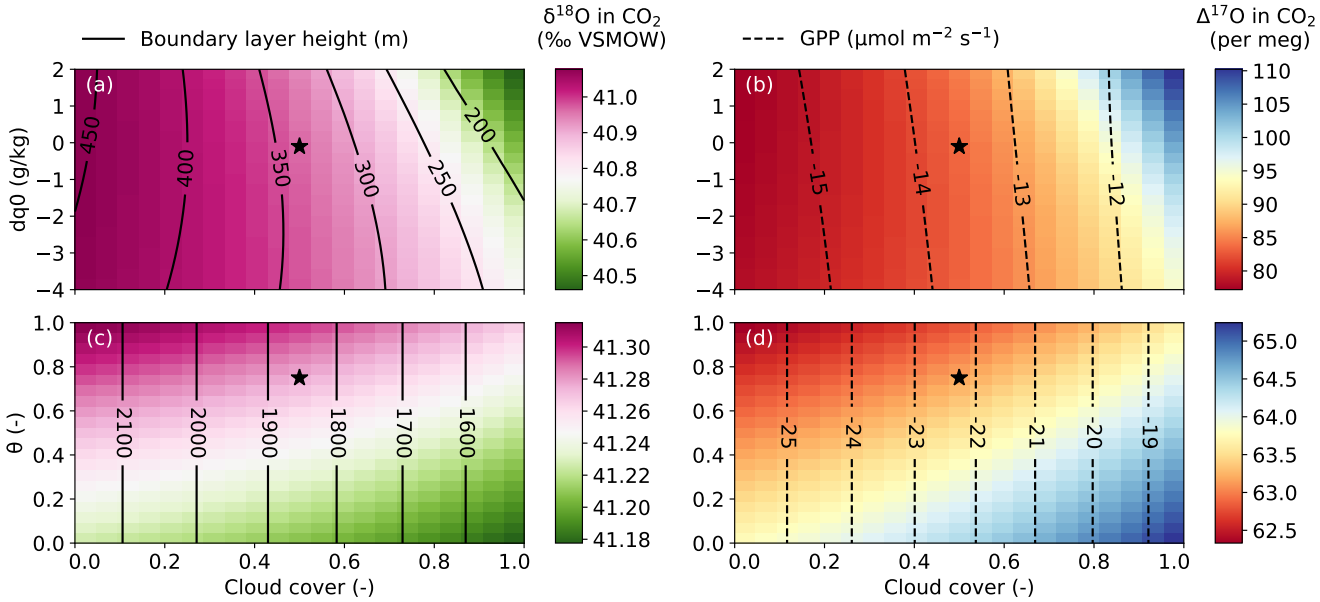

Figure 3.5: Sensitivity of isotopic composition of CO_2 simulated by the MXL model. (a) $\delta^{18}O$ in CO_2 at 9:00 as function of the cloud cover and the difference between initial humidity in the free troposphere and the boundary layer; (b) $\Delta^{17}O$ in CO_2 at 9:00 as function of the same variables as in a; (c) $\delta^{18}O$ in CO_2 at 15:00 as function of the cloud cover and the degree of isotopic equilibration inside leaves θ; and (d) $\Delta^{17}O$ in CO_2 at 15:00 as function of the same variables as in c. In addition, the boundary layer height and GPP are shown as solid and dashed curves, respectively. The star in the panels indicates the default conditions used for the Loobos case (i.e. cloud cover of 0.5, initial humidity difference of -0.1 g/kg and isotopic degree of equilibration 0.75).

CO_2 mole fraction and $\Delta^{17}O$ signature are shown as dashed black lines. Note that for CO_2 and for $\Delta^{17}O$ in CO_2, the sum of the individual contributions adds up to the total tracer (see also Sect. 3.2.3 for a description of the additive property of the Δ-anomalies).

For the diurnal cycle of CO_2 at Loobos in August, the main contributions are from the biosphere and fossil fuel emissions. The biosphere increases the CO_2 levels at night due to respiration, whereas photosynthesis drives down the CO_2 levels during daytime. Note that there is no diurnal cycle applied to the fossil fuel emissions; the diurnal cycle in fossil fuel CO_2 is due the boundary layer dynamics (accumulation of fossil fuel emitted CO_2 in the shallow nocturnal boundary layer). Note that CO_2 from the biosphere and from fossil fuels are synchronised such that the diurnal amplitude of the total CO_2 tracer exceeds the amplitude of the underlying processes.

For the isotope signature $\Delta^{17}O$, the main components are the stratosphere and the biosphere. The stratosphere is the main source of $\Delta^{17}O$ in CO_2 and it contributes less during the night, when the entrainment of air into the boundary layer is small. The biosphere is

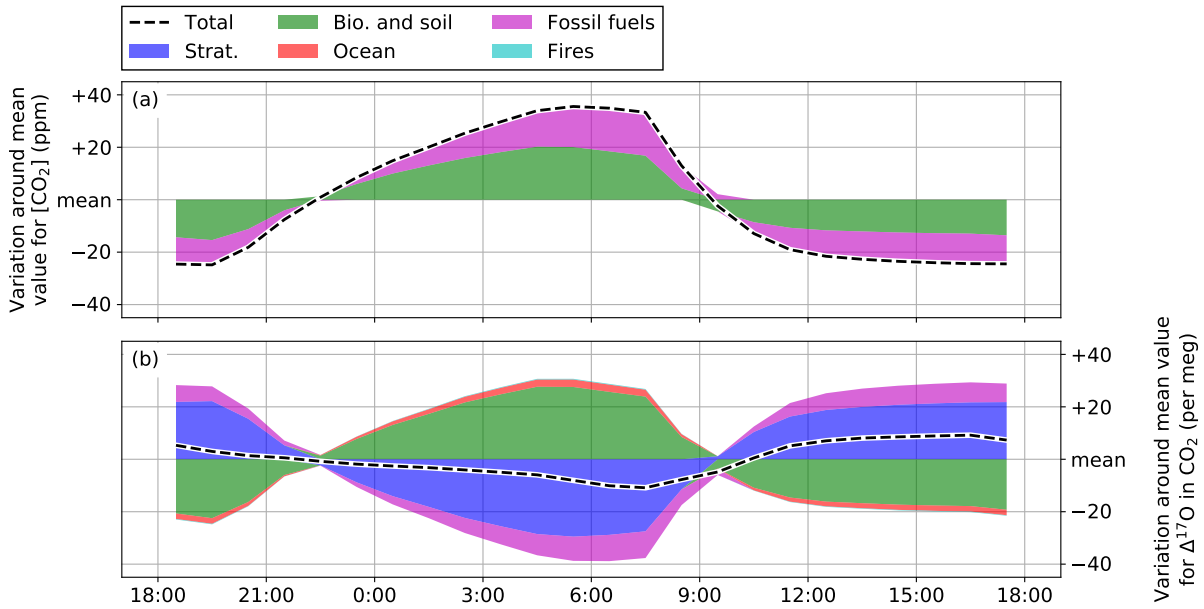

Figure 3.6: Variation around the mean value for 'tagged tracers' for (a) CO_2 mole fraction; and (b) $\Delta^{17}O$ in CO_2 for August at the Loobos site as simulated with global transport model TM5. Time is specified in local time (UTC+2).

a sink of $\Delta^{17}O$ in CO_2, and it is most effective during the daytime, because the gross leaf exchange fluxes scale linearly with the assimilation flux (see Eq. (8) in *Koren et al.*, 2019). Contrary to the CO_2 mole fractions, the diurnal amplitude of the total $\Delta^{17}O$ tracer does not exceed the amplitude of the individual contributions.

3.3.5 Diurnal cycle of $\Delta^{17}O$ in CO_2 for ecosystems across the globe

Here we use the global transport model TM5 to extend our analysis of the diurnal cycles to the global scale. Fig. 3.7 shows a map of the annual mean amplitude of the diurnal cycle of simulated $\Delta^{17}O$ in CO_2. Clearly, the amplitude is largest over land areas, which was also found for the seasonal cycle (Fig. 7 in *Koren et al.*, 2019) and the magnitude of the diurnal cycle is roughly the same as the magnitude of the previously reported seasonal cycle. Throughout the year, the simulated diurnal cycles of $\Delta^{17}O$ in CO_2 is highest for tropical land regions and industrialized areas of China. The amplitude of the diurnal cycle for land regions in the Northern Hemisphere experiences a substantial seasonal cycle, which is expected because of the strong seasonality of the atmosphere-leaf flux and the low $\Delta^{17}O$ signatures of leaf for water for this region (Figs. 4 and 5 in *Koren et al.*, 2019, respectively).

In Fig. 3.8 we show the $\Delta^{17}O$ signature from CO_2 that is released through leaves. The amplitude of the diurnal cycle for this tagged tracer exceeds that of the total isotopic signature shown in Fig. 3.7 (note the different color scales). Also, the main contribution from Asia is now shifted from the highly industrialized areas of China to the tropical ecosystems in Southeast Asia.

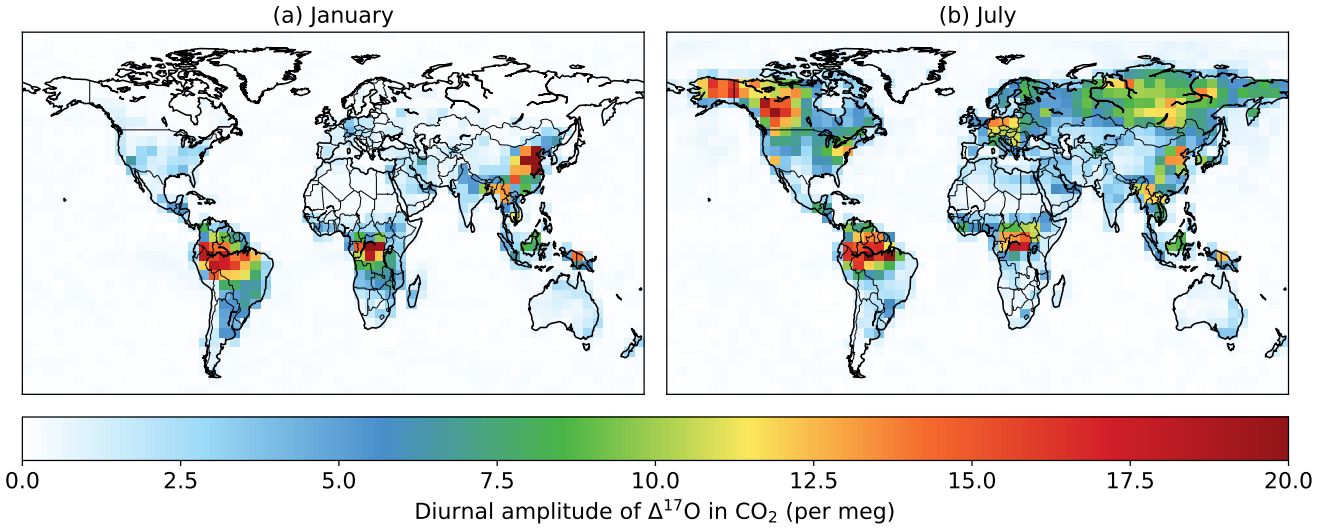

Figure 3.7: Monthly mean diurnal amplitude of the $\Delta^{17}O$ in CO_2 across the globe simulated with the global transport model TM5 at a spatial resolution of 6°×4° for the lowest 35 m of the atmosphere for (a) January and (b) July.

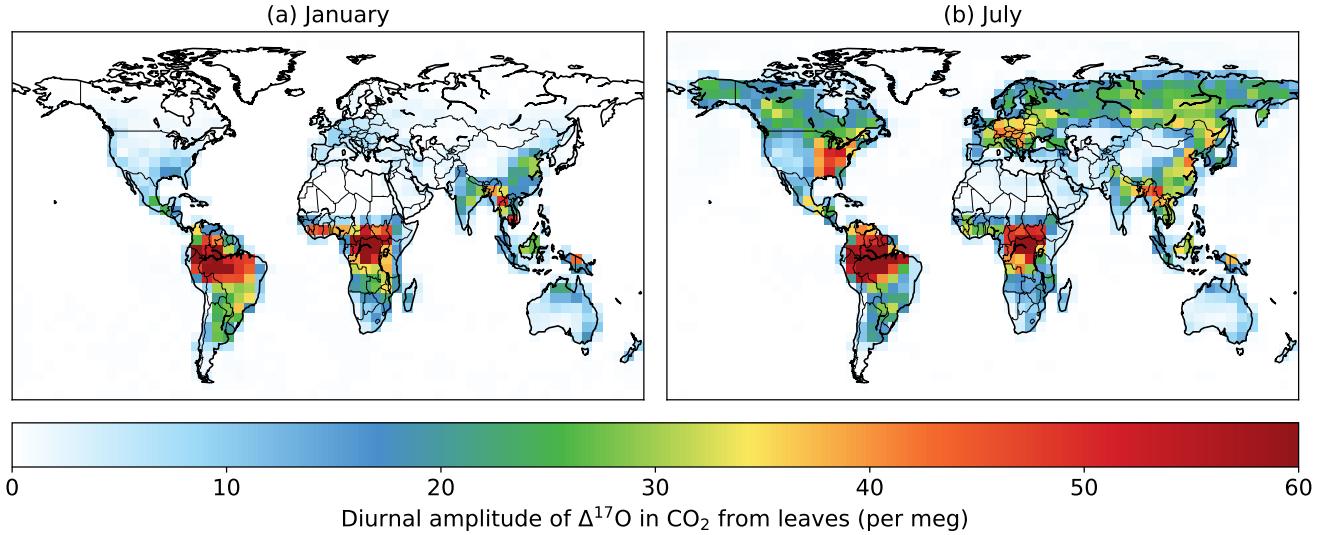

Figure 3.8: Monthly mean diurnal amplitude of the $\Delta^{17}O$ in CO_2 from leaves across the globe simulated with the global transport model TM5 at a spatial resolution of 6°×4° for the lowest 35 m of the atmosphere for (a) January and (b) July.

3.4 Discussion

3.4.1 Observed variation of $\Delta^{17}O$ in CO_2

In this section we discuss the observed diurnal variation for $\Delta^{17}O$ in CO_2 at Loobos. One of our goals was to test whether there is a measurable diurnal variation of $\Delta^{17}O$ in CO_2 at the ecosystem level and to relate this to the driving processes. We were partly successful by finding detectable variations in $\Delta^{17}O$ in CO_2, however the interpretation of these variations remains incomplete. Contrary to the variations during the daytime and nighttime regimes for CO_2, $\delta^{13}C$ and $\delta^{18}O$, we can not identify periods of sustained increase or decline. Therefore, the contribution of photosynthesis and respiration to the diurnal variation of $\Delta^{17}O$ in CO_2 is not clear.

For $\Delta^{17}O$ in CO_2 we find a substantial decrease in the early morning, that we tentatively ascribed to the entrainment of residual air masses. It should be noted that this is based on a single measurement point (at 6:30 hr) that could be wrong (some issues concerning the measurements are described below). This single measurement point also determines the initial condition for $\Delta^{17}O$ in CO_2 that we used in our MXL simulation, hence our MXL simulations should be interpreted with care. However, if this measurement point is accurate, it suggests that surface measurements in the early morning could potentially be used to constrain the isotopic composition of residual air masses.

An issue that deserves attention in the interpretation of the tower measurements is the closeness of the tower inlet to the top of the canopy. The average height of the trees at Loobos has increased over the years, and currently the top of the tower reaches just above the canopy of the forest (1–2 meters, as described in Sect. 3.2.1). Therefore measurements from the top of the tower have become more sensitive to local disturbances from the canopy, which complicates the interpretation of the measurements. In fact, the current tower height is not sufficient anymore according the Integrated Carbon Observation System (ICOS) guidelines (*Rebmann et al.*, 2018) and the tower height will be increased as part of the Ruisdael project (`https://www.ruisdael-observatory.nl`).

A critical issue related to the quality of oxygen isotope measurements in CO_2 is the possible isotopic equilibration with water. As described in Sect. 3.2.1, we used magnesium perchlorate to dry the air before sampling. However, there is no guarantee that the drying was sufficient for each individual flask. A small amount of residual water in the flasks could affect the measurement of $\Delta^{17}O$ in CO_2. However, this would also affect $\delta^{18}O$ in CO_2 and there are no indications in the observations of $\delta^{18}O$ in CO_2 that suggest that

this was the case.

Finally, we address some setbacks that we experienced during the campaign, that have affected our ability to study in particular the effect of respiration on $\Delta^{17}O$ in CO_2. We lost the opportunity to measure the CO_2 mole fractions from the flasks collected from the tower and therefore had to rely on the CO_2 observations from the tower system. However, due to issues with the power supply at Loobos, there are substantial gaps during the respiration dominated nighttime. Finally, the closing of lab facilities due to the COVID-19 pandemic, has prevented us from measuring the $\Delta^{17}O$ in CO_2 for surface samples that are likely strongly dominated by heterotrophic respiration.

3.4.2 MXL model limitations and alternatives

Another objective of this project was to implement $\Delta^{17}O$ in CO_2 as a new tracer in the MXL model and demonstrate its capability to systematically explore the sensitivity to different input variables. We successfully implemented $\Delta^{17}O$ in CO_2 and managed to reproduce the meteorological observations and isotopic measurements reasonably well. Since the measurements were used to adjust the input variables for the simulations, the quality of observations (as discussed in Sect. 3.4.1) has implications for the interpretation of the MXL model results.

As described in Sect. 3.2.2, the MXL model is only valid for convective conditions, which means that we cannot simulate the nighttime conditions in the current setup. The nighttime regime is of interest to the budget of $\Delta^{17}O$ in CO_2, since (1) respired CO_2 accumulates in the shallow nocturnal boundary layer; and (2) there can still be exchange with leaf water for stomates that remain partially open during the night. The partial opening of stomates during nighttime conditions was experimentally confirmed for water (*Snyder et al.*, 2003; *Caird et al.*, 2007; *Howard and Donovan*, 2007), CO_2 (*Cernusak et al.*, 2004) and COS (*Kooijmans et al.*, 2019). A possible alternative model is the Wageningen University Single Column Model (WUSCM), that was previously applied by *Aan de Brugh et al.* (2012) for their study on ammonium nitrate concentrations in the atmospheric boundary layer. The WUSCM model is able to simulate a full diurnal cycle (i.e. daytime and nighttime), while remaining computationally efficient and thus allowing to perform systematic sensitivity tests.

The canopy is a complex domain, with non-uniform distribution of incoming radiation, irregular geometries and turbulent mixing of tracers. These in-canopy processes are not

explicitly resolved in MXL, and we can thus not simulate the variation of CO_2, $\delta^{13}C$, and $\delta^{18}O$ in CO_2 of the surface samples that we collected. Some processes within the canopy could be simulated using the single-column model (turbulent mixing in this model is parameterized) developed by *Ganzeveld et al.* (2002b), that was used to simulate the soil and vegetation contributions of NO_x (*Ganzeveld et al.*, 2002a).

An alternative approach is to use a large eddy simulation (LES) model (e.g. DALES, *Heus et al.*, 2010) to resolve the largest turbulent scales. *Ouwersloot et al.* (2017) used DALES to simulate the dynamics inside the canopy. Currently, the distribution of radiation and the exchange of water and CO_2 at different levels in the canopy is being implemented in DALES. In a different LES model, *Wei et al.* (2018) simulated isotopologues of water in the atmospheric boundary layer, but here the processes inside the canopy were not explicitly resolved. Note that the more detailed description of atmospheric processes with LES also significantly increases the computational costs.

3.4.3 Applicability and added value of the TM5 model

The diurnal variation simulated with TM5 for $\Delta^{17}O$ in CO_2 is smaller (20 per meg) than the observed variability (100 per meg difference between lowest and highest point). A potential explanation for this discrepancy relates to the representativeness of the relatively coarse global model (1°×1°, see Fig. 3.1) for the Loobos tower (reaching just above the canopy and possibly sensitive to local disturbances, as discussed in Sect. 3.4.1). Finally, we note that some input fields in the TM5 model are only varying monthly, such as fossil fuel emissions and (GPP-weighted) C_i/C_a ratios. We did some tests with 3-hourly C_i/C_a ratios, but this did not substantially change the simulated diurnal cycles of $\Delta^{17}O$ in CO_2 (data not shown).

Our tagged tracer simulations in TM5 show that the biosphere results in a depletion of $\Delta^{17}O$ in CO_2 that is mostly occurring in the daytime, when the isotopic exchange with leaf water is most intense. This trend agrees reasonably with the observations (although there is some scatter during the day) and the MXL model. We have learned from the tagged tracer simulations (Fig. 3.6) that the combination of the fossil fuel and biosphere tracers result in a weakening of the diurnal amplitude of $\Delta^{17}O$ in CO_2. The fact that the 1°×1° grid cell also contains several urban areas (e.g. Utrecht, Almere, Amersfoort) with substantial fossil fuel emissions, can partly explain why the simulated amplitude in TM5 underestimates the observed amplitude for $\Delta^{17}O$ in CO_2.

The tracer tagging method that we implemented can be used for applications beyond the scope of our current study. For instance, *Peylin et al.* (1999) applied this method for $\delta^{18}O$ in CO_2 and found that the seasonal cycle of simulated $\delta^{18}O$ in CO_2 at high latitude stations was mainly driven by extra-tropical respiratory fluxes. In addition, the tracer tagging technique can be useful for further improvement of the model, because it shows which simulated processes are most important to specific features of the total $\Delta^{17}O$ signature, and thus indicates which processes should be scrutinized most critically.

An issue that we did not put much emphasis on so far, is the difference in the mean value of $\Delta^{17}O$ in CO_2 between the TM5 simulations ($\sim$0 per meg in August for the grid cell containing Loobos) and the observations ($\sim$80 per meg). Contrary to the MXL simulations, we did not adjust initial conditions of $\Delta^{17}O$ in CO_2 to match the observations. We started the TM5 simulation with 0 per meg for each grid cell and simulated for $\sim$20 years, after which we verified that there was no more trend in the $\Delta^{17}O$ signature. Our simulated $\Delta^{17}O$ in CO_2 is thus independent of the initial condition and fully driven by the simulated stratospheric production and surface sinks. Note that there are also substantial differences in the mean values of reported observations of $\Delta^{17}O$ in CO_2 from different labs (e.g. Fig. 6 in *Hofmann et al.*, 2017) and more research is needed to reconcile the observations and simulations.

Finally, we used the TM5 model to extend our analysis of the diurnal cycle of $\Delta^{17}O$ in CO_2 to the global scale. We find that the simulated diurnal cycle is largest for tropical ecosystems and during the respective summer months of the Northern and Southern Hemispheres, similar to spatiotemporal patterns in GPP. In contrast, we found previously (e.g. Fig. 12a in *Koren et al.*, 2019) that the simulated seasonal variation for $\Delta^{17}O$ in CO_2 in the tropics is small. This suggests that to detect interpretable signals for tropical GPP, collecting multiple air samples spread out over the day might be a more effective measurement strategy than collecting the same amount of air samples spread out over several months.

3.4.4 Recommendations for future campaigns

Here we analyzed the diurnal cycle of $\Delta^{17}O$ in CO_2 based on observations from a single day. For future measurement campaigns we suggest to cover a number of consecutive days, such that the repeating patterns in the diurnal cycle can be identified and stronger conclusions can be made. For instance, in our previous study on Harvard Forest (*Vilà-Guerau de Arellano et al.*, 2019) for $\delta^{13}C$ and $\delta^{18}O$ in CO_2, we used data from four

consecutive days that had similar meteorological conditions.

The day that we studied was a cloudy day, which affects the meteorological conditions, CO_2 fluxes and hence the isotope budget (as demonstrated in Sect. 3.3.3). *Still et al.* (2009) showed that photosynthetic uptake of CO_2 and $C^{18}OO$ can be higher during clouded days than during days with clear skies, due to the larger fraction of diffuse radiation. More recently, *Rap et al.* (2015) and *Hemes et al.* (2020) confirmed in their studies that increased diffuse radiation can lead to enhanced photosynthesis. For follow-up studies, it would be interesting to collect air samples for different seasons and weather conditions, such that the response of vegetation to these drivers can be explored further.

We have now focused on the pine forest Loobos. To better understand the role of the type of vegetation, a follow-up study in the deciduous broadleaf forest Speulderbos (*Brede et al.*, 2016; *Raj et al.*, 2016; *Cisneros Vaca et al.*, 2018) is considered. Speulderbos is in close proximity to Loobos (∼10 km) and has a comparable climate. In addition, a grass land study at the Cabauw tall tower (*Vilà-Guerau de Arellano et al.*, 2004; *Casso-Torralba et al.*, 2008) and the Veenkampen site operated by Wageningen University are possible within the same climate zone. Also, other climate zones are of interest, especially tropical forests that represent a large fraction of global GPP and where we expect a large diurnal variation of $\Delta^{17}O$ in CO_2 (as discussed in Sect. 3.4.3). A suitable sampling site is the ATTO tower in the Amazon (*Andreae et al.*, 2015), which (1) has air inlets at multiple heights; (2) is equipped with meteorological instruments; and (3) is well-characterised by previous studies (e.g. *Botía et al.*, 2020). Especially for up-scaling local findings to the global scale, it is important that the derived parameterisations are representative for larger regions and across environmental conditions.

To further constrain the different processes at the ecosystem level, measurements of other variables could be valuable. For instance, the $\delta^{18}O$ and $\Delta^{17}O$ isotopic composition of leaf water have a strong control on the oxygen isotopes in CO_2. Due to the lack of these leaf water observations, assumptions made in the modeling approaches could not be validated here. From a practical point of view, measuring $\delta^{18}O$ and $\Delta^{17}O$ in water vapor might be a more attractive alternative, since (1) it avoids the need of labor intensive extraction of water from leaves; and (2) it is representative for a larger part of the canopy than an individual leaf. In addition, measurement of stomatal conductance (as done during the recent CloudRoots campaign, *Vilà-Guerau de Arellano et al.*, 2020), soil chambers, branch measurements (e.g. *Kooijmans et al.*, 2019), and isotopic fluxes of $^{13}CO_2$ and $C^{18}OO$ (*Wehr et al.*, 2013) can be helpful to further constrain the system.

Besides $\Delta^{17}O$ in CO_2, there are other tracers for the terrestrial carbon cycle that have

recently gained interest. This includes carbonyl sulfide (COS), clumped isotopes of CO_2 (Δ_{47}) and oxygen (O_2) that are all strongly affected by diffusion through stomates into leaves followed by exchange or uptake. To facilitate research in this direction, we have implemented these established or promising carbon cycle tracers in the MXL model. We foresee that multi-tracer measurement campaigns can further enhance our understanding of the exchange of CO_2 between the atmosphere and vegetation.

3.5 Conclusions

We have studied the diurnal variation of $\delta^{13}C$, $\delta^{18}O$ and $\Delta^{17}O$ in atmospheric CO_2 at the ecosystem level using isotopic measurements and meteorological observations from the pine forest Loobos, the Netherlands. Our observations from Loobos show depletions in $\delta^{13}C$ and $\delta^{18}O$ during the night, that are most pronounced close to the surface. The $\Delta^{17}O$ observations from the tower show variations exceeding the measurement uncertainty. Most notable is a peak in $\Delta^{17}O$ in CO_2 in the early morning, suggesting entrainment of residual air masses with elevated $\Delta^{17}O$ in CO_2.

We used the meteorological observations and isotopic measurements to select appropriate initial conditions and boundary conditions for the MXL model and verified that the simulated variation for $\delta^{13}C$, $\delta^{18}O$ and $\Delta^{17}O$ in CO_2 agrees well with our observations. From this well-defined base scenario, we find that $\delta^{18}O$ and $\Delta^{17}O$ in CO_2 are sensitive towards the cloud cover and the humidity of entraining air during the morning. In contrast, we find that the degree of equilibration and cloud cover are of minor importance for $\delta^{18}O$ and $\Delta^{17}O$ in CO_2 in the afternoon.

A new tracer tagging feature in the TM5 model was implemented to simulate the contribution of different processes to $\Delta^{17}O$ in atmospheric CO_2. For the $1^\circ \times 1^\circ$ grid cell containing Loobos, we find that isotopic signatures originating from fossil fuels and the biosphere have the largest diurnal cycle. However, since these signals are in anti-phase, the diurnal cycle of their sum largely cancels out. Finally, we use TM5 to extend our analysis to the global scale, and find that tropical ecosystems have the largest diurnal amplitude in simulated $\Delta^{17}O$ in CO_2. This is in contrast to the seasonal variations that we simulated earlier (*Koren et al.*, 2019), that are largest over the boreal regions.

Additional ecosystem measurements can contribute to a further increase of the understanding of the budget of $\Delta^{17}O$ in atmospheric CO_2, and hence its applicability as tracer of GPP. Measurements for different climatic conditions and across a variety of biomes

would be valuable, especially when combined with measurements of CO_2 fluxes, biophysical parameters and other tracers of the terrestrial carbon cycle.

Acknowledgements

We acknowledge Jan Elbers from Wageningen University & Research (WUR) for his past on work on the Loobos site. We thank Elena Popa from Utrecht University for her help with the flask sampler. We thank Elena Popa from Utrecht University for her help with the flask sampler. We acknowledge Henk Klein Baltink from Royal Netherlands Meteorological Institute (KNMI) for providing weather balloon data from De Bilt and ceilometer data from Cabauw and Deelen. We also acknowledge KNMI for providing radiation data from Cabauw through their data portal (`http://www.cesar-database.nl/`). The European Research Council (ERC) is acknowledged for funding this research (649087) as part of the ASICA (Airborne Stable Isotopes of Carbon from the Amazon) project. The model simulations in this work have been performed using a grant for computing time (SH-312-14) from the Netherlands Organization for Scientific Research (NWO).

Supplemental information

S3.1 Implementation of $\Delta^{17}O$ in CO_2 in the MXL model

S3.1.1 Introduction

Here we describe the details of the implementation of $\delta^{17}O$ and $\Delta^{17}O$ in CO_2 into the MXL model. The implementation of these tracers follows closely the implementation of $\delta^{18}O$ in CO_2 that is described by *Vilà-Guerau de Arellano et al.* (2019). In Sect. S3.1.2 we describe the exchange between soil and the atmosphere. Finally, we describe the exchange between vegetation and the atmosphere in Sect. S3.1.3.

S3.1.2 Soil-atmosphere exchange

The isotopic signature of soil water $\delta^{17}O_{sw}$ can be related to $\delta^{18}O_{sw}$ by assuming that soil water falls on the global meteoric water line with $\lambda_{GMWL} = 0.528$ and $\gamma_{GMWL} = 0.033‰$ (*Luz and Barkan*, 2010)

$$\delta^{17}O_{sw} = \exp\left(\lambda_{GMWL} \cdot \ln(\delta^{18}O_{sw} + 1) + \gamma_{GMWL}\right) - 1 \tag{S3.1}$$

Next, we calculate the isotopic signature of CO_2 in isotopic equilibrium with soil water from

$$\delta^{17}O_{soil} = (\alpha_{CO_2-H_2O})^{\lambda_{CO_2-H_2O}} \cdot (\delta^{17}O_{sw} + 1) - 1 \tag{S3.2}$$

Here we use the triple oxygen isotope coefficient $\lambda_{CO_2-H_2O} = 0.5229$ from *Barkan and Luz* (2012) and the temperature dependent fractionation factor $\alpha_{CO_2-H_2O}$ from *Brenninkmeijer et al.* (1983).

$$\alpha_{CO_2-H_2O} = 1 + \frac{17604/T - 17.93}{1000} \tag{S3.3}$$

Finally, the kinetic fractionation of the isotopologues $C^{17}OO$ and $C^{18}OO$ for diffusion through the soil column is related by the coefficient $\lambda_{kin} = 0.509$ (*Young et al.*, 2002) as

$$\varepsilon^{17}_{soil} = 1 - (1 - \varepsilon^{18}_{soil})^{\lambda_{kin}} \tag{S3.4}$$

Note that usually a fractionation factor is calculated as $\alpha = 1 + \varepsilon$ (e.g. *Affek and Yakir*, 2014), but in this case we follow the sign convention from *Vilà-Guerau de Arellano et al.* (2019) where ε for diffusion is positive. However, air that has diffused through an opening is depleted relative to the initial isotopic composition ($\alpha < 1$), which explains the term '$1 - \varepsilon^{18}_{soil}$' in Eq. (S3.4).

S3.1.3 Leaf-atmosphere exchange

For the leaf-atmosphere exchange, we first calculate the ^{17}O signature of the xylem water $\delta^{17}O_x$ from $\delta^{18}O_x$ assuming that xylem water is on the global meteoric water line, analogous to Eq. (S3.1) for soil water (although recent research has shown that the isotopic signature of stem water can differ substantially from soil water, *Barbeta et al.*, 2020).

Next, we calculate the fractionation factor α_{transp} associated with transpiration for $H_2{}^{18}O$ relative to $H_2{}^{16}O$, from the xylem water signature $\delta^{18}O_x$ and the leaf water signature $\delta^{18}O_{lw}$ (the latter is fully coupled to the isotopic composition of water vapor following the

Craig-Gordon formulation, as described in more detail in *Vilà-Guerau de Arellano et al.* (2019)).

$$\alpha_{\text{transp}} = \frac{\delta^{18}\text{O}_{\text{lw}} + 1}{\delta^{18}\text{O}_{\text{x}} + 1} \tag{S3.5}$$

The triple oxygen isotope coefficient for transpiration depends on relative humidity (*Landais et al.*, 2006) as given in Eq. (3.3) of the main text and repeated here for convenience.

$$\lambda_{\text{transp}} = 0.522 - 0.008 \cdot \text{RH} \quad \text{for} \quad 0.3 < \text{RH} < 1 \tag{S3.6}$$

The isotopic signature of leaf water $\Delta^{17}\text{O}_{\text{lw}}$ can then be calculated using Eq. (3.4) of the main text, repeated here for convenience

$$\Delta^{17}\text{O}_{\text{lw}} = \Delta^{17}\text{O}_{\text{x}} + (\lambda_{\text{transp}} - \lambda_{\text{RL}}) \cdot \ln(\alpha_{\text{transp}}). \tag{S3.7}$$

The isotopic signature $\delta^{17}\text{O}_{\text{lw}}$ then follows directly from $\delta^{18}\text{O}_{\text{lw}}$ and $\Delta^{17}\text{O}_{\text{lw}}$

$$\delta^{17}\text{O}_{\text{lw}} = \exp\left(\Delta^{17}\text{O}_{\text{lw}} + \lambda_{\text{RL}} \cdot \ln(\delta^{18}\text{O}_{\text{lw}} + 1)\right) - 1 \tag{S3.8}$$

Finally, the kinetic fractionation of the isotopologue C^{17}OO for diffusion through the leaf stomates $\varepsilon^{17}_{\text{leaf}}$ is related by the coefficient λ_{kin} to $\varepsilon^{18}_{\text{leaf}}$, similar to Eq. (S3.4).

S3.2 Comparison of MXL and TM5 implementations for leaf and soil exchange

S3.2.1 Introduction

The implementation of the exchange fluxes between the atmosphere and the land surface (biosphere and soils) in the 3-D model of *Koren et al.* (2019) is based on the equations described by *Hofmann et al.* (2017). The implementation of oxygen isotopes in the MXL model is described by *Vilà-Guerau de Arellano et al.* (2019) (for $\delta^{18}\text{O}$, the extension to $\Delta^{17}\text{O}$ in CO_2 is described in Sect. S3.1) and is based on *Lee et al.* (2009).

Here we show that the methods for leaf exchange are equivalent when the degree of equilibration is $\theta = 1$ (Sect. S3.2.2) and different when $\theta < 1$ (Sect. S3.2.3). More specifically, different values are assigned to the non-equilibrated CO_2 that resides in the leaf, which is an uncertain term, since this CO_2 can be a mixture of mitochondrial CO_2 and CO_2 that has diffused into the leaf from its surroundings (*Cernusak et al.*, 2004). Also, we show that the formulation in *Lee et al.* (2009) is consistent with the approach of *Gillon and Yakir* (2000) (Sect. S3.2.4).

Finally we consider the implementation of the soil-atmosphere exchange. In the MXL approach, soil invasion and respiration are integrated into a single equation that contains the soil resistance, soil concentration C_{soil} and atmospheric concentration C_a (similar to the leaf exchange). In the 3-D model formulation, these processes are considered separately, where kinetic fractionation is applied to respiration but not to soil invasion.

S3.2.2 *Hofmann et al.* (2017) formulation for $\theta = 1$

We start with the discrimination for $\delta^{18}O$ in CO_2 as given in Eq. (4.9) of *Hofmann et al.* (2017), where we use the symbol δ_{eq} for the isotopic composition of CO_2 that has equilibrated with water inside the leaf.

$$F_{\mathrm{A}} \cdot D_{\mathrm{A}} = (\alpha_{\mathrm{leaf}} - 1) \cdot (F_{\mathrm{AL}} + F_{\mathrm{LAnoneq}}) + [(\delta_{\mathrm{eq}} + 1) \cdot \alpha_{\mathrm{leaf}} - 1 - \delta_{\mathrm{a}}] \cdot F_{\mathrm{LAeq}} \tag{S3.9}$$

Note that the fractionation factor α_{leaf} in *Hofmann et al.* (2017) is smaller than 1 and we rewrite this in terms of a positive $\varepsilon_{\mathrm{leaf}}$ by inserting $\alpha_{\mathrm{leaf}} = 1 - \varepsilon_{\mathrm{leaf}}$, and subsequently we use the approximation $\delta_{\mathrm{eq}} \cdot \varepsilon_{\mathrm{leaf}} \approx 0$

$$F_{\mathrm{A}} \cdot D_{\mathrm{A}} = -\varepsilon_{\mathrm{leaf}} \cdot (F_{\mathrm{AL}} + F_{\mathrm{LAnoneq}}) + [\delta_{\mathrm{eq}} - \varepsilon_{\mathrm{leaf}} - \delta_{\mathrm{a}}] \cdot F_{\mathrm{LAeq}} \tag{S3.10}$$

First we consider the case of full equilibration (i.e. $\theta = 1$), which means that

$$F_{\mathrm{LAnoneq}} = 0 \tag{S3.11}$$

$$F_{\mathrm{LAeq}} = F_{\mathrm{LA}} \tag{S3.12}$$

In this case, we can rewrite Eq. (S3.10) as

$$F_{\mathrm{A}} \cdot D_{\mathrm{A}} = -\varepsilon_{\mathrm{leaf}} \cdot F_{\mathrm{AL}} + [\delta_{\mathrm{eq}} - \varepsilon_{\mathrm{leaf}} - \delta_{\mathrm{a}}] \cdot F_{\mathrm{LA}} \tag{S3.13}$$

The gross fluxes are related to the net assimilation flux as

$$F_{\mathrm{AL}} = \frac{C_{\mathrm{a}}}{C_{\mathrm{a}} - C_{\mathrm{i}}} F_{\mathrm{A}} \tag{S3.14}$$

$$F_{\mathrm{LA}} = -\frac{C_{\mathrm{i}}}{C_{\mathrm{a}} - C_{\mathrm{i}}} F_{\mathrm{A}} \tag{S3.15}$$

Note that we follow the atmospheric sign convention, meaning that positive values are increasing the atmospheric CO_2 mass. We can now rewrite Eq. (S3.13) as

$$\begin{aligned} F_{\mathrm{A}} \cdot D_{\mathrm{A}} &= F_{\mathrm{A}} \left[-\varepsilon_{\mathrm{leaf}} \left(\frac{C_{\mathrm{a}}}{C_{\mathrm{a}} - C_{\mathrm{i}}} \right) + [\delta_{\mathrm{eq}} - \varepsilon_{\mathrm{leaf}} - \delta_{\mathrm{a}}] \left(-\frac{C_{\mathrm{i}}}{C_{\mathrm{a}} - C_{\mathrm{i}}} \right) \right] \\ &= F_{\mathrm{A}} \left[\frac{C_{\mathrm{i}}}{C_{\mathrm{i}} - C_{\mathrm{a}}} (\delta_{\mathrm{eq}} - \delta_{\mathrm{a}}) - \varepsilon_{\mathrm{leaf}} \right] \end{aligned} \tag{S3.16}$$

This expression agrees with Eq. (13) in *Lee et al.* (2009), which describes the effect of vegetation on atmospheric $\delta^{18}O$ in CO_2 when the degree of equilibration $\theta = 1$.

S3.2.3 *Hofmann et al.* (2017) formulation for $\theta \leq 1$

Finally, we consider the more general case $\theta \leq 1$. The equilibrated and non-equilibrated leaf-atmosphere flux can then be calculated as

$$F_{\mathrm{LAnoneq}} = (1-\theta)\cdot F_{\mathrm{LA}} \tag{S3.17}$$

$$F_{\mathrm{LAeq}} = \theta \cdot F_{\mathrm{LA}} \tag{S3.18}$$

Inserting this in Eq. (S3.10) and replacing the gross leaf fluxes using Eqs. (S3.14) and (S3.15) gives

$$\begin{aligned} F_{\mathrm{A}} \cdot D_{\mathrm{A}} &= F_{\mathrm{A}} \left[-\varepsilon_{\mathrm{leaf}} \left(\frac{C_{\mathrm{a}}}{C_{\mathrm{a}} - C_{\mathrm{i}}} - (1-\theta)\cdot \frac{C_{\mathrm{i}}}{C_{\mathrm{a}} - C_{\mathrm{i}}} \right) + \left[\delta_{\mathrm{eq}} - \varepsilon_{\mathrm{leaf}} - \delta_{\mathrm{a}} \right] \left(-\frac{C_{\mathrm{i}}}{C_{\mathrm{a}} - C_{\mathrm{i}}} \right) \cdot \theta \right] \\ &= F_{\mathrm{A}} \left[\frac{C_{\mathrm{i}}}{C_{\mathrm{i}} - C_{\mathrm{a}}} (\delta_{\mathrm{eq}} - \delta_{\mathrm{a}}) \cdot \theta - \varepsilon_{\mathrm{leaf}} \right] \end{aligned} \tag{S3.19}$$

This expression does not agree with Eq. (21) in *Lee et al.* (2009) that describes the exchange between the atmosphere and biosphere for $\delta^{18}\mathrm{O}$ in $\mathrm{CO_2}$ when $\theta \leq 1$.

S3.2.4 *Gillon and Yakir* (2000) formulation

Now we follow the procedure of *Gillon and Yakir* (2000) to describe the exchange between the atmosphere and biosphere. The isotopic composition of non-equilibrated $\mathrm{CO_2}$ inside the leaf, that we denote by δ_{noneq}, can be calculated following *Farquhar et al.* (1982) considering only fractionation by diffusion (see also the comments below Eq. (4) in *Gillon and Yakir*, 2000)

$$\begin{aligned} \delta_{\mathrm{noneq}} &= \delta_{\mathrm{a}} - \varepsilon_{\mathrm{leaf}} + \varepsilon_{\mathrm{leaf}} \frac{C_{\mathrm{i}}}{C_{\mathrm{a}}} \\ &= \delta_{\mathrm{a}} + \varepsilon_{\mathrm{leaf}} \frac{C_{\mathrm{i}} - C_{\mathrm{a}}}{C_{\mathrm{a}}} \end{aligned} \tag{S3.20}$$

The signature of $\mathrm{CO_2}$ inside the leaf can be expressed as follows

$$\delta_{\mathrm{leaf}} = \theta \cdot \delta_{\mathrm{eq}} + (1-\theta)\cdot \delta_{\mathrm{noneq}} \tag{S3.21}$$

Similarly, for the atmospheric isotopic composition we have

$$\delta_{\mathrm{a}} = \theta \cdot \delta_{\mathrm{a}} + (1-\theta)\cdot \delta_{\mathrm{a}} \tag{S3.22}$$

Here we repeat Eq. (13) from *Lee et al.* (2009), with slightly modified notation

$$F_{\mathrm{A}} \cdot D_{\mathrm{A}} = F_{\mathrm{A}} \left[\frac{C_{\mathrm{i}}}{C_{\mathrm{i}} - C_{\mathrm{a}}} (\delta_{\mathrm{leaf}} - \delta_{\mathrm{a}}) - \varepsilon_{\mathrm{leaf}} \right] \tag{S3.23}$$

We can rewrite this using Eqs. (S3.21) and (S3.22)

$$\begin{aligned} F_A \cdot D_A &= F_A \left[\frac{C_i}{C_i - C_a} (\delta_{leaf} - \delta_a) - \varepsilon_{leaf} \right] \\ &= F_A \left[\frac{C_i}{C_i - C_a} (\theta \cdot \delta_{eq} + (1-\theta) \cdot \delta_{noneq} - \theta \cdot \delta_a - (1-\theta) \cdot \delta_a) - \varepsilon_{leaf} \right] \\ &= F_A \left[\frac{C_i}{C_i - C_a} (\theta \cdot (\delta_{eq} - \delta_a) + (1-\theta) \cdot (\delta_{noneq} - \delta_a)) - \varepsilon_{leaf} \right] \end{aligned} \tag{S3.24}$$

We will now further expand the 'non-equilibrated' term, using Eq. (S3.20)

$$\begin{aligned} \frac{C_i}{C_i - C_a} ((1-\theta) \cdot (\delta_{noneq} - \delta_a)) &= (1-\theta) \cdot \left(\delta_a + \varepsilon_{leaf} \frac{C_i - C_a}{C_a} - \delta_a \right) \frac{C_i}{C_i - C_a} \\ &= (1-\theta) \cdot \left(\varepsilon_{leaf} \frac{C_i - C_a}{C_a} \right) \frac{C_i}{C_i - C_a} \\ &= (1-\theta) \cdot \varepsilon_{leaf} \frac{C_i}{C_a} \end{aligned} \tag{S3.25}$$

Inserting this expression back into Eq. (S3.24) results in

$$F_A \cdot D_A = F_A \left[\frac{C_i}{C_i - C_a} (\delta_{eq} - \delta_a) \cdot \theta + (1-\theta) \cdot \varepsilon_{leaf} \frac{C_i}{C_a} - \varepsilon_{leaf} \right] \tag{S3.26}$$

This last expression agrees with Eq. (21) in *Lee et al.* (2009). When we compare this with Eq. (S3.19) we see that there is one additional term in the expression from *Lee et al.* (2009) that is missing in the approach from *Hofmann et al.* (2017).

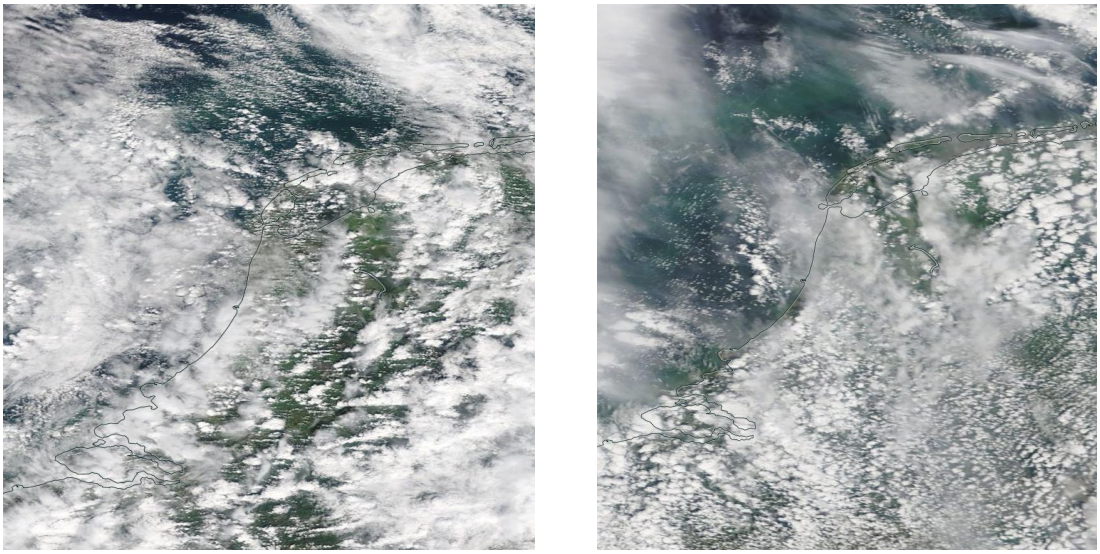

(a) **(b)**

Figure S3.1: Cloud cover as observed from MODIS for (a) August 15 and (b) August 16 of 2019 over the Netherlands. The thin black line indicates the coastline. Clearly there was substantial cloud coverage over the Netherlands for these days.

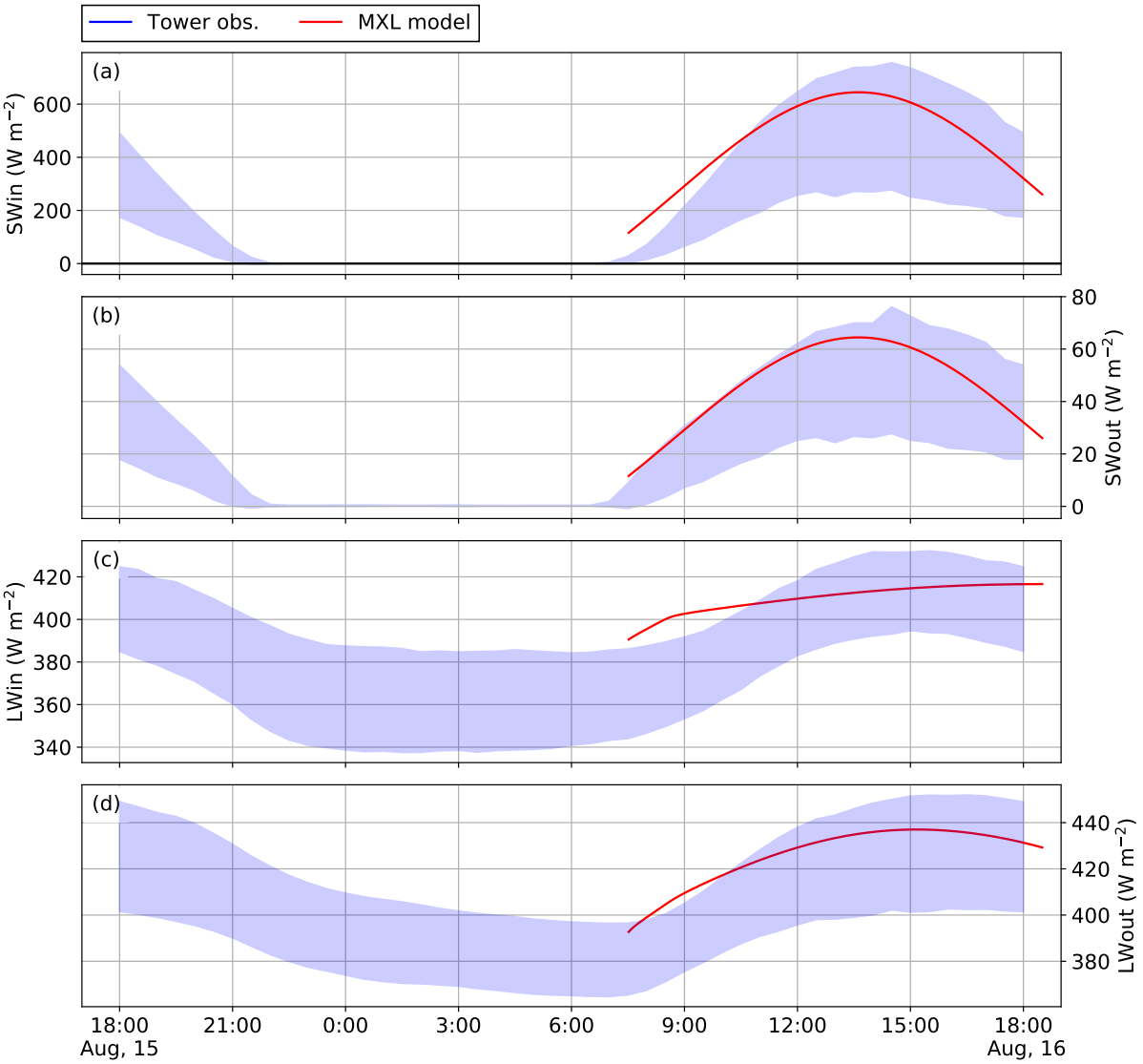

Figure S3.2: Radiation fluxes (a) shortwave incoming radiation; (b) shortwave outgoing radiation; (c) longwave incoming radiation; and (d) longwave outgoing radiation as observed at the Loobos site for August for the years 2013-2017 (the shading represents the standard deviation around the mean) and as simulated in the MXL mixed layer model. Time is specified in local time (UTC+2).

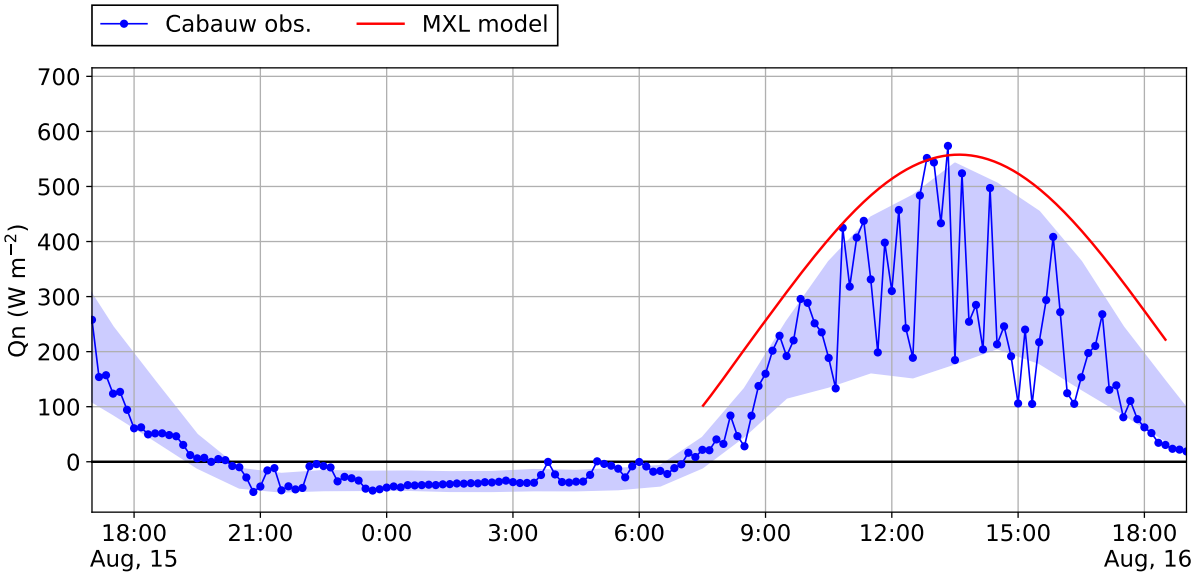

Figure S3.3: Net radiation as observed at the KNMI Cabauw site for August 15-16, 2019 (the shading represents the standard deviation around the mean for August 2019) and as simulated in the MXL mixed layer model. Time is specified in local time (UTC+2).

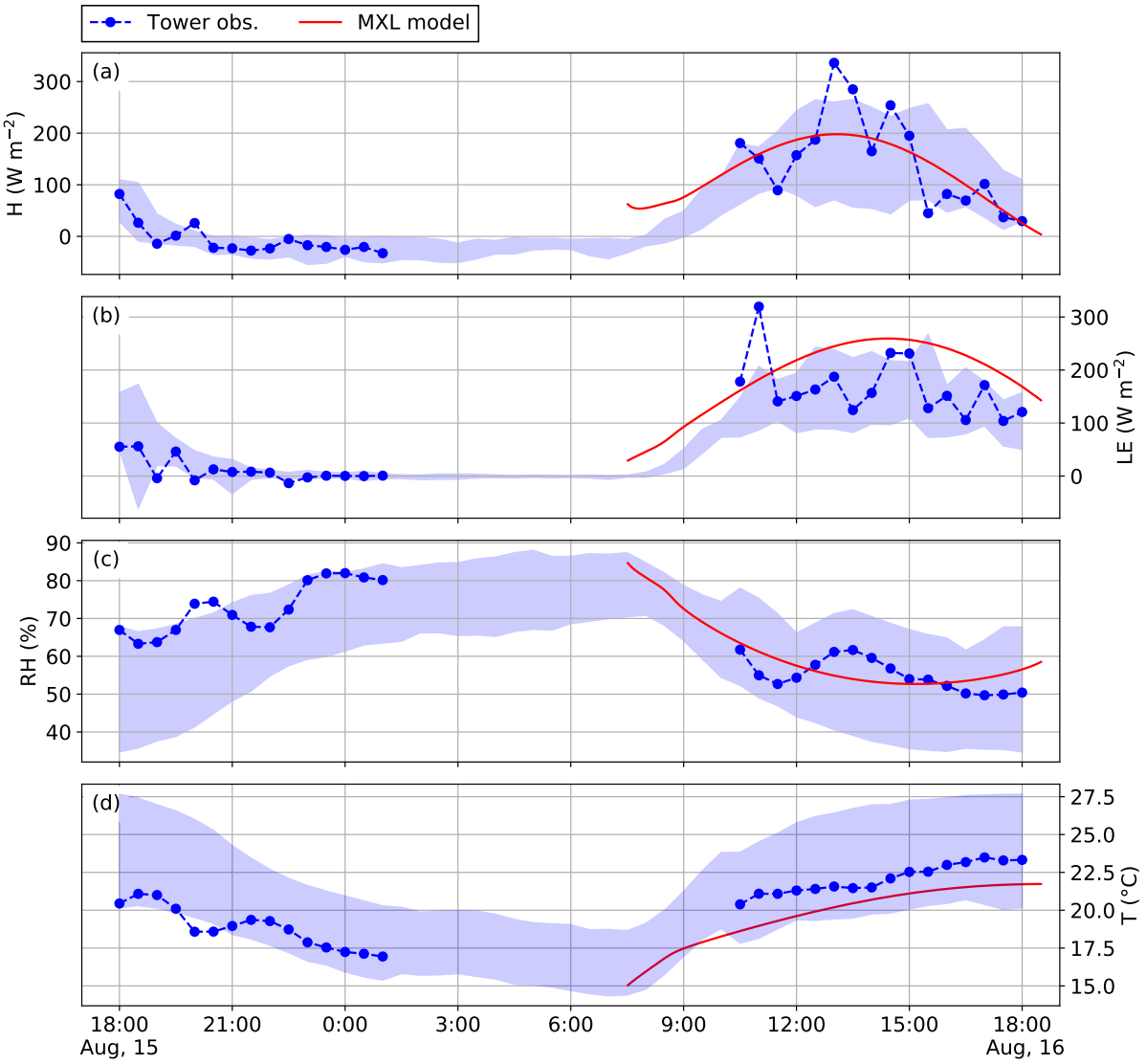

Figure S3.4: Meteorological variables (a) sensible heat; (b) latent heat; (c) relative humidity; and (d) temperature as observed at the Loobos site for August 15-16, 2019 (the shading indicates the standard deviation around the mean of the observations for August 2019), and as simulated in the MXL mixed layer model. Time is specified in local time (UTC+2).

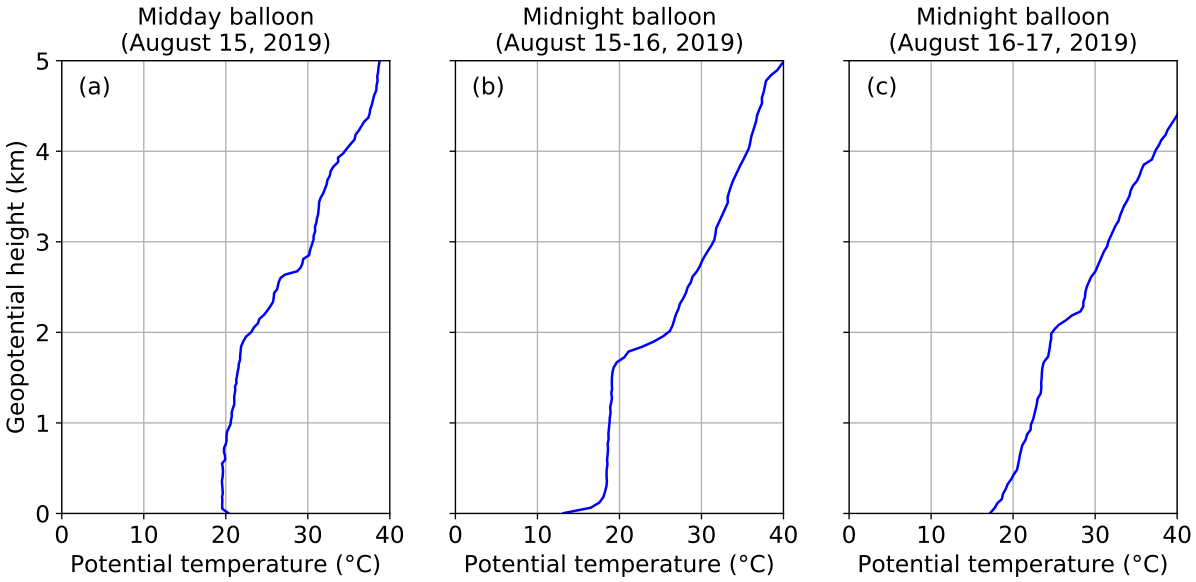

Figure S3.5: Potential temperature profiles measured by weather balloons launched from De Bilt by KNMI, for (a) midday balloon August 15, 2019; (b) midnight balloon for August 15–16, 2019; and (c) midnight balloon for August 16–17, 2019.

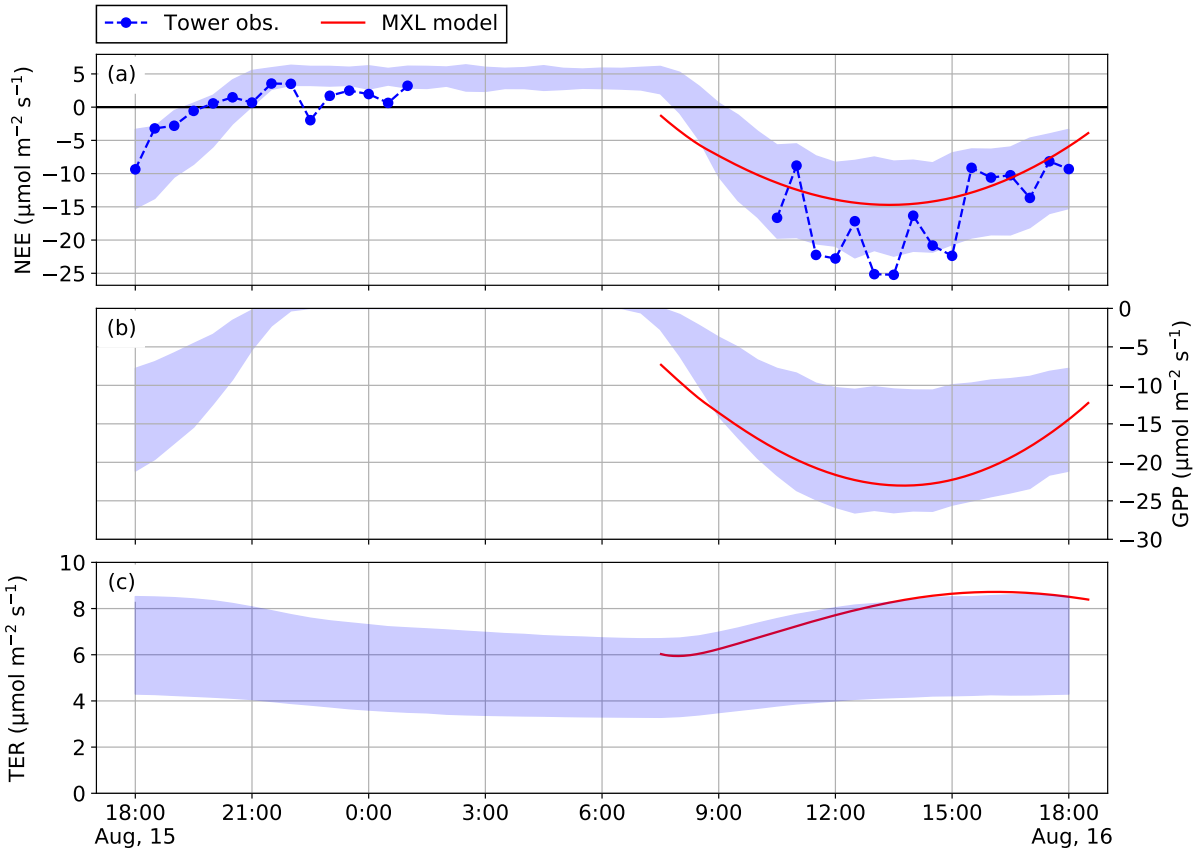

Figure S3.6: Temporal variation of (a) net ecosystem exchange (NEE); (b) gross primary production (GPP); and (c) terrestrial ecosystem respiration (TER) as observed at the Loobos site (the shading represents the standard deviation around the mean for August for the years 2013-2017; for NEE we also included the observations from August 15-16, 2019) and as simulated in the MXL mixed layer model. The processing of CO_2 fluxes was based on variable u-star filtering and day-time partitioning (*Lasslop et al.*, 2010). Time is specified in local time (UTC+2).

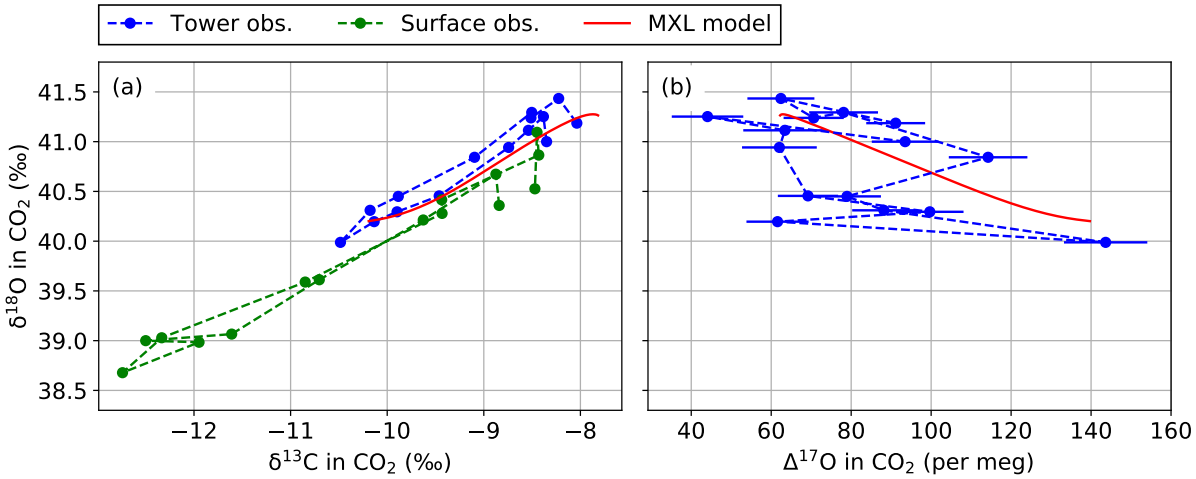

Figure S3.7: Correlations for (a) δ^{18}O versus δ^{13}C; and (b) δ^{18}O versus Δ^{17}O for the samples collected at the Loobos site on August 15 and 16, 2019, and as simulated by the MXL model.

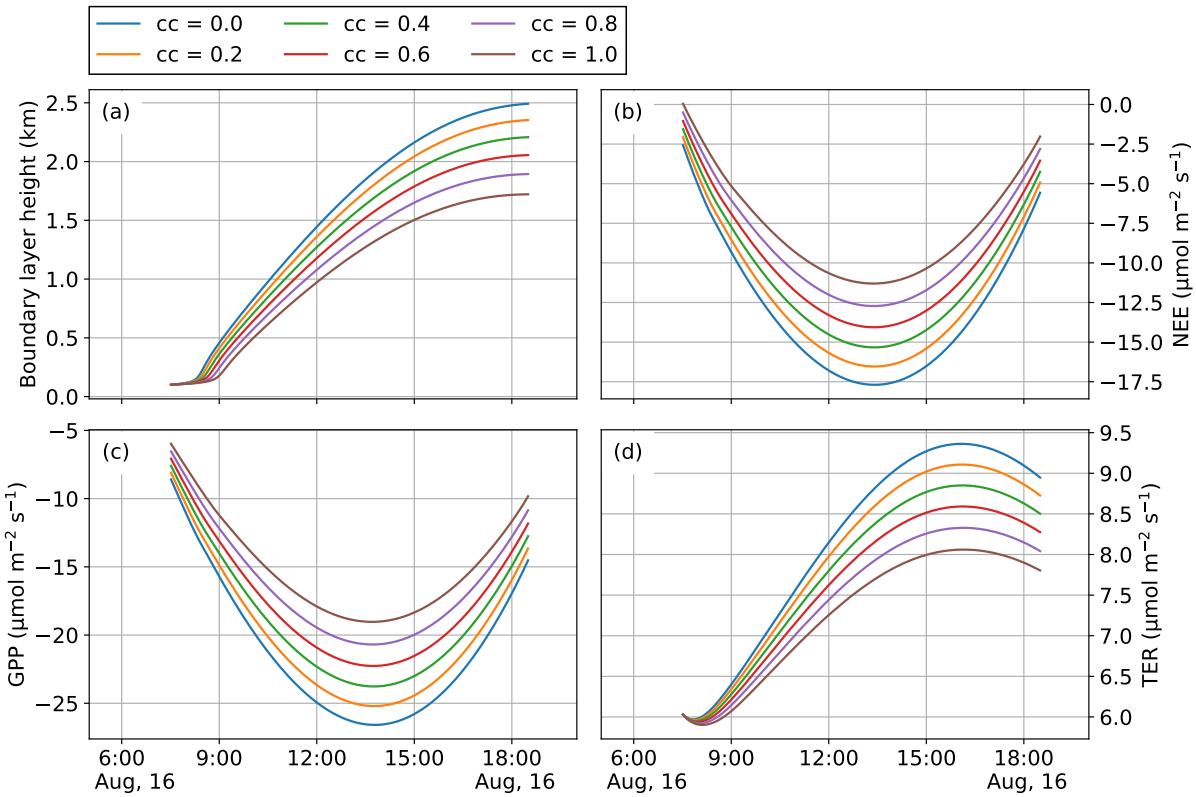

Figure S3.8: Sensitivity results for cloud cover 'cc' ranging from 0 to 1 for (a) boundary layer height; (b) net ecosystem exchange (NEE); (c) gross primary production (GPP); and (d) terrestrial ecosystem respiration (TER) as simulated by the MXL model. Time is specified in local time (UTC+2).

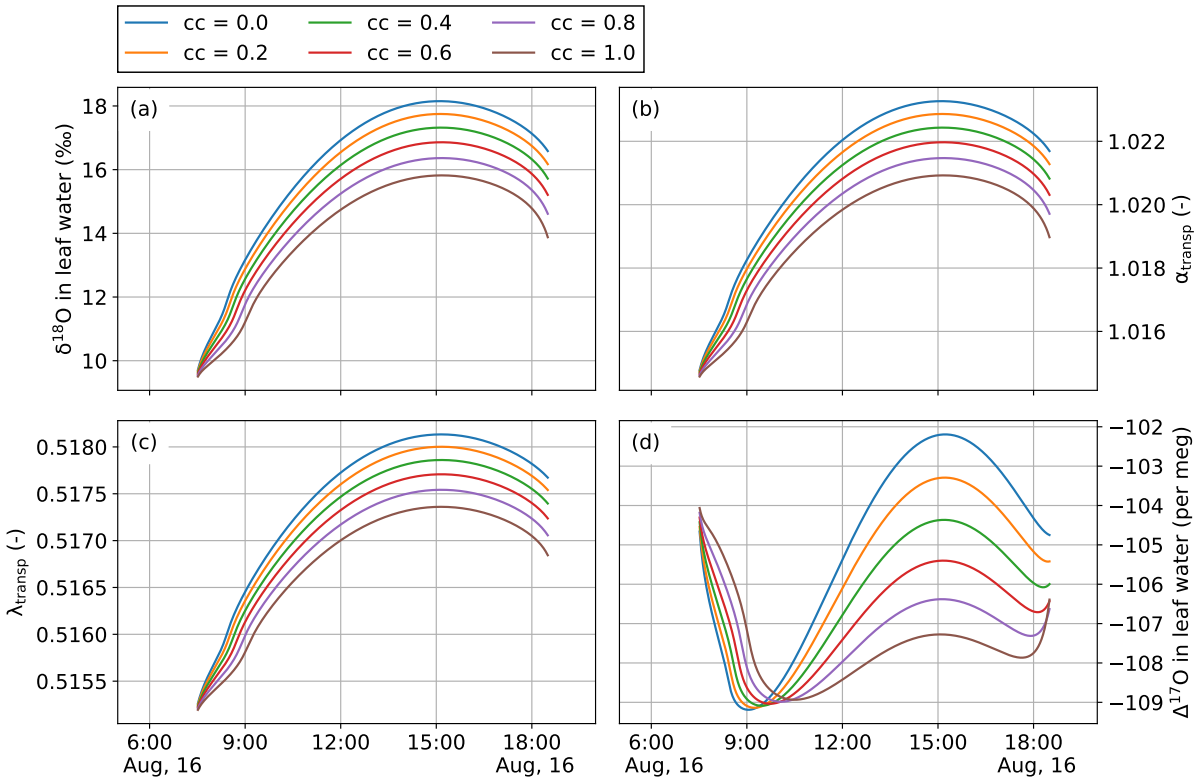

Figure S3.9: Sensitivity results for cloud cover 'cc' ranging from 0 to 1 for (a) $\delta^{18}O$ in leaf water; (b) fraction factor α_{transp}; (c) triple oxygen isotope coefficient λ_{transp}; and (d) $\Delta^{17}O$ of leaf water as simulated by the MXL model. Time is specified in local time (UTC+2).

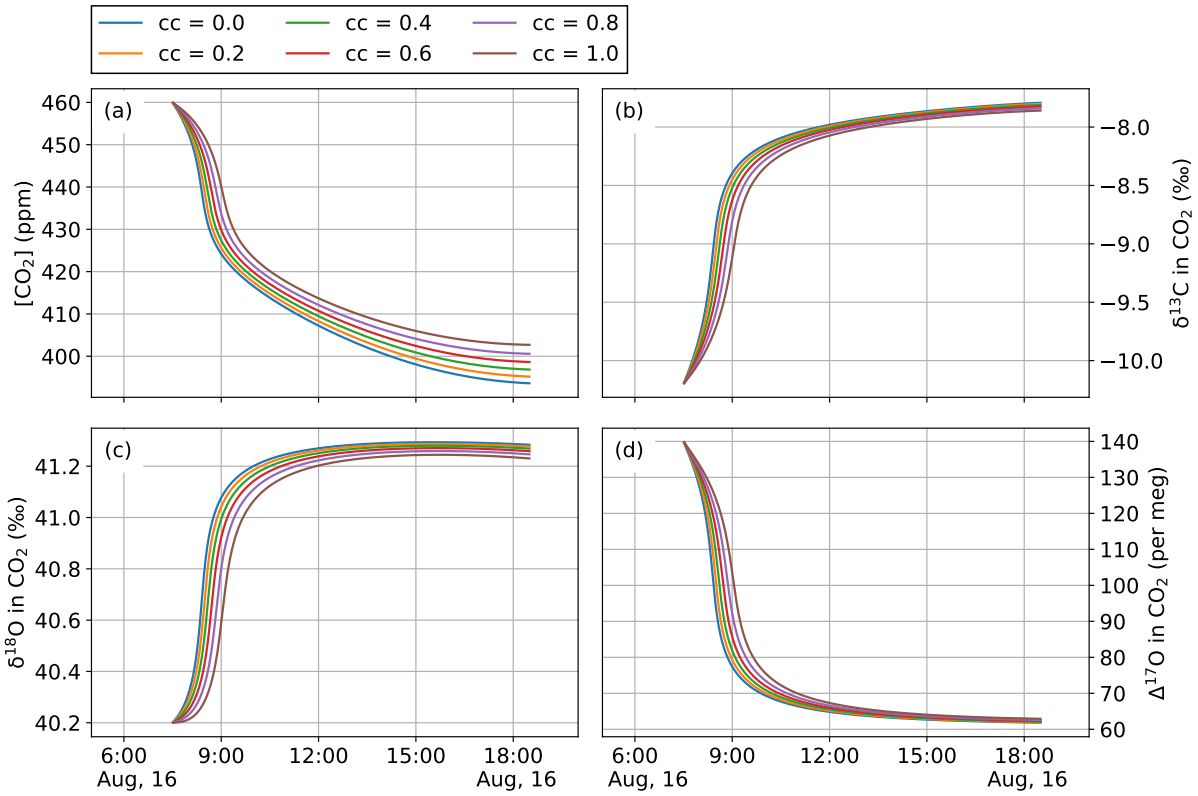

Figure S3.10: Sensitivity results for cloud cover 'cc' ranging from 0 to 1 for (a) $[CO_2]$; (b) $\delta^{13}C$ in CO_2; (c) $\delta^{18}O$ in CO_2; and (d) $\Delta^{17}O$ in CO_2 as simulated by the MXL model. Time is specified in local time (UTC+2).

Table S3.1: Summary of measurements for air samples collected from the top of the Loobos tower on August 15, 2019 (flasks T1–T4) and air samples collected on August 16, 2019 (flasks T5–T15). $\delta^{13}C$ is reported relative to VPDB, while $\delta^{17}O$ and $\delta^{18}O$ are reported relative to VSMOW. We included the individual $\delta^{17}O$ and $\delta^{18}O$ values to allow re-calculation of $\Delta^{17}O$ relative to a different reference line. 'SE' is the standard error.

Sample	Time	$\delta^{13}C$ (‰)		$\delta^{17}O$ (‰)		$\delta^{18}O$ (‰)		$\Delta^{17}O$ (per meg)	
		mean	SE	mean	SE	mean	SE	mean	SE
T1	17:54	-8.35	0.001	21.32883	0.008517	41	0.002	93.497	8.34
T2	19:19	-8.383	0.002	21.40762	0.009134	41.252	0.005	44.074	8.943
T3	20:09	-8.538	0.001	21.35661	0.010637	41.114	0.005	63.428	10.415
T4	22:05	-8.743	0.002	21.26696	0.009546	40.942	0.005	62.052	9.348
T5	0:10	-9.462	0.001	21.02439	0.007696	40.455	0.006	69.2	7.537
T6	3:11	-9.898	0.002	20.97339	0.008615	40.295	0.004	99.665	8.439
T7	5:53	-10.135	0.002	20.88371	0.007933	40.196	0.004	61.581	7.771
T8	6:29	-10.484	0.002	20.86073	0.010639	39.988	0.004	143.645	10.422
T9	7:35	-10.177	0.002	20.96937	0.008096	40.31	0.004	88.188	7.93
T10	8:37	-9.885	0.002	21.03179	0.008666	40.45	0.006	78.959	8.488
T11	9:52	-9.096	0.001	21.26948	0.010036	40.843	0.004	114.248	9.827
T12	10:59	-8.504	0.002	21.46393	0.008793	41.294	0.006	78.104	8.609
T13	12:57	-8.512	0.001	21.42807	0.007685	41.239	0.004	70.623	7.524
T14	14:49	-8.225	0.002	21.51972	0.00856	41.434	0.005	62.425	8.38
T15	16:58	-8.037	0.002	21.42184	0.007.523	41.186	0.007	91.135	7.365

Table S3.2: Summary of measurements for air samples collected ∼0.5 m above the surface for the Loobos tower site on August 15, 2019 (flasks S1–S4) and air samples collected on August 16, 2019 (flasks S5–S15). δ^{13}C is reported relative to VPDB, while δ^{18}O is reported relative to VSMOW.

Sample	Time	CO_2 (ppm)	δ^{13}C (‰)	δ^{18}O (‰)
S1	18:23	404.908994	-8.841	40.359
S2	19:33	405.960245	-8.875	40.673
S3	20:25	423.716192	-9.627	40.213
S4	22:23	451.017034	-10.703	39.612
S5	0:27	478.263256	-11.61	39.066
S6	3:28	498.302507	-12.5	39
S7	6:08	488.048412	-11.948	38.984
S8	6:47	516.115701	-12.74	38.678
S9	7:55	507.161296	-12.334	39.029
S10	8:54	467.582372	-10.849	39.589
S11	10:10	425.718246	-9.432	40.279
S12	11:15	422.444847	-9.436	40.416
S13	13:20	404.415484	-8.431	40.865
S14	15:06	396.78692	-8.449	41.094
S15	17:27	396.807871	-8.471	40.526

Table S3.3: Overview of model settings for the MXL simulations. For the tracer abundances, the subscripts '0' and 'FT' refers to the initial value in the atmospheric boundary layer and the free troposphere, respectively. The lapse rate is denoted by γ and is only stated for tracers that have a non-zero lapse rate. For all variables that are not listed here, we used the same values as were used for Harvard Forest by *Vilà-Guerau de Arellano et al.* (2019).

Variable	Symbol	Value
Meteorological variables		
Day of year	day	228
Latitude	lat	52.17°
Longitude	lon	5.74°
Cloud cover	cc	0.5
Init. air temperature	T_0	288.15 K
Soil temperature	T_{soil}	288.15 K
Tracer abundances		
Carbon dioxide	$[CO_2]_0$	460 ppm
	$[CO_2]_{FT}$	420 ppm
	γ_{CO_2}	-20 ppm/km
^{13}C in CO_2	$\delta^{13}C_0$	-10.2 ‰ VPDB
	$\delta^{13}C_{FT}$	-8.0 ‰ VPDB
^{18}O in CO_2	$\delta^{18}O_0$	40.2 ‰ VSMOW
	$\delta^{18}O_{FT}$	41.4 ‰ VSMOW
^{17}O-excess in CO_2	$\Delta^{17}O_0$	140 per meg
	$\Delta^{17}O_{FT}$	60 per meg
Specific humidity	q_0	9.0 g/kg
	q_{FT}	8.9 g/kg
	γ_q	-1.8 g/kg/km
^{18}O in water vapor	$\delta^{18}O_{w,0}$	-5.0 ‰ VSMOW
	$\delta^{18}O_{w,FT}$	-5.0 ‰ VSMOW

4

Widespread reduction in sun-induced fluorescence from the Amazon during the 2015/2016 El Niño

The tropical carbon balance dominates year-to-year variations in CO_2 exchange with the atmosphere through photosynthesis, respiration, and fires. Because of its high correlation with gross primary productivity (GPP), observations of sun-induced fluorescence (SIF) are of great interest. We developed a new remotely-sensed SIF product with improved signal-to-noise in the tropics, and use it here to quantify the impact of the 2015/2016 El Niño Amazon drought. We find that SIF was strongly suppressed over areas with anomalously high temperatures and decreased levels of water in the soil. SIF went below its climatological range starting from the end of the 2015 dry season (October) and returned

This chapter is published as: Koren, G., van Schaik, E., Araújo, A.C., Boersma, K.F., Gärtner, A., Killaars, L., Kooreman, M.L., Kruijt, B., van der Laan-Luijkx, I.T., von Randow, C., Smith, N.E. and Peters, W. (2018). Widespread reduction in sun-induced fluorescence from the Amazon during the 2015/2016 El Niño. Phil. Trans. R. Soc. B, 373. https://doi.org/10.1098/rstb.2017.0408.

to normal levels by February 2016 when atmospheric conditions returned to normal, but well before the end of anomalously low precipitation which persisted through June 2016. Impacts were not uniform across the Amazon basin, with the eastern part experiencing much larger (10-15%) SIF reductions than the western part of the basin (2-5%). We estimate the integrated loss of GPP relative to eight previous years to be 0.34–0.48 PgC in the 3-month period Oct-Nov-Dec 2015.

4.1 Introduction

Variations in the annual atmospheric increase of CO_2 in the atmosphere (the so-called growth rate of CO_2) are dominated by carbon exchange in the tropical regions (*Bacastow*, 1976; *Keeling and Revelle*, 1985; *Rayner et al.*, 1999; *Welp et al.*, 2011; *Liu et al.*, 2017). Measurements of ^{13}C in CO_2 in the atmosphere show unequivocally that the terrestrial biosphere is the main driver of such variability (*Townsend et al.*, 2002). The CO_2 growth rate variations in turn correlate strongly with tropical temperature and precipitation anomalies (*Fang et al.*, 2017). Years with higher than average temperatures and lower than average precipitation over tropical land areas have led to the highest annual increases of atmospheric CO_2 in the record. This was used by *Cox et al.* (2013) to calculate a climate sensitivity for tropical net ecosystem exchange (NEE), which can tentatively inform us on climate impacts over longer time scales, if the controlling mechanisms turn out to be the same.

Droughts play a central role in this mechanism, and the peak CO_2 growth rates of 1983, 1997/1998, 2005, 2010, and 2015/2016 can all be traced back to the impact of excessive heat or lack of precipitation in the tropics. The effect of the 2010 drought on the Amazon net carbon balance was quantified using inverse modelling of vertical profiles of atmospheric CO_2 and CO collected from aircraft over the Amazon forest (*Gatti et al.*, 2014; *van der Laan-Luijkx et al.*, 2015; *Alden et al.*, 2016). All three studies found that during the dry year 2010, the Amazon rainforest was near neutral in its net CO_2 exchange with the atmosphere in contrast to its functioning as a net carbon sink in 2011. Increased fires contributed substantially (0.1-0.3 PgC) to the anomalous annual CO_2 budget, but reduced biospheric uptake ($\sim$0.25 PgC) also played a significant role. An analysis by *Bowman et al.* (2017) based on an inverse analysis of remotely sensed data agreed with the increased fire emissions, but suggested that equal increases in GPP and respiration during 2010 left net ecosystem productivity unchanged.

An opportunity to study the effect of droughts on GPP is presented by sun-induced fluorescence (SIF), which is the re-emission of light by the chloroplast during photosynthesis. SIF can be retrieved from space-based remote sensing instruments aboard, for example, SCIAMACHY (*Joiner et al.*, 2012; *Köhler et al.*, 2015), MetOp (*Joiner et al.*, 2013, 2016; *Köhler et al.*, 2015; *Sanders et al.*, 2016), GOSAT (*Frankenberg et al.*, 2011; *Joiner et al.*, 2011, 2012; *Parazoo et al.*, 2013), OCO-2 (*Frankenberg et al.*, 2014) and Sentinel-5P (*Guanter et al.*, 2015). A fraction of the light detected by satellite instruments at the top-of-atmosphere around 740 nm originates directly from photosynthesis within vegetation foliage at the surface, and therefore is one of the most direct observations of primary productivity. Many studies have recently demonstrated the similarity between spatiotemporal patterns of SIF and of GPP (*Frankenberg et al.*, 2011; *Guanter et al.*, 2014; *Parazoo et al.*, 2014; *Zhang et al.*, 2014; *Sanders et al.*, 2016), but there are just a few studies of SIF during tropical droughts.

In their 2013 study of the Amazon basin, *Lee et al.* (2013) describe the seasonal cycle of SIF as retrieved from GOSAT, and link it to the seasonal cycle of precipitation and vapour pressure deficits as observed during the 2010 drought. The strongest response comes from vegetation in the eastern part of the basin, which experiences seasonal droughts (precipitation <100 mm/month). SIF reductions over evergreen rainforests in the western part of the basin were difficult to distinguish in the short time series (Jan 2009 through Dec 2010). Integrated over the full basin, SIF reduced by close to 15% in 2010 relative to their 2009 values though, suggesting a large impact of the 2010 drought on GPP. *Bowman et al.* (2017) used GOSAT SIF in an inverse system to constrain GPP separately from NEE and respiration, and suggested a reduction of GPP during the 2010 drought of 0.31 $\pm$ 0.20 PgC relative to 2011. *Alden et al.* (2016) supported this finding, and attempted to qualitatively link SIF to the inversely derived seasonal cycle of net carbon uptake by vegetation.

More recently, *Liu et al.* (2017) also used GOSAT SIF in one of the first quantifications of the 2015/2016 El Niño impact on the tropical carbon balance. These authors came to the conclusion that the atmospheric CO_2 increase was at least partially driven by a suppression of GPP in the Amazon region, but also by an increase of respiration over tropical Africa and an increase of tropical biomass burning over tropical Asia (also see *Nechita-Banda et al.*, 2018).

Finally, *Yang et al.* (2018a) report a reduction of 8.2% in NASA-retrieved GOME-2 SIF (*Joiner et al.*, 2013) during the 2015/2016 drought for the Amazon region. This coincided with an overall greening up of the Amazon region, which these authors tentatively ascribe

to increased light availability. The GOME-2 retrieval product used in their study is not particularly developed for high water vapour environments (*van Schaik*, 2016) and is subject to very high noise in the tropics, which translates into the lack of any clear spatial patterns in SIF over the Amazon in their analyses. Also, the degrading signal of GOME-2 SIF over recent years was not accounted for in this analysis, likely leading to incorrect conclusions on the 2015/2016 El Niño induced anomaly (*Zhang et al.*, 2018). In a recent analysis of the drought response of tropical vegetation (*Giardina et al.*, 2018) this degradation played less of a role as many years of NASA-retrieved GOME-2 SIF were averaged to find a lack of GPP/SIF variations in response to precipitation variations in tall tropical trees with deep roots in the wettest part of the Amazon basin.

Here, we present an analysis of the impact of the 2015/2016 El Niño on sun-induced fluorescence from an update to the retrieval product called SIFTER (*Sanders et al.*, 2016). Full details of this updated product (called SIFTER v2) are described by *van Schaik* (2016), while our main focus here is a first analysis of the response of fluorescence to drought over the Amazon forest. SIFTER v2 is retrieved from GOME-2A, but compared to the product used in *Yang et al.* (2018a) it has the advantage of specifically accounting for substantial water vapour absorption signatures imprinted in the satellite spectra over the hot and humid Amazonian atmosphere. Relative to GOSAT SIF, the SIFTER product has a larger spatial footprint (80×40 km^2 over most of the record) but achieves global coverage within one day, leading to many more valid retrievals over the cloudy tropical regions. Finally, GOME-2A spectra are available from 2007 onwards, providing us with a much longer background period (2007-2014) to contrast anomalies to than those obtainable from GOME-2B, OCO-2 or GOSAT. This allows us to very sharply define the observed seasonal cycles of SIF over the Amazon, as well as their anomalies during the recent El Niño.

4.2 Methods

4.2.1 SIFTER fluorescence

The level 3 (i.e. geospatial gridded data) SIFTER dataset has a temporal coverage from 2007 to 2017 for GOME-2A and from 2013 to 2017 for GOME-2B at a daily time resolution. It should be noted that the quality of the GOME-2A data decreases over time due to sensor degradation, while in June 2015 a change was made by ESA to the GOME-2B level-0 data that, for SIFTER, translates into less reliable retrievals past that moment.

In this work we use GOME-2A radiances and a slightly updated version of the SIFTER v2 retrieval algorithm, aimed at stabilizing the retrieval against ongoing degradation of the sensor. The resulting custom SIF dataset is made available along with this publication. Note that gathered spectra from South America are also unavoidably subject to larger measurement errors caused by the increased levels of highly energetic particles in this region, known as the South Atlantic Anomaly. The spatial resolution of the level 3 SIFTER product is 0.5°×0.5°.

The GOME-2A SIF signals exhibit a negative trend of -1%/yr due to instrument degradation as carefully documented in *Zhang et al.* (2018). This trend is easily visible in SIF over the Amazon region (see Fig. 4.2) with larger impacts on the latter part of the record. To remove this trend from the SIF signal and properly account for the 2015/2016 El Niño impact, we applied three different detrending methods over the full period (2007-2016): (1) using a first order polynomial (i.e., linear) to fit the trend, (2) using a second order polynomial (i.e, quadratic), and (3) using a curve fitting procedure based on *Thoning et al.* (1989), also known as CCGCRV. The latter is used widely for time series analysis in the field of atmospheric CO_2 studies, and fits a time series by a combination of a second order polynomial and four harmonics of different amplitude and phase after filtering the time series for short-term variations, in the frequency domain. A fourth method using principle component analysis was attempted, but found less effective in separating anomalies from the regular seasonal cycle. Method (1) was also tried as 12 separate fits for each calendar month, but this yielded very similar results to (1) suggesting that the negative SIF trend has minimal seasonal differences. *Zhang et al.* (2018) came to a similar conclusion for spatial differences in the downward trend.

In this work, we base our figures on the linear detrending from method 1 because it is effective, simple, transparent and easily reproducible for others. In the quantification of the anomalies in the text and tables we include the range of anomalies based on all three detrending methods, with their differences in estimated GPP reductions not exceeding 0.1 PgC over the periods analysed. Note that despite the detrending of the SIF signal over the Amazon region, the SIF from mid-2016 onwards shows a more rapid decline that persists in 2017 (not shown). We discuss the impact of this in the Discussion, and emphasize that our detrending method might not be suitable for every possible application of the SIFTER product.

Additional datasets used in our analysis are described in more detail in Sect. S4.3. This includes the MPI-BGC GPP product from *Beer et al.* (2010), GRACE terrestrial water storage (*Watkins et al.*, 2015), and the precipitation data set MSWEP (*Beck et al.*, 2017a).

4.2.2 Spatial analysis

Spatial averaging is based on the mask of the legal Amazon (`https://doi.org/10.18160/P1HW-0PJ6`). This mask was also used in the papers of *Gatti et al.* (2014) and *van der Laan-Luijkx et al.* (2015) to aggregate results, and ensures consistency between the comparisons. The border of this legal Amazon mask is indicated by the green contour in Fig. 4.3.

For the subregions we rely on Köppen-Geiger (KG) based definitions of climate zones, which take into account precipitation, temperature, and vegetation gradients (*Kottek et al.*, 2006). This leads to the recognition of three dominant regions within the Amazon basin: Region A (KG-code: Af) with evergreen forest that receive continuously high precipitation (> 100 mm/month precipitation); Region B (KG-code: Am) with evergreen forest that is seasonally dry (< 100 mm/month precipitation); and Region C (KG-code: Aw/As) with a very strong seasonality in precipitation and containing savannah-like vegetation, i.e., the Brazilian 'Cerrado'. The location of the subregions is shown in the insets in Fig. 4.4. Note that these definitions are similar to, but not the same as, those used in *Lee et al.* (2013), since they had to focus specifically on small rectangular areas that contained sufficient retrievals. With its much higher coverage, SIFTER attains enough retrievals per 0.5°×0.5° grid box (see Fig. S4.1) to allow integration over the climate regions chosen.

The conversion of SIF to GPP is done by fitting a slope+intercept to all annual mean SIFTER / GPP pairs within a region (A, B, C), and applying these fits to all monthly SIF values inside the region. Alternatively, we made the same fits but based on separating points by plant-functional type (tropical, savannah/shrubs, other), and by fitting to the annual mean GPP from SiBCASA (*van Schaik et al.*, 2018) instead of from *Beer et al.* (2010). The different slopes and intercepts attained are presented in Table S4.2 and the differences over the three fitting methods is propagated into the range of GPP values quoted in this work. This approach acknowledges that the SIF-GPP relationship can be climate or vegetation dependent (*Parazoo et al.*, 2014).

4.3 Results

The high resolution of our SIF product presents the most detailed view of photosynthetic activity over the Amazon so far. Fig. 4.1 shows the spatial gradients of SIF averaged over

2007-2016 compared to GPP from *Beer et al.* (2010), which is partly based on surface NEE observations, partly on remote sensing, and partly on a vegetation-specific relation of GPP to various drivers. The high correlation between GPP and SIF is immediately obvious when looking at the spatial patterns in Fig. 4.1. The correlation coefficient for SIF and GPP for all land area shown in Fig. 4.1 is $r = 0.88$ ($r = 0.80$ for cells within the Amazon region). Both large-scale gradients across the basin as well as smaller scale gradients such as the forest-savannah transition in central Brazil are captured by SIF. Importantly, we note that in contrast to the GPP product, SIF retrievals have no information on vegetation properties nor distributions, and thus form a fully independent view of the productivity of this region.

The SIFTER product can also capture the seasonal cycle of GPP as measured from the eddy-covariance tower at K34 (*Araújo et al.*, 2002), near Manaus (2.6°S, 60.2°W). Fig. 4.1c shows this data averaged over the period 2000-2010, together with the mean seasonal cycle of the detrended SIFTER product for the period 2007-2016 for an aggregated 1.5°×1.5° cell containing the location of the K34 tower. During JJA, the incoming short wave radiation increases but GPP decreases likely due to a reduced photosynthetic capacity of fresh leaves (*Restrepo-Coupe et al.*, 2013; *Jones et al.*, 2014). This is followed by an increase in GPP during Sep-Oct when leaf photosynthetic capacity has increased again, a feature missed by most biosphere models that only consider light- and temperature limitations on GPP (*Restrepo-Coupe et al.*, 2017). Both the initial GPP decrease and its increase in the late dry season at K34 are well captured by the remotely sensed SIFTER product (correlation coefficient $r = 0.81$). The good spatial and temporal correspondence between SIFTER and GPP for the Amazon basin, as demonstrated in Fig. 4.1, further motivates the use of SIFTER for analysing the impact of the 2015/2016 El Niño event on the carbon uptake by the Amazon rainforest.

Fig. 4.2 shows the temporal evolution from 2007 through mid-2016 of SIF from the legal Amazon (its extent is indicated in Fig. 4.3), which follows a substantial seasonal cycle that ranges over nearly 40% of the long-term average value (1.2 $\mathrm{mW{\cdot}sr^{-1}{\cdot}m^{-2}{\cdot}nm^{-1}}$). SIF maxima occur during the wet season and minima during the early dry season seen also by *Lee et al.* (2013) and *Restrepo-Coupe et al.* (2013). The long-term decrease of the raw SIF signal starts around 2013, and shows a negative trend that is caused by the functioning of the instrument and the processing of the data. We refer to Sect. S4.1 for an overview of its possible causes. A sharp decline of SIF is visible too at the end of the record (2016-06) and persists into 2017 (not shown), which renders analysis of post-2016 impossible for now. Despite this, the climatological seasonal cycle, the anomalous dry season SIF in JJA of 2010, and the anomalous early wet season SIF in OND of 2015 are distinguishable,

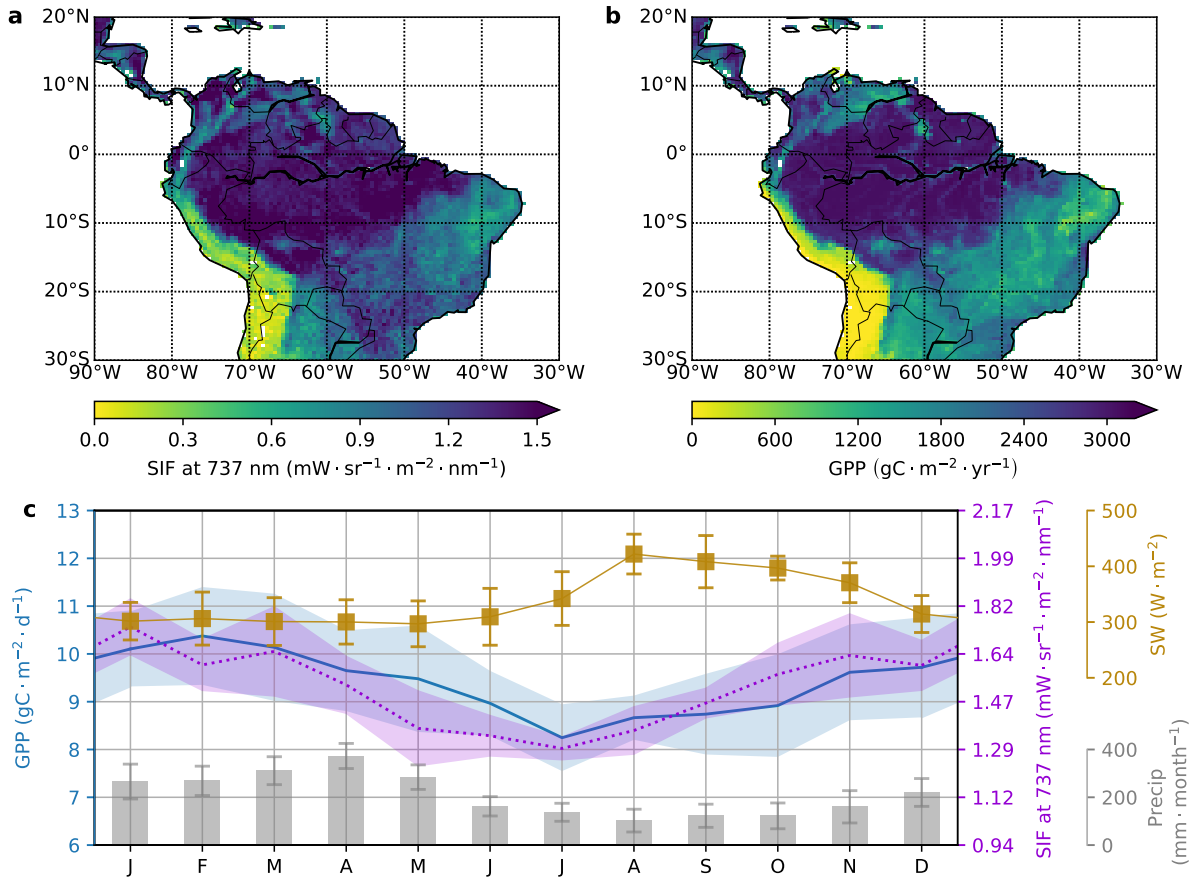

Figure 4.1: Spatio-temporal distributions of SIFTER fluorescence and observation based estimates of gross primary productivity for the Amazon region and K43 tower. **(a)** Detrended SIFTER signal averaged over 2007-2016 at 0.5°×0.5° resolution. **(b)** Annual mean MPI-BGC gross primary productivity at 0.5°×0.5° resolution. **(c)** Seasonal cycle of GPP measured at the eddy-covariance tower K34, near Manaus (2.6°S, 60.2°W) averaged over the period 2000-2010. Also shown is the SIFTER product for an aggregated 1.5°×1.5° cell containing the location of the K34 tower. In addition, the seasonal cycles of the observed precipitation and short wave radiation at the K34 tower are included. The standard deviation of the monthly variables is indicated by either shading or error bars.

and we attribute this to actually reduced SIF by vegetation. Here, we analyse the latter anomaly further starting from a whole-basin perspective, and then zooming in on regional differences.

Precipitation, SIF values, and terrestrial water-storage, became anomalously low in the Amazon basin (outside the 1-σ range) relative to their climatological seasonal cycle in September, October, and prior to December of 2015 respectively (Fig. S4.3). The time lag of terrestrial water-storage compared to precipitation is expected, and confirmed by detailed simulations of soil moisture anomalies which became anomalously low in Octo-

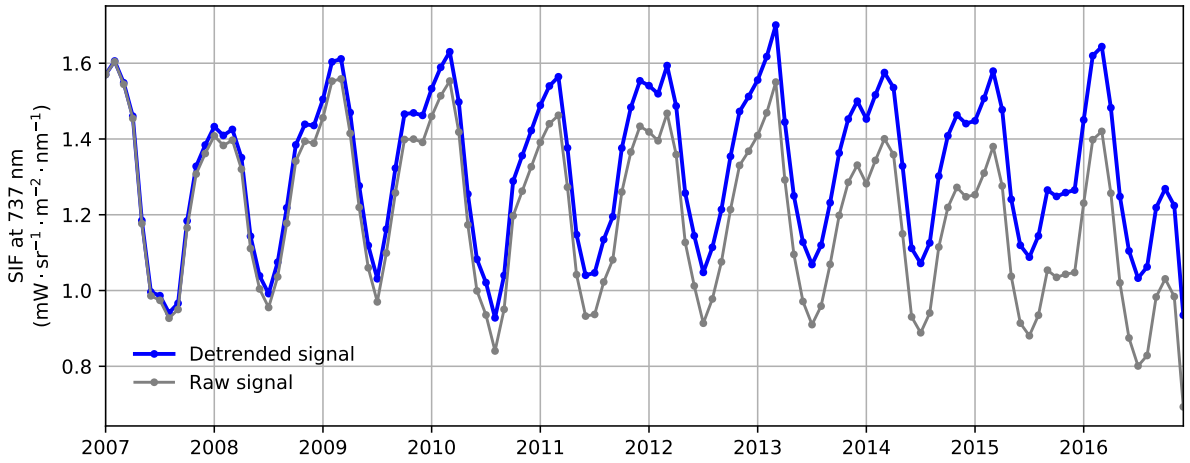

Figure 4.2: Time series of raw and detrended (see text) SIFTER signals averaged over the legal Amazon region for the period 2007-2016.

ber 2015 (*van Schaik et al.*, 2018). The onset of the SIF anomaly corresponds to the peak temperature anomaly (+1.5 °C) reported by *Jiménez-Muñoz et al.* (2016), and Fig. S4.3d shows how SIF in October 2015 remains at the same intensity as the month before, whereas it would normally increase by 10-15% coming out of the dry season. In 2015 though, dry season conditions with below 100 mm/month of precipitation and temperature anomalies persisted much longer (+1 °C temperature anomalies continued for at least 6 months, *Jiménez-Muñoz et al.*, 2016), likely maintaining the water-stress limitations on productivity. By February 2016, basin integrated SIF had returned to climatological values despite the anomalously low precipitation that persisted throughout the 2016 dry season (Fig. S4.3). Terrestrial water storage was last to start recovery (Fig. S4.3), which is expected, as it presents the integrated balance between precipitation, run-off, and evaporation, which lags precipitation itself. Even in August 2016 it still remained 10% below normal values.

The east-west asymmetry reported by *Jiménez-Muñoz et al.* (2016) for temperature has a strong analogue in SIF (Fig. S4.3a), with values in the eastern part of the basin more strongly reduced (10-15%) than in the western part (2-5%). In addition to temperature and SIF, this pattern is also present in GRACE water storage (Fig. S4.3b, and *Gloor et al.*, 2018), in atmospheric demand for water vapour (Fig. S4.4), and in soil moisture anomalies and GPP (*van Schaik et al.*, 2018). We note though that this asymmetry is much less obvious in precipitation anomalies (Fig. S4.3c), highlighting the role of land-surface interactions in shaping the vegetation response. To account for the climatic variations and different vegetation responses within the Amazon basin we will focus our further analysis on three distinct subregions (shown in the insets of Fig. 4.4), each described in

Sect. 4.2.2.

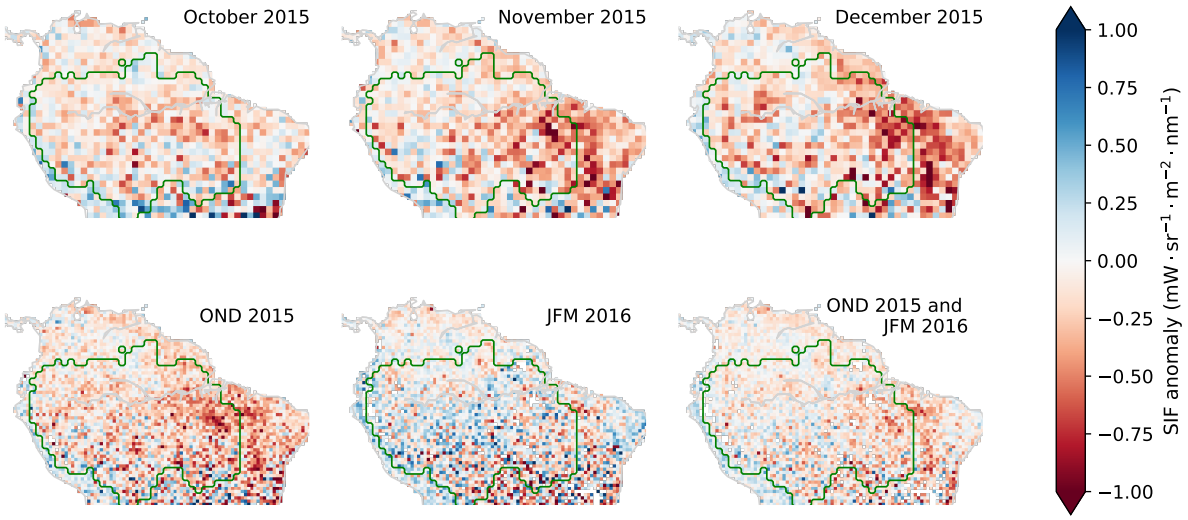

Figure 4.3: Monthly mean SIF anomalies relative to the climatology for the individual months Oct-Nov-Dec-2015 (top row), as well as for 3- and 6-month averages (bottom row). Negative values refer to reduced SIF. The resolution of the SIFTER product is 0.5°×0.5° as shown in the bottom row and each grid cell typically contains between 5-12 retrievals (see Fig. S4.1). The top row has grid cells averaged to 1°×1° to reduce noise in the monthly spatial patterns. The green contour illustrates the legal Amazon area used throughout this work.

Fig. 4.4 shows the climatological seasonal cycle of SIF as well as the 2015/2016 SIF anomalies in these regions. We note that due to the excellent coverage of the SIFTER product, we were able to construct very clear seasonal patterns with a well-defined range of interannual variability, from which the 2015/2016 values clearly deviate beyond the 1-σ standard deviation. The amplitude of the SIF seasonal cycle is largest in Region C, where seasonal rainfall is also most pronounced and drops below 100 mm/month for 5 months per year. This is in clear contrast with Regions A and B which have a higher SIF minimum during July and August, but also a lower SIF maximum that is reached first in Oct-Nov, and peaks again at the end of the wet season in Feb-Mar, when Region C also has maximum SIF.

The 2015/2016 El Niño changed the seasonal cycle in each of the three regions, with the largest relative SIF reductions in Region C. Region C includes both rainforest and savannah, which responds strongly to precipitation (*Santos and Negri*, 1997). Using a set of linear relations between regional SIF and GPP from the *Beer et al.* (2010) product (see Fig. S4.2) the impact on GPP integrates to the largest reduction in Region C (0.15–0.26 PgC in OND-2015, see Table 4.1). This is 16% of its total GPP, and more than twice as large an anomaly as in Region A (8%, or 0.01–0.11 PgC). Region B falls in between these

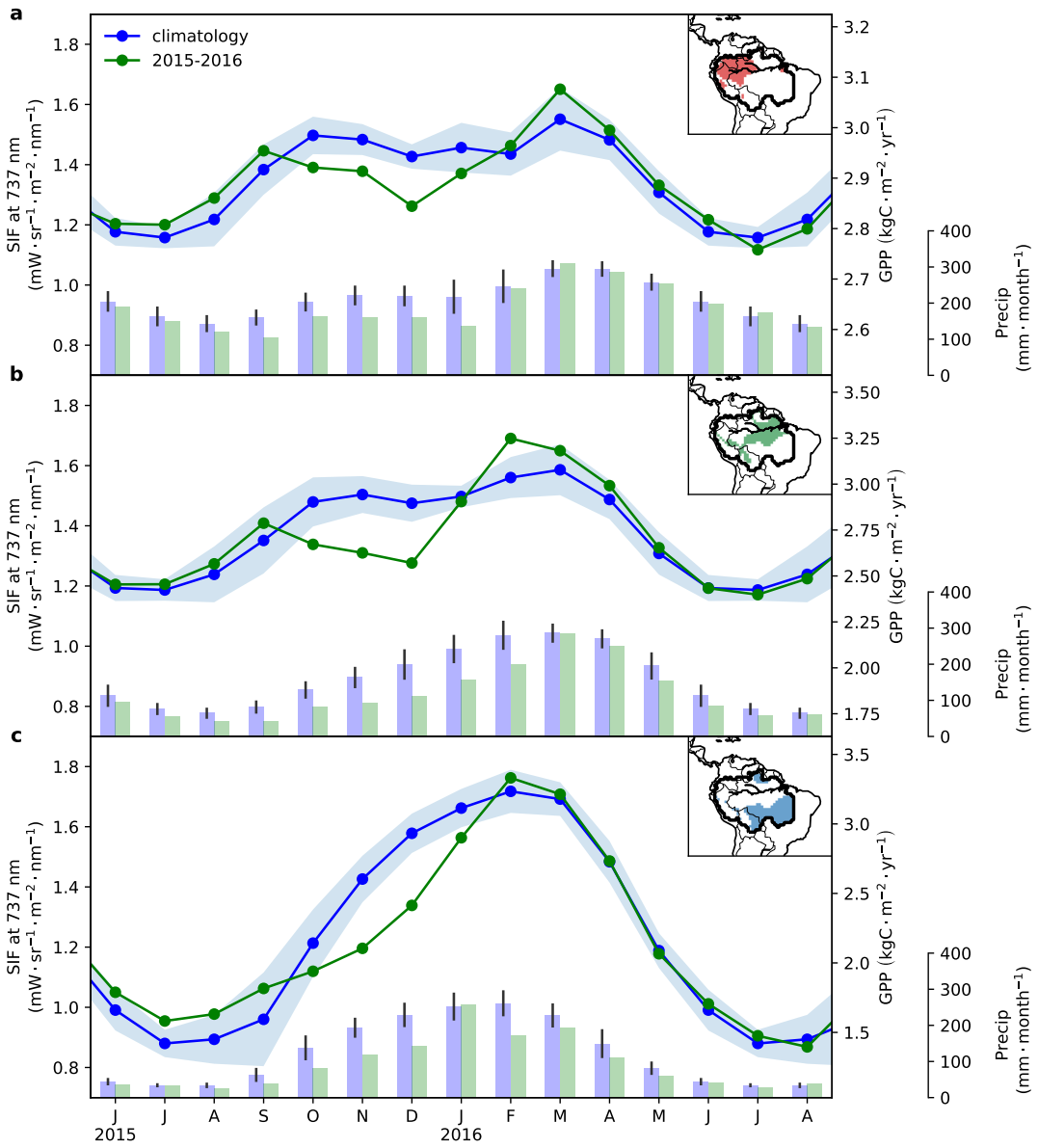

Figure 4.4: Temporal variation of the climatological SIFTER fluorescence and the 2015/2016 anomalies for different regions inside the legal Amazon based on the Köppen-Geiger climate classification system. The locations of the Regions (A, B, C, see main text for a description) are indicated by the coloured areas on the map insets. Corresponding GPP units are provided on the secondary y-axis using region-specific conversion factors (note the different ranges on the GPP-axis). Monthly MSWEP precipitation during the period 2007-2014 (blue) and 2015/2016 (green) are given on the tertiary y-axis.

estimates, and together the amount of 'missed' GPP relative to the climatology (GPP = 4.8 PgC in OND-2015) is 0.34–0.48 PgC. Note that over the subsequent Jan-Feb-Mar months the integrated GPP anomaly is very small and even slightly positive (0.06–0.18 PgC), caused by the return of SIF to normal values in Region C and a slightly higher

(but within the regular variability) SIF in Regions A and B in Feb and Mar. This return to normal values coincides with the return to normal of atmospheric drought conditions, whereas precipitation and soil moisture levels remained low. This atmospheric control suggested by the SIF recovery is discussed further in the Discussion.

Table 4.1: Anomaly in GPP of the terrestrial biosphere for different climate zones in the legal Amazon. Values are derived using three methods for detrending SIFTER fluorescence, two methods for fitting SIF-vs-GPP relations, against two gross primary productivity products (*Schaefer et al.*, 2008; *Beer et al.*, 2010). Anomalies are integrated over 3-month periods, and regions are defined in the main text. Percentages refer to changes relative to the 2007-2014 baseline climatological values, presented in Table S4.1.

Regions	**Area (km^2)**	**ΔC_{OND} (PgC)**	%	**ΔC_{JFM} (PgC)**	%
Amazon	$7.05 \cdot 10^6$	-0.34 – -0.48	(-8.5%)	+0.06 – +0.18	(+3.1%)
A	$1.96 \cdot 10^6$	-0.01 – -0.11	(-2.5%)	+0.01 – +0.013	(+0.3%)
B	$2.11 \cdot 10^6$	-0.13 – -0.18	(-10.0%)	+0.05 – +0.09	(+3.2%)
C	$2.54 \cdot 10^6$	-0.15 – -0.26	(-15.9%)	-0.02 – +0.04	(+0.7%)

The strong influence of VPD and soil moisture on SIF is especially clear for Region C. Fig. 4.5 shows the progression of these variables for the climatological seasonal cycle and the concurrent decrease of observed SIF. Note that we have normalized the SIF values using the solar zenith angle to account for the absolute amount of light reaching each point at the satellite overpass time in the Amazon over the seasons. Also, the soil moisture stress is model-derived and could lead or lag the actual climatological plant stress, suggesting a hysteresis in panel B that is not actually derived from observations.

Highest VPDs of more than 15 hPa occur typically in the dry season in Region C (Fig. 4.5), values that are never present over the wetter Regions A and B (see Fig. S4.5). These values go along with lowest soil moisture values, highest atmospheric water vapour demand (Fig. S4.4) and hence highest vegetation stress (with a correlation coefficient of r=0.81). The 2015/2016 El Niño drought occurred in the months following the dry season, and the figure shows how typical values observed for SIF and VPD + soil moisture stress values occurred one month later than normal during El Niño. We note that although both SIF and VPD + soil moisture anomalies are large for the month they occur in, they do not fall outside the range of values experienced by the vegetation during a typical year. This contrasts with the dry season drought of 2010 which peaked in JJA, sending VPD, soil moisture stress, and SIF to well outside the regular range. Tentatively, the 2010 drought shows a sign of a change in the VPD-SIF slope at the high end of the VPD range (Figs. S4.5 and S4.6), suggesting that additional drought stress from soil moisture (and possibly also heat) played an important role here too, as discussed below and in

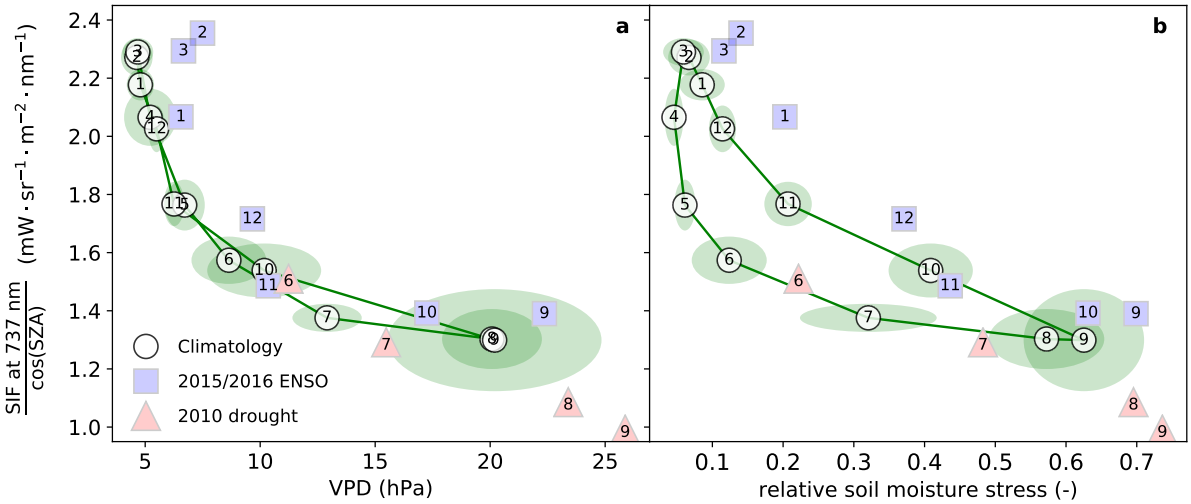

Figure 4.5: The relationship between **(a)** vapour pressure deficit and **(b)** soil moisture stress, with SIF over Region C of our domain. Green ovals show the variability of VPD or soil moisture stress and SIF in each month of our climatology, labelled in white by the number of the month. Blue numbered squares show the corresponding months during the 2015/2016 El Niño (SOND-JFM), while red numbered triangles are for the 2010 drought event (JJAS).

van Schaik et al. (2018). The return of high SIF values by Feb and March 2016 in both figures occurs while VPD and soil moisture stress are still somewhat high for the time of year, but at levels that belong to the lowest over a full seasonal cycle. This suggests that the return of clouds and atmospheric moisture, although below typical wet season levels, marked the end of the drought impact on SIF.

4.4 Discussion

Our results demonstrate the substantial impact of the 2015/2016 El Niño on GPP of the Amazon basin, but we caution against a direct extrapolation of the impact on the net carbon balance. Droughts also change the emissions of CO_2 from fires (*van der Laan-Luijkx et al.*, 2015; *Aragão et al.*, 2018; *Nechita-Banda et al.*, 2018) and from ecosystem respiration (*Doughty et al.*, 2015; *Feldpausch et al.*, 2016) and the latter often correlates positively to GPP in its anomaly (*Bowman et al.*, 2017), dampening the impact on net biome exchange (NBE). Several publications that assessed the impact of the 2010 Amazon drought indeed calculated a smaller reduction of net carbon uptake by the vegetation (NBE, 0.0-0.39 PgC/yr, *Gatti et al.*, 2014; *van der Laan-Luijkx et al.*, 2015; *Alden et al.*, 2016; *Feldpausch et al.*, 2016; *Bowman et al.*, 2017) than the independently estimated reduction on GPP (0.3-0.8 PgC/yr, *Lee et al.*, 2013; *Bowman et al.*, 2017) and net primary

productivity (NPP, 0.14 PgC/yr, *Feldpausch et al.*, 2016). Recent work by *Doughty et al.* (2015) furthermore suggests a shift in carbon allocation that increases carbon use efficiency (NPP/GPP) during large droughts, allowing trees to maintain high primary productivity from other sources (most likely carbohydrate reserves) while closing stomata to reduce water-loss (and increase water-use efficiency). This would mean that a SIF-based GPP anomaly would not directly translate to a carbon balance anomaly in vegetation, and that expected relations between environmental drivers (T, VPD, soil moisture, fPAR) and GPP would change during droughts.

Liu et al. (2017) estimated a substantially higher GPP anomaly over South America from GOSAT SIF (0.9 ± 0.96 PgC) than we report here for October 2015-March 2016 (0.16–0.39 PgC). However, this estimate from *Liu et al.* (2017) was based on the entire year 2015 and integrated over a 44% larger mask that also covers parts to the east of the legal Amazon where SIF anomalies were high (see Fig. S4.7 for a comparison of the masks). The baseline reference period could also play a role, which is much longer in our study than the 2011 La Niña year used as baseline in their work. Changing our baseline to be only the year 2011 we would find an increase in the GPP anomaly of 0.00-0.15 PgC over the 6 months we consider in this work.

The results from *Liu et al.* (2017) furthermore suggest that the GPP anomaly translated fully to an NBE anomaly. This was partly based on their assessment from space-based CO that fires were not anomalous during the Sep-Mar period over which El Niño developed, but also by the need to close the atmospheric CO_2 mass-balance observed from satellite X_{CO_2} column retrievals. To close this balance, a total 0.9 PgC NBE anomaly was needed, thus leaving no room for a contribution from ecosystem respiration. *Gloor et al.* (2018) estimated a GPP anomaly of 0.9 PgC but over a shorter time window, and a total NBE anomaly of 0.5 PgC which is also closer to the NBE anomaly of *van Schaik et al.* (2018) derived from a soil moisture constrained biosphere model. The largest difference between the GPP anomaly estimates from these different sources though is the timing of the recovery of GPP: our SIF product places this 3-4 months earlier in 2016 than the end of the drought viewed from the perspective of precipitation and soil moisture, and also 1-2 months earlier than GOSAT SIF and the biosphere model. Further comparisons should thus focus on the period Feb-March-April 2016 to understand the drought dynamics at the end of the wet season, following the peak anomaly.

According to *Jiménez-Muñoz et al.* (2016), the 2015/2016 El Niño stands out "by having the most extensive area under extreme drought severity (scPDSI < -4), with up to 13% of the rainforests undergoing extreme drought in February-March 2016". During this

drought the normally moderately wet Region B received even less precipitation than the seasonally dry Region C, which along with high vapour pressure deficits led to a large soil moisture anomaly (*van Schaik et al.*, 2018). Nevertheless, our SIF product suggests that photosynthesis showed an initial response to the El Niño drought in late 2015 but, with the belated onset of wet season precipitation, SIF returned to (above) normal at the end of the wet season (Feb-March). Especially in Region B, most drought indicators suggest that anomalous environmental conditions persisted into the 2016 dry season (June-July) before returning to normal. But atmospheric demand for water vapour (i.e., potential evapotranspiration) returned to normal much earlier, and in our analysis seems to have ended drought stress on vegetation leading to a recovery of SIF/GPP. With our SIF retrievals becoming less reliable throughout 2016 though, it is difficult to say whether (a) the recovery was only temporary as fresh rain brought some relief, but SIF and GPP declined strongly again during the 2016 dry season, or (b) the recovery persisted and SIF remained near climatological values for most of 2016. The recovery of SIF we find in Feb-March is robust against detrending in our analysis though and provides a strong indication that the end of the SIF/GPP response of the 2015/2016 El Niño was under atmospheric control.

Other factors can play a role in comparing our results to existing estimates. Our SIF product only covers scenes with moderate to no cloud cover (cloud fraction <0.4), and we thus typically see the part of the canopy that receives a lot of direct sunlight. This means that, through SIF, we would not see the GPP response of the fraction of vegetation that is more strongly shaded by clouds. This would be the less productive part of the forest under non-stressed conditions, but possibly a more productive area under drought stressed conditions. Since large-scale cloud cover also changes during El Niño we have verified (Fig. S4.1) that our cloud selection does not influence the retrieval coverage across the different years. We furthermore note that GOME-2 and GOSAT have local overpass times of 9:30 and 13:00, respectively, and that VPD and stomatal closure will change during the day. In a model-based analysis this changed the GPP/SIF correlation and slope, with smaller VPD impact on GPP in the morning. This could complicate a comparison between the different SIF products, but was found to have no effect on the GOME-2A anomalies presented in this paper. Similar to GOSAT, the recently launched TROPOMI instrument provides a view on the more drought-affected afternoon. However, TROPOMI attains daily global coverage with a high spatial resolution of 7 km $\times$ 7 km, and is therefore a promising tool for future drought studies, especially over clouded tropical rainforests (*Guanter et al.*, 2015).

4.5 Conclusions

We have presented an analysis of spatiotemporal patterns of SIF across the Amazon basin using a new retrieval product that reduces noise and improves signals particularly for tropical regions, as evidenced by high correlations with the observation-driven *Beer et al.* (2010) GPP product and independent flux-tower data. Our results show a clear difference in SIF response to droughts from the western to the eastern part of the legal Amazon basin, which was not detectable in the gradients from GOME-2 presented before (*Yang et al.*, 2018a), nor discussed in the earlier GOSAT SIF based study by *Liu et al.* (2017). This pattern is in very good agreement with the locations of the largest anomalies of temperature (*Jiménez-Muñoz et al.*, 2016), evapotranspiration, terrestrial water storage (*Gloor et al.*, 2018; *Yang et al.*, 2018a), and soil moisture (*van Schaik et al.*, 2018). Anomalies in all these variables start to build up after September 2015, and accumulate to an 0.51 PgC GPP anomaly by the end of January 2016. The largest contribution to this anomaly comes from the seasonally dry vegetation in the south-eastern part of the basin, with smaller contributions from the wetter regions in the north-east where the drought is most intense. By February 2016, SIF returns to climatological values in our product despite persisting anomalies in temperature, precipitation, terrestrial water storage, and soil moisture into the following 2016 dry season. This suggests that the return to wet season conditions was sufficient to rapidly bring SIF back to normal levels, ending the drought from a GPP perspective.

Acknowledgements

We acknowledge Markus Reichstein from MPI-BGC for providing their GPP product. We thank JPL for hosting the GRACE water storage product and Princeton University for the MSWEP precipitation product. The Royal Society and Guest Editors are acknowledged for the organisation of the Discussion Meeting on the impact of the 2015/2016 El Niño on the terrestrial tropical carbon cycle. Three anonymous reviewers are kindly thanked for their constructive suggestions.

Data availability

The Amazon dataset used in this paper is based on a customized retrieval that builds on further developments of the SIFTER v2 algorithm. The customized dataset is available

through its DOI `https://doi.org/10.18160/ECK0-1Y4C`. A global prototype SIFTER v2 dataset and a preliminary Algorithm Theoretical Baseline Document (*Kooreman et al.*, 2018) are available through the data portal at `http://www.temis.nl`.

Authors' contributions

Gerbrand Koren and Wouter Peters wrote the manuscript and performed the analyses. Erik van Schaik contributed to the analyses and processed SIFTER v2 data together with Maurits L. Kooreman. Alessandro C. Araújo, Bart Kruijt, and Celso von Randow provided meteorological and carbon flux data for the K34 tower near Manaus, which was analysed by Antje Gärtner. All authors contributed to the design of the research, and commented on the manuscript.

Competing interests

The authors have no competing interests.

Funding

Gerbrand Koren, Erik van Schaik and Wouter Peters received funding from the European Research Council (ERC) for the Airborne Stable Isotopes of Carbon from the Amazon (ASICA) project, contract number 649087. Lars Killaars is funded by Groningen University (RUG). Naomi E. Smith received funding from OCW/NWO for ICOS-NL (Carbon Portal). Ingrid T. van der Laan-Luijkx received funding from Netherlands Organisation for Scientific Research (NWO) under contract number 016.Veni.171.095. K. Folkert Boersma and Maurits L. Kooreman are funded by the Royal Netherlands Meteorological Institute (KNMI). Bart Kruijt was funded by a Science Without Borders fellowship from Brazilian CAPES.

Supplemental information

S4.1 SIFTER fluorescence

Sun-induced fluorescence (SIF) is the re-emission of light by the chloroplast during photosynthesis. Since SIF is directly linked to the photosynthesis process, it can serve as a proxy for photosynthetic CO_2 uptake by vegetation. It was shown in laboratory and field studies that SIF can be used to detect water stress of vegetation (*Flexas et al.*, 2002; *Daumard et al.*, 2010). SIF can also be measured from space, which provides a unique opportunity to study large-scale vegetation response to climatic events.

We use SIF obtained from the Global Ozone Monitoring Experiment-2 (GOME-2) instruments on board of the MetOp-A satellite that is operated by the European Organization for the Exploitation of Meteorological Satellites (EUMETSAT). The MetOp-A satellite was launched in October 2006, followed by the MetOp-B satellite in September 2012. MetOp-C, a third satellite in this series, is scheduled to be launched in 2018. The MetOp satellites have a sun-synchronous orbit and have a local overpass time of 9:30 in the morning.

Our analysis is based on a custom version of Sun-Induced Fluorescence of Terrestrial Ecosystems Retrieval (SIFTER) developed at the Royal Netherlands Meteorological Institute (KNMI). This SIFTER version is an update of the retrieval described by *Sanders et al.* (2016). The SIFTER retrieval is based on a stochastic representation of the atmospheric reflectance spectrum by a set of principal components. These principal components are derived from GOME-2 observations over a reference region over the Sahara where vegetation (and hence SIF) is absent. In the retrieval algorithm the surface albedo and fluorescence are estimated from the GOME-2 observations and the principal components by minimizing a cost function. Note that SIF is retrieved without ancillary datasets such as pre-defined land cover type maps.

The following major changes were made in the retrieval method for SIFTER: (1) the principal components representing the atmospheric disturbance are now determined for the period from 2007-2016, instead of a moving yearly window; (2) the spectral fitting window is reduced from 712-783 nm to 734-758 nm and the number of principal components used to simulate atmospheric effects is reduced from 35 to 8; (3) SIF retrievals are rejected when autocorrelation in the fit residuals is larger than 0.2; and (4) a correction for the remaining irradiance bias and latitudinal bias was applied.

SIFTER values were retrieved with a set of principal components that represents the atmospheric effects on measured irradiance. As mentioned above, the principal components are derived from the period 2007-2016 for a reference area over the Sahara. Experiments with different settings for the retrieval algorithm have shown that the inter-annual variability (IAV) in the SIF signal strongly increases when a shorter reference periods is selected (data not shown). A possible explanation for this effect is that the IAV in the water vapour over the Saharan reference area translates into IAV in the retrieved SIF signal for e.g. the Amazon region.

Analysis of the raw SIF signal reveals that there is a negative trend in the SIF signal over the Amazon region (see Fig. 4.2). To remove the trend from the SIF signal, we used the following detrending methods: (1) linear detrending; (2) quadratic detrending; and (3) detrending using the CCGCRV routine that was developed by *Thoning et al.* (1989) for the analysis of CO_2 time series. The effect of the selected detrending method on the resulting GPP anomalies is discussed in Chapter 4.

Possible explanations for the observed SIF trend are changes related to (1) the physical instruments (e.g. sensor degradation or drift of the satellite from its original orbit); (2) the instrument settings and low level data processing (e.g. the pixel size that changed for GOME-2A from 80×40 km^2 to 40×40 km^2 in 2013 and changes in the processing of level 0 and level 1 data) or (3) geophysical changes in the Earth system (e.g. the atmospheric composition which can make the set of principal components less representative). Our method, using a long baseline period to derive these PCs and reduce noise, is likely more sensitive to this decline in signal than other GOME retrievals.

S4.2 Coverage of SIFTER over time

Fig. S4.1 shows the mean number of 'valid' samples that were used to determine the monthly mean SIF signal for the 0.5°×0.5° grid boxes within the different subregions of the legal Amazon. The most important reasons for disregarding an observation are (1) cloud fraction over the grid box is higher than the maximum of 0.4; (2) the autocorrelation in the residue is higher than 0.2, which is an indication of an erroneous fit (*van Schaik*, 2016). Note that each subregion A, B, or C contains 636, 688, and 840 gridboxes respectively, such that the total number of SIF values used per aggregated region is highly robust.

The number of samples per month follows a strong seasonal cycle and also an upward trend, similar to the downward trend that we find in the raw SIFTER signal. As noted

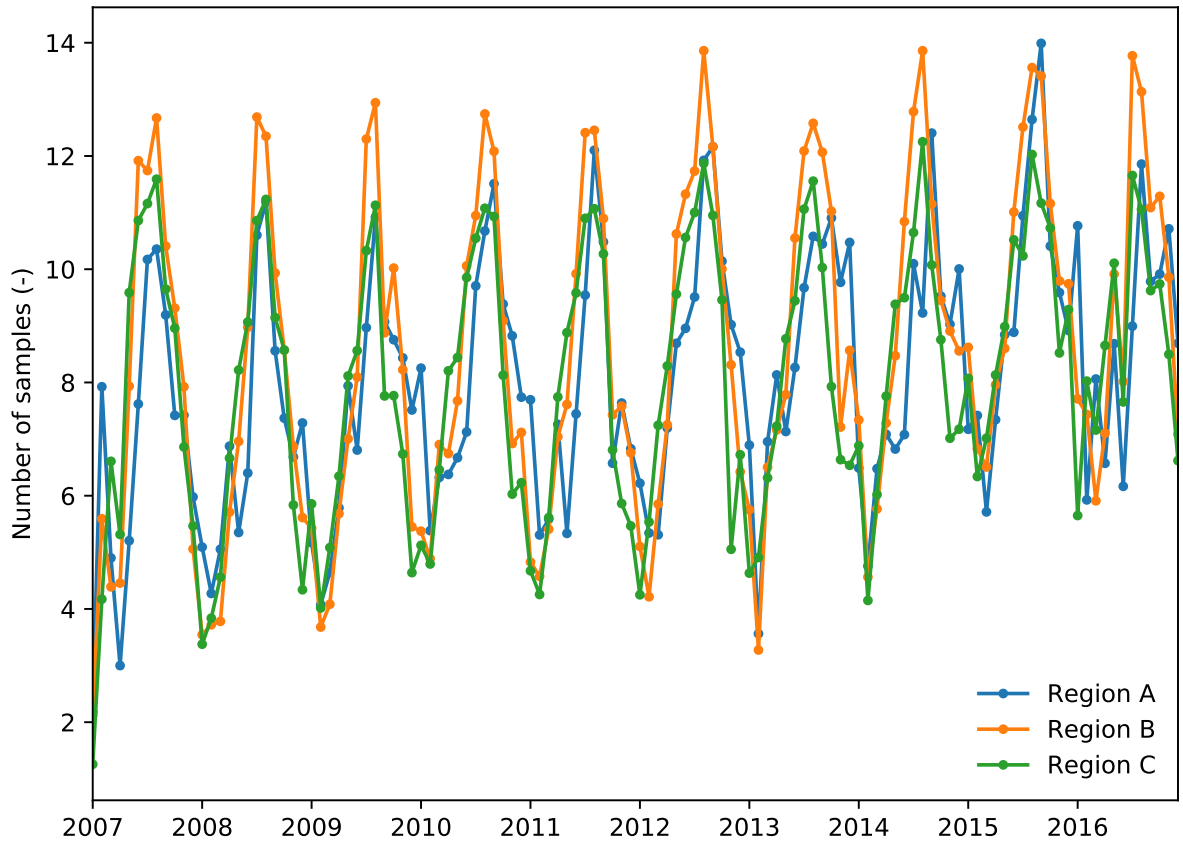

Figure S4.1: Time series of the mean number of samples constituting the monthly SIF from SIFTER retrieval of GOME-2A for different regions inside the legal Amazon.

above, the number of samples per grid box per month contains indirect information about the clouds, since a maximum cloud fraction of 0.4 was imposed. The seasonal cycle in number of retrievals thus closely follows the seasonal cycle of cloudiness, and thus the wet seasons and dry seasons.

The number of samples over the Amazon regions is about 50% lower than the number of samples over all tropical land (from 30°N-30°S, including the Amazon region itself, data not shown), which is due to (1) the above average cloudy conditions over the forested Amazon and (2) the noise originating from the South Atlantic Anomaly.

S4.3 Additional datasets

S4.3.1 MPI-BGC gross primary productivity

We use the annual mean GPP product from the Max Planck Institute for Biogeochemistry (MPI-BGC) (*Beer et al.*, 2010) that was created by extrapolating a database of eddy-covariance measurements using different machine learning approaches. This GPP product has a spatial resolution of 0.5°×0.5°.

S4.3.2 GRACE terrestrial water storage

We use the GRACE JPL-RL05M mascon product from the Jet Propulsion Laboratory (JPL). This mascon product is based on prior model information which results in a better signal-to-noise ratio than GRACE products based on the spherical harmonics retrieval (*Watkins et al.*, 2015).

The JPL-RL05M GRACE data is available from April 2002 to June 2017 at (nearly) monthly time resolution and a spatial resolution of 3°×3°. This dataset is hosted in the data portal at `https://podaac.jpl.nasa.gov/` (*Wiese et al.*, 2016).

Note that the JPL GRACE product does not represent an absolute value for the terrestrial water storage, but it is a series of anomalies in terrestrial water storage. Since these anomalies are defined relative to a multi-year baseline (2004-2009), the anomalies still contain a seasonal cycle.

S4.3.3 MSWEP precipitation

We also use precipitation from the Multi-Source Weighted-Ensemble Precipitation (MSWEP) (*Beck et al.*, 2017a) dataset in this study. MSWEP is a global precipitation dataset derived from gauge measurements, satellite observations and re-analysis products. The spatial resolution of MSWEP is 0.1°×0.1° and MSWEP has a 3-hourly temporal resolution. It was found in a comparative study that MSWEP has the highest correlation with local gauge measurements out of 22 precipitation products (*Beck et al.*, 2017b). The MSWEP product is available through the data portal `http://www.gloh2o.org/`.

S4.4 SIF-GPP scaling

To quantify the observed SIF-reductions in terms of PgC, a conversion from SIF to GPP is required. We derive a linear fit for GPP vs. SIF, similar to *Parazoo et al.* (2014). Fig. S4.2 shows GPP from *Beer et al.* (2010) versus annual mean SIFTER for cells within the Amazon region. To prevent that large concentrations of points within a small SIF range are dominating the constructed fit, we have first calculated the mean GPP over equal bins of 0.2 $mW \cdot sr^{-1} \cdot m^{-2} \cdot nm^{-1}$. Subsequently, the fit was determined based on the binned representation of the data, where equal weights were assigned to each bin. Bins with less than 3 points were discarded.

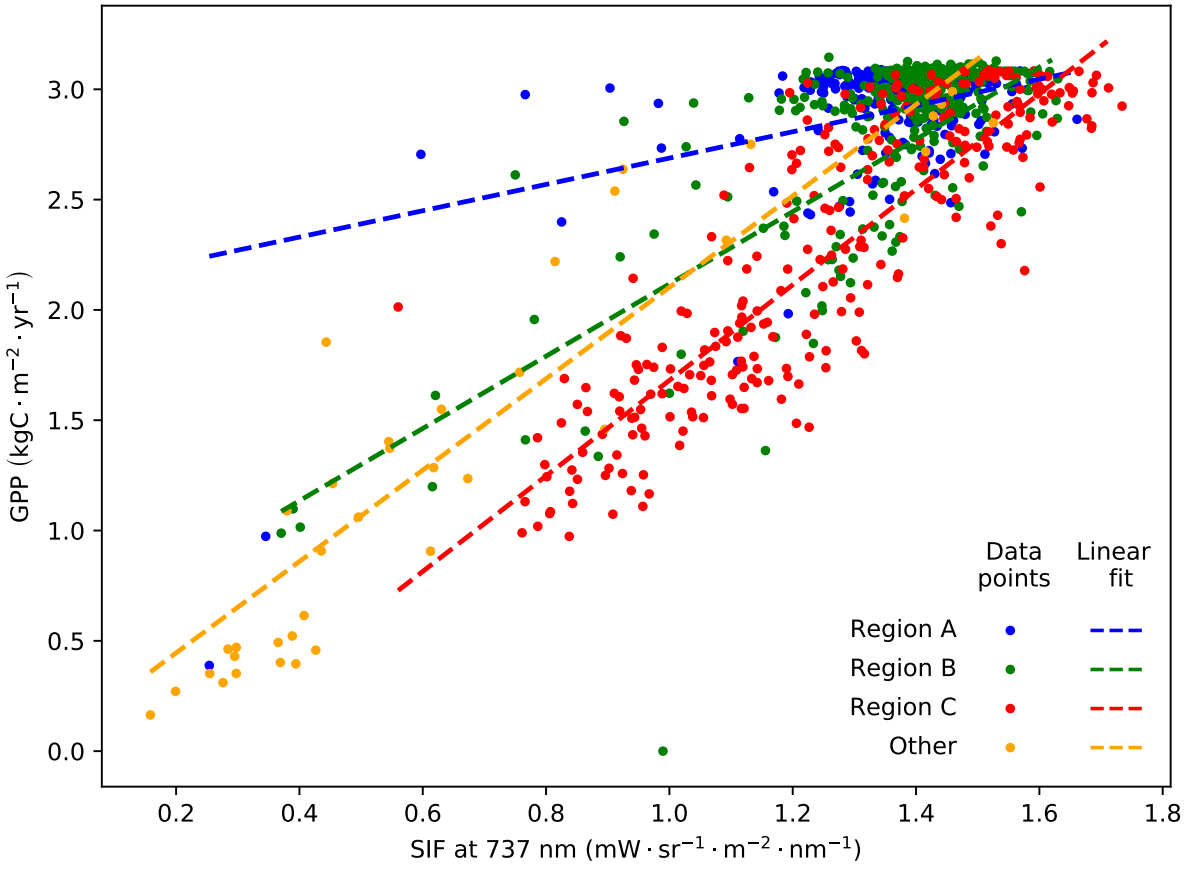

Figure S4.2: GPP from the *Beer et al.* (2010) product versus annual mean detrended SIFTER fluorescence for each 0.5°×0.5° grid box within the Amazon region. Colours correspond to the climate zones defined in Sect. 4.2.2.

The default set-up for calculating the GPP-SIF slope is using a linear SIF detrending, for different climate zones (Regions A, B and C) and using the *Beer et al.* (2010) GPP product (see Fig. S4.2). For our error analysis we also use the quadratic and CCGCRV (*Thoning*

Table S4.1: Climatological GPP for different climate zones in the Amazon regions. Values are derived from SIFTER fluorescence and MPI-BGC gross primary productivity (*Beer et al.*, 2010), and integrated over 3-month periods, and regions defined in Sect. 4.2.2.

Regions	Area (km^2)	SIF ($mW \cdot sr^{-1} \cdot m^{-2} \cdot nm^{-1}$)		GPP (PgC)	
		OND	JFM	OND	JFM
Legal Amazon	$7.05 \cdot 10^6$	1.42	1.55	4.83	5.29
Region A	$1.96 \cdot 10^6$	1.47	1.48	1.45	1.46
Region B	$2.11 \cdot 10^6$	1.49	1.55	1.54	1.59
Region C	$2.54 \cdot 10^6$	1.41	1.69	1.63	2.02
Other	$4.34 \cdot 10^5$	0.90	0.99	0.21	0.23

et al., 1989) detrending method as alternative to the linear detrending. Furthermore we tested the effect of plant functional type (PFT) specific scaling as alternative to the division in climate zones. Finally, we used GPP from terrestrial biosphere model SiBCASA (*Schaefer et al.*, 2008) as alternative to the *Beer et al.* (2010) GPP product. The resulting slopes and intercepts are summarized in Table S4.2.

S4.5 SIF correlations with environmental variables

Fig. S4.5 shows the relationship between SIF and VPD after aggregation over the regions A, B, and C (see Sect. 4.2.2 for definition), for each month of our climatology (colour) as well as for the 2015/2016 El Niño and the 2010 drought event. It illustrates the larger sensitivity of regions B, and especially C, to VPD compared to Region A. Highest VPD values are consistently found over Region C. Lowest normalized SIF values correspond to these points, with the 2010 drought having the highest impact and the relation appearing to drop below the exponential curve that would connect the coloured (climatological) values.

Fig. S4.6 presents this same view, but now using soil moisture stress on the horizontal axis. This is derived from the simulations presented in *van Schaik et al.* (2018). High values of relative soil moisture stress correspond to high reductions in SIF. The figure shows that VPD and soil moisture stress likely both play a role in reducing SIF over Region C, but likely also have contributed to the reduction of SIF in Region B. Disentangling this relative influence is challenging, but would give further insights into the drought dynamics of vegetation in this region.

Table S4.2: Values of the GPP/SIF slope and intercept derived for the Amazon.

Aggregation	**Slope** [kgC·yr^{-1}/ mW·sr^{-1}·nm^{-1}]	**Intercept** [kgC·m^{-2}·yr^{-1}]	**SIF range** [mW·sr^{-1}·m^{-2}·nm^{-1}]
	Climate zones, Amazon, GOME-2A vs Beer et al. (2010)		
Region A	0.60	2.09	0.8–1.6
Region B	1.64	0.48	0.6–1.8
Region C	2.17	-0.48	0.6–1.8
Other	2.07	0.03	0.2–1.6
All Amazon	1.80	0.18	0.2–1.8
	PFTs, Amazon, GOME-2A vs Beer et al. (2010)		
Tropical forest	1.38	0.84	0.6–1.8
Savanna	1.78	0.08	0.2–1.8
Others	1.99	-0.14	0.2–1.8
	Climate zones, Amazon, GOME-2A vs SiBCASA (Schaefer et al., 2008)		
Region A	1.87	0.85	0.8–1.6
Region B	1.86	0.32	0.6–1.8
Region C	1.41	0.30	0.6–1.8
Other	3.35	-1.56	0.2–1.6
All Amazon	2.31	-0.53	0.2–1.8
	Parazoo et al. (2014), global, GOSAT vs Beer et al. (2010)		
Evergreen broad-leaf forest	5.77	0.62	0.05–0.45
Savanna	5.59	0.22	0.05–0.38
All	6.63	0.04	-0.1–0.45

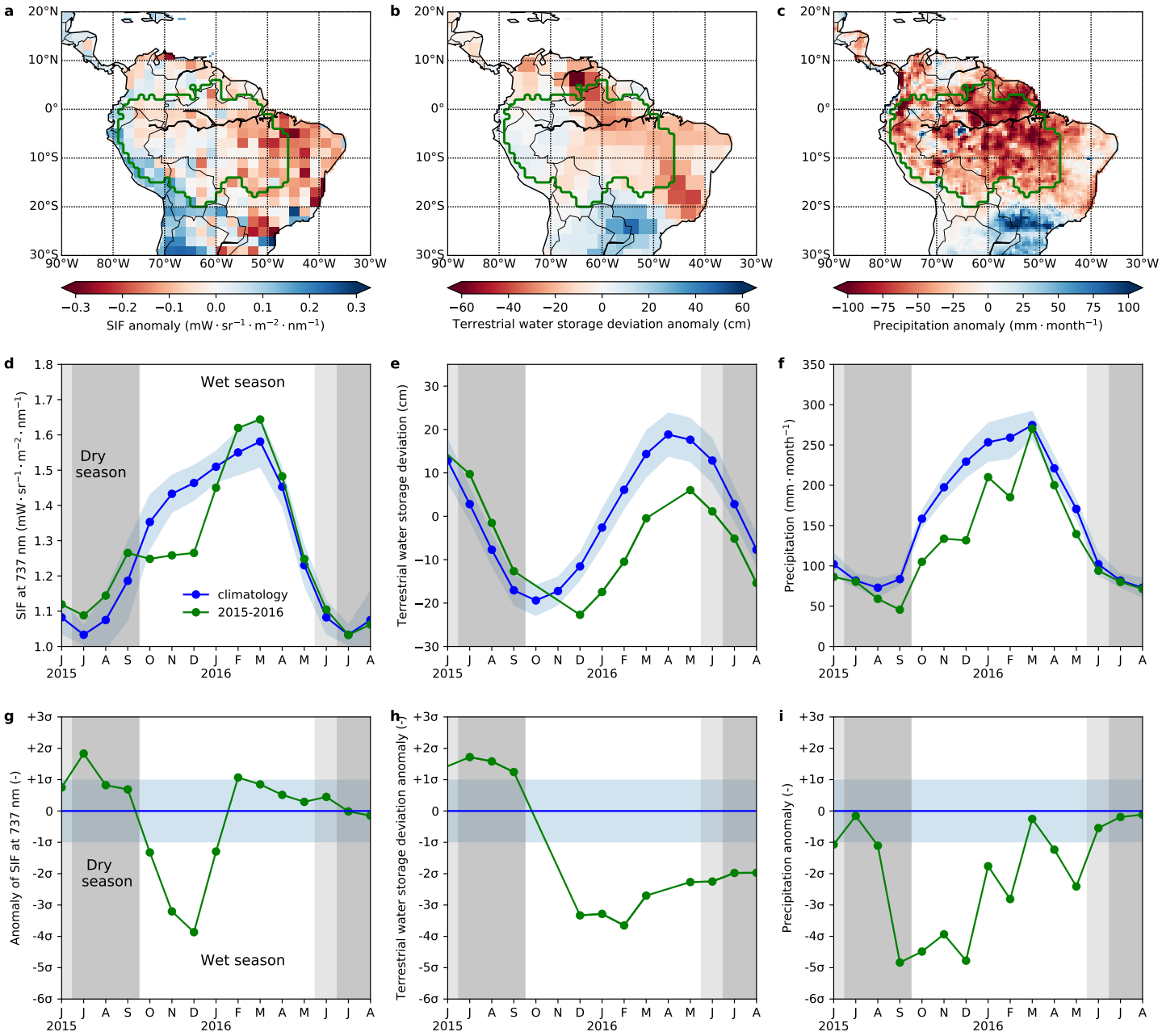

Figure S4.3: Spatio-temporal distributions of 2015/2016 anomalies in the Amazon region of **(a, d, g)** SIFTER fluorescence; **(b, e, h)** GRACE terrestrial water storage anomalies; and **(c, f, i)** MSWEP precipitation. The spatial distributions show the cumulative anomaly of the variable integrated over the period September 2015 to May 2016 for the northern part of South America. The location of the legal Amazon region is indicated by a thick green line. The time series show the climatological values, and values during the 2015/2016 El Niño period integrated over the legal Amazon region. The bands surrounding the climatological values indicate the year-to-year variability (1-σ) around the climatology. For SIF and precipitation we used the period 2007-2014, whereas the baseline for GRACE terrestrial water storage is 2002-2014. The dark grey shaded area indicates the climatological dry season (< 100 mm/month precipitation) for the Amazon region, the light grey shaded area indicates the extended dry season for 2015 and 2016.

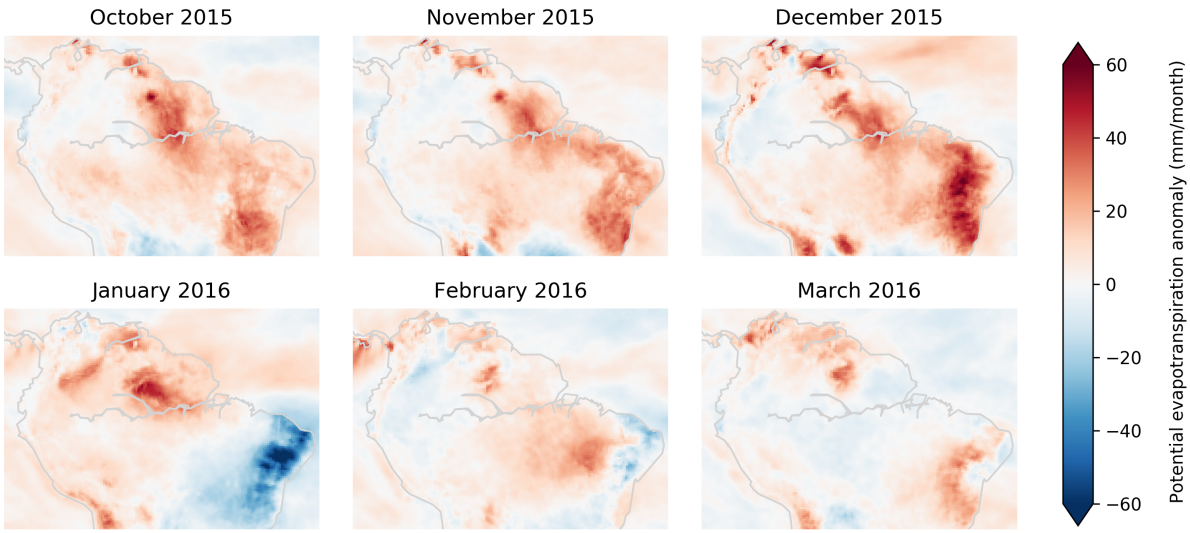

Figure S4.4: Anomaly of potential evapotranspiration, relative to the 2010-2016 period. Red colours show higher than normal atmospheric demand. Numbers are based on a Penman-Monteith calculation with ERA5 atmospheric variables.

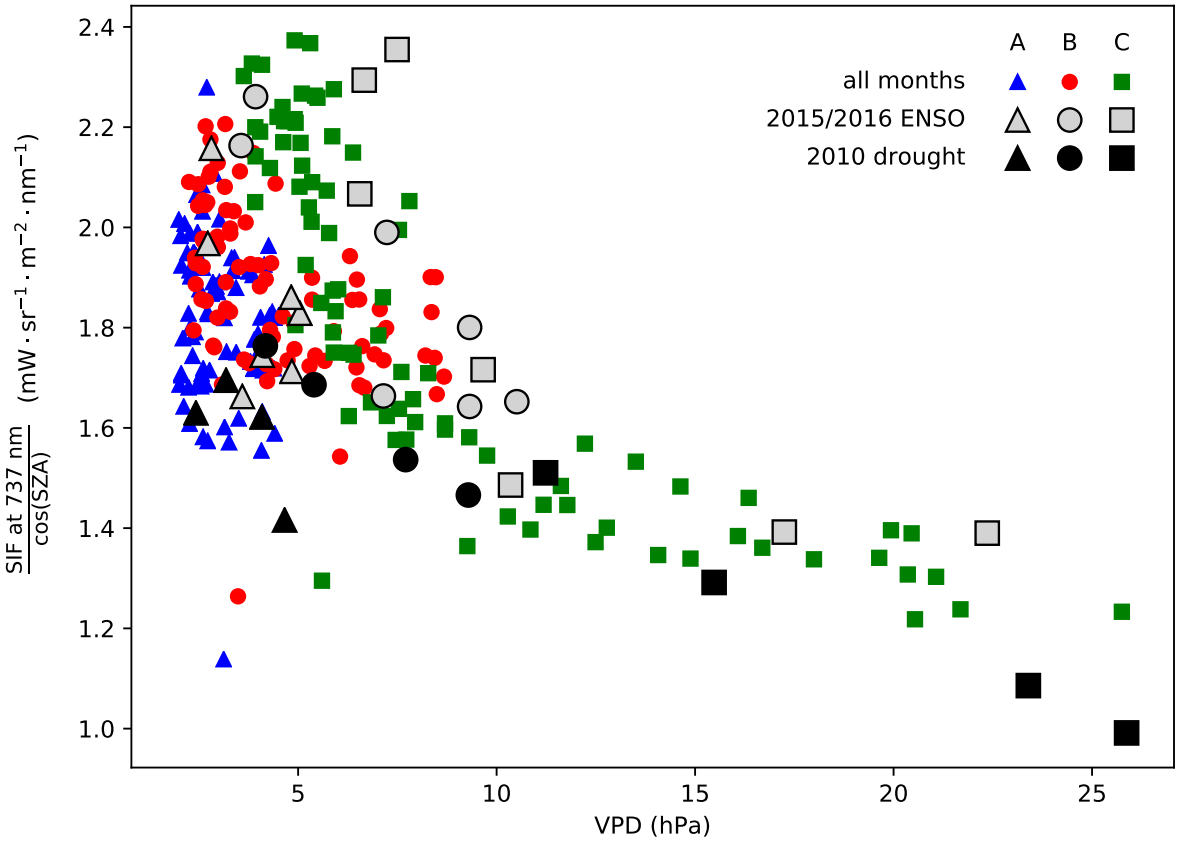

Figure S4.5: Average SIF for each region normalised by the cosine of the solar zenith angle, versus VPD. Each dot corresponds to one month from either the climatology (colours), from the 2015/2016 El Niño period (gray), or from the 2010 drought (black). Shapes and colours are used to distinguish between Regions A, B, and C. A summary view of this figure is presented in Chapter 4.

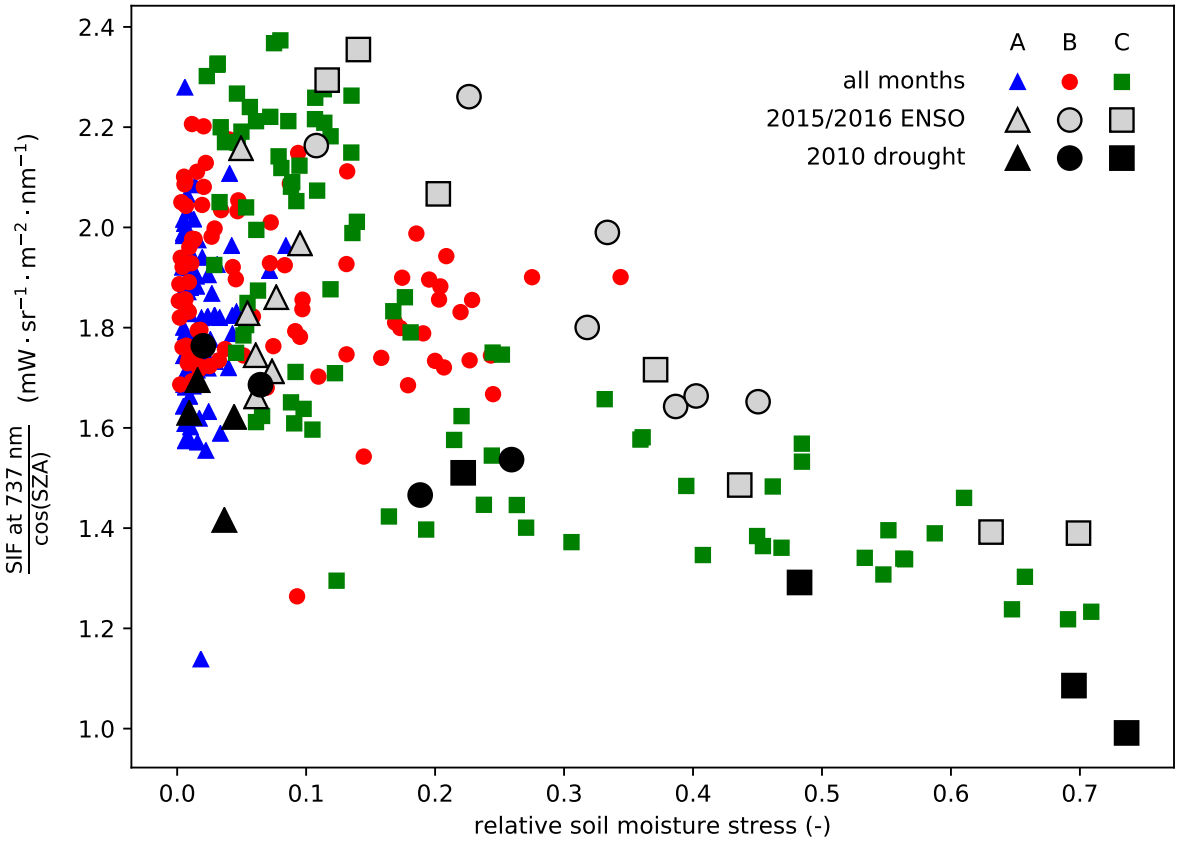

Figure S4.6: Average SIF for each region normalised by the cosine of the solar zenith angle, versus relative soil moisture stress as calculated by *van Schaik et al.* (2018). Each dot corresponds to one month from either the climatology (colours), from the 2015/2016 El Niño period (gray), or from the 2010 drought (black). Shapes and colours are used to distinguish between Regions A, B, and C. A summary view of this figure is presented in Chapter 4.

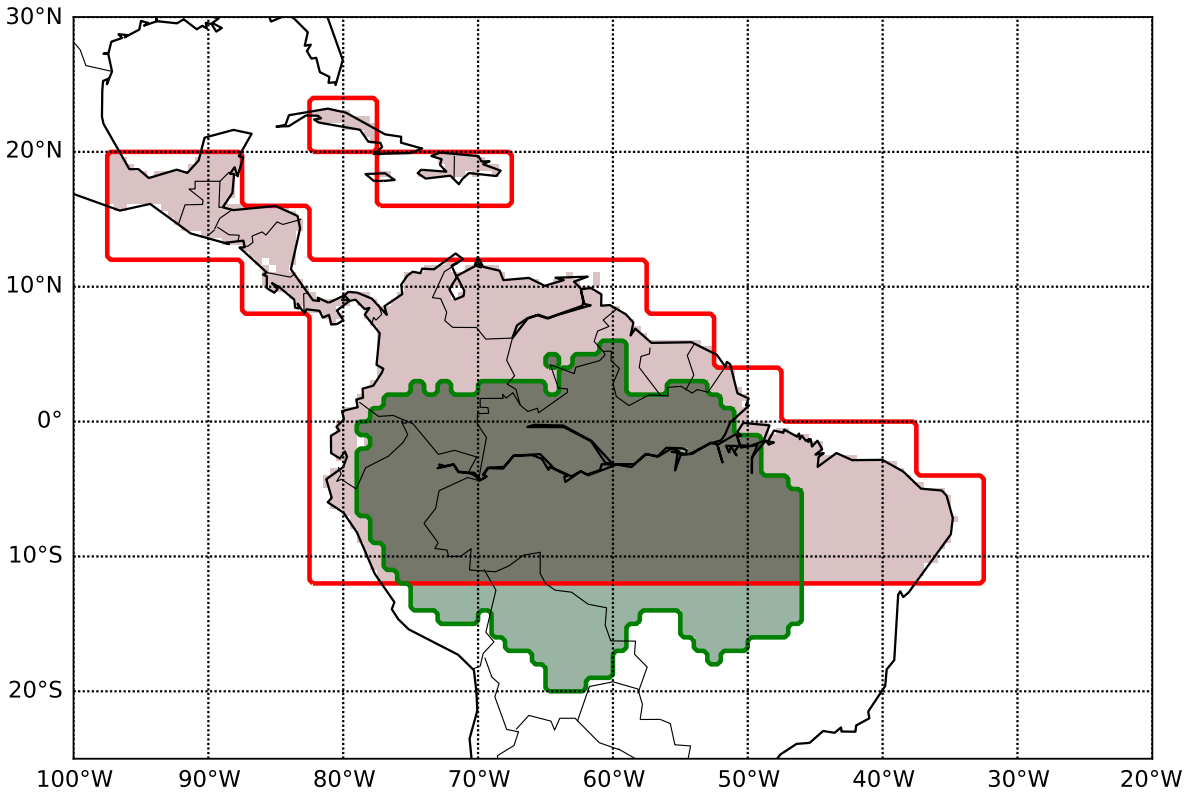

Figure S4.7: Comparison of the Legal Amazon mask (`https://doi.org/10.18160/P1HW-0PJ6`) used in this study and the "Trop SA" mask used by *Liu et al.* (2017). The *Liu et al.* (2017) mask is about 44% larger in land area and contains 34% more GPP according to the *Beer et al.* (2010) GPP product.

5

Persistent impact of the 2015/16 El Niño drought on the 2016 dry season in the Amazon

The Amazon experienced major droughts in 2010 and 2015 that resulted in a reduction of CO_2 uptake by vegetation and an increase of CO_2 fire emissions, leading to anomalously high global growth rates of atmospheric CO_2. The direct effects of these droughts on the Amazon carbon balance were studied before, but little is known about their delayed impacts. We used CO_2 profiles collected by aircraft over the Amazon to quantify the net ecosystem exchange for drought years and post-drought years in the period 2010-2017 using the CarbonTracker South America (CTSAM) inverse modelling system. In addition, we performed inversions using independent CO_2 column observations from OCO-2 to quantify CO_2 exchange for the years 2015-2017. We estimate that the total Amazon CO_2

This chapter by Koren, G., Luijkx, I.T., Florentie, L., Naus, S., Nechita, N., Krol, M.C., van Schaik, E., Gatti, L.V., Domingues, L.G., Neves, R.A.L., Correia, C.S.C., Gloor, M., Miller, J.B., and Peters, W., is in preparation for submission

emissions for the years 2010 and 2016 are 0.3–0.5 PgC and 0.0–0.3 PgC larger than the subsequent years 2011 and 2017, respectively. Furthermore, we used near-infrared reflectance of terrestrial vegetation (NIRv), from MODIS and MAIAC, to diagnose the direct and delayed response of GPP to the 2015/2016 drought. We find a substantial reduction in NIRv in the 2016 dry season, when precipitation and temperature have returned to normal values, while soil moisture is still anomalously low, suggesting a persistent impact of the preceding 2015/2016 El Niño drought.

5.1 Introduction

The feedbacks between climate and the terrestrial carbon cycle are currently poorly known (*Booth et al.*, 2012), especially for tropical ecosystems. The Amazon forest is the largest tropical biome in terms of biomass (*Saatchi et al.*, 2011) and has experienced major droughts in 2005, 2010 and 2015/16 (*Marengo et al.*, 2008; *Lewis et al.*, 2011; *Jiménez-Muñoz et al.*, 2016; *Erfanian et al.*, 2017). Over the last decades, the Amazon has taken up carbon from the atmosphere, but the uptake rate has declined over recent years (*Brienen et al.*, 2015; *Hubau et al.*, 2020). This is partly due to the recent droughts that have hit the Amazon, and these large-scale droughts might become more frequent in the future (*Doughty et al.*, 2015). A more accurate quantification of carbon losses and gains in the Amazon, and improved understanding of the underlying processes is required.

Most notably, recent studies have taught us that there is not a single underlying process that controls the Amazon drought response. Its complexity is suggested by observations, and our limited ability to reproduce these with current state-of-the-art models (*Boisier et al.*, 2015; *Restrepo-Coupe et al.*, 2017). Initially, Amazon droughts trigger a vegetation response to excessive heat (*Toomey et al.*, 2011; *Sullivan et al.*, 2020) high vapor-pressure deficits (VPD, *Powell et al.*, 2013; *Koren et al.*, 2018; *Yuan et al.*, 2019), and reductions in plant-available soil moisture levels (*Miguez-Macho and Fan*, 2012; *Humphrey et al.*, 2018; *Solander et al.*, 2020). The response of Gross Primary Productivity (GPP) to these factors, although well-observed from proxies, is not easy to reproduce (*Hilker et al.*, 2014; *Joetzjer et al.*, 2014; *van Schaik et al.*, 2018) as VPD-responses are species-specific and often delayed (*Sakschewski et al.*, 2016; *Wolf et al.*, 2016b; *Giardina et al.*, 2018), while access to soil moisture depends on the rooting depth of plants (*Baker et al.*, 2008; *Harper et al.*, 2014). Upward transport of this soil water through the xylem is controlled by hydraulic conductance (*Adams et al.*, 2017), and a plant's capacity to counteract its decrease during droughts by maintaining a high water potential through stomatal control

(*Wolf et al.*, 2016a; *Eller et al.*, 2018). Failure leads to mortality and was suggested a dominant drought impact in previous studies (*Phillips et al.*, 2009; *Rowland et al.*, 2015). Plants moreover respond actively to droughts by changing carbon allocation patterns that affect for example root growth and turn-over, as seen in current forests (*Doughty et al.*, 2015), as well as in enhanced CO_2-experiments (*Jiang et al.*, 2020). Different time-scales of drought forcing and response, together with the distinct seasonal cycle of water and direct sunlight make the response asynchronous, especially when it comes to leaf-phenology (*Jones et al.*, 2014; *Gonçalves et al.*, 2020), which further complicates the interpretation of satellite-data. Finally, the frequency of droughts experienced recently in the basin trigger a need to understand the impact of repeated droughts as studied by *Saatchi et al.* (2013), *Feldpausch et al.* (2016) and *Gonçalves et al.* (2020).

The major Amazon drought in 2005 was caused by anomalously high sea-surface temperatures (SST) in the north Atlantic that reduced especially dry season (JJAS) rainfall amounts over the basin (*Marengo et al.*, 2008). Its impacts were mainly recorded through forest inventory plots that were part of the RAINFOR network (*Malhi et al.*, 2002). Differences between pre- and post-2005 conditions in biomass amounts as well as gains/losses suggested a carbon loss of 1.2–1.9 PgC from the Amazon forests (*Phillips et al.*, 2009). This occurred over multiple subsequent years, and was attributed to recorded moisture deficits. The net loss in above-ground biomass contrasted the earliest reports on the 2005 drought impacts from satelites, that indicated a "greening up" (*Saleska et al.*, 2007) during the event. Later work by *Samanta et al.* (2010) and *Restrepo-Coupe et al.* (2013) showed the underlying Enhanced Vegetation Index (EVI) to be sensitive to seasonal solar irradiation changes, and unsuitable to conclude a green-up. Only much later, alternative remote sensing analyses of biomass changes confirmed the earlier ground-based reports with estimated losses of 0.3 ± 0.2 PgC/yr (*Saatchi et al.*, 2013; *Yang et al.*, 2018b). The subsequent drought in 2010 brought renewed interest in the drought impact because of two 1-in-50 year events occurring within a five year time-span (*Feldpausch et al.*, 2016).

The 2010 Amazon drought was caused by a similar (non-El Niño) related SST anomaly as in 2005, and also had largest impacts during the dry season (*Lewis et al.*, 2011). Observational capacity had increased since 2005 though, and several lines of evidence for a strong impact on fires and forest carbon uptake followed each other. Forest inventories (*Lewis et al.*, 2011; *Doughty et al.*, 2015) first identified strong declines of biomass accumulation, and new airborne measurements of CO_2 and CO over the basin (*Gatti et al.*, 2014) suggested that vegetation uptake of CO_2 by the biosphere was reduced during the drought year 2010 relative to the 'normal' year 2011 (0.22 PgC less uptake), while the release of CO_2 through fires was higher (increase of 0.21 PgC). Based on a mass-balance approach

of changes in 0–5 km columns of CO_2, the Amazon was estimated to be a source of 0.48 PgC to the atmosphere for the drought year 2010. Later, formal inverse studies including our 'CarbonTracker South-America' (CTSAM, described in more detail in Sect. 5.2.3) largely confirmed these numbers (*van der Laan-Luijkx et al.*, 2015; *Alden et al.*, 2016). In addition to the traditional remote sensing indices (*Potter et al.*, 2011) the 2010 drought was also observed through sun-induced fluorescence (SIF) from GOSAT, which suggested strongly reduced photosynthesis during the peak drought (*Lee et al.*, 2013; *Parazoo et al.*, 2013) to again have played a role.

Only five years later, a strong El Niño caused the next widespread drought that severely impacted the basin, but this time extending into the wet season (Oct-Feb) of 2015/2016. This event was by far the best-observed and intensively recorded drought event of the three (*Malhi et al.*, 2018), with forest inventories, eddy-covariance sites, tall towers and aircraft CO_2 profiling, and remote sensing that included XCO_2 column observations from both GOSAT and OCO-2 in addition to biomass and SIF products. Using remotely-sensed SIF from GOSAT, *Liu et al.* (2017) report a reduction in gross primary production by 0.9 PgC over tropical South America, focused on the northwestern part of the basin where precipitation anomalies were highest. *Koren et al.* (2018) assessed SIF following the 2015/16 El Niño and found a reduction of 0.34–0.48 PgC for the Amazon for the last three months of 2015, relative to a baseline of eight previous years (see Chapter 4 of this thesis). *Wigneron et al.* (2020) used the correlation of the low frequency satellite product L-VOD with biomass to estimate changes in above ground biomass following the 2015/16 El Niño event. For tropical South America, the above ground biomass of the forest was reduced by 0.5 PgC between the years 2014 and 2017. The most severe reductions were found for the eastern part of the Amazon forest and the adjacent Cerrado regions (Fig. 2 in *Wigneron et al.*, 2020) and these regions had not yet recovered by 2017.

Inverse modeling, first by *Bowman et al.* (2017), and later by *Liu et al.* (2017) used column CO_2 observations from OCO-2 and GOSAT, suggested also a *net* carbon uptake reduction of 0.9 PgC for 2015, which, together with the 0.9 PgC GPP reduction derived from SIF, left little room for a response in respiration fluxes. These numbers were all relative to the wet year 2011 for the South-American tropics (containing the Amazon and other biomes) though. Later, *Palmer et al.* (2019) also performed pan-tropical inversions using XCO_2 from GOSAT and OCO-2 and reported biosphere fluxes for tropical South America with median values of -0.26 PgC and +0.20 PgC for 2015 and 2016, respectively. Finally, the El Niño drought was quantified by an atmospheric inversion using data from the Amazon aircraft network by *Gloor et al.* (2018), and a net source of 0.5 ± 0.3 was found for the period September 2015 to June 2016. A purely model-based estimate of the GPP

reduction in the Amazon following the 2015 El Niño was obtained by *van Schaik et al.* (2018) by feeding the soil moisture calculated from hydrological model PCRaster GLOBal Water Balance (PCR-GLOBWB, *Sutanudjaja et al.*, 2018) to terrestrial biosphere model SiBCASA (*Schaefer et al.*, 2008). The hydrological model was validated by comparing its simulated river discharge with observations from gauge stations across the Amazon basin. With this coupled model framework the GPP reduction was estimated to be 0.53 PgC for the last three months of 2015 and 0.42 PgC for the first three months of 2016.

Amongst this focus on the 2015/16 El Niño drought, a secondary drought that occurred in the transition from wet- to dry season 2016 (M-J-J) mostly escaped attention so far. This was because large-scale atmospheric forcing was not anomalous like in the previous three events, and because impacts did not show themselves in canonical data products focused on the typical excessive burning during droughts. Instead, its only report known to us was from a phenocam study on leaf-phenology of the canopy at the ATTO and K34 sites near Manaus, recently published by *Gonçalves et al.* (2020). They describe how an anomalous leaf-flush following the return to normal atmospheric conditions in February 2016 showed up as a larger than normal amount of young leaves in the subsequent months, and a lack of leaf flushing later during the start of the dry season (July-August). How this change in phenology would impact carbon uptake was not speculated on though. The lack of strong atmospheric temperature and VPD anomalies suggest this secondary drought to be strongly controlled by a combination of leaf-phenological changes, and reduced soil moisture levels that continued to be lower than average following the El Niño drought earlier in 2015/16. This makes this secondary drought a possibly unique new situation to study further.

In this work, we assess multiple lines of evidence to answer the research question: *In what way, and with what magnitude, did vegetation across the Amazon basin respond to the recently recorded drought events?* We focus on the thus-far sparsely reported secondary drought that occurred months after the well-documented 2015/16 El Niño drought. We use a combination of remote sensing products, atmospheric CO_2 observations and inverse modelling to study the impact of this drought, together with earlier ones, from different perspectives and using a baseline of multiple years to quantify the anomalous nature of the described events.

5.2 Methods

We used (1) hydrological and climate data sets; (2) satellite proxies for gross primary productivity; and (3) the inverse modelling system CTSAM constrained with the Amazon aircraft flask record (*Gatti et al.*, 2014) and OCO-2 retrieved XCO_2 columns. These three components are described in the next sections. For the inversion, we considered different biosphere flux estimates and biomass burning emissions as input, which results in a range of optimized net biosphere fluxes that represents their uncertainty. The use of remote sensing proxies for GPP allows us to distinguish the NEE changes by separately estimating the contributions of photosynthesis and respiration.

5.2.1 Soil moisture and precipitation products

To assess the drought status of the Amazon, we analyse the anomalies of both precipitation and soil moisture. The first precipitation dataset that we used is the Multi-Source Weighted-Ensemble Precipitation (MSWEP) (*Beck et al.*, 2017a). MSWEP is a high resolution (3-hourly, 0.1°×0.1°) global data set, and is derived from gauge measurements, satellite observations and re-analysis products. In a study with 22 gridded precipitation products, MSWEP was found to correlate best with local gauge measurements (*Beck et al.*, 2017b). Also, *van Schaik et al.* (2018) concluded that for the Amazon region, MSWEP precipitation propagated through the PCRaster GLOBal Water Balance (PCR-GLOBWB, *Sutanudjaja et al.*, 2018) hydrological model, resulted in better agreement with discharge observations than when using precipitation from ERA5 from European Centre for Medium-range Weather Forecasts (ECMWF, *Balsamo et al.*, 2015), and the Tropical Rainfall Measuring Mission (TRMM) product (*Huffman et al.*, 2007).

Secondly, we have analyzed precipitation anomalies from the ERA-Interim dataset (*Dee et al.*, 2011) that is produced by the ECMWF. We calculated the total precipitation by adding the convective precipitation and the large-scale precipitation. The ERA-Interim data is also used to drive the atmospheric transport in the flask and satellite inversions included in this study (Sect. 5.2.3). Since ERA-Interim is one of the inputs for the MSWEP product, these two precipitation estimates are not fully independent. We expect that the precipitation-dedicated MSWEP estimate is most accurate, and we included ERA-Interim precipitation as a measure to show the variation among different products. We have also used two further datasets from ERA-Interim: temperature (mean and maximum) and near-surface vapor pressure deficit (VPD, similar to *Barkhordarian et al.*, 2019).

To estimate soil moisture levels and anomalies, we use two different data sets. The first product that we analyze is the terrestrial water storage anomalies from the Gravity Recovery and Climate Experiment (GRACE, *Watkins et al.*, 2015). Many satellite based soil moisture products are mostly sensitive to the top layers of the surface as the microwave does not penetrate into deeper soil layers (e.g. *Buitink et al.*, in review). Hence these products have limited value to diagnose water stress for vegetation with deep roots. GRACE does not suffer from this limitation, as it is based on detecting variations in gravity, which is an entirely different principle. We use the GRACE JPL-RL05M mascon product, which was shown to have better signal-to-noise ratio than GRACE products based on the spherical harmonics retrieval (*Watkins et al.*, 2015). The JPL-RL05M GRACE data is available from April 2002 to June 2017 at an irregular (approximately monthly) temporal resolution and a spatial resolution of 3°×3°.

Furthermore, we use the Global Land Evaporation Amsterdam Model (GLEAM) soil moisture fields at a monthly 0.25°×0.25° resolution (*Miralles et al.*, 2011; *Martens et al.*, 2017). In their recent study on South America, *Moreira et al.* (2019) report that "the combination of MSWEP and GLEAM yielded lower uncertainties in the water balance". We use GLEAM version v3.3a, which is mostly based on ERA-5 reanalysis data; and version v3.3b, which is mostly based on satellite data.

5.2.2 Satellite proxies for GPP: SIF and NIRv

Sun-Induced Fluorescence (SIF) is a small fraction of light (∼1%) that is re-emitted from the chloroplast during photosynthesis. *Frankenberg et al.* (2011) showed that SIF can be detected from satellites and can be used as proxy for GPP over large spatial and temporal scales. In addition, Near-Infrared Reflectance of Vegetation (NIRv) was introduced by *Badgley et al.* (2017) as a measure for the fitness of the canopy structure and also a proxy for GPP. Recently, *Baldocchi et al.* (2020) studied NIRv for a network of sites in central California and reported high correlations between canopy photosynthesis and reflected near infrared radiation for "half-hourly, daily, seasonal, annual and decadal time scales across the wide range of function and structure and weather conditions". We use SIF and NIRv to study the drought response of the Amazon forest productivity and to further interpret the patterns in optimized NEE fluxes from CTSAM.

We use a custom version of the SIFTER retrieval that is dedicated to the humid conditions in the tropics and that was previously used by *Koren et al.* (2018) (in the remainder of the text we refer to this preliminary release as 'SIFTER v2-prelim'). The SIFTER v2-prelim

retrieval algorithm is an update to SIFTER v1 (*Sanders et al.*, 2016) and operates on radiances measured by the GOME-2A instrument on-board the MetOp-A satellite. Our SIFTER v2-prelim dataset covers the period 2007-2016 at a monthly temporal resolution and 0.5°×0.5° spatial resolution (the dataset is available at: `https://doi.org/10.18160/ECK0-1Y4C`). It is known that the SIF signal from GOME-2A exhibits a decreasing trend, particularly in the Amazon (*Zhang et al.*, 2018). To correct for this, we applied a linear trend correction for the Amazon region (similiar to *Koren et al.*, 2018).

We also used the official SIFTER v2 product that is described by *van Schaik et al.* (2020) and that is available on the KNMI data portal (`http://www.temis.nl`). This version has a more elaborate correction for the sensor degradation, based on the measured radiances at the reference site Libya-4 (*Neigh et al.*, 2015). Unfortunately, the more sophisticated sensor degradation correction is not sufficient to remove the decaying trend for the Amazon (see Fig. 9 in *van Schaik et al.*, 2020), suggesting a latitudinal dependence of the sensor degradation. To correct for this, we removed the residual trend in the SIFTER v2 over the Amazon, similar to *Koren et al.* (2018).

Another proxy for GPP is the Near-Infrared Reflectance of terrestrial vegetation (NIRv) which is defined as the product of (soil corrected) Normalized Difference Vegetation Index (NDVI) with Near-Infrared Reflectance (NIR) (*Badgley et al.*, 2017). We use two NIRv datasets. First, we calculated NIRv from a Moderate Resolution Imaging Spectroradiometer (MODIS) surface reflectance product (available at: `https://doi.org/10.5067/MODIS/MCD43C4.006`) that combines measurements from the MODIS Terra and MODIS Aqua satellites. The surface reflectances are corrected for the position of the sun and the viewing angle of the satellite (Nadir Bidirectional Reflectance Distribution Function (BRDF)-corrected) as documented in detail on the MODIS data portal. The data set has a spatial resolution of 0.05°×0.05° and a daily temporal resolution. Fig. 5.1 shows the annual mean MODIS NIRv over South America for the year 2012.

Secondly, we also calculated NIRv from the Multi-Angle Implementation of Atmospheric Correction (MAIAC) surface reflectance product (`https://doi.org/10.5067/MODIS/MCD19A1.006`). This product is also based on measurements from the MODIS Aqua and Terra satellites, but has a different cloud detection algorithm and an aerosol correction scheme (*Lyapustin et al.*, 2011a,b, 2012, 2018). Before calculating NIRv, we normalized the surface reflectances to a fixed nadir view and 45° solar zenith angle using the provided MAIAC BRDF parameters (`https://doi.org/10.5067/MODIS/MCD19A3.006`). Finally, we re-gridded the MAIAC NIRv from its 1 km resolution in sinusoidal projection to a 1°×1° grid. This allows us to create anomaly maps on a regular latitude-longitude grid,

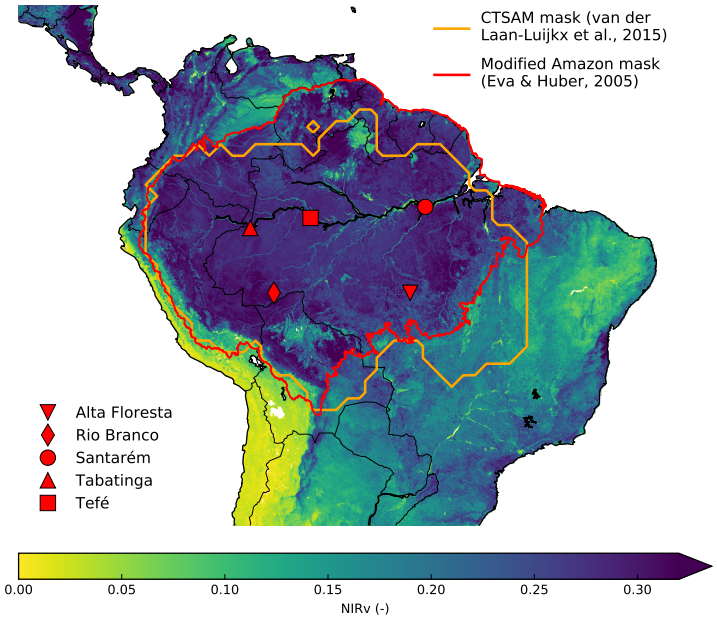

Figure 5.1: Annual mean NIRv calculated from MODIS surface reflectance for the year 2012. Regions with high NIRv can be interpreted as region with high CO_2 uptake by vegetation (Sect. 5.2.2). Transitions between the Amazon forest and rivers and mountains are clearly visible in the NIRv signal, while subtle gradients in NIRv can also be recognized within the heterogeneous Amazon region. The orange contour represents the 'CTSAM' Amazon mask that we used in this study and the previous studies by *van der Laan-Luijkx et al.* (2015), *Koren et al.* (2018) and *van Schaik et al.* (2018). The red contour defines the Amazon mask that is used in other studies of the CARBAM project (a modification of the mask defined by *Eva and Huber*, 2005, also see Sect. 5.2.4). The symbols indicate the location of the airports in the Amazon network.

similar to the other used products, and easily integrate over the Amazon mask.

5.2.3 CarbonTracker South America

5.2.3.1 Inverse modelling system

CarbonTracker South America (CTSAM) is a version of the inverse modelling system CarbonTracker Europe (*Peters et al.*, 2010; *van der Laan-Luijkx et al.*, 2017) dedicated to South America. CTSAM was introduced by *van der Laan-Luijkx et al.* (2015) to study the effect of the 2010 drought on the Amazon carbon balance. Here we give a brief description of the model system components: (1) the atmospheric transport model TM5; (2) the structure of the covariance matrix; and (3) the method for scaling prior fluxes to obtain optimized fluxes. The set of CO_2 observations used in the inversions are described

in more detail in Sect. 5.2.3.2 and the prior fluxes used in the inversions are described in Sects. 5.2.3.3–5.2.3.5.

The atmospheric transport in CTSAM is simulated by the atmospheric transport model TM5 (*Krol et al.*, 2005) which is driven by ERA-Interim meteorological fields (*Dee et al.*, 2011) from the ECMWF. We use a global resolution of 6°×4° with nested zoom regions of 3°×2° and 1°×1° over South America. The size and position of these zoom regions in CTSAM is shown in Fig. S2 in the Supplemental Material of *van der Laan-Luijkx et al.* (2015).

Ocean and Net Ecosystem Exchange (NEE) fluxes are optimized using an ensemble Kalman filter (*Peters et al.*, 2005) by adjusting weekly scaling factors λ_r for each land and ocean region:

$$F(x,y,t) = \lambda_r^{\text{bio}} \cdot F_{\text{bio}}(x,y,t) + \lambda_r^{\text{ocean}} \cdot F_{\text{ocean}}(x,y,t) + F_{\text{ff}}(x,y,t) + F_{\text{fire}}(x,y,t) \quad (5.1)$$

The sources of CO_2 from fossil fuels (F_{ff}) and fires (F_{fire}) are imposed (i.e. not optimized). For land regions outside South America, the scaling factor λ_r is constant within 'ecoregions': these are the different Olson land cover regions (*Olson, J. S. and Watts, J. A. and Allison, L. J.*, 1985) within the different TransCom regions (*Gurney et al.*, 2002). Within South America, a gridded 1°×1° state vector is used, with an exponentially decreasing covariance based on the distance (relative to length scale of 300 km) for grid cells within the same biome (described in more detail by *van der Laan-Luijkx et al.*, 2015). The ocean fluxes are solved for 30 different ocean regions with a covariance structure based on the ocean inversion by *Jacobson et al.* (2007). The total number of degrees of freedom for one statevector (spanning 7 days) is approximately 409.

Note that throughout the text, we use 'NEE' to refer to the prior and optimized biosphere fluxes, whereas the term 'Net Biome Exchange' (NBE) is used to refer to the combination of NEE and fires, following the conventions laid out by *Kirschbaum et al.* (2001). Note that this differs from the terminology that was used in the previous studies about the Amazon carbon cycle by *Gatti et al.* (2014) and *van der Laan-Luijkx et al.* (2015), where NBE referred to the sum of NEE and non-fire disturbances.

All simulations (See Table 5.1) are performed using the CarbonTracker data assimilation shell (CTDAS) (*van der Laan-Luijkx et al.*, 2017), which is accessible in the Wageningen University software repository (`https://git.wur.nl/ctdas`). More background information about CarbonTracker Europe can be found online (`https://www.carbontracker.eu`).

Table 5.1: Overview of different CO_2 inversions that were performed in our study. We performed 15 flask-based inversions (denoted by 'F') by combining the 5 biosphere flux estimates with the 3 sets of biomass burning emissions. In addition we did 5 inversions using XCO_2 from OCO-2 as observational constraint (without flask data).

		Fire fluxes		
		GFED4	GFAS	GFASopt
Biosphere fluxes	3-hrly SiBCASA	F	F	F
	3-hrly SiBCASA-PCR	F	F	F
	3-hrly SiBCASA clim.	F/XCO_2	F/XCO_2	F/XCO_2
	3-hrly SiB4	F	F/XCO_2	F
	1.5-hrly Bodesheim neutral	F	F/XCO_2	F

5.2.3.2 CO_2 observations

Atmospheric CO_2 observations are essential inputs to our CO_2 inversions. In this study, we used vertical profiles of CO_2 sampled with small aircraft over the Amazon and measured at the LaGEE lab in the Instituto Nacional de Pesquisas Espaciais (INPE). The locations of the aircraft sites are depicted in Fig. 5.1. The effect of water vapor on the measured CO_2 mole fractions is currently under investigation. In addition, a vast amount of measurements contained in the ObsPack GLOBALVIEWplus v4.2 (*Cooperative Global Atmospheric Data Integration Project*, 2019) are assimilated in the inversions. To avoid 'double use' of data, we did not assimilate the Amazon aircraft data that are part of the ObsPack GLOBALVIEWplus v4.2.

In addition, we have performed inversions where we used CO_2 columns (XCO_2) from the OCO-2 satellite (NASA retrieval algorithm v9, *Crisp et al.*, 2004) in a modified CTDAS framework that can assimilate them (*Florentie et al.*, 2019). To cope with the large volume of data from OCO-2, we averaged the observations over 10 second time intervals ('superobservations', *Crowell et al.*, 2019) before assimilation, yielding about 205.4 data points/month over the Amazon (see Fig. S5.1). In the inversions we used only OCO-2 observations over land, from both glint and nadir view. The OCO-2 data product starts in 2014 and thus does not have a full coverage over the 2010–2017 period that we consider.

Note that for the inversions described here, we used either flask data or OCO-2 data, such that there is some degree of independence between these two approaches to optimize CO_2 fluxes. Moreover, we note that our flask-based inversions stopped halfway December 2017, and that we used the mean fluxes of this period in previous years for the missing weeks of 2017.

5.2.3.3 Biosphere prior fluxes

In this study, we focus on the biosphere fluxes in the Amazon, and we therefore want to assess the influence of the choice of prior biosphere fluxes on our results. We therefore use different biosphere priors in our inversions which are derived using different approaches.

For the majority of the simulations (see Table 5.1) we use the Simple Biosphere Carnegie-Ames-Stanford Approach (SiBCASA) model (*Schaefer et al.*, 2008). SiBCASA is a terrestrial biosphere model that uses meteorological fields from ERA-Interim (*Dee et al.*, 2011) and remotely sensed Normalized Difference Vegetation Index (NDVI) as its inputs. This model is also used as default biosphere prior for the CarbonTracker Europe (CTE) inversions (*van der Laan-Luijkx et al.*, 2017). The SiBCASA fluxes are available at 3-hourly temporal resolution at a $1^\circ \times 1^\circ$ spatial resolution.

Previous research has shown that the drought response of SiBCASA needs to be improved. *Peters et al.* (2018) showed that the positive effects of increased radiation are in some cases too strong compared with the stress from limited water availability. To improve the soil moisture levels in SiBCASA, *van Schaik et al.* (2018) coupled SiBCASA to the high resolution hydrological model PCR-GLOBWB (*Sutanudjaja et al.*, 2018). The PCR-GLOBWB model uses precipitation as input and calculates the hydrological balance for each grid cell. Horizontal exchange of water follows a detailed rooting scheme and the resulting river discharge was validated using independent gauge measurements. We used the CO_2 fluxes from the coupled PCR-GLOBWB-SiBCASA model as prior for our inversions (in the remainder of the text we abbreviate this as 'SiBCASA-PCR'). We use the resulting monthly totals of GPP and Terrestrial Ecosystem Respiration (TER) for the years 2010–2016, which we scaled with the mean diurnal cycle of GPP and TER from the default SiBCASA prior to reconstruct a diurnal cycle for the SiBCASA-PCR GPP and TER. These were subsequently added to obtain the NEE prior for our inversions. For the year 2017 we used the mean fluxes from the years 2010–2016.

In addition to the SiBCASA model, we have used prior biosphere fluxes from the improved biosphere model SiB4 (*Haynes et al.*, 2019a,b), which has prognostic phenology, multiple Plant Functional Types (PFTs) per grid cell and also includes carbonyl sulfide and SIF modules. The recent study from *Smith et al.* (2020) for the European drought of 2018 indicates that SiB4 biosphere fluxes agree better with independent observations from flux sites and remote sensing during droughts in Europe, in comparison to those from SiBCASA.

In addition to the biosphere priors from the process-based models SiBCASA and SiB4,

we use CO_2 fluxes from *Bodesheim et al.* (2018), which is a data-based product developed at the Max Planck Institute (MPI) for Biogeochemistry. These CO_2 fluxes are based on machine learning methods applied to measurements from the FLUXNET community to derive patterns between CO_2 fluxes, meteorological variables and remotely sensed data (not including SIF and NIRv). Using their patterns, the algorithm predicts CO_2 fluxes globally at a spatial resolution of $0.5^\circ \times 0.5^\circ$ and half-hourly temporal resolution. We have coarsened the fluxes to be $1^\circ \times 1^\circ$ and 1.5-hourly, which is the rate at which the biosphere fluxes are read by the atmospheric model TM5.

There is a caveat in the use of the machine learned fluxes from *Bodesheim et al.* (2018) in our atmospheric model, which is related to the magnitude of its annual global NEE of –21.42 PgC/yr. This is caused by the time scales at which the CO_2 fluxes are estimated and possibly also related to the unequal distribution of flux sites over different ecosystems. This estimate is an order of magnitude too large (e.g. *Friedlingstein et al.*, 2019) and would result in a rapid decay of atmospheric CO_2 in a forward model simulation. An inverse model would reduce the magnitude of this number, but would likely still be incorrect unless very large uncertainties were assigned. To overcome this issue, we have made the CO_2 fluxes carbon neutral on annual basis for each grid cell by adding a constant value (different for each grid cell, constant in time) to NEE. This approach avoids that unrealistic uptake (negative NEE) in the tropics is compensated by excessive release of CO_2 in the extra-tropics, while maintaining the characteristic shapes of the diurnal and seasonal cycles that are shown in Fig. 5.2 and described below.

Following the examples of *Alden et al.* (2016) and *Gloor et al.* (2018), we have also used prior fluxes from which we removed the interannual variability ('SiBCASA-clim' and 'Bodesheim-neutral'), to create climatological CO_2 fluxes from the years 2001–2014. By using a climatological biosphere prior we ensure that the interannual variability (IAV) in the posterior biosphere flux is driven by the atmospheric CO_2 observations assimilated into the inverse model.

Table 5.1 shows an overview of the different inverse simulation that we have performed. To highlight the differences between the biosphere priors, we show the mean diurnal cycle for September and the mean seasonal cycle for the Amazon region in Fig. 5.2. The diurnal cycle of NEE is dominated by light-availability and is reasonably similar for the different products shown. For SiBCASA, the morning zero-crossing of NEE occurs earlier than for the fluxes from *Bodesheim et al.* (2018), whereas the difference in timing of the afternoon zero-crossing is relatively small. Due to the higher temporal resolution of *Bodesheim et al.* (2018), the structure in NEE during the morning/afternoon transition and the day-time

is better resolved.

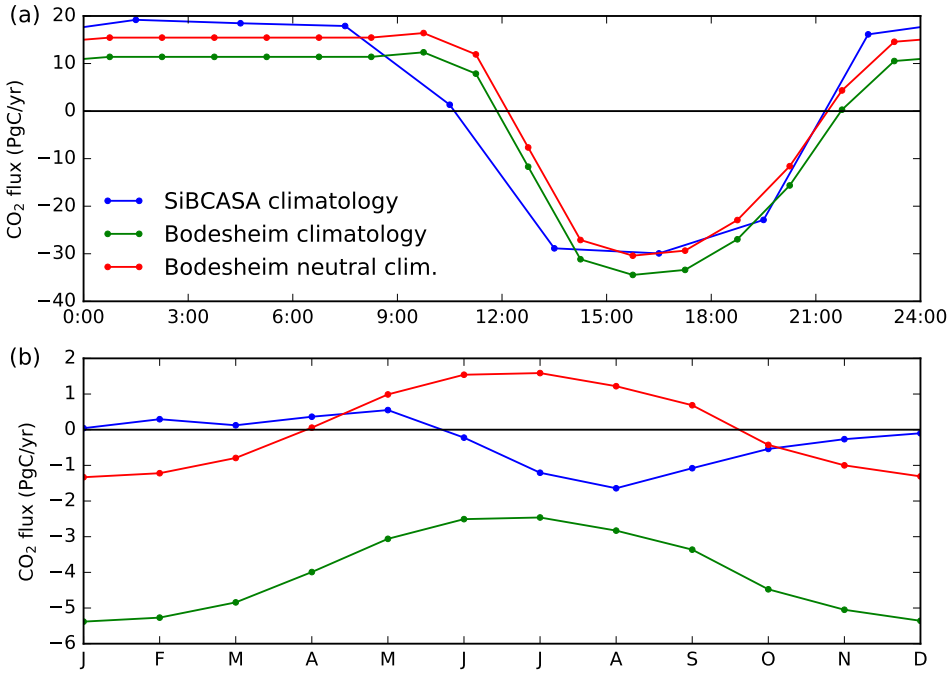

Figure 5.2: Mean temporal variation of prior NEE fluxes within the Amazon region for climatologies derived from the terrestrial biosphere model SiBCASA (*Schaefer et al.*, 2008) and a machine learned product (*Bodesheim et al.*, 2018). **(a)** Mean diurnal cycle of NEE for September. The time axis is in UTC; the local time for the Amazon region ranges from UTC-3 to UTC-5. **(b)** Mean seasonal cycle of NEE.

As can be seen in Fig. 5.2b, the original NEE climatology from *Bodesheim et al.* (2018) is substantially lower (i.e. more uptake of CO_2) than the NEE from SiBCASA. Contrary to the original fluxes from *Bodesheim et al.* (2018), the NEE from SiBCASA shows months where respiration dominates photosynthesis (NEE > 0) and periods in which the reverse (NEE < 0) occurs. By making the NEE fluxes from *Bodesheim et al.* (2018) carbon neutral on annual basis, the seasonal cycle becomes nearly the opposite of the SiBCASA NEE. This gives us substantial variation from the different biosphere priors, which allows to assess the sensitivity of the optimized biosphere fluxes to the choice of prior fluxes.

5.2.3.4 Biomass burning emissions

Fire is one of the major components of the carbon cycle in the Amazon. In the CTSAM inversion system, the CO_2 fire emissions are imposed, and not optimized, as described in Sect. 5.2.3.1 and therefore have an effect on the optimized biosphere fluxes. To assess the effect of the imposed fire emissions on our inversion results, we have used different biomass

burning emissions. We used the SiBCASA Global Fire Emissions Database v4 (SiBCASA-GFED4, *van der Velde et al.*, 2014) emissions and the Global Fire Assimilation System (GFAS, *Kaiser et al.*, 2012) emissions. In addition to the default GFAS CO_2 emissions, we have derived 'optimized' GFAS CO_2 emissions from the CO inversion by *Naus et al.* (in prep.), which we describe briefly below.

The CO inversion is performed with the TM5-4DVAR system (*Hooghiemstra et al.*, 2011; *Nechita-Banda et al.*, 2018) to optimize GFAS CO emissions. CO observations from NOAA background stations are used to optimize total CO emissions outside the TM5 zoom regions over South America and CO columns from satellite observations by the Infrared Atmospheric Sounding Interferometer (IASI) instrument are used to optimize CO emissions released through biomass burning within the TM5 zoom regions over South America (see Fig. S2 in *van der Laan-Luijkx et al.*, 2015, for the extent of the zoom regions). Within the zoom regions, CO biomass burning emissions are optimized in steps of 3 days for the months April to December (i.e. 9 months), which contains the typical Amazon burning season. Only for the El Niño year 2015, the burning continued longer (as discussed by *Naus et al.*, in prep.) and an additional inversion from November 2015 to May 2016 (i.e. 7 months) was performed.

To translate the optimized CO inversion results into CO_2 fire emissions for our imposed prior, we used the following method. For every $1^\circ \times 1^\circ$ grid cell in the zoom region over South America of the CO inversion (*Naus et al.*, in prep.), we determine a scaling factor $CO_{opt}/CO_{prior}(x,y,t)$ that is applied to the prior GFAS CO_2 emissions to get at 'optimized' CO_2 biomass burning emissions. The implicit assumption in this approach is that the CO:CO_2 emission ratios used by GFAS are correct and that the change between the posterior and prior CO emissions are attributable to uncertainty in the amount of burned carbon. In the scaling, we discarded the first and last months of the CO inversion to account for spin-up or spin-down effects. For the months outside the CO inversion window and for grid cells outside the Amazon region, we use the GFAS prior emissions. We realize that these optimized GFAS emissions also include uncertainties, which is why we use the three alternative biomass burning emission estimates as imposed priors in our CO_2 inversion (see Table 5.1 for the overview).

5.2.3.5 Fossil fuel and ocean fluxes

In CTSAM, we use imposed fossil fuel emissions that were derived by the Institute of Energy Economics and Rational Energy Use (IER) for the CARBONES project. These

fossil fuel fluxes are also used in the global CarbonTracker Europe (CTE) inversions and, like the fire emissions, these are not optimized. Combustion of fossil fuels is the largest source of CO_2 to the atmosphere, of about 9.5 PgC/yr globally for the decade 2009-2018 (*Friedlingstein et al.*, 2019). Within the Amazon region, the CO_2 released through local fossil fuel emissions is relatively small compared to net ecosystem exchange and fire emissions, which are described in more detail in Sects. 5.2.3.3 and 5.2.3.4, respectively.

The prior ocean CO_2 fluxes are calculated from the partial pressure difference of CO_2 from the ocean inversions by *Jacobson et al.* (2007). The air-sea gas exchange is further enhanced by windspeed according to *Wanninkhof* (1992), based on the meteorological fields from ERA-Interim (*Dee et al.*, 2011). Finally, the sea ice fraction from ERA-interim is used to scale down the ocean exchange of CO_2 for each grid cell in the domain. Within CTSAM, ocean fluxes are optimized weekly as described in Sect 5.2.3.1.

5.2.4 Integration over Amazon basin area

It is important to note the choice of the mask to define 'the Amazon'. Previous studies have used different masks, which compromises the comparison of the results. For instance, the tropical South American domain selected by *Liu et al.* (2017) exceeds the area of our Amazon mask by ∼40% (Fig. S7 in *Koren et al.*, 2018). In this study we used the same mask as in our previous works (*van der Laan-Luijkx et al.*, 2015; *Koren et al.*, 2018; *van Schaik et al.*, 2018), and we have made this publicly available here: `https://doi.org/10.18160/P1HW-0PJ6`. Throughout the text we will refer to our integration over the CTSAM mask, and specifically mention results created over the modified mask from *Eva and Huber* (2005, see Fig. 5.1) which is also used in other studies. Their boundaries are illustrated in Figure 5.1, and one critical difference is the extension of the CTSAM beyond the forest-savannah transition that forms the arc-of-deforestation, thus including more signals (e.g., from biomass burning).

5.3 Results

We start our analysis of the Amazon carbon cycle and its relation with environmental drivers from an annual perspective in Sect. 5.3.1, with the analysis kept brief because a separate analysis of the full record 2010–2017 will be presented by Gatti et al. (in prep.). Subsequently, we look at droughts in 2010 and 2015/16 and the recoveries in the

post-drought years specifically (Sect. 5.3.2) as seen from the net CO_2 exchange over the Amazon derived with CTSAM. Finally we move towards a sub-yearly description for 2016 and highlight the secondary drought observed in the 2016 dry season in Sect. 5.3.3.

5.3.1 Interannual variability in the Amazon

The droughts of 2010 and 2015/16 had distinctly different characters in hydrological forcing. The 2010 dry season experiencing lower than average precipitation and soil moisture simultaneously, while in 2015 the vegetation first suffered from anomalously low precipitation, later followed by very strong depletion of soil moisture in 2016. Fig. 5.3 shows the annual anomalies in precipitation from MSWEP and ERA-Interim and soil moisture estimates diagnosed by GRACE and GLEAM integrated over the Amazon basin ('CTSAM' mask in Fig. 5.1) along with their spatial anomalies in Fig. 5.4. The latter immediately highlights the spatial differences in the recent droughts. Reductions in both precipitation and soil moisture occurred in 2010 in the central Amazon region, whereas in 2015, specifically precipitation was very low throughout the Amazon, with the most extreme values in the northeastern region. We furthermore note the widespread soil moisture depletion in 2016, in agreement with reductions of GRACE terrestrial water storage for 2016 reported by *Erfanian et al.* (2017). This large area affected suggests a potentially important role for soil moisture drought stress on photosynthesis in 2015/2016, as we investigated specifically in *Koren et al.* (2018) and in *van Schaik et al.* (2018).

Reductions in primary production of the Amazon basin follow the patterns of soil moisture depletion. In 2010 and 2011 this creates a dipole with most severe reductions to the south of the Amazon, and positive anomalies in the Cerrado region to the east of the Amazon, whereas the reductions are more widespread and distributed uniformly for the years 2015 and 2016. Fig. 5.3 shows these annual anomalies for NIRv calculated from MODIS and MAIAC surface reflectance, and for SIF from the SIFTER product from GOME-2 integrated over the Amazon. The most extreme reductions in NIRv and SIF occur in the drought years 2010 and 2015, and to a lesser extent in 2016, indicating the reductions in GPP in those years. The spatial distribution of the NIRv anomalies is shown in Fig. 5.4. Comparison between the top and bottom panel in Fig. 5.3 shows that years with negative anomalies in soil water correspond to years with negative anomalies in NIRv and SIF, and therefore reduced GPP, confirming reported strong controls of water on the carbon cycle of the Amazon, further discussed in Sect. 5.4.

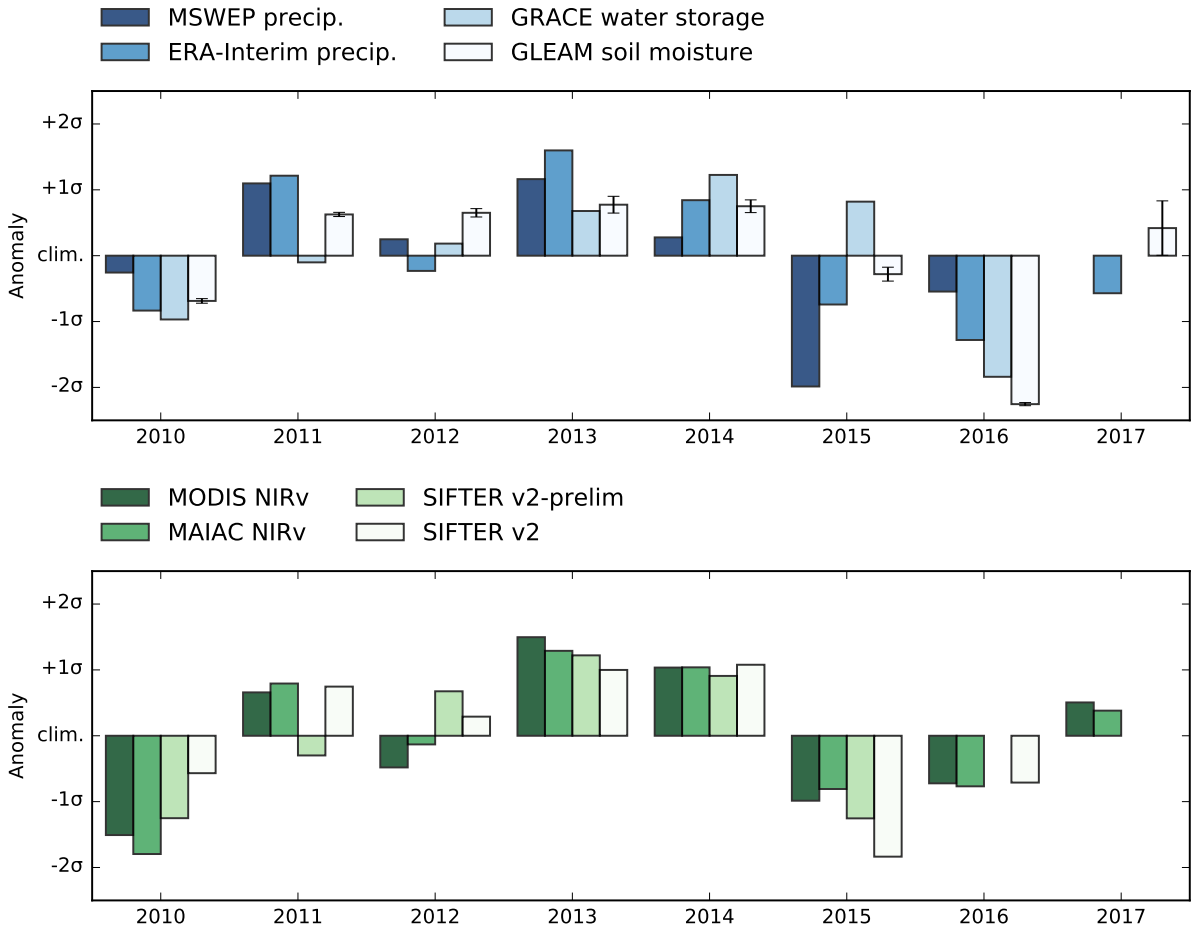

Figure 5.3: Annual anomalies of (top) precipitation, soil moisture, and (bottom) NIRv, and SIF integrated over the CTSAM domain. Anomalies are expressed in standard deviation relative to the years 2010-2017. Note that the GRACE satellites did not complete the year 2017 and we could thus not determine an annual anomaly for that year. The error bar for GLEAM shows the range between GLEAM v3.3a and v3.3b. Note that the SIFTER data is not included over the full record, since the SIFTER data suffers from sensor degradation, which is most pronounced in the later years (described in Sect. 5.2.2).

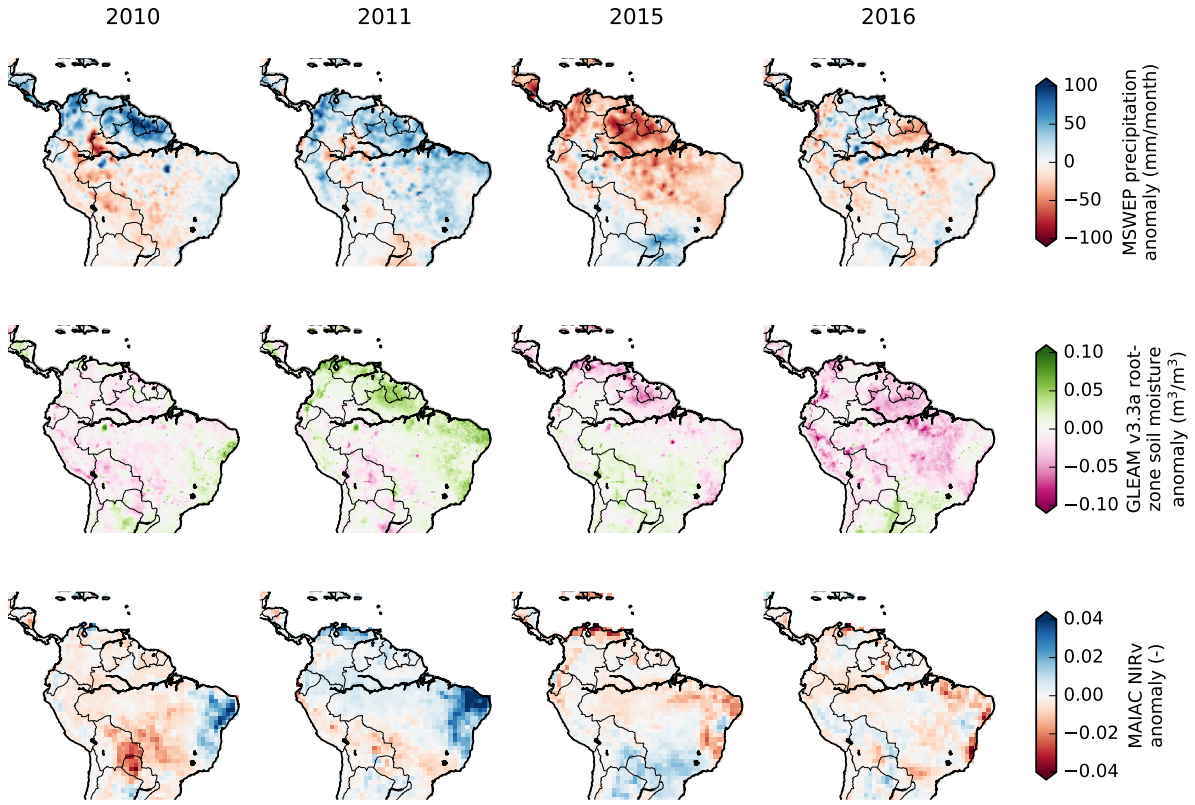

Figure 5.4: Overview of annual anomalies of MSWEP precipitation (first row), GLEAM root-zone soil moisture (second row) and MAIAC NIRv (third row) for the years 2010 (first column), 2011 (second column), 2015 (third column), and 2016 (fourth column) for tropical South America. The anomalies are calculated relative to the baseline 2010-2017.

5.3.2 Net CO_2 fluxes during and after drought years

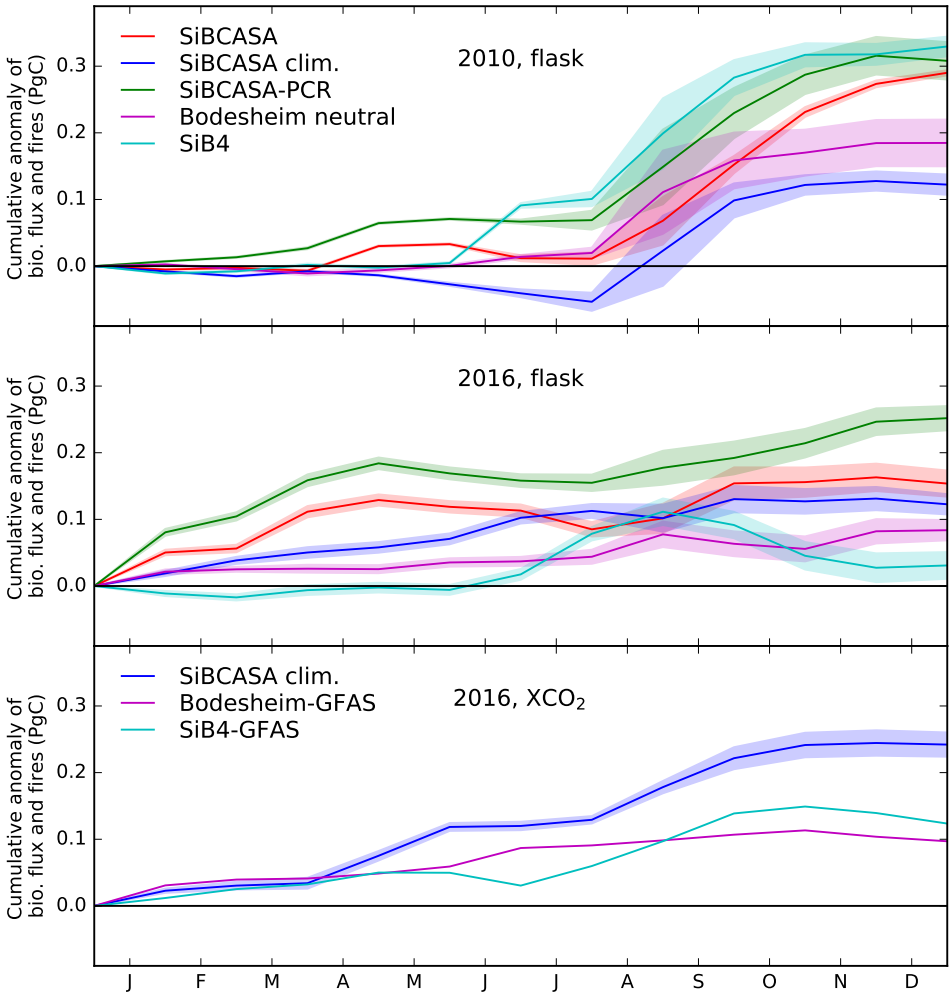

Figure 5.5: Accumulated anomaly of total CO_2 exchange (optimized biosphere fluxes and imposed fire fluxes) over the Amazon region for the drought years 2010 (first row) and 2016 for flask-based inversions (second row) and 2016 for XCO_2 inversions (third row). For flask-based inversions, the anomalous emissions are calculated relative to the baseline 2010-2017. For the XCO_2 inversions we used a shorter baseline (October 2014 - December 2017). The shading indicates the standard deviation due to the different fire products.

The timing of the drought impacts on net biome exchange (NBE, the sum of net ecosystem exchange (NEE) and disturbance losses, *Kirschbaum et al.*, 2001) strongly differed between 2010 and the 2015/16 El Niño and aligns with the hydrological forcings shown in the previous section. This confirms that sub-annual NBE variations due to large droughts can be observed robustly from the atmosphere, both in flask-based inversions as well as in XCO_2-based estimates. In Fig. 5.5 we show the accumulated anomalies in the total exchange of CO_2 for the Amazon region during the drought years 2010 and 2016. We did

not include the year 2015, which included the start of the El Niño drought, since in that period, there were no observations from the Amazon aircraft network. Clearly, the 2010 NBE anomalies accumulated from the anomalous dry season and leveled off before the end of the year when conditions returned to normal. In contrast, the 2016 anomalies first accumulate as soil moisture stress resulting from the El Niño-induced drought persisted until late February, and a secondary accumulation occurs after June, to be discussed in the next section. Note that in this figure, we show the accumulation starting from January, whereas the accumulation in early 2016 builds on the anomaly already started at the end of 2015 (not shown). Uncertainty on these estimates mostly concerns the magnitude of the impact but not its sign, and we acknowledge that also the assumed a-priori information plays a role in the inverse results.

We find that in the flask-based inversions, the choice of biosphere priors has a larger impact on the optimized fluxes than the choice of biomass burning emissions. This is seen from the different lines in Fig. 5.5, which represent different simulations with alternative prior biosphere fluxes. The shaded uncertainty on each line is based on the alternative simulations with different imposed biomass burning emissions (see Sect. 5.2.3.4). Biosphere-only and fire-only versions of this result are included as Figs. S5.2 and S5.3, illustrating the important role of fires in this area. For the XCO_2 inversions, we find different absolute net fluxes than from the flask-based inversions, with the Amazon basin representing a source of carbon based on XCO_2 (not shown). The interannual variability is similar between the flask-based and XCO_2 inversions with positive anomalies in 2016. There is more convergence among the XCO_2 inversions in the absolute flux estimates, and the choice of prior biosphere fluxes has less influence on these optimized results (not shown), which can be explained by the larger amount of observations that can be assimilated. Alternative ocean priors from CarboScope did not impact our results or conclusions.

The persistence of reduced carbon uptake by vegetation seen through atmospheric CO_2 inversions during these major droughts is quantified in Table 5.2, which shows the anomalies of the net CO_2 fluxes derived by CTSAM relative to the baseline from 2010–2017. The table includes different simulations with alternative prior biosphere fluxes and the uncertainty is based on the alternative simulation with different biomass burning emissions. The consistently positive anomalies in 2010 and 2016 are contrasted by the near-neutral or even negative anomalies in the following years, which coincide with an absence of fire-anomalies as well. Each drought leads to reductions in biospheric uptake, the magnitude of which depends on the character of the drought, which also determines the magnitude as fire-induced carbon emissions.

Table 5.2: Annual anomalies of total biosphere fluxes (imposed fire fluxes and optimized biosphere fluxes), optimized biosphere fluxes, and fire fluxes, integrated over the Amazon for drought years (2010, 2016) and post-drought years (2011, 2017), relative to the baseline 2010-2017 for our flask-based inversions. For the total fluxes and optimized biosphere fluxes, the inversions are aggregated for each biosphere prior and the specified uncertainty denotes the standard deviation between the inversions with different fire products.

	CTSAM prior	2010	2011	2016	2017
Total flux anomaly (PgC)	SiBCASA	0.29 ± 0.0	0.02 ± 0.04	0.15 ± 0.02	-0.12 ± 0.02
	SiBCASA clim.	0.12 ± 0.02	-0.07 ± 0.04	0.12 ± 0.02	-0.06 ± 0.03
	SiBCASA-PCR	0.31 ± 0.03	-0.24 ± 0.05	0.25 ± 0.02	-0.05 ± 0.04
	Bodesheim neutral	0.19 ± 0.04	-0.24 ± 0.06	0.08 ± 0.02	0.04 ± 0.04
	SiB4	0.33 ± 0.02	-0.1 ± 0.05	0.03 ± 0.02	-0.04 ± 0.01
Bio opt flux anomaly (PgC)	SiBCASA	0.12 ± 0.04	0.14 ± 0.04	0.12 ± 0.01	-0.2 ± 0.03
	SiBCASA-PCR	-0.05 ± 0.03	0.06 ± 0.04	0.09 ± 0.01	-0.14 ± 0.02
	SiBCASA-PCR	0.14 ± 0.02	-0.12 ± 0.02	0.22 ± 0.01	-0.13 ± 0.01
	Bodesheim neutral	0.01 ± 0.01	-0.11 ± 0.01	0.05 ± 0.01	-0.04 ± 0.01
	SiB4	0.16 ± 0.03	0.02 ± 0.02	0.0 ± 0.01	-0.12 ± 0.04
Fire anomaly (PgC)	SiBCASA-GFED4	0.24	-0.2	0.03	0.13
	GFAS	0.12	-0.04	0.0	0.01
	GFAS opt.	0.16	-0.14	0.06	0.1

The 2010 drought led to strong impact from additional biomass burning emissions, which were added to the impact from reduced biosphere uptake. The 2015/16 El Niño drought did impact the biosphere uptake, but did not lead to enhanced fire emissions, as the main impact occurred towards the end of the typical fire-season. Fig. 5.6 shows further results from our flask-based inversions, separately for the anomalies of the prior and posterior biosphere fluxes, and the imposed fire fluxes for the drought years and post-drought years. The contrast between drought and post-drought years is clearly visible for the total (fire plus biosphere), and the agreement between the different inversions is large there. Also, the biomass burning emissions from the three alternative estimates are in good agreement. The largest differences are found for the biosphere response, both in the prior estimate as well as in the optimized results. The differences in the prior biosphere estimates show that this is still poorly constrained from biosphere models alone, and that combining with atmospheric CO_2 observations leads to convergence of the estimates, specifically in 2016-2017. For 2010, the optimized biosphere fluxes show a large degree of variation. This is also caused by the large imposed fire anomaly, which leaves little flexibility in the inversion. By using the neutral Bodesheim prior biosphere estimate, we independently derive the drought-post-drought contrast, which matches well with the

other estimates that did have this response already included in the prior. For 2015, the spread in the optimized biosphere fluxes is large. This is caused by the lack of aircraft samples collected over the Amazon in that year. This spread shows the important value of the aircraft samples, which confirms the experiments that were reported by *van der Laan-Luijkx et al.* (2015) and *Gloor et al.* (2018) to purposely leave out aircraft data in some of their inversions.

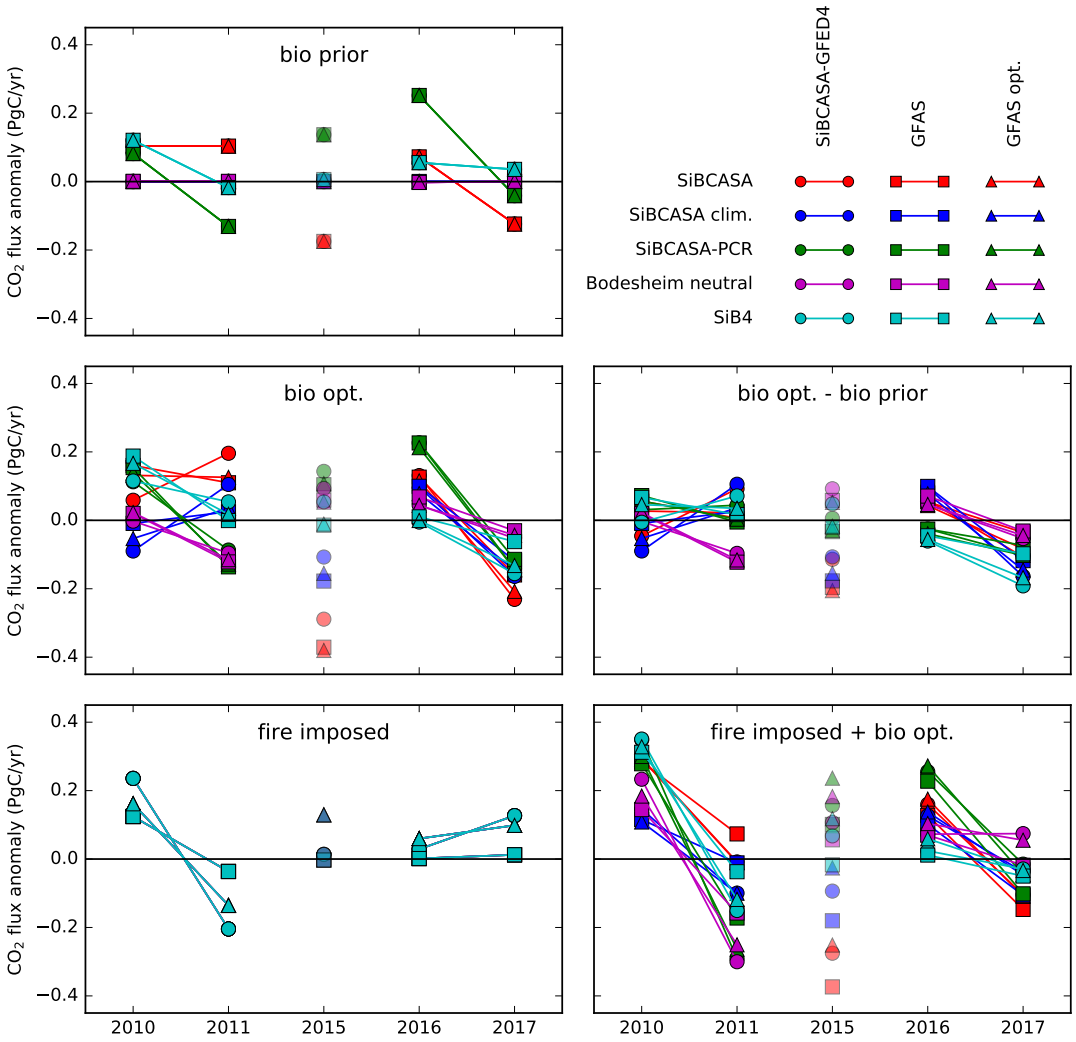

Figure 5.6: Annual anomalies of land fluxes integrated over the Amazon CTSAM mask, relative to the years 2010-2017. These results are from the flask-based inversions. Inversions with different biosphere priors are indicated with different colors, while different symbols/markers differentiate between inversions with different biomass burning inputs.

The atmospheric CO_2 observations are of high importance in our inversions, and the aircraft profiles cover a large region over the Amazon basis (Fig. 5.1). The number of samples (one profile contains roughly ten samples) from each aircraft site is shown in Fig. S5.4. The figure furthermore includes the annual RMSE between simulated and observed

CO_2 mole fractions for each location. As expected, there is a clear improvement in the simulated CO_2 from flask-optimized fluxes compared to that from the prior fluxes. In contrast, there is not a clear improvement for all sites and years for the OCO-2 inversions, according to this metric. RMSE is sensitive to outliers, and a more detailed analysis of the OCO-2 residuals is required.

5.3.3 Extended carbon cycle drought impact in 2016

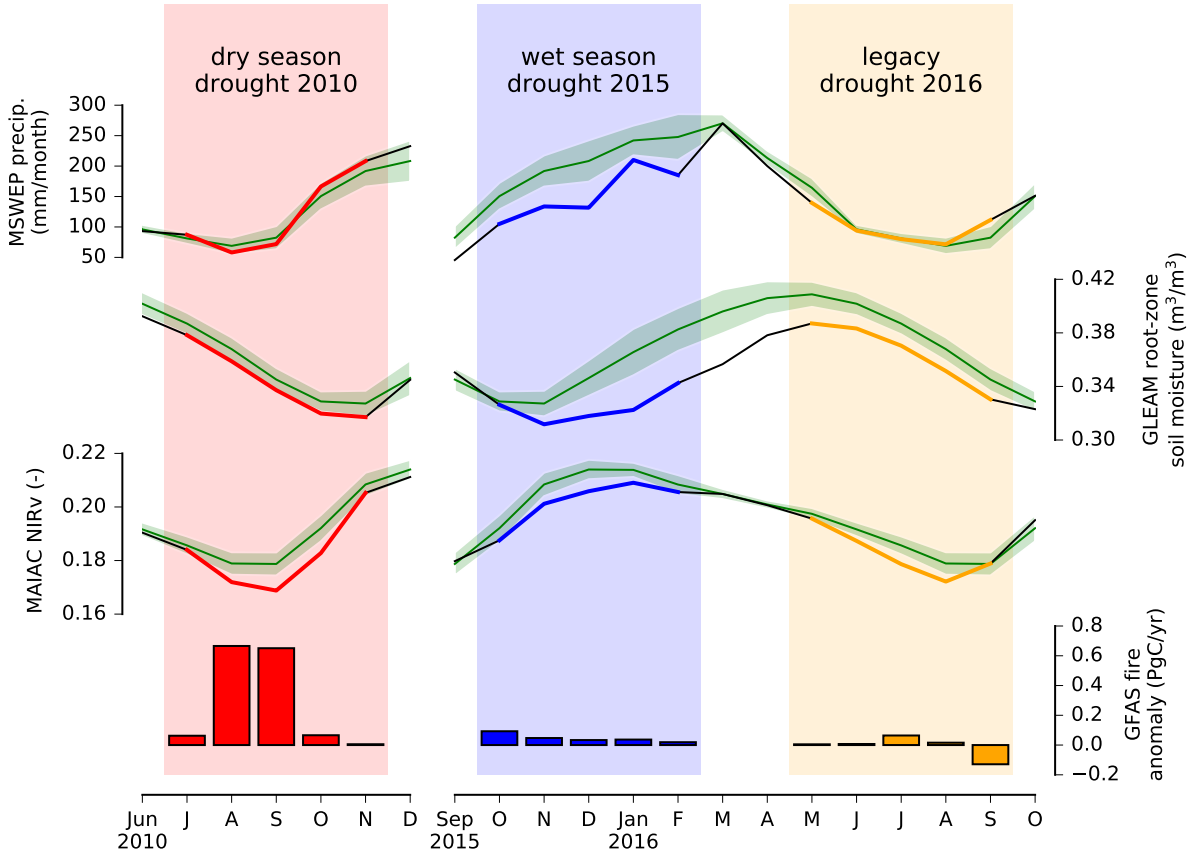

Figure 5.7: Variations of MSWEP precipitation (first row), GLEAM root-zone soil moisture (second row), MAIAC NIRv (third row), and GFAS fire emission anomalies (fourth row) in the Amazon region. The climatology of the baseline (2010-2017) is shown in green and the green shading indicates the standard deviation around the mean. The conditions during the drought events of 2010, 2015 and 2016 are indicated in red, blue, orange, respectively.

The secondary drought in 2016 is, in contrast to the 2010 and the 2015/16 El Niño events, not accompanied by a strong reduction in precipitation, and both temperature and VPD have come down to climatological values by April 2016. Only soil moisture levels remain well-below normal levels, as a legacy of the earlier precipitation deficit from the preceding

El Niño drought. Fig. 5.7 illustrates this legacy drought (alternative estimates, including temperature, VPD and SIF, are shown in Figs. S5.5–S5.10). Compared to the monthly climatological values over 2010–2017, patterns of anomalies for the drought periods in 2010, 2015 and 2016 for precipitation, soil moisture, and NIRv demonstrate their large ($\gg$1-σ) magnitude, and concurrence in time. The secondary 2016 drought event did not lead to excessive fire emissions that were typical for earlier droughts, suggesting a possibly unique role of biospheric signals in our observations.

The 2016 legacy drought comes after the recovery of atmospheric forcings, and also NIRv shows an initial return to high primary production during the 2016 wet season suggesting that vegetation has left its earlier stressed state. Recovery of soil moisture does not occur until October 2016 however, and we speculate that the secondary reduction in productivity results from renewed stress on vegetation, which tries to maintain hydraulic conductance needed for photosynthesis, but cannot maintain sufficient water potential unless stomata are opened beyond a tolerable level given the high VPD typical for the dry season. This would have been less of a problem during the wet months before, where VPD was much lower and precipitation exceeded the 100 mm/month thresholds typically used as indicator for stress (January-February-March, 270 mm/month). Other mechanisms contributing to reduced primary productivity might relate to the changes in leaf-age and canopy structure observed by *Gonçalves et al.* (2020), or to insufficient recovery of the xylem or mesophyll from previous stress. Both would represent legacy effects from the previous drought, which we discuss further in Sect. 5.4. We furthermore note that the shown reduction in NIRv is likely to reflect changes in GPP, but the reductions could also reflect a sub-optimal light-interception by the canopy because of changes in the canopy structure, leaf-angles, and leaf-age and/or chlorophyll content.

To add a spatial dimension to the 2016 event, which would be the basis also for more mechanistic modeling of the observed NIRv reductions, we show in Fig. 5.8 the progression of the anomalies of precipitation, soil moisture and NIRv for 3-monthly periods in 2016. These figures show that in early 2016 (JFM), the Amazon region was severely affected by the ongoing El Niño drought in terms of low precipitation and low soil moisture levels, and that it took longer for soil moisture to recover, especially in the eastern parts. For NIRv, the figures also show the widespread nature of the negative impact of the drought on GPP, with lower than average NIRv throughout the Amazon in JAS-2016, and largest reductions in the northeastern region near Santarém that was the epicenter of the 2015/16 El Niño event. Future modeling of the vegetation in this specific doubly-impacted area, and possibly combining it with eddy-covariance measurements and forest inventory data from this region would be of great interest.

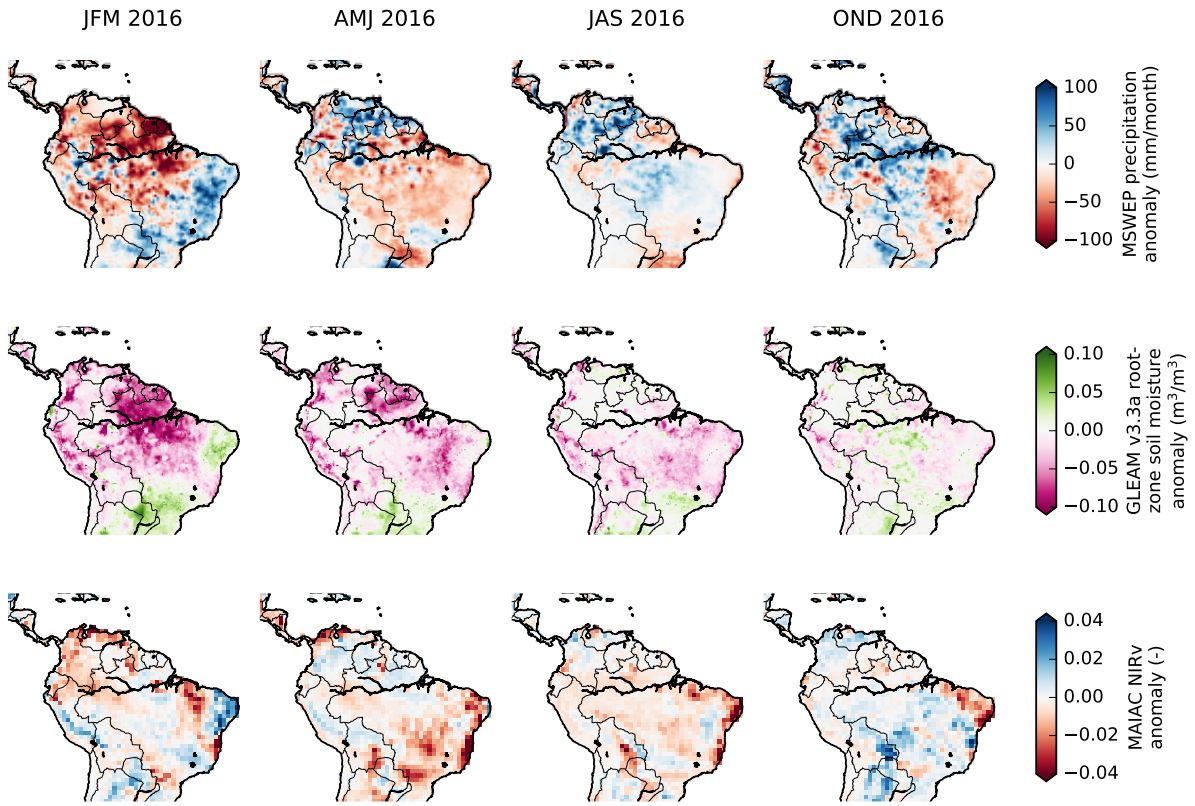

Figure 5.8: Overview of 3-monthly anomalies of MSWEP precipitation (first row), GLEAM root-zone soil moisture (second row) and MAIAC NIRv (third row) for the periods January-February-March, 2016 (first column), April-May-June, 2016 (second column), July-August-September, 2016 (third column), and October-November-December, 2016 (fourth column) for tropical South America. The anomalies are calculated relative to the respective 3-month periods of the baseline 2010-2017.

5.4 Discussion

We describe a secondary drought impact on the carbon cycle in 2016, shown as a reduction of both MODIS and MAIAC NIRv, after an initial recovery from the 2015/2016 El Niño drought. Its impact manifests itself in NIRv, and its relatively small impact on NEE is also suggested from atmospheric CO_2 inversions. Interestingly, excessive fires do not seem to have played a role in contrast to the earlier 2005, 2010, and 2015/16 drought events. We would have expected that the continuation of low soil moisture conditions and possible availability of extra fuel (in the form of coarse woody debris and weakened vegetation) post El-Niño would have created conducive conditions for extra deforestation and biomass burning (*van der Werf et al.*, 2009). We can therefore currently not explain the absence of large fire emissions in the dry season of 2016. As for the impact on GPP, NIRv, and ultimately NEE, we currently only present hypotheses to be tested using

further observations from eddy-covariance and forest inventory data, and from biosphere modeling. Figure 5.9 summarizes our current view.

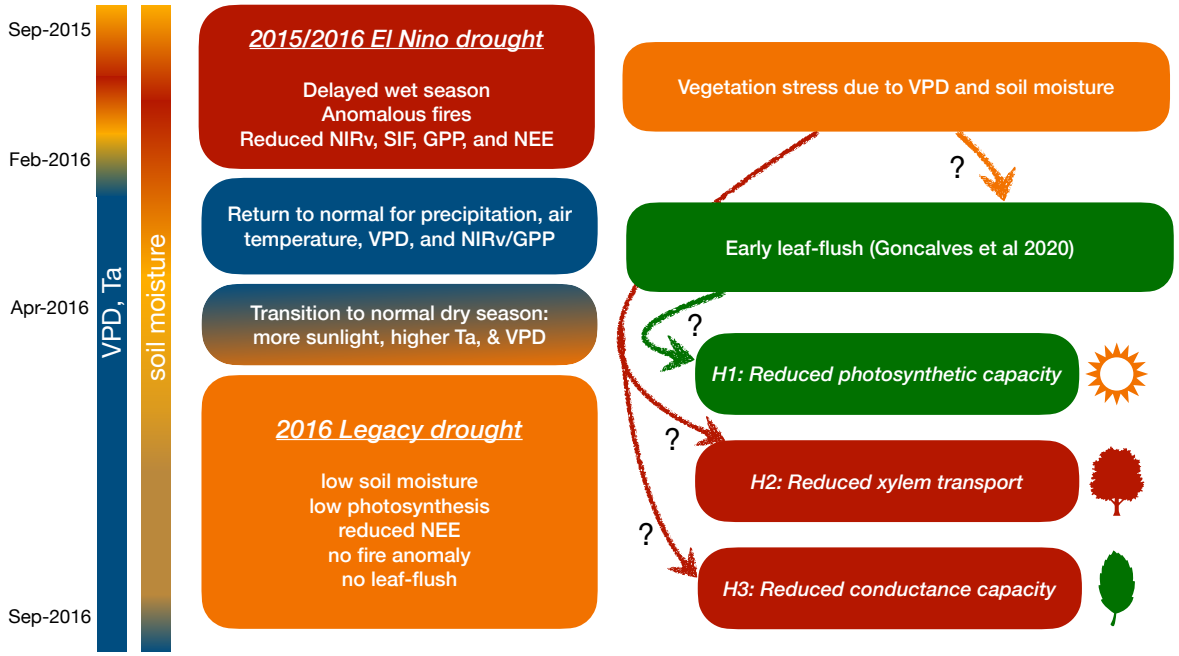

Figure 5.9: Schematic of the timing of several events during the 2015/2016 El Niño drought and the subsequent 2016 dry season legacy drought, that lead to the formulation of three hypotheses (H1, H2, H3) discussed in the main text.

From multiple lines of evidence, we know that soil moisture depletion during the El Niño event led to enhanced stress in vegetation, and in turn to strong reductions in GPP (and its proxies). Impacts on plant physiology are largely unknown, but belated drought effects were observed by *Gonçalves et al.* (2020) for the ATTO and K34 towers. Based on MAIAC EVI and phenocam data, the observed "paucity of flushing crowns" in June and July 2016 was ascribed to precocious leaf flush in February and March 2016, when the El Niño drought was considered to be over (*Gonçalves et al.*, 2020). A first hypothesis (labeled H1 in our schematic and extensively discussed in *Gonçalves et al.* (2020)) is that these new leaves were an early replacement of drought-damaged ones, leading to suboptimal leaf demography with reduced photosynthetic capacity (Pc) during the following dry season, reducing primary productivity (and hence NIRv). The Pc of tropical vegetation was shown to be an important control on seasonal fluxes of GPP previously (*Restrepo-Coupe et al.*, 2017).

A second hypothesis (labeled H2) we put forward recognizes that where precipitation, temperature and VPD had indeed recovered to normal values in March 2016, soil moisture continued to be low through October 2016 when a regular wet season returned to the

basin. Access to this reduced soil moisture could have been maintained during the wet season when VPD is low, and stomatal control can maintain the canopy water potential (*Wolf et al.*, 2016a), even if hydraulic conductance is impaired from the previous (and ongoing) drought (*Eller et al.*, 2018; *Klein et al.*, 2018). This capacity to transport moisture upwards through the xylem was lost when regular dry season conditions returned along with higher atmospheric temperatures and vapor pressure deficits, necessitating stomatal closure to reduce evaporative water-loss. This would have resulted in a loss of evaporation and thus canopy water potential, and subsequent reduction of upward soil moisture transport which (along with stomatal closure) leads to a loss of primary productivity, an increase in water-use efficiency (*Peters et al.*, 2018), and a reduction in NIRv. Where normally the plants' carbohydrate reserves could have helped overcome this loss of photosynthesis, the occurrence of the 2016 legacy drought on top of the previous season's El Niño would have made for quite unique circumstances. Several models are available to further test this hypothesis, and we believe that this 2016 drought in fact constitutes an interesting opportunity to improve this branch of mechanistic biosphere modeling that has gained considerable traction in recent years (see *Zhou et al.*, 2013, for an overview).

A final mechanism to consider (H3) is that the conductance of the vegetation itself was impaired due to impacts of the previous and ongoing drought. For hydraulic conductance this would be due to continued moisture stress and high xylem embolism (*Wolf et al.*, 2016a; *Klein et al.*, 2018), although this apparently did not reach the point where it resulted in widespread mortality in subsequent years, which has not been reported. Alternatively, conductance of the mesophyll and even stomata could have been impaired due to drought stress and turgor in cells of the large fraction of leaves that was not flushed immediately following the 2015/16 drought event. We currently do not know if such physiological measurements from specifically this period are available, but it would be worth to engage the large community that monitors plant traits across the Amazon (e.g. *Oliveira et al.*, 2019) to further discuss this idea. As far as we are aware, only a few vegetation models (e.g. *Sperry et al.*, 2016) that cover the full Amazon basin would include such longer-term impacts on conductances, mostly for a lack of data to parameterize this impact.

We have performed a large set of inversions with alternative prior biosphere fluxes, biomass burning emissions and CO_2 observations. We find that these biosphere priors already show are large spread in their estimates, indicating that vegetation fluxes from the Amazon region are still less well-known in comparison to mid-latitude regions. Moreover, the interaction of these diurnally changing fluxes with the diurnal cycle in vertical transport

is particularly strong in tropical regions, giving rise to a strong 'rectifier' effect (*Gerbig et al.*, 2008; *Law et al.*, 2008). This means that up to ∼5km altitude, mixing by turbulence and shallow-cumulus clouds creates surface signals that preferentially express the daytime uptake that coincides with largest buoyancy (*Ouwersloot et al.*, 2013). Such vertical transport is notoriously difficult to present in large-scale models (e.g. *Peylin et al.*, 2013; *Krol et al.*, 2017), and we realize that replacing TM5 with a different global transport model (i.e., LMDz, IFS, or GEOS-CHEM) will give rise to similar spread as the biosphere priors that we show in Fig. 5.6. Using suites of prior fluxes in multiple transport models, and confronting them with independent observations (i.e., those not used by the data assimilation system to inform on the fluxes) remains our current preferred approach to assess the results (*Gaubert et al.*, 2019).

Our analysis is based on anomalies in comparison to the baseline of the years 2010–2017, across the Amazon region. This long baseline is unique, and overcomes he criticism on earlier studies (*Gatti et al.*, 2014; *van der Laan-Luijkx et al.*, 2015; *Alden et al.*, 2016; *Liu et al.*, 2017) where a contrast was made between a drought year, and the neighboring year that was considered to represent 'normal' conditions. We found this earlier criticism to be partly justified, and the choice of baseline to calculate the anomalies to indeed be important. We have selected 2010–2017 as the baseline for our analysis, which is the longest time span across which all variables that we study are available. This period includes two major droughts, plus the secondary drought in 2016. To check how our results depend on the baseline that we have selected, we have extended the NIRv record forward and backward in time, to cover the 15-year period 2005-2019, containing the major droughts of 2005, 2010 and 2015/16. Fig. S5.11 shows MODIS NIRv integrated over the CTSAM mask and the modified mask from *Eva and Huber* (2005, see Fig. 5.1). In both cases the minimum of the NIRv record occurs for July 2016, which further reinforces that this was a special event. We have compared the NIRv climatology based on the extended record (2005-2019) and our default baseline (2010-2017), and find that there is strong agreement between both, which suggests that our default baseline is sufficiently representative. If we take the years 2012-2013-2014 as a baseline, then the July 2016 NIRv reduction would be a '9-sigma event', which illustrates how sensitive the anomaly analysis can be to the baseline, and the importance of establishing datasets across long periods. The work of Gatti et al. (in prep) will present the full record of CO_2 observations from the Amazon aircraft network over the 2010–2017 period.

Finally, we briefly consider some innovations that can further increase our capability to monitor the Amazon carbon cycle from an atmospheric persecitve. We noted that the biosphere fluxes in the Amazon have a strong diurnal cycle (see Fig. 5.2), but the total

over any number of integral days is close to zero, as the large GPP and TER fluxes nearly balance (in constrast with the large seasonal cycle in the mid-latitudes). Our weekly multiplicative scaling factors scale the amplitude of this diurnal, weekly, and seasonal cycle based on daytime measurements during convective conditions, but changes must be very large ($\lambda \gg 1$) or small ($\lambda \ll 1$) to change the mean flux. We therefore also experimented with a setup where only uptake biosphere fluxes (i.e., NEE<0, 'daytime fluxes') or only positive biosphere fluxes can be scaled (i.e., NEE>0, 'nighttime fluxes'). These inversions resulted in optimized fluxes with a similar pattern in IAV, but with a larger amplitude than the fluxes that we reported here. This novel scaling method is potentially better suited for tropical regions, but it has not been rigorously tested and more research will be devoted to this in the near future. In addition, we have experimented with parameter inversions using SIF and NIRv as additional constraint (*Florentie et al.*, 2019). Initial tests have shown that this approach can be suitable for observational records that suffer from gaps (*Rödenbeck et al.*, 2018a,b), and this could potentially inform us better on the year 2015, which was not well observed from the aircraft network. Finally we mention other tracers, such as COS *Kooijmans et al.* (2019) and $\Delta^{17}O$ in CO_2 (*Hoag et al.*, 2005; *Koren et al.*, 2019), that have the potential to add additional constraints for disentangling the contributions of photosynthesis and respiration on the net CO_2 exchange.

5.5 Conclusions

We have presented an analysis of the Amazon carbon cycle and its environmental drivers for the period 2010–2017. We showed that the interannual variability in hydrological variables (precipitation, soil moisture) correlates with variations in proxies for GPP (NIRv and SIF). The years 2010, 2015 and 2016 were dry and we found associated basin-wide reductions in productivity. In addition, we performed atmospheric inversions using aircraft profiles of CO_2 collected over the Amazon forest and XCO_2 from OCO-2 to estimate variations in NEE over the Amazon region. We focused on the drought years 2010 and 2016 and found that for these drought years the Amazon exchange of CO_2 was 0.3–0.5 PgC and 0.0–0.3 PgC higher (i.e., less uptake, or more release) than for the subsequent years, 2011 and 2017, respectively. The large-scale droughts of 2010 and the 2015/2016 El Niño drought have been studied extensively in recent literature, whereas a secondary drought in 2016 received little attention. *Gonçalves et al.* (2020) reported reductions in MAIAC EVI for two tower sites near Manaus, and related this to a cascade of leaf-phenology events that was set off by the 2015/2016 El Niño drought. Based on MODIS and MAIAC NIRv, we show for the first time that there was a basin-wide reduction in productivity,

occurring in the 2016 dry season. Furthermore, we showed that soil moisture anomalies are substantial at the onset of the 2016 dry season drought, whereas VPD is close to its climatological value, suggesting that soil moisture depletion is a possible cause of the 2016 dry season drought.

Supplemental information

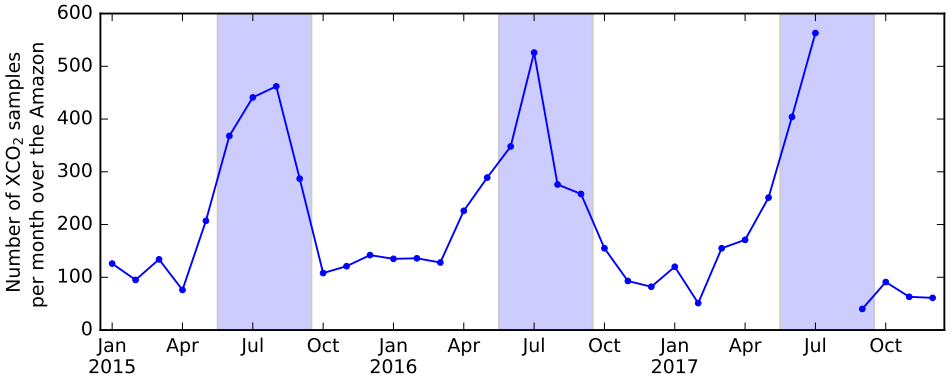

Figure S5.1: Total number of XCO_2 'superobservations' over the Amazon that were assimilated in our XCO_2 inversions. The shading indicates the dry season period (the months June-July-August-September), where more XCO2 retrievals were obtained. Note that in August 2017 there was no XCO_2 data due to technical issues that affected the satellite.

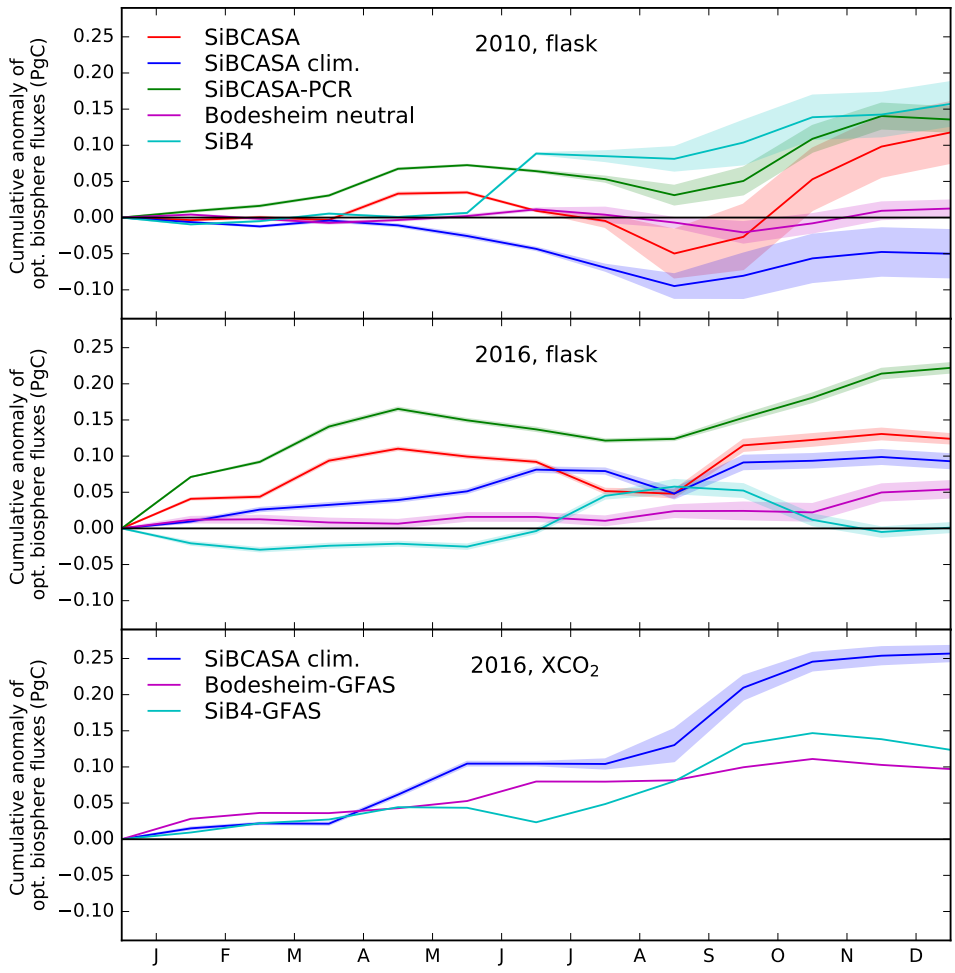

Figure S5.2: Accumulated anomaly of optimized biosphere CO_2 exchange over the Amazon region for the drought years 2010 (first row) and 2016 for flask-based inversions (second row) and 2016 for XCO_2 inversions (third row). For flask-based inversions, the anomalous emissions are calculated relative to the baseline 2010-2017. For the XCO_2 inversions we used a shorter baseline (October 2014 - December 2017). The shading indicates the standard deviation due to the different fire products.

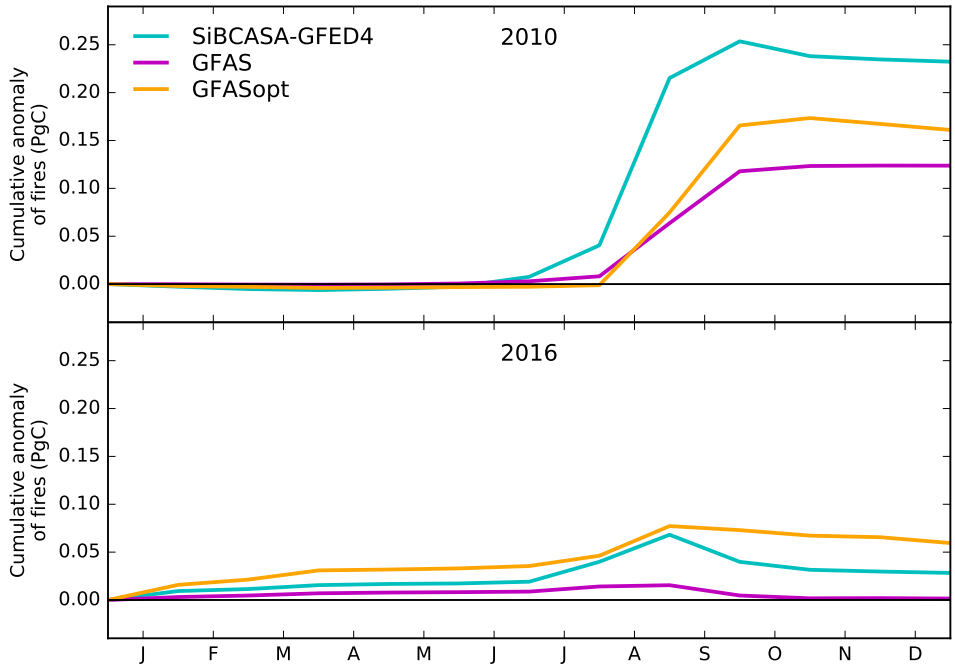

Figure S5.3: Accumulated anomaly of imposed fire CO_2 emissions over the Amazon region for the drought years 2010 (top) and 2016 (bottom). The anomalous emissions are calculated relative to the baseline 2010-2017.

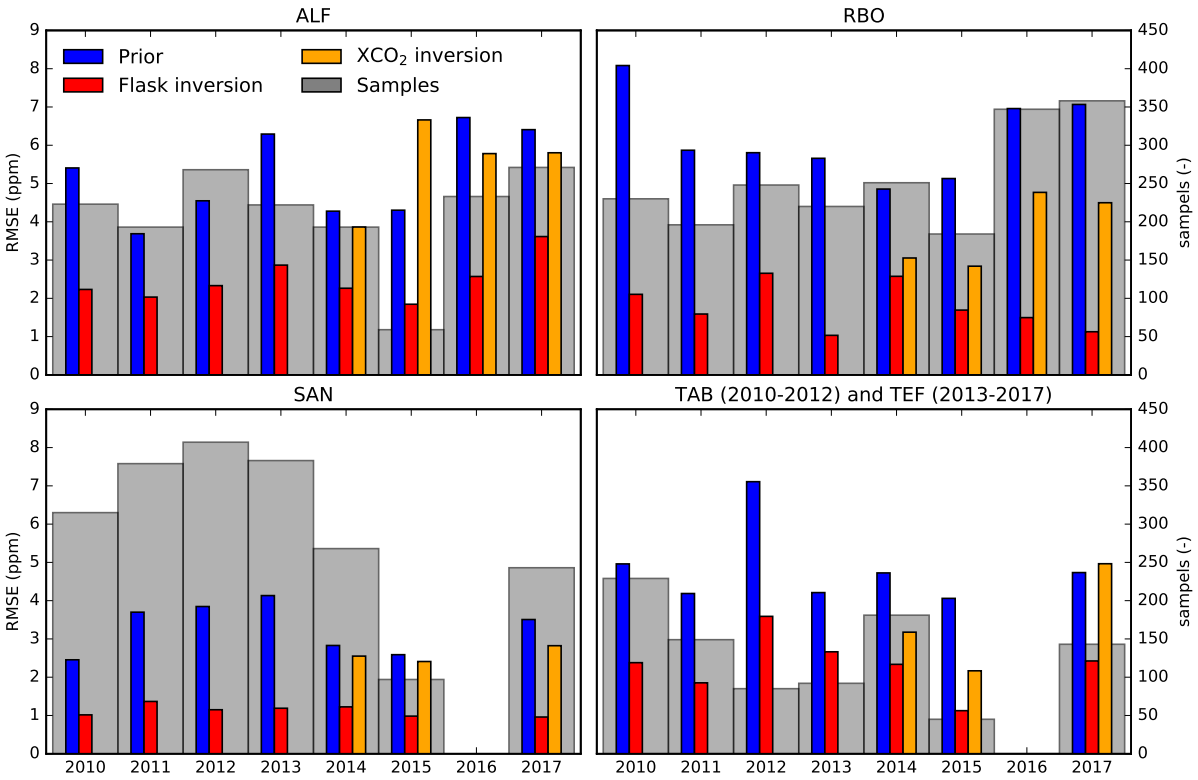

Figure S5.4: Annual Root Mean Squared Error (RMSE) of the residuals between the simulated and observed CO_2 mole fractions for the aircraft sites Alta Floresta (ALF), Rio Branco (RBO), Santarém (SAN) and Tabatinga/Tefé (TAB/TEF). The prior flux simulation and the two inversions are based on the combination of the SiBCASA clim. biosphere fluxes with GFAS fires. We also included OCO-2 data for 2014, but is should be noted that the OCO-2 record does not cover that full year. The number of flask samples from the Amazon aircraft sites is also indicated.

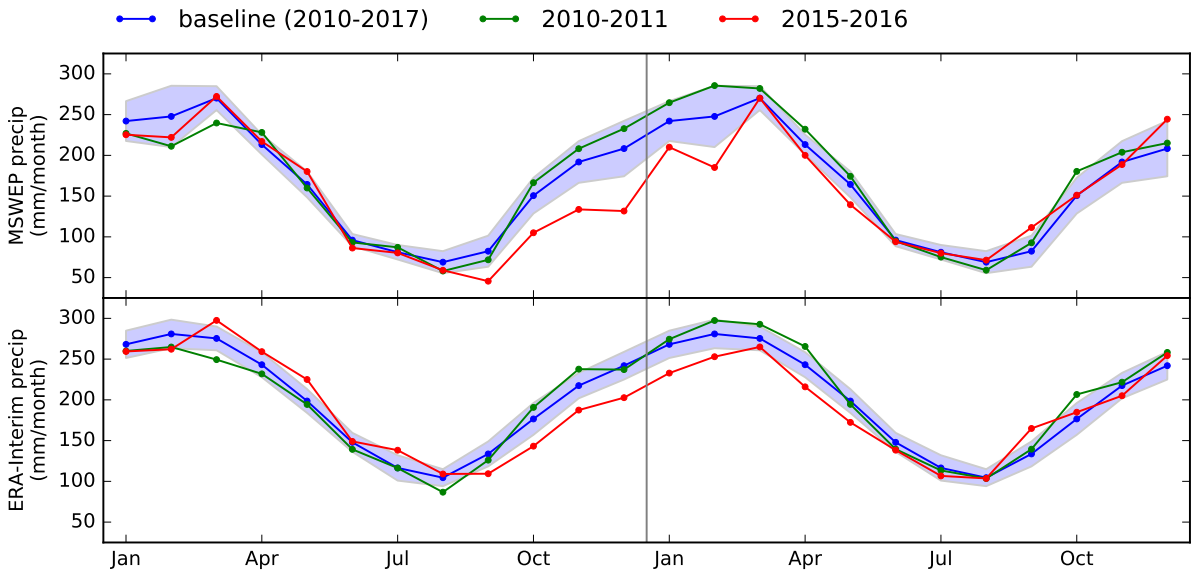

Figure S5.5: Monthly variation of MSWEP precipitation (top) and ERA-Interim precipitation (bottom) integrated over the Amazon region for periods of two consecutive years. The baseline was determined for the years 2010-2017, the shading indicates the standard deviation around the mean.

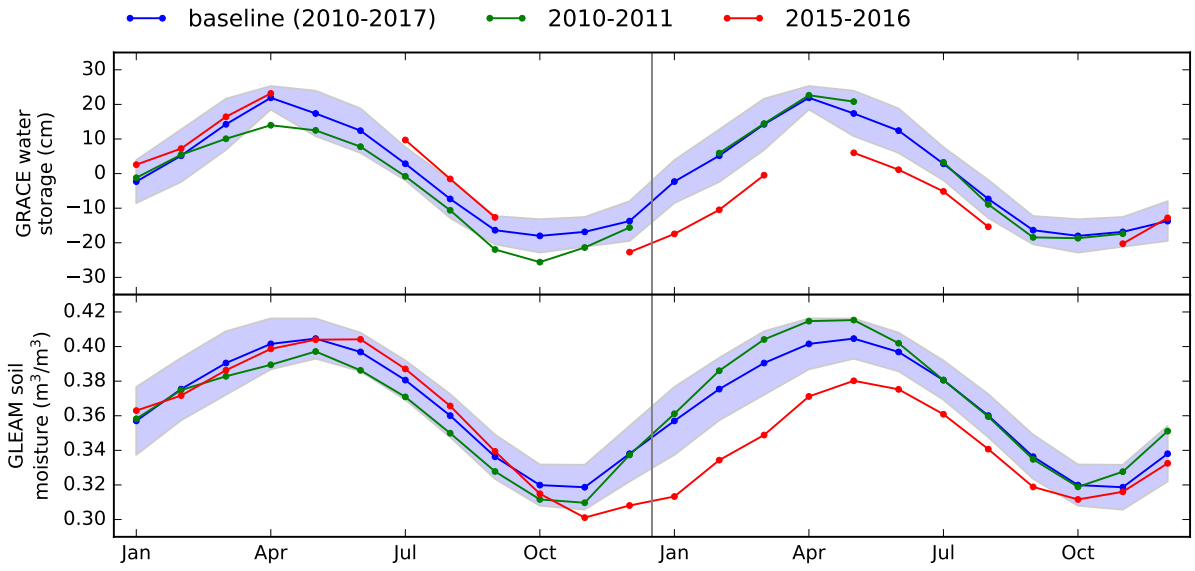

Figure S5.6: Monthly variation of GRACE terrestrial water storage anomalies (top) and GLEAM root-zone soil moisture (bottom) integrated over the Amazon region for periods of two consecutive years. The baseline was determined for the years 2010-2017, the shading indicates the standard deviation around the mean. Note that not all months contain valid retrievals for the GRACE product.

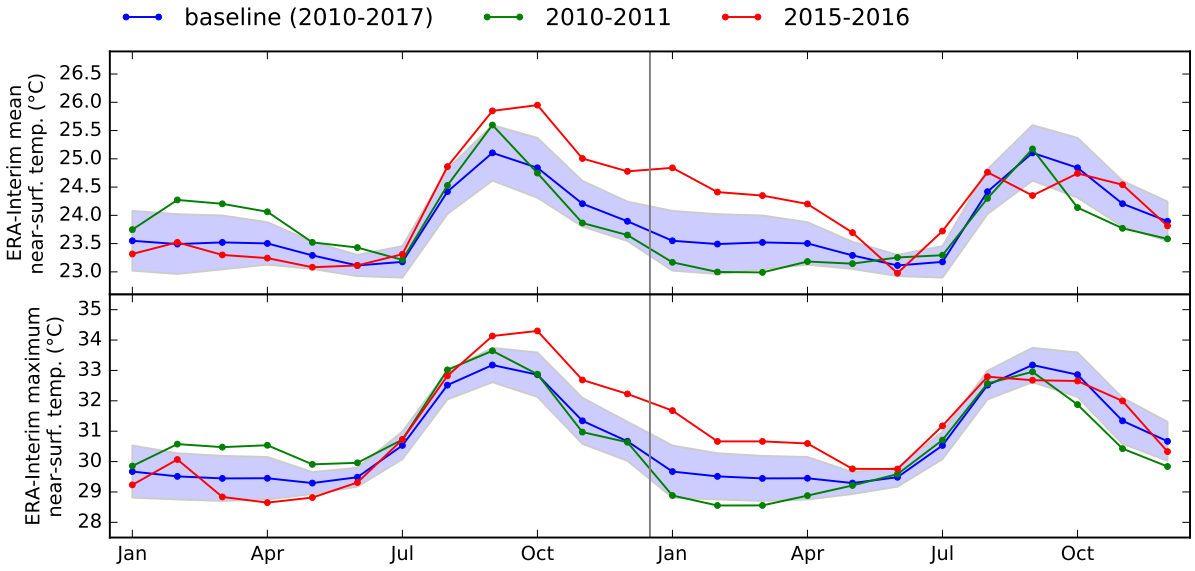

Figure S5.7: Monthly variation of ERA-Interim mean near-surface temperature (top) and ERA-Interim maximum near-surface temperature (bottom) integrated over the Amazon region for periods of two consecutive years. The baseline was determined for the years 2010-2017, the shading indicates the standard deviation around the mean.

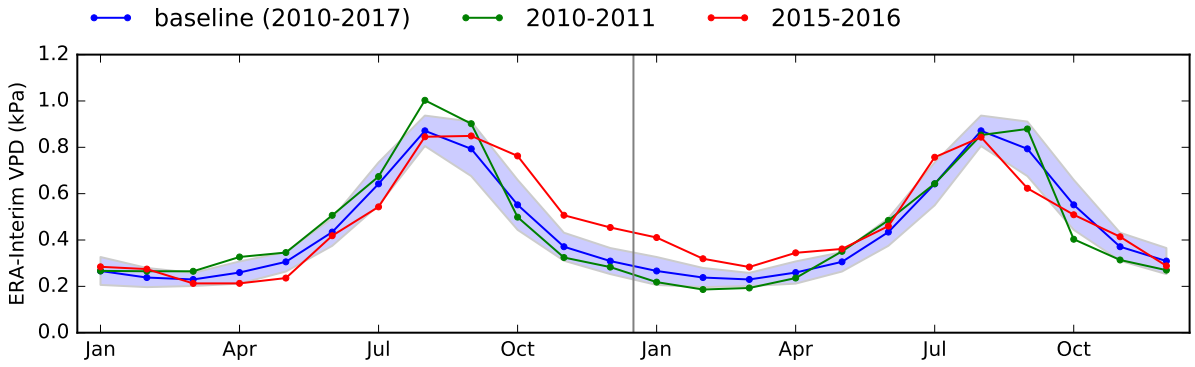

Figure S5.8: Monthly variation of ERA-Interim vapor pressure deficit (VPD) integrated over the Amazon region for periods of two consecutive years. The baseline was determined for the years 2010-2017, the shading indicates the standard deviation around the mean.

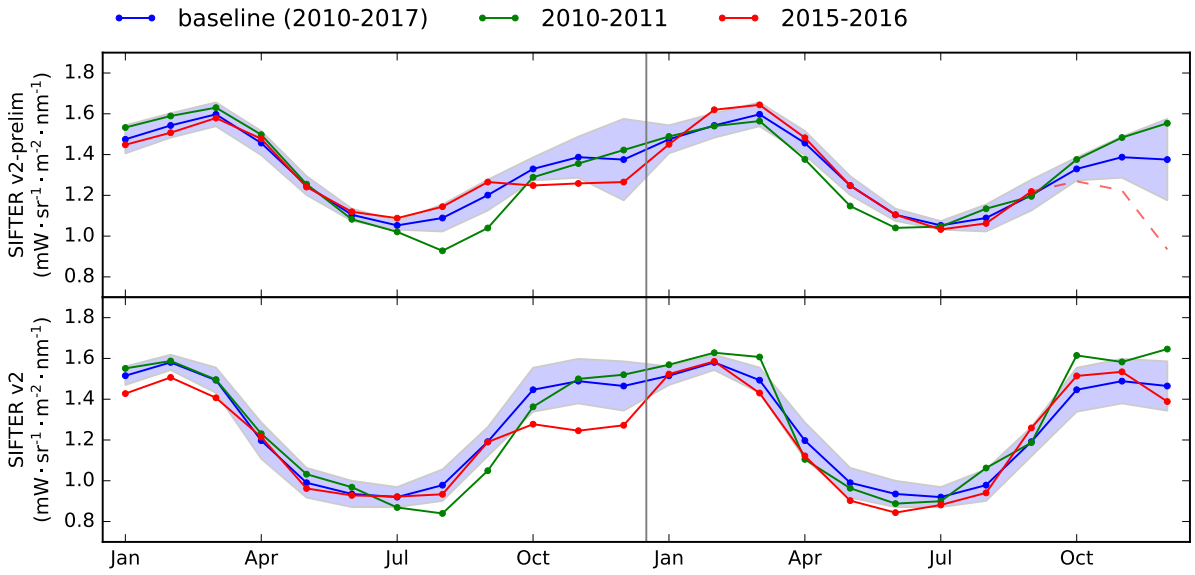

Figure S5.9: Monthly variation of SIFTER v2-prelim (top) and SIFTER v2 (bottom) integrated over the Amazon region for periods of two consecutive years. The baseline was determined for the years 2010-2017, the shading indicates the standard deviation around the mean. Note that both products were linearly detrended over the Amazon region.

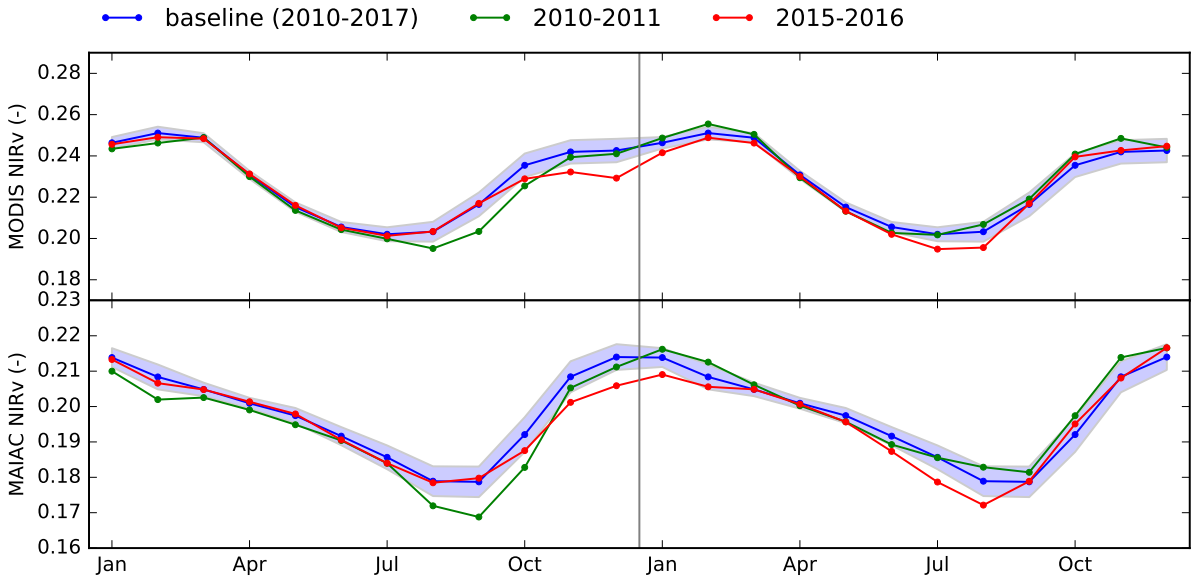

Figure S5.10: Monthly variation of MODIS NIRv (top) and MAIAC NIRv (bottom) integrated over the Amazon region for periods of two consecutive years. The baseline was determined for the years 2010-2017, the shading indicates the standard deviation around the mean.

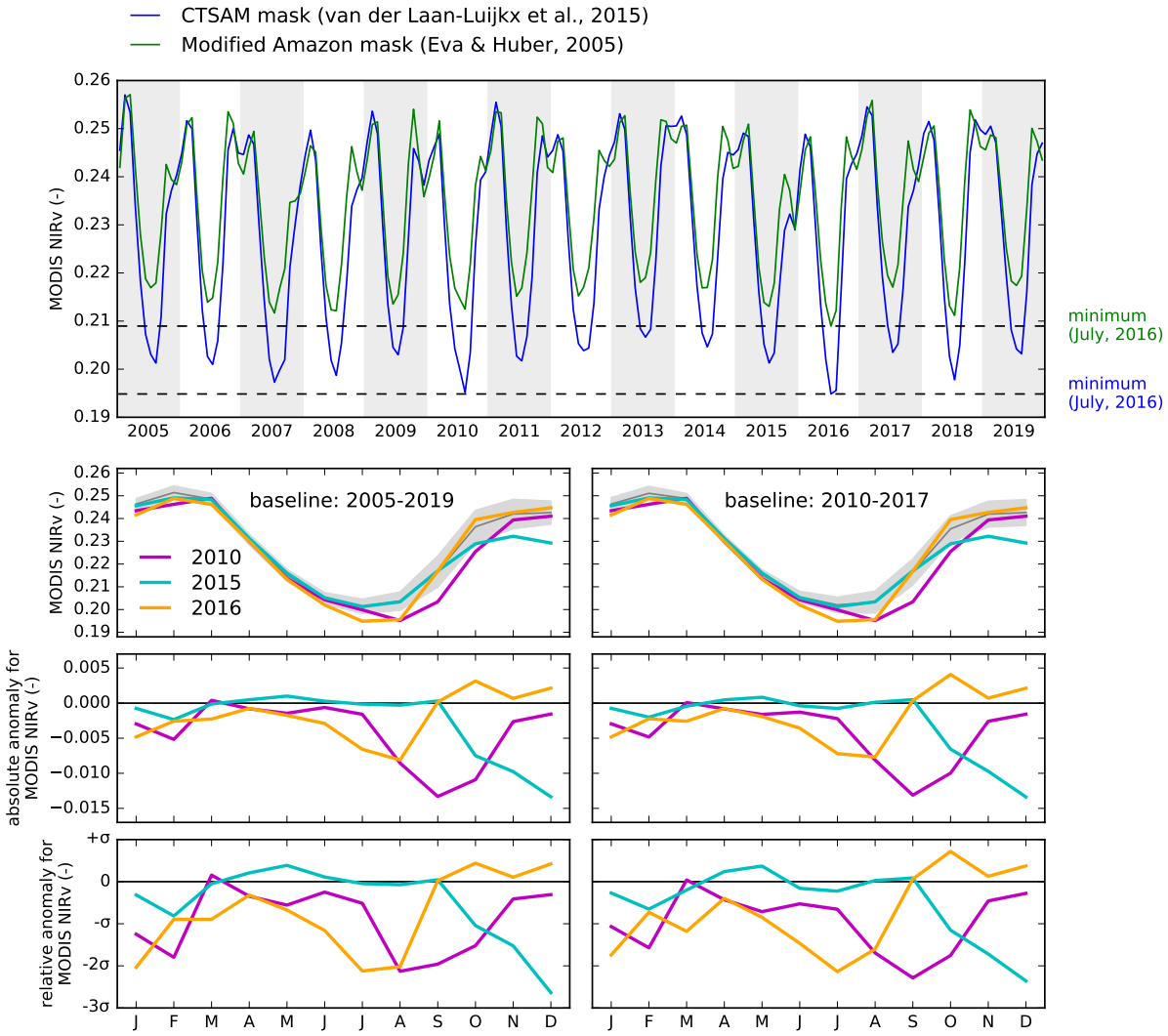

Figure S5.11: MODIS NIRv for the Amazon region. Top panel: MODIS NIRv integrated over the CTSAM mask and a modified version of the Amazon mask from *Eva and Huber* (2005) (both described in more detail in Sect. 5.2.4). Second row: MODIS NIRv over the CTSAM mask for the years 2010, 2015 and 2016 compared with the baselines 2005-2019 (left column) and 2010-2017 (right column), the shading indicates the standard deviation around the mean. Third row: absolute anomaly for MODIS NIRv over the CTSAM mask for the years 2010, 2015 and 2016 compared to the baseline 2005-2019 (left column) and 2010-2017 (right column). Bottom row: relative anomaly for MODIS NIRv over the CTSAM mask for the years 2010, 2015 and 2016 compared to the baseline 2005-2019 (left column) and 2010-2017 (right column).

6

General discussion and outlook

6.1 Introduction

In this final chapter we go across the previous chapters of this thesis and identify links between the different methods and studied topics. In this thesis we have worked with different techniques to estimate the exchange of CO_2 between the atmosphere and the biosphere. These methods differ in the type of carbon flux that they can diagnose: $\Delta^{17}O$ in CO_2, SIF and NIRv are proxies for GPP, whereas atmospheric CO_2 inversions can be used to infer the net exchange of CO_2 at the surface. We have also used biosphere models and data based methods in which all the biospheric CO_2 fluxes (i.e. GPP, TER, NEE) are explicitly simulated or predicted based on environmental drivers.

In addition, there is a major difference in the level of maturity of the methods used to study CO_2 fluxes. $\Delta^{17}O$ in CO_2 is still in a conceptual stage, whereas remote sensing and inverse modeling have been widely adopted in the carbon cycle community. This different level of maturity is also reflected in the regions that were studied: for $\Delta^{17}O$ in CO_2 we focused on large scale patterns (Chapter 2) and understanding its budget at the ecosystem level (Chapter 3). Our SIF and inverse model based studies (Chapters 4

and 5, respectively) focused on the Amazon, which is the main region of interest of this thesis. The work on $\Delta^{17}O$ in CO_2 described in this thesis is indirectly related to the Amazon, because it forms a basis for the interpretation of $\Delta^{17}O$ in CO_2 measurements for air samples collected over the Amazon forest within the Airborne Stable Isotopes of CO_2 from the Amazon (ASICA) program.

The following sections in this chapter are dedicated to a specific theme that is relevant for this thesis. In these sections, we also reflect on the relation with tropical biomes, or more specifically the Amazon forest. The modeling of CO_2 exchange between the atmosphere and vegetation is covered in all chapters of this thesis and discussed further in Sect. 6.2. Next, in Sect. 6.3 we discuss the potential of $\Delta^{17}O$ in CO_2 as a tracer for GPP and describe the remaining challenges and possible other applications. This is followed in Sect. 6.4 by a discussion of the use of remote sensing capabilities, a field that is rapidly evolving due to many technical innovations, to study the carbon cycle. After that, the use of atmospheric inversions to constrain CO_2 surface fluxes is discussed in Sect. 6.5. Finally, we end with an outlook of future research opportunities in Sect. 6.6.

6.2 Leaf exchange modeling

The exchange of CO_2 between the atmosphere and vegetation is the main topic of this thesis, and we have quantified this process using different models. To simulate the budget of $\Delta^{17}O$ in CO_2 it is necessary to calculate the CO_2 diffusing into and out of the leaves (F_{AL} and F_{LA}, respectively). In Chapter 2 we calculated these gross fluxes using the C_i/C_a ratio and the assimilation flux from terrestrial biosphere model SiBCASA (*Schaefer et al.*, 2008). Similarly, we calculated the leaf exchange at the ecosystem level using the discrimination concept in Chapter 3 and in *Vilà-Guerau de Arellano et al.* (2019) for Loobos ($\delta^{13}C$, $\delta^{18}O$, $\Delta^{17}O$) and Harvard Forest ($\delta^{13}C$, $\delta^{18}O$), respectively. Note that for the global and ecosystem level studies we applied different signatures to the non-equilibrated leaf-atmosphere flux, as described in more detail in Sect. S3.2.

In addition, we implemented a steady state leaf conductance model, that describes the fractionation of isotopologues ($^{13}CO_2$, $C^{17}OO$, $C^{18}OO$ and $^{13}C^{18}OO$) during assimilation (the implementation and a brief description is available at `https://git.wur.nl/leaf_model`). The model is dedicated to leaf scale experiments carried out in a leaf-cuvette and was used by *Adnew et al.* (2020), *Adnew et al.* (in review) and *Hofmann et al.* (in prep.) to calculate isotopic fractionation of $\Delta^{17}O$ and Δ_{47} of CO_2 for a given assimilation rate,

stomatal conductance and mesophyll conductance.

Across the different scales (from global to ecosystem and leaf scale) the implementation is consistent, except that for the global and ecosystem study we used the degree of equilibration θ to quantify the fraction of F_{LA} that is equilibrated with leaf water (*Gillon and Yakir*, 2001), whereas for the leaf scale model (`https://git.wur.nl/leaf_model`) we assumed that full equilibration was reached for CO_2 that diffused into the mesophyll (a fraction of the leaf internal CO_2 that varies with residence time inside the leaf). The advantage of the latter approach is that it connects more to our understanding of the structure of the leaf, with most of the carbonic anhydrase being present in the mesophyll. However, the uncertainty in mesophyll conductance is currently considerable (as discussed further in Sect. 6.3) and we have therefore relied on the θ-formulation for the global and ecosystem studies.

For the atmospheric CO_2 inversions described in Chapter 5 we used the net exchange of CO_2 from vegetation as a prior (the gross fluxes F_{AL} and F_{LA} are necessary for the oxygen isotopes of CO_2, but not for CO_2 itself) as simulated by SiBCASA (*Schaefer et al.*, 2008) and its successor SiB4 (*Haynes et al.*, 2019a,b). SiBCASA is known to have a weak drought response (the positive effect of increased radiation on GPP is stronger than its reduction due to limited water availability, *Peters et al.*, 2018), which is improved in SiB4 (*Smith et al.*, 2020). For the Amazon, we also implemented soil moisture fields generated by the hydrological model PCR-GLOBWB in SiBCASA to get a more realistic drought response following the 2015/2016 El Niño (*van Schaik et al.*, 2018).

The seasonal cycle of CO_2 fluxes in the Amazon is determined by leaf phenology (*Restrepo-Coupe et al.*, 2013). This is typically not well captured by biosphere models that are biased towards mid-latitudes (*Restrepo-Coupe et al.*, 2017), where most of the models are developed, and where most of the validation data is collected. Recently, *Chen et al.* (2020) implemented a leaf phenology scheme for tropical evergreen forests that relates the abscission of old leaves and growth of fresh leaves to environmental conditions (e.g. sunlight and vapor pressure deficit), which better captures the seasonal dynamics for the Amazon according to leaf litter observations and eddy covariance fluxes (and also affects the drought response of the model). Another mechanism that is relevant for tropical biomes is the increase of photosynthetic efficiency due to aerosols released by fires (*Rap et al.*, 2015; *Hemes et al.*, 2020), that occur every year in the Amazon during its dry season (*Naus et al.*, in prep.). Implementing this effect in biosphere models could improve their capabilities to simulate tropical ecosystems.

6.3 Applications of $\Delta^{17}O$ in CO_2

A prerequisite for the use of $\Delta^{17}O$ in CO_2 as tracer of GPP is the availability of sufficient high quality observations (i.e. with high measurement precision and observations for well-characterised locations). The early measurements from La Jolla, U.S. (*Thiemens et al.*, 2014) and from Antarctica (John B. Miller, personal communication) suffered from high uncertainty, whereas some more recent measurements are collected from poorly characterized locations. In contrast, there is a great amount of measurements available for $\delta^{18}O$ in CO_2 at NOAA background sites (see `https://www.esrl.noaa.gov/gmd/`). Fortunately, the measurement precision for $\Delta^{17}O$ in CO_2 has improved over the years and there are now multiple techniques available that can measure $\Delta^{17}O$ in CO_2 at a precision of $\sim$10 per meg (see Sect. 2.1 for a brief overview of different measurement techniques). Furthermore, measurements of $\Delta^{17}O$ in CO_2 performed by *Steur et al.* (2018) for air samples from the well-characterized sites Mace Head, Ireland, and Halley Bay, Antarctica, are hopeful for the application of $\Delta^{17}O$ in CO_2 as tracer for GPP.

Hoag et al. (2005) were the first to propose $\Delta^{17}O$ in CO_2 as a tracer for gross primary production. According to *Hoag et al.* (2005) the main advantage of $\Delta^{17}O$ over $\delta^{18}O$ is that the first is not sensitive to the hydrological cycle and thus easier to interpret. However, recent studies (*Angert et al.*, 2004; *Landais et al.*, 2010; *Affolter et al.*, 2015; *Tian et al.*, 2018; *Tian and Wang*, 2019; *Pierchala et al.*, 2020) have shown that $\Delta^{17}O$ in precipitation and soil water can also vary considerably due to kinetic effects associated with evaporation and precipitation. Furthermore, *Thiemens et al.* (2014) showed that $\Delta^{17}O$ in CO_2 measured at La Jolla, U.S., varies strongly with El Niño indices, which resembles the variations found for $\delta^{18}O$ (*Welp et al.*, 2011) that are known to be driven by the hydrological cycle. These effects complicate the interpretation of $\Delta^{17}O$ in CO_2 and its application as a tracer of GPP.

Another challenge in the use of $\Delta^{17}O$ in CO_2 as a tracer for GPP, is that it requires the conversion from the gross exchange fluxes (F_{AL} and F_{LA}) to GPP, which depends on the C_i/C_a ratio, as described by Eqs. (2.8) and (2.9). In the box models from *Hoag et al.* (2005) and *Hofmann et al.* (2017) the C_i/C_a was taken as a constant value (for C_3 and C_4 vegetation in the Northern Hemisphere and Southern Hemisphere, or a global value). However, in reality, C_i/C_a is time dependent and uncertain (*Cuntz*, 2011), thus complicating the relationship between GPP and $\Delta^{17}O$ in CO_2. For instance, non-zero nocturnal stomatal conductance, that was observed for water (*Snyder et al.*, 2003; *Caird et al.*, 2007; *Howard and Donovan*, 2007), CO_2 (*Cernusak et al.*, 2004) and COS (*Kooijmans et al.*, 2019), can result in isotopic equilibration inside leaves, even though there is no GPP at

that time.

An inconvenience in the application of $\Delta^{17}O$ in CO_2 is the inconsistent use of definitions (see also Sect. S2.1) and the different values that are used for the reference line λ_{RL}. The group at Utrecht University uses $\lambda_{RL} = 0.528$ (*Adnew et al.*, 2019, 2020, in review), the group at Research Center for Environmental Changes, Academia Sinica in Taiwan prefers $\lambda_{RL} = 0.516$ (e.g. *Liang et al.*, 2017b) and we use $\lambda_{RL} = 0.5229$ in Chapters 2 and 3. The advantage of our selection is that most equations become simpler, since isotopic equilibration between CO_2 and H_2O follows $\lambda_{CO_2-H_2O} = 0.5229$ (*Barkan and Luz*, 2012). However, this choice also results in a strong gradient in the $\Delta^{17}O$ signature of soil water that is on the Global Meteoric Water Line (see Fig. 2.5). In general, the different definitions and λ_{RL} values imply that numbers from different papers can not be compared directly, but should first be recalculated to a common scale.

There are also some alternative applications for $\Delta^{17}O$ in atmospheric CO_2. One of the first proposed applications was the use as a tracer for mesospheric and stratospheric transport (*Alexander et al.*, 2001; *Liang et al.*, 2008), since the production of $\Delta^{17}O$ in CO_2 is dependent on UV-radiation levels and concentration of ozone and thus $\Delta^{17}O$ in CO_2 contains information on the origin of air parcels. More recently, $\Delta^{17}O$ in CO_2 was used as a tracer for fossil fuel emissions, based on the specific isotope signature of CO_2 released by fossil fuel combustion (*Laskar et al.*, 2016). In addition, $\Delta^{17}O$ in CO_2 was used to quantify CO_2 released from the burning of crop residues, which is contributing to severe air pollution in Delhi, India (*Laskar et al.*, 2020).

As mentioned in Sect. 6.2, the mesophyll conductance of plants is an uncertain parameter. Currently, there is interest from the biological community to measure this plant property more accurately (*Cousins et al.*, 2020). The mesophyll conductance between the intercellular area and the chloroplast can be determined using $\delta^{13}C$ measurements and is therefore denoted by $g_{m^{13}C}$. Somewhat confusing, the conductance between the intercellular area and the mesophyll is also referred to as the mesophyll conductance. The latter can be measured using $\delta^{18}O$ in CO_2 and is therefore denoted by $g_{m^{18}O}$ (*Barbour et al.*, 2016; *Holloway-Phillips et al.*, 2019). Recently, *Adnew et al.* (in review) used $\Delta^{17}O$ in CO_2 to estimate $g_{m^{18}O}$, which can be favorable because the $\Delta^{17}O$ signature of leaf water is nearly constant, whereas $\delta^{18}O$ in leaf water can be enriched due to transpiration.

6.4 Remote sensing of the carbon cycle

Satellite observations are omnipresent in environmental sciences and are becoming increasingly important due to technical improvements (e.g. higher resolution, wider coverage and better signal-to-noise ratios) and identification of new applications. For instance, satellite observations are assimilated during the production of the reanalysis dataset ERA-Interim (*Dee et al.*, 2011) that is used to drive the atmospheric transport in TM5 (*Krol et al.*, 2005) that we used in Chapters 2, 3 and 5. In our chapters that focus on the Amazon, we use SIF from GOME-2, NIRv calculated from MODIS surface reflectance, terrestrial water storage from GRACE and CO_2 columns from OCO-2. Here we discuss the use of these satellites with a focus on the Amazon region.

In Chapter 4 we described that the SIF from GOME-2A suffers from sensor degradation (see also *Zhang et al.*, 2018). To correct for this effect we used several relatively simple methods that were applied directly to the extracted SIF signal for the Amazon. Recently, *van Schaik et al.* (2020) used a more sophisticated method to correct for sensor degradation, based on the measured radiances for the reference site Libya-4 (*Neigh et al.*, 2015). Even though that method is more advanced, it does not necessarily perform better for the Amazon region, since there is still a substantial decline in the SIF values that is not corroborated by other remote sensing data or local measurements. This suggests that the sensor degradation is not uniform across latitudes and that more effort is needed to correct GOME-2 SIF for the Amazon specifically.

In October 2017, the TROPOMI instrument was launched. This instrument has a large spatial coverage (2600 km swath), high spatial resolution (up to 7 km $\times$ 3.5 km) and low noise levels and is therefore a powerful tool to study photosynthesis from space (*Köhler et al.*, 2018). Recently, *Doughty et al.* (2019) showed SIF retrieved from TROPOMI for the Amazon region. Although the TROPOMI SIF data is less noisy than the GOME-2 SIF data that we used in Chapter 4, the patterns in TROPOMI SIF confirmed the patterns that we described earlier using GOME-2 SIF. This reinforces the suitability of the SIFTER product to tropical ecosystems and motivates its use for our study of African biomes (*Mengistu et al.*, in review). In Sect. 6.6, we will describe some of the upcoming satellite missions, that will further increase the capabilities to monitor vegetation from space.

In Chapters 4 and 5 we used GOME-2 SIF and MODIS NIRv as proxies for GPP in the Amazon to estimate its response to droughts. We also used SIF and NIRv to assess the response of GPP during the European drought of 2018 on the local scale (*Buitink et al.*, in review) and the regional scale (*Smith et al.*, 2020). A notable difference between GOME-2

SIF and MODIS NIRv is the higher resolution and higher signal-to-noise ratio of NIRv, which is especially important when comparing with EC sites in heterogeneous environments. For the European ecosystems we found that the correlations of the anomalies in SIF, NIRv and GPP during droughts are lower than the correlation of these absolute signals. This implies that estimating a reduction in GPP from SIF or NIRv reductions, as done in Chapter 4, can have considerable uncertainty, which motivates further research of SIF and NIRv during its seasonal cycle and during anomalous events at the ecosystem level.

Besides the aforementioned difference in resolution, there are some more practical differences between SIF and NIRv. Obtaining SIF from GOME-2 is achieved by fitting a spectrally smooth albedo, principal components representing the atmospheric effects on the signal, and a Gaussian fluorescence curve peaking at 737 nm. This last component is a small part of the total signal observed by the satellite, and as a result there can be substantial uncertainty in the retrieved SIF signal (*Sanders et al.*, 2016; *van Schaik et al.*, 2020). In contrast, retrieval of NIRv is easier and the signal-to-noise ratio is better. Also for local studies, NIRv is an attractive proxy for GPP, given the high reported correlations and low costs of sensors (*Baldocchi et al.*, 2020). Interestingly, SIF and NIRv can also be used in a complimentary way, rather than as alternative proxies for GPP. An example is the use of NIRv to estimate the escape ratio of photons from the canopy, which can be used to estimate the total emitted SIF, as described by (*Zeng et al.*, 2019). This method was recently used to estimate GPP from crop sites (*Dechant et al.*, 2020) and to estimate global GPP (*Zhang et al.*, 2020).

An important issue for the application of remote sensing to humid tropical regions is the frequent coverage by clouds, which can obstruct or distort satellite observations. In the SIF retrieval used for our analysis in Chapter 4, pixels with a cloud fraction exceeding 0.4 are rejected. We verified that still sufficient valid SIF retrievals were available for our analysis (Fig. S4.1) and that the retrieved signal agrees with independent data (Fig. 4.1). In Chapter 5 we study NIRv over the Amazon calculated from MODIS surface reflectance. To be less dependent on the capability of the MODIS algorithm to correctly detect clouds, we also used the MAIAC reflectance data (*Lyapustin et al.*, 2011a,b, 2012, 2018), which is based on a different cloud masking and an aerosol correction scheme. More specifically for the Amazon region, the release of high energy particles known as the South Atlantic Anomaly can affect the quality of observations from satellites. The frequent cloud coverage and the South Atlantic Anomaly further reinforces the importance of validation with independent data (e.g. flux tower data) for this region.

As discussed in Sect. 6.2 there are some specific mechanisms for tropical biomes that are not always well captured by terrestrial biosphere models. Remote sensing proxies for GPP, such as SIF and NIRv, can be used to guide further development of terrestrial biosphere models for tropical regions. For instance, the seasonality as diagnosed using SIF (Fig. 4.4) and NIRv can serve as a benchmark for further improvement of seasonality simulated by biosphere models for tropical biomes where flux towers are sparse. Also our finding based on SIF in Chapter 4 that the photosynthetic uptake recovered rapidly following the 2015/2016 El Niño drought, when the atmospheric demand for water returned to normal values, can be useful to improve drought parameterisations in terrestrial biosphere models. Finally, the 2016 legacy drought (described in Chapter 5) is a potential test case for the soil moisture stress parametrisations in terrestrial biosphere models.

A popular alternative method for studying the carbon cycle is machine learning of eddy covariance fluxes (e.g. *Beer et al.*, 2010; *Jung et al.*, 2011; *Tramontana et al.*, 2016; *Bodesheim et al.*, 2018). The machine learning based methods used in Chapters 4 and 5 are not simulating leaf interaction explicitly, but these mechanisms are implicit in the model that is trained on EC-data. Since, EC-towers in tropical regions are underrepresented, it is conceivable that machine learning methods are biased towards mid latitudes and fail to capture the driving mechanisms for tropical ecosystems. An indication that the machine learned GPP products are not capturing the behaviour of tropical ecosystems completely, is shown in Fig. S4.2, where the variability in SIF over the productive regions of the Amazon (Regions A and B) exceeds the variability of machine learned GPP. More EC observations for tropical ecosystems or the use of more direct proxies for GPP as explanatory variables in machine learning approaches (e.g. NIRv, *Badgley et al.*, 2019) can possibly improve machine learned GPP products for the tropics.

6.5 Atmospheric inversions

Although atmospheric inversions are only covered extensively in Chapter 5, we feel that it is important to reflect on the use of atmospheric inversions as a tool to learn about the carbon cycle. A major difference between the CO_2 inversions and some of the other methods used in this thesis (stable isotopes, SIF, NIRv), is that it only allows to diagnose the net exchange of CO_2 at the surface. However, atmospheric inversions of other trace gases can be used to estimate different components of the carbon cycle. For example, in Chapter 5 we used CO inversions from *Naus et al.* (in prep.) to estimate CO_2 emissions from fires. In addition, inversions of COS can give constraints on the spatial distribution

and temporal dynamics of GPP (*Ma et al.*, 2020). Given sufficient high quality measurements, atmospheric inversions of $\Delta^{17}O$ in CO_2 could also be used to constrain GPP. This shows that atmospheric inversions are a powerful technique to quantify multiple processes in the carbon cycle.

In Sect. 6.4 we already touched upon the increasing role of remote sensing in studying the carbon cycle, which also has its effect on atmospheric inversions. The precision of satellite retrievals for CO_2 columns has increased substantially (*Crowell et al.*, 2019; *Palmer et al.*, 2019), and it is now feasible to use satellite data to estimate CO_2 surface fluxes, as demonstrated in Chapter 5. The use of satellite data has far-reaching consequences, especially for tropical areas where the coverage of in-situ CO_2 observations is relatively sparse. Due to the limited availability of in-situ observations over the tropics, attributing sources and sinks across the tropical regions is uncertain (*Gloor et al.*, 2018), and satellite data can help to better distinguish between the different continents.

In Chapter 5 we described inversions using either flask data or XCO_2 data as observational constraint. As mentioned previously, an advantage of the XCO_2 data is that it provides better coverage over certain areas. However, the ability of satellites to measure XCO_2 can be obscured by clouds (see e.g. Fig. S5.1 where OCO-2 has more valid retrievals during the less-clouded dry season in the Amazon), which can result in a fair-weather bias. This is not an issue for flask samples, and despite the aforementioned improvement of accuracy for the OCO-2 retrievals, the flask observations remain more accurate. Considering these strong points of XCO_2 and flask observations, it can be attractive to combine XCO_2 and flask data in an inverse model (*Florentie et al.*, 2019). A challenge related to this combination of data streams, is that there is typically more satellite data, and weighting factors might be needed to avoid that satellite data dominates the cost function, as was also done for the combined flask-satellite CO inversions by *Naus et al.* (in prep.).

For the inversions used in Chapter 5, we used alternative biosphere priors and fire products to assess the impact of these priors on the optimized fluxes. In contrast, for the atmospheric transport we fully relied on a single product (ERA-Interim, *Dee et al.*, 2011, from ECMWF) and one transport model (TM5, *Krol et al.*, 2005), although we realize that atmospheric transport can have a large impact on emission estimates obtained from inverse modeling (e.g. *Schuh et al.*, 2019). Further improvement of atmospheric transport thus requires unabated attention, and the recent model intercomparison study by *Krol et al.* (2017) and the ongoing SF6 model intercomparison (Andy Jacobson, NOAA) provide important opportunities to test atmospheric transport in different models.

In the inversions described in Chapter 5, we estimate weekly scaling factors that are used

to obtain posterior fluxes from the prior fluxes through multiplication. This approach is also used in the CarbonTracker (*van der Laan-Luijkx et al.*, 2017) simulations that are submitted to the annual Global Carbon Budget reports (*Le Quéré et al.*, 2015, 2016, 2018a,b; *Friedlingstein et al.*, 2019). Recently, *Rödenbeck et al.* (2018a,b) introduced a method that goes beyond the scaling of fluxes, and that allows to estimate the 'climate sensitivity', which is the response of the biosphere to climate variations. The climate sensitivity is a descriptive property of the Earth system, which in turn explains much of the spatial and temporal variations of the CO_2 surface fluxes. Recently, this novel approach was extended by *Florentie et al.* (2019) using SIF and NIRv, to estimate trends and interannual variability in NEE. In addition, the Carbon Cycle Data Assimilation System (CCDAS, *MacBean et al.*, 2016; *Peylin et al.*, 2016) is another example of a system where observational data are used to optimize model parameters, which can potentially lead to systematic improvements of the model simulations.

There are some striking similarities and differences between atmospheric inversions and the machine learning approaches based on EC-data. From a mathematical point of view, both are methods in which observations are used to produce an estimate that minimizes a cost function. However the time scales and spatial scales associated with eddy covariance fluxes (hours to days, for a footprint of $\sim$1 km^2) are smaller than the information that can be inferred from atmospheric CO_2 concentrations (months to years, regional to global scale). In Chapter 5 we used half-hourly machine learned NEE from *Bodesheim et al.* (2018) as prior in our inversions. Although, this is a state-of-the art product, it estimates global NEE to be -21.4 PgC/year (i.e. approximately twice the fossil fuel CO_2 flux), which is outside any reasonable range of global NEE estimates (the net land uptake was estimated to be 3.2$\pm$0.6 PgC/yr by *Friedlingstein et al.*, 2019). This clearly shows that there is more work to do, to bridge the scales between machine learning and atmospheric inversions.

6.6 Outlook

There are quite some measurements of $\Delta^{17}O$ in CO_2 in progress or planned that will increase our understanding of this tracer. During the ASICA project, air samples were collected over the Amazon using small aircraft, that were equipped with air dryers to avoid isotopic equilibration with water in the flasks (*Paul et al.*, 2020). This has resulted in a unique dataset of $\delta^{13}C$, $\delta^{18}O$ and $\Delta^{17}O$ in CO_2 profiles, for which a comprehensive analysis has yet to take place. In addition, there are plans to continue collecting observations of

$\Delta^{17}O$ in CO_2 at the ecosystem level for Loobos and possibly other locations. Also, there is interest to follow-up on the leaf and plant scale research that was carried out using $\Delta^{17}O$ in CO_2. The Aerodyne isotope analyzer that will be shipped to the Netherlands could be a part of these upcoming activities.

The advantage of new tracers like $\Delta^{17}O$ in CO_2, is that they give more information on a specific process. However, usually the interpretation of these tracers also involves other variables that are uncertain. To alleviate this, and further constrain the carbon cycle, it can be helpful to combine different tracers, remote sensing proxies and observations of other biophysical parameters. Especially $\delta^{13}C$ and $\Delta^{17}O$ in CO_2 can be a fruitful combination, since $\delta^{13}C$ gives information on stomatal conductance, which is one of the big unknowns for the interpretation of $\Delta^{17}O$ in CO_2. The combination of different measurement techniques is also possible at the field scale. For instance, during the recent CloudRoots campaign (*Vilà-Guerau de Arellano et al.*, 2020), different measurements were carried out (including stable isotopes, scintillometers, sap flow and leaf chamber measurements). We expect that for the analysis of these measurements, and for the follow-up LIASE campaign (*Boone et al.*, 2019), there will be synergy from the different approaches.

There are a number of upcoming satellite missions that could lead to scientific breakthroughs. This includes the ESA FLEX satellite that is the first satellite that is dedicated to sensing SIF (*Drusch et al.*, 2017) and the proposed EU CO2M mission that consists of three satellites that can detect CO_2 columns and SIF. For the Amazon specifically, the CO_2, CO, CH_4 and SIF observations from the geostationary GeoCarb mission are expected to give new insights in the carbon cycle (*Moore III et al.*, 2018). In addition to the obvious new scientific opportunities from satellites that will be launched in the upcoming years, there is also the possibility to 'go back in time' by creating a NIRv climate record (e.g. by merging Landsat-5 data, covering the years 1984-2013, with MODIS data, that started in 2000 and is currently still active), that could be used to infer trends in GPP over the last forty years.

Atmospheric CO_2 inversions have been around for some time (e.g. *Gurney et al.*, 2002; *Peylin et al.*, 2013), but there are still quite some developments in this field. This includes moving towards higher resolutions, which is facilitated by the increase of computational resources and motivated by the demand of more accurate emission estimates by national governments and international organisations. As already mentioned in Sect. 6.5, we expect that satellite data will become more important for inverse modelling studies of CO_2. For example, satellite data that is available quickly after its retrieval facilitates the production of near-real time emission estimates, which is a direction that several groups

in the field of CO_2 inverse modeling are moving towards.

We conclude this section with a remark on the future of the Amazon. We study this ecosystem, and as the ecosystem is perturbed further due to climate change, our understanding is improving. There is some irony in this, and we should realize that to save the Amazon forest, scientific progress alone is not sufficient. In the end we are relying on governments to draft and execute effective policies against deforestation and climate change, including the reduction of the use of fossil fuels as our energy source.

Bibliography

Aan de Brugh, J. M. J., J. S. Henzing, M. Schaap, W. T. Morgan, C. C. van Heerwaarden, E. P. Weijers, H. Coe, and M. C. Krol, Modelling the partitioning of ammonium nitrate in the convective boundary layer, *Atmospheric Chemistry and Physics*, *12*(6), 3005–3023, doi:10.5194/acp-12-3005-2012, 2012.

Adams, H. D., et al., A multi-species synthesis of physiological mechanisms in drought-induced tree mortality, *Nature Ecology and Evolution*, *1*(9), 1285–1291, doi:10.1038/s41559-017-0248-x, 2017.

Adnew, G. A., T. L. Pons, G. Koren, W. Peters, and T. Röckmann, Leaf-scale quantification of the effect of photosynthetic gas exchange on $\Delta^{17}O$ of atmospheric CO_2, *Biogeosciences*, *17*, 3903–3922, doi:10.5194/bg-17-3903-2020, 2020.

Adnew, G. A., T. L. Pons, G. Koren, W. Peters, and T. Röckmann, $\Delta^{17}O$ in CO_2 as alternative tracer for mesophyll conductance, in review.

Adnew, G. A., et al., Determination of the triple oxygen and carbon isotopic composition of CO_2 from atomic ion fragments formed in the ion source of the 253 Ultra high-resolution isotope ratio mass spectrometer, *Rapid Communications in Mass Spectrometry*, *33*(17), 1363–1380, doi:10.1002/rcm.8478, 2019.

Affek, H. P., and D. Yakir, The Stable Isotopic Composition of Atmospheric CO_2, in *Treatise on Geochemistry*, vol. 5, 2 ed., pp. 179–212, Elsevier, doi:10.1016/B978-0-08-095975-7.00407-1, 2014.

Affolter, S., A. D. Häuselmann, D. Fleitmann, P. Häuselmann, and M. Leuenberger, Triple isotope (δD, $\delta^{17}O$, $\delta^{18}O$) study on precipitation, drip water and speleothem fluid inclusions for a Western Central European cave (NW Switzerland), *Quaternary Science Reviews*, *127*, 73–89, doi:10.1016/j.quascirev.2015.08.030, 2015.

Alden, C. B., et al., Regional atmospheric CO_2 inversion reveals seasonal and geographic differences in Amazon net biome exchange, *Global Change Biology*, *22*(10), 3427–3443, doi:10.1111/gcb.13305, 2016.

Alexander, B., M. K. Vollmer, T. Jackson, R. F. Weiss, and M. H. Thiemens, Stratospheric CO_2 isotopic anomalies and SF_6 and CFC tracer concentrations in the Arctic polar vortex, *Geophysical Research Letters*, *28*(21), 4103–4106, doi:10.1029/2001GL013692, 2001.

Andreae, M. O., et al., The Amazon Tall Tower Observatory (ATTO): overview of pilot measurements on ecosystem ecology, meteorology, trace gases, and aerosols, *Atmospheric Chemistry and Physics*, *15*(18), 10,723–10,776, doi:10.5194/acp-15-10723-2015, 2015.

Andres, R. J., et al., A synthesis of carbon dioxide emissions from fossil-fuel combustion, *Biogeosciences*, *9*(5), 1845–1871, doi:10.5194/bg-9-1845-2012, 2012.

Angert, A., C. D. Cappa, and D. J. DePaolo, Kinetic ^{17}O effects in the hydrologic cycle: Indirect evidence and implications, *Geochimica et Cosmochimica Acta*, *68*(17), 3487–3495, doi:10.1016/j.gca.2004.02.010, 2004.

Appenzeller, C., J. R. Holton, and K. H. Rosenlof, Seasonal variation of mass transport across the tropopause, *Journal of Geophysical Research: Atmospheres*, *101*(D10), 15,071–15,078, doi:10.1029/96JD00821, 1996.

Aragão, L. E. O. C., et al., 21st Century drought-related fires counteract the decline of Amazon deforestation carbon emissions, *Nature Communications*, *9*(1), 536, doi:10.1038/s41467-017-02771-y, 2018.

Araújo, A. C., et al., Comparative measurements of carbon dioxide fluxes from two nearby towers in a central Amazonian rainforest: The Manaus LBA site, *Journal of Geophysical Research*, *107*(D20), 8090, doi:10.1029/2001JD000676, 2002.

Arrhenius, S., XXXI. On the influence of carbonic acid in the air upon the temperature of the ground, *The London, Edinburgh, and Dublin Philosophical Magazine and Journal of Science*, *41*(251), 237–276, doi:10.1080/14786449608620846, 1896.

Assonov, S. S., and C. A. M. Brenninkmeijer, A redetermination of absolute values for $^{17}R_{\mathrm{VPDB-CO2}}$ and $^{17}R_{\mathrm{VSMOW}}$, *Rapid Communications in Mass Spectrometry*, *17*(10), 1017–1029, doi:10.1002/rcm.1011, 2003.

Assonov, S. S., and C. A. M. Brenninkmeijer, Reporting small $\Delta^{17}O$ values: existing definitions and concepts, *Rapid Communications in Mass Spectrometry*, *19*(5), 627–636, doi:10.1002/rcm.1833, 2005.

Assonov, S. S., C. A. M. Brenninkmeijer, T. Schuck, and T. Umezawa, N_2O as a tracer of mixing stratospheric and tropospheric air based on CARIBIC data with applications for CO_2, *Atmospheric Environment*, *79*, 769–779, doi:10.1016/j.atmosenv.2013.07.035, 2013.

Aubinet, M., et al., Estimates of the annual net carbon and water exchange of forests: The EUROFLUX methodology, in *Advances in Ecological Research*, edited by A. H. Fitter and D. G. Raffaelli, pp. 113–175, Academic Press, doi:10.1016/S0065-2504(08)60018-5, 1999.

Bacastow, R. B., Modulation of atmospheric carbon dioxide by the Southern Oscillation, *Nature*, *261*, 116–118, doi:10.1038/261116a0, 1976.

Badgley, G., C. B. Field, and J. A. Berry, Canopy near-infrared reflectance and terrestrial photosynthesis, *Science Advances*, *3*(3), e1602,244, doi:10.1126/sciadv.1602244, 2017.

Badgley, G., L. D. L. Anderegg, J. A. Berry, and C. B. Field, Terrestrial gross primary production: Using NIRv to scale from site to globe, *Global Change Biology*, p. gcb.14729, doi:10.1111/gcb.14729, 2019.

Baertschi, P., Absolute ^{18}O content of standard mean ocean water, *Earth and Planetary Science Letters*, *31*(3), 341–344, doi:10.1016/0012-821X(76)90115-1, 1976.

Baker, I. T., L. Prihodko, A. S. Denning, M. Goulden, S. Miller, and H. R. da Rocha, Seasonal drought stress in the Amazon: Reconciling models and observations, *Journal of Geophysical Research: Biogeosciences*, *113*(G1), doi:10.1029/2007JG000644, 2008.

Baldocchi, D., et al., FLUXNET: A new tool to study the temporal and spatial variability of ecosystem-scale carbon dioxide, water vapor, and energy flux densities, *Bulletin of the American Meteorological Society*, *82*(11), 2415–2434, doi:10.1175/1520-0477(2001)082<2415:FANTTS>2.3.CO;2, 2001.

Baldocchi, D. D., B. B. Hincks, and T. P. Meyers, Measuring biosphere-atmosphere exchanges of biologically related gases with micrometeorological methods, *Ecology*, *69*(5), 1331–1340, doi:10.2307/1941631, 1988.

Baldocchi, D. D., et al., Outgoing near infrared radiation from vegetation scales with canopy photosynthesis across a spectrum of function, structure, physiological capacity and weather, *Journal of Geophysical Research: Biogeosciences*, doi:10.1029/2019jg005534, 2020.

Balsamo, G., et al., ERA-Interim/Land: A global land surface reanalysis data set, *Hydrology and Earth System Sciences*, *19*(1), 389–407, doi:10.5194/hess-19-389-2015, 2015.

Barbeta, A., T. E. Gimeno, L. Clavé, B. Fréjaville, S. P. Jones, C. Delvigne, L. Wingate, and J. Ogée, An explanation for the isotopic offset between soil and stem water in a temperate tree species, *New Phytologist*, doi:10.1111/nph.16564, 2020.

Barbour, M. M., J. R. Evans, K. A. Simonin, and S. von Caemmerer, Online CO_2 and H_2O oxygen isotope fractionation allows estimation of mesophyll conductance in C_4 plants, and reveals that mesophyll conductance decreases as leaves age in both C_4 and C_3 plants, *New Phytologist*, *210*(3), 875–889, doi:10.1111/nph.13830, 2016.

Barkan, E., and B. Luz, High-precision measurements of $^{17}O/^{16}O$ and $^{18}O/^{16}O$ ratios in CO_2, *Rapid Communications in Mass Spectrometry*, *26*(23), 2733–2738, doi:10.1002/rcm.6400, 2012.

Barkhordarian, A., S. S. Saatchi, A. Behrangi, P. C. Loikith, and C. R. Mechoso, A recent systematic increase in vapor pressure deficit over tropical South America, *Scientific Reports*, *9*(1), 1–12, doi:10.1038/s41598-019-51857-8, 2019.

Beck, H. E., A. I. J. M. van Dijk, V. Levizzani, J. Schellekens, D. G. Miralles, B. Martens, and A. de Roo, MSWEP: 3-hourly 0.25° global gridded precipitation (1979-2015) by merging gauge, satellite, and reanalysis data, *Hydrology and Earth System Sciences*, *21*(1), 589–615, doi:10.5194/hess-21-589-2017, 2017a.

Beck, H. E., et al., Global-scale evaluation of 22 precipitation datasets using gauge observations and hydrological modeling, *Hydrology and Earth System Sciences*, *21*(12), 6201–6217, doi:10.5194/hess-21-6201-2017, 2017b.

Beer, C., et al., Terrestrial gross carbon dioxide uptake: global distribution and covariation with climate, *Science*, *329*(5993), 834–838, doi:10.1126/science.1184984, 2010.

Bergamaschi, P., et al., Top-down estimates of European CH_4 and N_2O emissions based on four different inverse models, *Atmospheric Chemistry and Physics*, *15*(2), 715–736, doi:10.5194/acp-15-715-2015, 2015.

Betts, R. A., C. D. Jones, J. R. Knight, R. F. Keeling, and J. J. Kennedy, El Niño and a record CO_2 rise, *Nature Climate Change*, *6*(9), 806–810, doi:10.1038/nclimate3063, 2016.

Bodesheim, P., M. Jung, F. Gans, M. D. Mahecha, and M. Reichstein, Upscaled diurnal cycles of land–atmosphere fluxes: a new global half-hourly data product, *Earth System Science Data*, *10*(3), 1327–1365, doi:10.5194/essd-10-1327-2018, 2018.

Boering, K. A., T. Jackson, K. J. Hoag, A. S. Cole, M. J. Perri, M. Thiemens, and E. Atlas, Observations of the anomalous oxygen isotopic composition of carbon dioxide in the lower stratosphere and the flux of the anomaly to the troposphere, *Geophysical Research Letters*, *31*(3), L03,109, doi:10.1029/2003GL018451, 2004.

Boisier, J. P., P. Ciais, A. Ducharne, and M. Guimberteau, Projected strengthening of Amazonian dry season by constrained climate model simulations, *Nature Climate Change*, *5*(7), 656–660, doi:10.1038/nclimate2658, 2015.

Bönisch, H., P. Hoor, C. Gurk, W. Feng, M. Chipperfield, A. Engel, and B. Bregman, Model evaluation of CO_2 and SF_6 in the extratropical UT/LS region, *Journal of Geophysical Research*, *113*(D6), D06,101, doi:10.1029/2007JD008829, 2008.

Boone, A., M. Best, J. Cruxart, J. Polcher, P. Quintana, J. Bellvert, J. Brooke, G. Canut-Rocafort, and J. Price, Land Surface Interactions with the Atmosphere over the Iberian Semi-Arid Environment (LIAISE), *GEWEX News*, *29*(1), 8–10, 2019.

Booth, B. B. B., et al., High sensitivity of future global warming to land carbon cycle processes, *Environmental Research Letters*, *7*(2), 024,002, doi:10.1088/1748-9326/7/2/024002, 2012.

Botía, S., et al., Understanding nighttime methane signals at the Amazon Tall Tower Observatory (ATTO), *Atmospheric Chemistry and Physics*, *20*, 6583–6606, doi:10.5194/acp-20-6583-2020, 2020.

Bowen, G. J., and J. Revenaugh, Interpolating the isotopic composition of modern meteoric precipitation, *Water Resources Research*, *39*(10), 1299, doi:10.1029/2003WR002086, 2003.

Bowman, K. W., et al., Global and Brazilian Carbon Response to El Niño Modoki 2011-2010, *Earth and Space Science*, *4*(10), 637–660, doi:10.1002/2016EA000204, 2017.

Brede, B., H. Bartholomeus, J. Suomalainen, J. Clevers, J. Verbesselt, M. Herold, D. Culvenor, and F. Gascon, The Speulderbos fiducial reference site for continuous monitoring

of forest biophysical variables, in *Living Planet Symposium 2016*, vol. SP-740, pp. 1–5, European Space Agency, 2016.

Bregman, B., E. Meijer, and R. Scheele, Key aspects of stratospheric tracer modeling using assimilated winds, *Atmospheric Chemistry and Physics*, *6*(12), 4529–4543, doi:10.5194/acp-6-4529-2006, 2006.

Brenninkmeijer, C. A. M., P. Kraft, and W. G. Mook, Oxygen isotope fractionation between CO_2 and H_2O, *Chemical Geology*, *41*, 181–190, doi:10.1016/S0009-2541(83)80015-1, 1983.

Brenninkmeijer, C. A. M., T. Röckmann, M. Bräunlich, P. Jöckel, and P. Bergamaschi, Review of progress in isotope studies of atmospheric carbon monoxide, *Chemosphere - Global Change Science*, *1*(1-3), 33–52, doi:10.1016/S1465-9972(99)00018-5, 1999.

Brienen, R. J. W., et al., Long-term decline of the Amazon carbon sink, *Nature*, *519*(7543), 344–348, doi:10.1038/nature14283, 2015.

Brühl, C., B. Steil, G. Stiller, B. Funke, and P. Jöckel, Nitrogen compounds and ozone in the stratosphere: comparison of MIPAS satellite data with the chemistry climate model ECHAM5/MESSy1, *Atmospheric Chemistry and Physics*, *7*(21), 5585–5598, doi:10.5194/acp-7-5585-2007, 2007.

Buitink, J., et al., Anatomy of the 2018 agricultural drought in The Netherlands using in situ soil moisture and canopy nearinfrared reflectance satellite imagery, *Hydrology and Earth System Sciences*, in review.

Caird, M. A., J. H. Richards, and L. A. Donovan, Nighttime stomatal conductance and transpiration in C_3 and C_4 plants, *Plant Physiology*, *143*(1), 4–10, doi:10.1104/pp.106.092940, 2007.

Campbell, J. E., et al., Photosynthetic control of atmospheric carbonyl sulfide during the growing season, *Science*, *322*(5904), 1085–1088, doi:10.1126/science.1164015, 2008.

Casso-Torralba, P., J. Vilà-Guerau de Arellano, F. Bosveld, M. R. Soler, A. Vermeulen, C. Werner, and E. Moors, Diurnal and vertical variability of the sensible heat and carbon dioxide budgets in the atmospheric surface layer, *Journal of Geophysical Research*, *113*(D12), D12,119, doi:10.1029/2007JD009583, 2008.

Cernusak, L. A., G. D. Farquhar, S. C. Wong, and H. Stuart-Williams, Measurement and interpretation of the oxygen isotope composition of carbon dioxide respired by leaves in the dark, *Plant Physiology*, *136*(2), 3350–3363, doi:10.1104/pp.104.040758, 2004.

Chakraborty, S., and S. K. Bhattacharya, Experimental investigation of oxygen isotope exchange between CO_2 and $O(^1D)$ and its relevance to the stratosphere, *Journal of Geophysical Research*, *108*(D23), 4724, doi:10.1029/2002JD002915, 2003.

Chen, X., et al., Novel representation of leaf phenology improves simulation of Amazonian evergreen forest photosynthesis in a land surface model, *Journal of Advances in Modeling Earth Systems*, *12*(1), doi:10.1029/2018MS001565, 2020.

Ciais, P., et al., A three-dimensional synthesis study of $\delta^{18}O$ in atmospheric CO_2: 1. Surface fluxes, *Journal of Geophysical Research: Atmospheres*, *102*(D5), 5857–5872, doi:10.1029/96JD02360, 1997a.

Ciais, P., et al., A three-dimensional synthesis study of $\delta^{18}O$ in atmospheric CO_2: 2. Simulations with the TM2 transport model, *Journal of Geophysical Research: Atmospheres*, *102*(D5), 5873–5883, doi:10.1029/96JD02361, 1997b.

Cisneros Vaca, C., C. van der Tol, and C. P. Ghimire, The influence of long-term changes in canopy structure on rainfall interception loss: a case study in Speulderbos, the Netherlands, *Hydrology and Earth System Sciences*, *22*(7), 3701–3719, doi:10.5194/hess-22-3701-2018, 2018.

Collatz, G. J., J. T. Ball, C. Grivet, and J. A. Berry, Physiological and environmental regulation of stomatal conductance, photosynthesis and transpiration: a model that includes a laminar boundary layer, *Agricultural and Forest Meteorology*, *54*(2-4), 107–136, doi:10.1016/0168-1923(91)90002-8, 1991.

Collatz, G. J., M. Ribas-Carbo, and J. A. Berry, Coupled photosynthesis-stomatal conductance model for leaves of C_4 plants, *Australian Journal of Plant Physiology*, *19*(5), 519, doi:10.1071/PP9920519, 1992.

Cooperative Global Atmospheric Data Integration Project, Multi-laboratory compilation of atmospheric carbon dioxide data for the period 1957-2017; obspack_co2_1_GLOBALVIEWplus_v4.2_2019-03-19, doi:10.25925/20190319, 2019.

Coplen, T. B., Guidelines and recommended terms for expression of stable-isotope-ratio and gas-ratio measurement results, *Rapid Communications in Mass Spectrometry*, *25*(17), 2538–2560, doi:10.1002/rcm.5129, 2011.

Corazza, M., et al., Inverse modelling of European N_2O emissions: assimilating observations from different networks, *Atmospheric Chemistry and Physics*, *11*(5), 2381–2398, doi:10.5194/acp-11-2381-2011, 2011.

Cousins, A. B., D. L. Mullendore, and B. V. Sonawane, Recent developments in mesophyll conductance in C_3, C_4, and crassulacean acid metabolism plants, *The Plant Journal*, p. tpj.14664, doi:10.1111/tpj.14664, 2020.

Cox, P. M., D. Pearson, B. B. Booth, P. Friedlingstein, C. Huntingford, C. D. Jones, and C. M. Luke, Sensitivity of tropical carbon to climate change constrained by carbon dioxide variability, *Nature*, *494*(7437), 341–344, doi:10.1038/nature11882, 2013.

Crisp, D., et al., The Orbiting Carbon Observatory (OCO) mission, *Advances in Space Research*, *34*(4), 700–709, doi:10.1016/j.asr.2003.08.062, 2004.

Crowell, S., et al., The 2015–2016 carbon cycle as seen from OCO-2 and the global in situ network, *Atmospheric Chemistry and Physics*, *19*(15), 9797–9831, doi:10.5194/acp-19-9797-2019, 2019.

Cuntz, M., A dent in carbon's gold standard, *Nature*, *477*(7366), 547–548, doi:10.1038/477547a, 2011.

Cuntz, M., P. Ciais, and G. Hoffmann, Modelling the continental effect of oxygen isotopes over Eurasia, *Tellus B*, *54*(5), 895–911, doi:10.3402/tellusb.v54i5.16738, 2002.

Cuntz, M., P. Ciais, G. Hoffmann, C. E. Allison, R. J. Francey, W. Knorr, P. P. Tans, J. W. C. White, and I. Levin, A comprehensive global three-dimensional model of $\delta^{18}O$ in atmospheric CO_2: 2. Mapping the atmospheric signal, *Journal of Geophysical Research*, *108*(D17), 4528, doi:10.1029/2002JD003154, 2003a.

Cuntz, M., P. Ciais, G. Hoffmann, and W. Knorr, A comprehensive global three-dimensional model of $\delta^{18}O$ in atmospheric CO_2: 1. Validation of surface processes, *Journal of Geophysical Research*, *108*(D17), 4527, doi:10.1029/2002JD003153, 2003b.

Daumard, F., S. Champagne, A. Fournier, Y. Goulas, A. Ounis, J.-F. Hanocq, and I. Moya, A field platform for continuous measurement of canopy fluorescence, *IEEE Transactions on Geoscience and Remote Sensing*, *48*(9), 3358–3368, doi:10.1109/TGRS.2010.2046420, 2010.

Davidson, M., M. Berger, I. Moya, J. Moreno, T. Laurila, M.-P. Stoll, and J. Miller, Mapping photosynthesis from space - A new vegetation-fluorescence technique, *ESA Bulletin*, *116*, 34–37, 2003.

De Haij, M., A. Apituley, W. Koetse, and H. Bloemink, Transition towards a new ceilometer network in the Netherlands: Challenges and experiences, in *CIMO TECO*, WMO, Madrid, 2016.

Dechant, B., et al., Canopy structure explains the relationship between photosynthesis and sun-induced chlorophyll fluorescence in crops, *Remote Sensing of Environment*, *241*, doi:10.1016/j.rse.2020.111733, 2020.

Dee, D. P., et al., The ERA-Interim reanalysis: configuration and performance of the data assimilation system, *Quarterly Journal of the Royal Meteorological Society*, *137*(656), 553–597, doi:10.1002/qj.828, 2011.

DeMore, W. B., S. P. Sander, D. M. Golden, R. F. Hampson, M. J. Kurylo, C. J. Howard, A. R. Ravishankara, C. E. Kolb, and M. J. Molina, Chemical kinetics and photochemical data for use in stratospheric modeling. Evaluation Number 12, *Tech. rep.*, Jet Propulsion Laboratory, Pasadena, California, 1997.

Dolman, A. J., E. J. Moors, and J. A. Elbers, The carbon uptake of a mid latitude pine forest growing on sandy soil, *Agricultural and Forest Meteorology*, *111*(3), 157–170, doi:10.1016/S0168-1923(02)00024-2, 2002.

Doughty, C. E., et al., Drought impact on forest carbon dynamics and fluxes in Amazonia, *Nature*, *519*(7541), 78–82, doi:10.1038/nature14213, 2015.

Doughty, R., P. Köhler, C. Frankenberg, T. S. Magney, X. Xiao, Y. Qin, X. Wu, and B. Moore, TROPOMI reveals dry-season increase of solar-induced chlorophyll fluorescence in the Amazon forest, *Proceedings of the National Academy of Sciences*, p. 201908157, doi:10.1073/pnas.1908157116, 2019.

Drusch, M., et al., The FLuorescence EXplorer mission concept: ESA's Earth Explorer 8, *IEEE Transactions on Geoscience and Remote Sensing*, *55*(3), 1273–1284, doi:10.1109/TGRS.2016.2621820, 2017.

Dubey, M. K., R. Mohrschladt, N. M. Donahue, and J. G. Anderson, Isotope specific kinetics of hydroxyl radical (OH) with water (H_2O): Testing models of reactivity and atmospheric fractionation, *The Journal of Physical Chemistry A*, *101*(8), 1494–1500, doi:10.1021/jp962332p, 1997.

Dutkiewicz, V. A., and L. Husain, Stratospheric and tropospheric components of ^{7}Be in surface air, *Journal of Geophysical Research*, *90*(D3), 5783, doi:10.1029/JD090iD03p05783, 1985.

Eiler, J. M., and E. Schauble, $^{18}O^{13}C^{16}O$ in Earth's atmosphere, *Geochimica et Cosmochimica Acta*, *68*(23), 4767–4777, doi:10.1016/j.gca.2004.05.035, 2004.

Elbers, J. A., C. M. J. Jacobs, B. Kruijt, W. W. P. Jans, and E. J. Moors, Assessing the uncertainty of estimated annual totals of net ecosystem productivity: A practical approach applied to a mid latitude temperate pine forest, *Agricultural and Forest Meteorology*, *151*(12), 1823–1830, doi:10.1016/j.agrformet.2011.07.020, 2011.

Eller, C. B., et al., Modelling tropical forest responses to drought and El Niño with a stomatal optimization model based on xylem hydraulics, *Philosophical Transactions of the Royal Society B: Biological Sciences*, *373*(1760), doi:10.1098/rstb.2017.0315, 2018.

Erfanian, A., G. Wang, and L. Fomenko, Unprecedented drought over tropical South America in 2016: significantly under-predicted by tropical SST, *Scientific Reports*, *7*(1), 5811, doi:10.1038/s41598-017-05373-2, 2017.

Etheridge, D. M., L. P. Steele, R. L. Langenfelds, R. J. Francey, J.-M. Barnola, and V. I. Morgan, Natural and anthropogenic changes in atmospheric CO_2 over the last 1000 years from air in Antarctic ice and firn, *Journal of Geophysical Research: Atmospheres*, *101*(D2), 4115–4128, doi:10.1029/95JD03410, 1996.

Eva, H. D., and O. Huber, *A proposal for defining the geographical boundaries of Amazonia*, European Communities, 2005.

Fang, Y., et al., Global land carbon sink response to temperature and precipitation varies with ENSO phase, *Environmental Research Letters*, *12*(6), 064,007, doi:10.1088/1748-9326/aa6e8e, 2017.

Farquhar, G. D., S. von Caemmerer, and J. A. Berry, A biochemical model of photosynthetic CO_2 assimilation in leaves of C_3 species, *Planta*, *149*(1), 78–90, doi:10.1007/BF00386231, 1980.

Farquhar, G. D., M. H. O'Leary, and J. A. Berry, On the relationship between carbon isotope discrimination and the intercellular carbon dioxide concentration in leaves, *Australian Journal of Plant Physiology*, *9*(2), 121, doi:10.1071/PP9820121, 1982.

Farquhar, G. D., J. Lloyd, J. A. Taylor, L. B. Flanagan, J. P. Syvertsen, K. T. Hubick, S. C. Wong, and J. R. Ehleringer, Vegetation effects on the isotope composition of oxygen in atmospheric CO_2, *Nature*, *363*(6428), 439–443, doi:10.1038/363439a0, 1993.

Feilberg, K. L., S. R. Sellevåg, C. J. Nielsen, D. W. T. Griffith, and M. S. Johnson, $CO + OH \rightarrow CO_2 + H$: The relative reaction rate of five CO isotopologues, *Physical Chemistry Chemical Physics*, *4*(19), 4687–4693, doi:10.1039/B204827M, 2002.

Feilberg, K. L., M. S. Johnson, and C. J. Nielsen, Relative rates of reaction of $^{13}C^{16}O$, $^{12}C^{18}O$, $^{12}C^{17}O$ and $^{13}C^{18}O$ with OH and OD radicals, *Physical Chemistry Chemical Physics*, *7*(11), 2318, doi:10.1039/b503350k, 2005.

Feldpausch, T. R., et al., Amazon forest response to repeated droughts, *Global Biogeochemical Cycles*, *30*(7), 964–982, doi:10.1002/2015GB005133, 2016.

Flexas, J., J. M. Escalona, S. Evain, J. Gulias, I. Moya, C. B. Osmond, and H. Medrano, Steady-state chlorophyll fluorescence (Fs) measurements as a tool to follow variations of net CO_2 assimilation and stomatal conductance during water-stress in C_3 plants, *Physiologia Plantarum*, *114*(2), 231–240, doi:10.1034/j.1399-3054.2002.1140209.x, 2002.

Florentie, L., W. Peters, G. Koren, E. van Schaik, F. Boersma, and M. Krol, Exploiting SIF and NIRv anomalies to enhance biosphere flux estimates in an atmospheric CO_2 inversion, CHE-VERIFY Joint General Assembly, Reading, United Kingdom, 2019.

Francey, R. J., and P. P. Tans, Latitudinal variation in oxygen-18 of atmospheric CO_2, *Nature*, *327*(6122), 495–497, doi:10.1038/327495a0, 1987.

Frankenberg, C., and J. Berry, Solar Induced Chlorophyll Fluorescence: Origins, Relation to Photosynthesis and Retrieval, in *Comprehensive Remote Sensing*, pp. 143–162, Elsevier, doi:10.1016/B978-0-12-409548-9.10632-3, 2018.

Frankenberg, C., C. O'Dell, J. Berry, L. Guanter, J. Joiner, P. Köhler, R. Pollock, and T. E. Taylor, Prospects for chlorophyll fluorescence remote sensing from the Orbiting Carbon Observatory-2, *Remote Sensing of Environment*, *147*, 1–12, doi:10.1016/J.RSE.2014.02.007, 2014.

Frankenberg, C., et al., New global observations of the terrestrial carbon cycle from GOSAT: Patterns of plant fluorescence with gross primary productivity, *Geophysical Research Letters*, *38*(17), L17,706, doi:10.1029/2011GL048738, 2011.

Friedlingstein, P., et al., Global carbon budget 2019, *Earth System Science Data*, *11*(4), 1783–1838, doi:10.5194/essd-11-1783-2019, 2019.

Ganzeveld, L. N., J. Lelieveld, F. J. Dentener, M. C. Krol, A. J. Bouwman, and G.-J. Roelofs, Global soil-biogenic NOx emissions and the role of canopy processes, *Journal of Geophysical Research*, *107*(D16), 4298, doi:10.1029/2001JD001289, 2002a.

Ganzeveld, L. N., J. Lelieveld, F. J. Dentener, M. C. Krol, and G.-J. Roelofs, Atmosphere-biosphere trace gas exchanges simulated with a single-column model, *Journal of Geophysical Research*, *107*(D16), 4297, doi:10.1029/2001JD000684, 2002b.

Gatti, L. V., et al., Drought sensitivity of Amazonian carbon balance revealed by atmospheric measurements, *Nature*, *506*(7486), 76–80, doi:10.1038/nature12957, 2014.

Gaubert, B., et al., Global atmospheric CO_2 inverse models converging on neutral tropical land exchange, but disagreeing on fossil fuel and atmospheric growth rate, *Biogeosciences*, *16*(1), 117–134, doi:10.5194/bg-16-117-2019, 2019.

Gerbig, C., S. Körner, and J. C. Lin, Vertical mixing in atmospheric tracer transport models: Error characterization and propagation, *Atmospheric Chemistry and Physics*, *8*(3), 591–602, doi:10.5194/acp-8-591-2008, 2008.

Giardina, F., A. G. Konings, D. Kennedy, S. H. Alemohammad, R. S. Oliveira, M. Uriarte, and P. Gentine, Tall Amazonian forests are less sensitive to precipitation variability, *Nature Geoscience*, *11*(6), 405–409, doi:10.1038/s41561-018-0133-5, 2018.

Giglio, L., J. T. Randerson, and G. R. van der Werf, Analysis of daily, monthly, and annual burned area using the fourth-generation global fire emissions database (GFED4), *Journal of Geophysical Research: Biogeosciences*, *118*(1), 317–328, doi:10.1002/jgrg.20042, 2013.

Gillon, J., and D. Yakir, Influence of carbonic anhydrase activity in terrestrial vegetation on the ^{18}O content of atmospheric CO_2, *Science*, *291*(5513), 2584–2587, doi:10.1126/science.1056374, 2001.

Gillon, J. S., and D. Yakir, Naturally low carbonic anhydrase activity in C_4 and C_3 plants limits discrimination against $C^{18}OO$ during photosynthesis, *Plant, Cell and Environment*, *23*(9), 903–915, doi:10.1046/j.1365-3040.2000.00597.x, 2000.

Gloor, E., et al., Tropical land carbon cycle responses to 2015/16 El Niño as recorded by atmospheric greenhouse gas and remote sensing data, *Philosophical Transactions of the Royal Society B: Biological Sciences*, *373*(1760), 20170,302, doi:10.1098/rstb.2017.0302, 2018.

Gloor, M., J. L. Sarmiento, and N. Gruber, What can be learned about carbon cycle climate feedbacks from the CO_2 airborne fraction?, *Atmospheric Chemistry and Physics*, *10*(16), 7739–7751, doi:10.5194/acp-10-7739-2010, 2010.

Gonçalves, N. B., A. P. Lopes, R. Dalagnol, J. Wu, D. M. Pinho, and B. W. Nelson, Both near-surface and satellite remote sensing confirm drought legacy effect on tropical forest leaf phenology after 2015/2016 ENSO drought, *Remote Sensing of Environment*, *237*, 111,489, doi:10.1016/j.rse.2019.111489, 2020.

Graven, H. D., et al., Enhanced seasonal exchange of CO_2 by northern ecosystems since 1960, *Science*, *341*(6150), 1085–1089, doi:10.1126/science.1239207, 2013.

Gromov, S. S., Stable isotope composition of atmospheric carbon monoxide: A modelling study, Ph.D. thesis, Johannes Gutenberg-Universität Mainz, doi:10.13140/RG.2.2.30769.17760, 2013.

Guanter, L., et al., Global and time-resolved monitoring of crop photosynthesis with chlorophyll fluorescence, *Proceedings of the National Academy of Sciences*, *111*(14), E1327–E1333, doi:10.1073/pnas.1320008111, 2014.

Guanter, L., et al., Potential of the TROPOspheric Monitoring Instrument (TROPOMI) onboard the Sentinel-5 Precursor for the monitoring of terrestrial chlorophyll fluorescence, *Atmospheric Measurement Techniques*, *8*(3), 1337–1352, doi:10.5194/amt-8-1337-2015, 2015.

Gurney, K. R., et al., Towards robust regional estimates of CO_2 sources and sinks using atmospheric transport models, *Nature*, *415*(6872), 626–630, doi:10.1038/415626a, 2002.

Harper, A., I. T. Baker, A. S. Denning, D. A. Randall, D. Dazlich, and M. Branson, Impact of evapotranspiration on dry season climate in the Amazon forest, *Journal of Climate*, *27*(2), 574–591, doi:10.1175/JCLI-D-13-00074.1, 2014.

Haynes, K. D., I. T. Baker, A. S. Denning, R. Stöckli, K. Schaefer, E. Y. Lokupitiya, and J. M. Haynes, Representing grasslands using dynamic prognostic phenology based on biological growth stages: 1. Implementation in the Simple Biosphere model (SiB4), *Journal of Advances in Modeling Earth Systems*, *11*(12), 4423–4439, doi:10.1029/2018MS001540, 2019a.

Haynes, K. D., I. T. Baker, A. S. Denning, S. Wolf, G. Wohlfahrt, G. Kiely, R. C. Minaya, and J. M. Haynes, Representing grasslands using dynamic prognostic phenology based on biological growth stages: 2. Carbon cycling, *Journal of Advances in Modeling Earth Systems*, *11*(12), 4440–4465, doi:10.1029/2018MS001541, 2019b.

Heidenreich, J. E., and M. H. Thiemens, A non-mass-dependent isotope effect in the production of ozone from molecular oxygen, *The Journal of Chemical Physics*, *78*(2), 892–895, doi:10.1063/1.444791, 1983.

Heimann, M., and C. D. Keeling, A three-dimensional model of atmospheric CO_2 transport based on observed winds: 2. Model description and simulated tracer experiments, in *Aspects of Climate Variability in the Pacific and the Western Amer-*

icas, edited by D. Peterson, American Geophysical Union, Washington, D. C., doi:10.1029/GM055p0237, 1989.

Heimann, M., et al., The Zotino Tall Tower Observatory (ZOTTO): Quantifying large scale biogeochemical changes in Central Siberia, *Nova Acta Leopoldina*, *117*(399), 51–64, 2014.

Hemes, K. S., J. Verfaillie, and D. D. Baldocchi, Wildfire-smoke aerosols lead to increased light use efficiency among agricultural and restored wetland land uses in California's Central Valley, *Journal of Geophysical Research: Biogeosciences*, *125*(2), doi:10.1029/2019JG005380, 2020.

Heus, T., et al., Formulation of the Dutch Atmospheric Large-Eddy Simulation (DALES) and overview of its applications, *Geoscientific Model Development*, *3*(2), 415–444, doi:10.5194/gmd-3-415-2010, 2010.

Hilker, T., A. I. Lyapustin, C. J. Tucker, F. G. Hall, R. B. Myneni, Y. Wang, J. Bi, Y. M. de Moura, and P. J. Sellers, Vegetation dynamics and rainfall sensitivity of the Amazon, *Proceedings of the National Academy of Sciences of the United States of America*, *111*(45), 16,041–16,046, doi:10.1073/pnas.1404870111, 2014.

Hirsch, A. I., A. M. Michalak, L. M. Bruhwiler, W. Peters, E. J. Dlugokencky, and P. P. Tans, Inverse modeling estimates of the global nitrous oxide surface flux from 1998-2001, *Global Biogeochemical Cycles*, *20*(1), GB1008, doi:10.1029/2004GB002443, 2006.

Hoag, K. J., C. J. Still, I. Y. Fung, and K. A. Boering, Triple oxygen isotope composition of tropospheric carbon dioxide as a tracer of terrestrial gross carbon fluxes, *Geophysical Research Letters*, *32*(2), 1–5, doi:10.1029/2004GL021011, 2005.

Hofmann, M. E. G., B. Horváth, L. Schneider, W. Peters, K. Schützenmeister, and A. Pack, Atmospheric measurements of $\Delta^{17}O$ in CO_2 in Göttingen, Germany reveal a seasonal cycle driven by biospheric uptake, *Geochimica et Cosmochimica Acta*, *199*, 143–163, doi:10.1016/j.gca.2016.11.019, 2017.

Hofmann, M. E. G., T. L. Pons, M. Ziegler, G. Koren, L. J. Lourens, and T. Röckmann, Fractionation of clumped isotopes of CO_2 during photosynthesis, in prep.

Holloway, T., H. Levy II, and P. Kasibhatla, Global distribution of carbon monoxide, *Journal of Geophysical Research: Atmospheres*, *105*(D10), 12,123–12,147, doi:10.1029/1999JD901173, 2000.

Holloway-Phillips, M., L. A. Cernusak, H. Stuart-Williams, N. Ubierna, and G. D. Farquhar, Two-source δ^{18}O method to validate the CO^{18}O-photosynthetic discrimination model: Implications for mesophyll conductance, *Plant Physiology*, *181*(3), 1175–1190, doi:10.1104/pp.19.00633, 2019.

Holton, J. R., On the global exchange of mass between the stratosphere and troposphere, *Journal of the Atmospheric Sciences*, *47*(3), 392–395, doi:10.1175/1520-0469(1990)047<0392:OTGEOM>2.0.CO;2, 1990.

Hooghiemstra, P. B., M. C. Krol, J. F. Meirink, P. Bergamaschi, G. R. van der Werf, P. C. Novelli, I. Aben, and T. Röckmann, Optimizing global CO emission estimates using a four-dimensional variational data assimilation system and surface network observations, *Atmospheric Chemistry and Physics*, *11*(10), 4705–4723, doi:10.5194/acp-11-4705-2011, 2011.

Horváth, B., M. E. G. Hofmann, and A. Pack, On the triple oxygen isotope composition of carbon dioxide from some combustion processes, *Geochimica et Cosmochimica Acta*, *95*, 160–168, doi:10.1016/j.gca.2012.07.021, 2012.

Houweling, S., et al., Iconic CO_2 Time Series at Risk, *Science*, *337*(6098), 1038–1040, doi:10.1126/science.337.6098.1038-b, 2012.

Howard, A. R., and L. A. Donovan, Helianthus nighttime conductance and transpiration respond to soil water but not nutrient availability, *Plant Physiology*, *143*(1), 145–155, doi:10.1104/pp.106.089383, 2007.

Hubau, W., et al., Asynchronous carbon sink saturation in African and Amazonian tropical forests, *Nature*, *579*(7797), 80–87, doi:10.1038/s41586-020-2035-0, 2020.

Huff, A. K., and M. H. Thiemens, ^{17}O/^{16}O and ^{18}O/^{16}O isotope measurements of atmospheric carbon monoxide and its sources, *Geophysical Research Letters*, *25*(18), 3509–3512, doi:10.1029/98GL02603, 1998.

Huffman, G. J., D. T. Bolvin, E. J. Nelkin, D. B. Wolff, R. F. Adler, G. Gu, Y. Hong, K. P. Bowman, and E. F. Stocker, The TRMM Multisatellite Precipitation Analysis (TMPA): Quasi-global, multiyear, combined-sensor precipitation estimates at fine scales, *Journal of Hydrometeorology*, *8*(1), 38–55, doi:10.1175/JHM560.1, 2007.

Huijnen, V., et al., The global chemistry transport model TM5: description and evaluation of the tropospheric chemistry version 3.0, *Geoscientific Model Development*, *3*(2), 445–473, doi:10.5194/gmd-3-445-2010, 2010.

Humphrey, V., J. Zscheischler, P. Ciais, L. Gudmundsson, S. Sitch, and S. I. Seneviratne, Sensitivity of atmospheric CO_2 growth rate to observed changes in terrestrial water storage, *Nature*, *560*(7720), 628–631, doi:10.1038/s41586-018-0424-4, 2018.

IPCC, *Workshop Report of the Intergovernmental Panel on Climate Change. Workshop on Impacts of Ocean Acidification on Marine Biology and Ecosystems*, 164 pp., IPCC Working Group II Technical Support Unit, Carnegie Institution, Stanford, CA, USA, 2011.

IPCC, *Climate Change 2013: The Physical Science Basis. Contribution of Working Group I to the Fifth Assessment Report of the Intergovernmental Panel on Climate Change*, 1535 pp., Cambridge University Press, Cambridge, United Kingdom and New York, NY, USA, 2013.

IPCC, *Climate Change 2014: Impacts, Adaptation, and Vulnerability. Part A: Global and Sectoral Aspects. Contribution of Working Group II to the Fifth Assessment Report of the Intergovernmental Panel on Climate Change*, 1132 pp., Cambridge University Press, Cambridge, United Kingdom and New York, NY, USA, 2014.

Jacobson, A. R., S. E. Mikaloff Fletcher, N. Gruber, J. L. Sarmiento, and M. Gloor, A joint atmosphere-ocean inversion for surface fluxes of carbon dioxide: 1. Methods and global-scale fluxes, *Global Biogeochemical Cycles*, *21*(1), GB1019, doi:10.1029/2005GB002556, 2007.

Jiang, M., et al., The fate of carbon in a mature forest under carbon dioxide enrichment, *Nature*, *580*(7802), 227–231, doi:10.1038/s41586-020-2128-9, 2020.

Jiménez-Muñoz, J. C., C. Mattar, J. Barichivich, A. Santamaría-Artigas, K. Takahashi, Y. Malhi, J. A. Sobrino, and G. V. D. Schrier, Record-breaking warming and extreme drought in the Amazon rainforest during the course of El Niño 2015-2016, *Scientific Reports*, *6*(1), 33,130, doi:10.1038/srep33130, 2016.

Joetzjer, E., et al., Predicting the response of the Amazon rainforest to persistent drought conditions under current and future climates: A major challenge for global land surface models, *Geoscientific Model Development*, *7*(6), 2933–2950, doi:10.5194/gmd-7-2933-2014, 2014.

Johnston, J. C., T. Röckmann, and C. A. M. Brenninkmeijer, CO_2 + $O(^1D)$ isotopic exchange: Laboratory and modeling studies, *Journal of Geophysical Research: Atmospheres*, *105*(D12), 15,213–15,229, doi:10.1029/2000JD900070, 2000.

Joiner, J., Y. Yoshida, A. P. Vasilkov, Y. Yoshida, L. A. Corp, and E. M. Middleton, First observations of global and seasonal terrestrial chlorophyll fluorescence from space, *Biogeosciences*, *8*(3), 637–651, doi:10.5194/bg-8-637-2011, 2011.

Joiner, J., Y. Yoshida, A. P. Vasilkov, E. M. Middleton, P. K. E. Campbell, Y. Yoshida, A. Kuze, and L. A. Corp, Filling-in of near-infrared solar lines by terrestrial fluorescence and other geophysical effects: simulations and space-based observations from SCIAMACHY and GOSAT, *Atmospheric Measurement Techniques*, *5*(4), 809–829, doi:10.5194/amt-5-809-2012, 2012.

Joiner, J., L. Guanter, R. Lindstrot, M. Voigt, A. P. Vasilkov, E. M. Middleton, K. F. Huemmrich, Y. Yoshida, and C. Frankenberg, Global monitoring of terrestrial chlorophyll fluorescence from moderate-spectral-resolution near-infrared satellite measurements: methodology, simulations, and application to GOME-2, *Atmospheric Measurement Techniques*, *6*(10), 2803–2823, doi:10.5194/amt-6-2803-2013, 2013.

Joiner, J., Y. Yoshida, L. Guanter, and E. M. Middleton, New methods for the retrieval of chlorophyll red fluorescence from hyperspectral satellite instruments: simulations and application to GOME-2 and SCIAMACHY, *Atmospheric Measurement Techniques*, *9*(8), 3939–3967, doi:10.5194/amt-9-3939-2016, 2016.

Jones, M. O., J. S. Kimball, and R. R. Nemani, Asynchronous Amazon forest canopy phenology indicates adaptation to both water and light availability, *Environmental Research Letters*, *9*(12), 124,021, doi:10.1088/1748-9326/9/12/124021, 2014.

Jung, M., et al., Global patterns of land-atmosphere fluxes of carbon dioxide, latent heat, and sensible heat derived from eddy covariance, satellite, and meteorological observations, *Journal of Geophysical Research*, *116*(3), G00J07, doi:10.1029/2010JG001566, 2011.

Kaiser, J., Reformulated ^{17}O correction of mass spectrometric stable isotope measurements in carbon dioxide and a critical appraisal of historic 'absolute' carbon and oxygen isotope ratios, *Geochimica et Cosmochimica Acta*, *72*(5), 1312–1334, doi:10.1016/j.gca.2007.12.011, 2008.

Kaiser, J. W., et al., Biomass burning emissions estimated with a global fire assimilation system based on observed fire radiative power, *Biogeosciences*, *9*(1), 527–554, doi:10.5194/bg-9-527-2012, 2012.

Kawagucci, S., U. Tsunogai, S. Kudo, F. Nakagawa, H. Honda, S. Aoki, T. Nakazawa, M. Tsutsumi, and T. Gamo, Long-term observation of mass-independent oxygen isotope

anomaly in stratospheric CO_2, *Atmospheric Chemistry and Physics*, *8*(20), 6189–6197, doi:10.5194/acp-8-6189-2008, 2008.

Keeling, C. D., The carbon dioxide cycle: Reservoir models to depict the exchange of atmospheric carbon dioxide with the oceans and land plants, in *Chemistry of the Lower Atmosphere*, edited by S. Rasool, Plenum Press, New York, doi:10.1007/978-1-4684-1986-3_6, 1973.

Keeling, C. D., and R. Revelle, Effects of El Niño/Southern Oscillation on the atmospheric content of carbon dioxide, *Meteoritics*, *20*(2), 437–450, 1985.

Keeling, C. D., R. B. Bacastow, A. E. Bainbridge, C. A. Ekdahl Jr., P. R. Guenther, L. S. Waterman, and J. F. S. Chin, Atmospheric carbon dioxide variations at Mauna Loa Observatory, Hawaii, *Tellus*, *28*(6), 538–551, doi:10.3402/tellusa.v28i6.11322, 1976.

Keeling, R. F., S. C. Piper, and M. Heimann, Global and hemispheric CO_2 sinks deduced from changes in atmospheric O_2 concentration, *Nature*, *381*(6579), 218–221, doi:10.1038/381218a0, 1996.

Keeling, R. F., A. C. Manning, E. M. McEvoy, and S. R. Shertz, Methods for measuring changes in atmospheric O_2 concentration and their application in southern hemisphere air, *Journal of Geophysical Research: Atmospheres*, *103*(D3), 3381–3397, doi:10.1029/97JD02537, 1998.

Keeling, R. F., H. D. Graven, L. R. Welp, L. Resplandy, J. Bi, S. C. Piper, Y. Sun, A. Bollenbacher, and H. A. J. Meijer, Atmospheric evidence for a global secular increase in carbon isotopic discrimination of land photosynthesis, *Proceedings of the National Academy of Sciences*, *114*(39), 10,361–10,366, doi:10.1073/pnas.1619240114, 2017.

Kirschbaum, M. U. F., D. Eamus, R. M. Grifford, S. H. Roxburgh, and P. J. Sands, Definitions of some ecological terms commonly used in carbon accounting, in *Net Ecosystem Exchange*, edited by M. U. F. Kirschbaum and R. Mueller, Cooperative Research Centre for Greenhouse Accounting, 2001.

Klein, T., et al., Xylem embolism refilling and resilience against drought-induced mortality in woody plants: Processes and trade-offs, *Ecological Research*, *33*(5), 839–855, doi:10.1007/s11284-018-1588-y, 2018.

Köhler, P., L. Guanter, and J. Joiner, A linear method for the retrieval of sun-induced chlorophyll fluorescence from GOME-2 and SCIAMACHY data, *Atmospheric Measurement Techniques*, *8*(6), 2589–2608, doi:10.5194/amt-8-2589-2015, 2015.

Köhler, P., C. Frankenberg, T. S. Magney, L. Guanter, J. Joiner, and J. Landgraf, Global retrievals of solar-induced chlorophyll fluorescence with TROPOMI: First results and intersensor comparison to OCO-2, *Geophysical Research Letters*, *45*(19), 456–10, doi:10.1029/2018GL079031, 2018.

Kooijmans, L. M. J., W. Sun, J. Aalto, K.-M. Erkkilä, K. Maseyk, U. Seibt, T. Vesala, I. Mammarella, and H. Chen, Influences of light and humidity on carbonyl sulfide-based estimates of photosynthesis, *Proceedings of the National Academy of Sciences*, p. 201807600, doi:10.1073/pnas.1807600116, 2019.

Kooreman, M., P. Stammes, O. Tuinder, F. Boersma, E. van Schaik, and S. Botia, GOME-2 Sun-Induced Fluorescence of Terrestrial Ecosystems Retrieval (SIFTER), Algorithm Theoretical Basis Document, *Tech. rep.*, KNMI, De Bilt, 2018.

Koren, G., et al., Widespread reduction in sun-induced fluorescence from the Amazon during the 2015/2016 El Niño, *Philosophical Transactions of the Royal Society B: Biological Sciences*, *373*(1760), 20170,408, doi:10.1098/rstb.2017.0408, 2018.

Koren, G., et al., Global 3-D simulations of the triple oxygen isotope signature $\Delta^{17}O$ in atmospheric CO_2, *Journal of Geophysical Research: Atmospheres*, doi:10.1029/2019JD030387, 2019.

Kottek, M., J. Grieser, C. Beck, B. Rudolf, and F. Rubel, World map of the Köppen-Geiger climate classification updated, *Meteorologische Zeitschrift*, *15*(3), 259–263, doi:10.1127/0941-2948/2006/0130, 2006.

Krol, M., S. Houweling, B. Bregman, M. van den Broek, A. Segers, P. van Velthoven, W. Peters, F. Dentener, and P. Bergamaschi, The two-way nested global chemistry-transport zoom model TM5: algorithm and applications, *Atmospheric Chemistry and Physics*, *5*(2), 417–432, doi:10.5194/acp-5-417-2005, 2005.

Krol, M., et al., Age of Air as a diagnostic for transport time-scales in global models, *Geoscientific Model Development Discussions*, *11*(8), 1–33, doi:10.5194/gmd-2017-262, 2017.

Lämmerzahl, P., T. Röckmann, C. A. M. Brenninkmeijer, D. Krankowsky, and K. Mauersberger, Oxygen isotope composition of stratospheric carbon dioxide, *Geophysical Research Letters*, *29*(12), 1582, doi:10.1029/2001GL014343, 2002.

Landais, A., E. Barkan, D. Yakir, and B. Luz, The triple isotopic composition of oxygen in leaf water, *Geochimica et Cosmochimica Acta*, *70*(16), 4105–4115, doi:10.1016/j.gca.2006.06.1545, 2006.

Landais, A., C. Risi, S. Bony, F. Vimeux, L. Descroix, S. Falourd, and A. Bouygues, Combined measurements of ^{17}Oexcess and d-excess in African monsoon precipitation: Implications for evaluating convective parameterizations, *Earth and Planetary Science Letters*, *298*(1-2), 104–112, doi:10.1016/j.epsl.2010.07.033, 2010.

Langenfelds, R. L., R. J. Francey, B. C. Pak, L. P. Steele, J. Lloyd, C. M. Trudinger, and C. E. Allison, Interannual growth rate variations of atmospheric CO_2 and its δ^{13}C, H2, CH_4, and CO between 1992 and 1999 linked to biomass burning, *Global Biogeochemical Cycles*, *16*(3), 21–1, doi:10.1029/2001gb001466, 2002.

Laskar, A. H., S. Mahata, and M.-C. Liang, Identification of anthropogenic CO_2 using triple oxygen and clumped isotopes, *Environmental Science & Technology*, *50*(21), 11,806–11,814, doi:10.1021/acs.est.6b02989, 2016.

Laskar, A. H., S. Mahata, S. K. Bhattacharya, and M. Liang, Triple oxygen and clumped isotope compositions of CO_2 in the middle troposphere, *Earth and Space Science*, p. 2019EA000573, doi:10.1029/2019EA000573, 2019.

Laskar, A. H., A. S. Maurya, V. Singh, B. R. Gurjar, and M.-C. Liang, A new perspective of probing the level of pollution in the megacity Delhi affected by crop residue burning using the triple oxygen isotope technique in atmospheric CO_2, *Environmental Pollution*, *263*, doi:10.1016/j.envpol.2020.114542, 2020.

Lasslop, G., M. Reichstein, D. Papale, A. D. Richardson, A. Arneth, A. Barr, P. Stoy, and G. Wohlfahrt, Separation of net ecosystem exchange into assimilation and respiration using a light response curve approach: Critical issues and global evaluation, *Global Change Biology*, *16*(1), 187–208, doi:10.1111/j.1365-2486.2009.02041.x, 2010.

Launois, T., P. Peylin, S. Belviso, and B. Poulter, A new model of the global biogeochemical cycle of carbonyl sulfide – Part 2: Use of carbonyl sulfide to constrain gross primary productivity in current vegetation models, *Atmospheric Chemistry and Physics*, *15*(16), 9285–9312, doi:10.5194/acp-15-9285-2015, 2015.

Law, R. M., et al., TransCom model simulations of hourly atmospheric CO_2: Experimental overview and diurnal cycle results for 2002, *Global Biogeochemical Cycles*, *22*(3), doi:10.1029/2007GB003050, 2008.

Le Quéré, C., et al., Global carbon budget 2015, *Earth System Science Data*, *7*(2), 349–396, doi:10.5194/essd-7-349-2015, 2015.

Le Quéré, C., et al., Global carbon budget 2016, *Earth System Science Data*, *8*(2), 605–649, doi:10.5194/essd-8-605-2016, 2016.

Le Quéré, C., et al., Global Carbon Budget 2017, *Earth System Science Data*, *10*(1), 405–448, doi:10.5194/essd-10-405-2018, 2018a.

Le Quéré, C., et al., Global Carbon Budget 2018, *Earth System Science Data*, *10*(4), 2141–2194, doi:10.5194/essd-10-2141-2018, 2018b.

Lee, J.-E., et al., Forest productivity and water stress in Amazonia: observations from GOSAT chlorophyll fluorescence, *Proceedings of the Royal Society B: Biological Sciences*, *280*(1761), 1–9, doi:10.1098/rspb.2013.0171, 2013.

Lee, X., T. J. Griffis, J. M. Baker, K. A. Billmark, K. Kim, and L. R. Welp, Canopy-scale kinetic fractionation of atmospheric carbon dioxide and water vapor isotopes, *Global Biogeochemical Cycles*, *23*(1), GB1002, doi:10.1029/2008GB003331, 2009.

Lewis, S. L., P. M. Brando, O. L. Phillips, G. M. F. van der Heijden, and D. Nepstad, The 2010 Amazon drought, *Science*, *331*(6017), 554–554, doi:10.1126/science.1200807, 2011.

Li, W., B. Ni, J. Deqiu, and Z. Qinglian, Measurement of the absolute abundance of oxygen-17 in V-SMOW, *Chinese Science Bulletin*, *33*(19), 1610–1613, doi:10.1360/sb1988-33-19-1610, 1988.

Liang, M.-C., and S. Mahata, Oxygen anomaly in near surface carbon dioxide reveals deep stratospheric intrusion, *Scientific Reports*, *5*, 11,352, doi:10.1038/srep11352, 2015.

Liang, M.-C., G. a. Blake, and Y. L. Yung, Seasonal cycle of $C^{16}O^{16}O$, $C^{16}O^{17}O$, and $C^{16}O^{18}O$ in the middle atmosphere: Implications for mesospheric dynamics and biogeochemical sources and sinks of CO_2, *Journal of Geophysical Research*, *113*(D12), D12,305, doi:10.1029/2007JD008392, 2008.

Liang, M.-C., S. Mahata, A. H. Laskar, and S. K. Bhattacharya, Spatiotemporal variability of oxygen isotope anomaly in near surface air CO_2 over urban, semi-urban and ocean areas in and around Taiwan, *Aerosol and Air Quality Research*, *17*(3), 706–720, doi:10.4209/aaqr.2016.04.0171, 2017a.

Liang, M.-C., S. Mahata, A. H. Laskar, M. H. Thiemens, and S. Newman, Oxygen isotope anomaly in tropospheric CO_2 and implications for CO_2 residence time in the atmosphere and gross primary productivity, *Scientific Reports*, *7*(1), 13,180, doi:10.1038/s41598-017-12774-w, 2017b.

Liu, J., et al., Contrasting carbon cycle responses of the tropical continents to the 2015-2016 El Niño, *Science*, *358*(6360), eaam5690, doi:10.1126/science.aam5690, 2017.

Luus, K. A., et al., Tundra photosynthesis captured by satellite-observed solar-induced chlorophyll fluorescence, *Geophysical Research Letters*, *44*(3), 1564–1573, doi:10.1002/2016GL070842, 2017.

Luz, B., and E. Barkan, Variations of $^{17}O/^{16}O$ and $^{18}O/^{16}O$ in meteoric waters, *Geochimica et Cosmochimica Acta*, *74*(22), 6276–6286, doi:10.1016/j.gca.2010.08.016, 2010.

Luz, B., E. Barkan, M. L. Bender, M. H. Thiemens, and K. A. Boering, Triple-isotope composition of atmospheric oxygen as a tracer of biosphere productivity, *Nature*, *400*(6744), 547–550, doi:10.1038/22987, 1999.

Lyapustin, A., J. Martonchik, Y. Wang, I. Laszlo, and S. Korkin, Multiangle implementation of atmospheric correction (MAIAC): 1. Radiative transfer basis and look-up tables, *Journal of Geophysical Research: Atmospheres*, *116*(D3), 1–9, doi:10.1029/2010JD014985, 2011a.

Lyapustin, A., Y. Wang, I. Laszlo, R. Kahn, S. Korkin, L. Remer, R. Levy, and J. S. Reid, Multiangle implementation of atmospheric correction (MAIAC): 2. Aerosol algorithm, *Journal of Geophysical Research: Atmospheres*, *116*(D3), 1–15, doi:10.1029/2010JD014986, 2011b.

Lyapustin, A., Y. Wang, S. Korkin, and D. Huang, MODIS Collection 6 MAIAC algorithm, *Atmospheric Measurement Techniques*, *11*(10), 5741–5765, doi:10.5194/amt-11-5741-2018, 2018.

Lyapustin, A. I., Y. Wang, I. Laszlo, T. Hilker, F. G. Hall, P. J. Sellers, C. J. Tucker, and S. V. Korkin, Multi-angle implementation of atmospheric correction for MODIS (MAIAC): 3. Atmospheric correction, *Remote Sensing of Environment*, *127*, 385–393, doi:10.1016/j.rse.2012.09.002, 2012.

Lyons, J. R., Transfer of mass-independent fractionation in ozone to other oxygen-containing radicals in the atmosphere, *Geophysical Research Letters*, *28*(17), 3231–3234, doi:10.1029/2000GL012791, 2001.

Ma, J., L. M. J. Kooijmans, A. Cho, S. A. Montzka, N. Glatthor, J. R. Worden, L. Kuai, E. L. Atlas, and M. C. Krol, Inverse modelling of carbonyl sulfide: Implementation, evaluation and implications for the global budget, *Atmospheric Chemistry and Physics Discussions*, pp. 1–39, doi:10.5194/acp-2020-603, 2020.

MacBean, N., P. Peylin, F. Chevallier, M. Scholze, and G. Schürmann, Consistent assimilation of multiple data streams in a carbon cycle data assimilation system, *Geoscientific Model Development*, *9*(10), 3569–3588, doi:10.5194/gmd-9-3569-2016, 2016.

Mahata, S., S. K. Bhattacharya, C.-H. Wang, and M.-C. Liang, Oxygen isotope exchange between O_2 and CO_2 over hot platinum: An innovative technique for measuring $\Delta^{17}O$ in CO_2, *Analytical Chemistry*, *85*(14), 6894–6901, doi:10.1021/ac4011777, 2013.

Mahata, S., S. K. Bhattacharya, and M.-C. Liang, An improved method of high-precision determination of $\Delta^{17}O$ of CO_2 by catalyzed exchange with O_2 using hot platinum, *Rapid Communications in Mass Spectrometry*, *30*(1), 119–131, doi:10.1002/rcm.7423, 2016a.

Mahata, S., C.-H. Wang, S. K. Bhattacharya, and M.-C. Liang, Near surface CO_2 triple oxygen isotope composition, *Terrestrial, Atmospheric and Oceanic Sciences*, *27*(1), 99–106, doi:10.3319/TAO.2015.09.16.01(A), 2016b.

Malhi, Y., L. Rowland, L. E. O. C. Aragão, and R. A. Fisher, New insights into the variability of the tropical land carbon cycle from the El Niño of 2015/2016, *Philosophical Transactions of the Royal Society B: Biological Sciences*, *373*(1760), 20170,298, doi:10.1098/rstb.2017.0298, 2018.

Malhi, Y., et al., An international network to monitor the structure, composition and dynamics of Amazonian forests (RAINFOR), *Journal of Vegetation Science*, *13*(3), 439–450, doi:10.1111/j.1654-1103.2002.tb02068.x, 2002.

Marengo, J. A., C. A. Nobre, J. Tomasella, M. D. Oyama, G. S. de Oliveira, R. de Oliveira, H. Camargo, L. M. Alves, and I. F. Brown, The drought of Amazonia in 2005, *Journal of Climate*, *21*(3), 495–516, doi:10.1175/2007JCLI1600.1, 2008.

Martens, B., D. G. Miralles, H. Lievens, R. van der Schalie, R. A. M. de Jeu, D. Fernández-Prieto, H. E. Beck, W. A. Dorigo, and N. E. C. Verhoest, GLEAM v3: Satellite-based land evaporation and root-zone soil moisture, *Geoscientific Model Development*, *10*(5), 1903–1925, doi:10.5194/gmd-10-1903-2017, 2017.

McManus, J. B., D. D. Nelson, and M. S. Zahniser, Design and performance of a dual-laser instrument for multiple isotopologues of carbon dioxide and water, *Optics Express*, *23*(5), 6569, doi:10.1364/OE.23.006569, 2015.

Mebel, A. M., M. Hayashi, V. V. Kislov, and S. H. Lin, Theoretical study of oxygen isotope exchange and quenching in the $O(^1D) + CO_2$ reaction, *The Journal of Physical Chemistry A*, *108*(39), 7983–7994, doi:10.1021/jp049315h, 2004.

Meijer, H. A. J., and W. J. Li, The use of electrolysis for accurate $\delta^{17}O$ and $\delta^{18}O$ isotope measurements in water, *Isotopes in Environmental and Health Studies*, *34*(4), 349–369, doi:10.1080/10256019808234072, 1998.

Mengistu, A. G., G. Mengistu Tsidu, G. Koren, M. L. Kooreman, K. F. Boersma, and W. Peters, Sun-induced fluorescence and near infrared reflectance of vegetation track the seasonal dynamics of gross primary production over Africa, in review.

Miguez-Macho, G., and Y. Fan, The role of groundwater in the Amazon water cycle: 2. Influence on seasonal soil moisture and evapotranspiration, *Journal of Geophysical Research :Atmospheres*, *117*(D15), doi:10.1029/2012JD017540, 2012.

Miller, J. B., D. Yakir, J. W. C. White, and P. P. Tans, Measurement of $^{18}O/^{16}O$ in the soil-atmosphere CO_2 flux, *Global Biogeochemical Cycles*, *13*(3), 761–774, doi:10.1029/1999GB900028, 1999.

Miralles, D. G., T. R. H. Holmes, R. A. M. De Jeu, J. H. Gash, A. G. C. A. Meesters, and A. J. Dolman, Global land-surface evaporation estimated from satellite-based observations, *Hydrology and Earth System Sciences*, *15*(2), 453–469, doi:10.5194/hess-15-453-2011, 2011.

Moncrieff, J. B., et al., A system to measure surface fluxes of momentum, sensible heat, water vapour and carbon dioxide, *Journal of Hydrology*, *188-189*, 589–611, doi:10.1016/S0022-1694(96)03194-0, 1997.

Monge-Sanz, B. M., M. P. Chipperfield, A. J. Simmons, and S. M. Uppala, Mean age of air and transport in a CTM: Comparison of different ECMWF analyses, *Geophysical Research Letters*, *34*(4), L04,801, doi:10.1029/2006GL028515, 2007.

Montzka, S. A., P. Calvert, B. D. Hall, J. W. Elkins, T. J. Conway, P. P. Tans, and C. Sweeney, On the global distribution, seasonality, and budget of atmospheric carbonyl sulfide (COS) and some similarities to CO_2, *Journal of Geophysical Research*, *112*(D9), D09,302, doi:10.1029/2006JD007665, 2007.

Moore III, B., et al., The potential of the Geostationary Carbon Cycle Observatory (GeoCarb) to provide multi-scale constraints on the carbon cycle in the americas, *Frontiers in Environmental Science*, *6*(OCT), doi:10.3389/fenvs.2018.00109, 2018.

Moreira, A. A., A. L. Ruhoff, D. R. Roberti, V. d. A. Souza, H. R. da Rocha, and R. C. D. de Paiva, Assessment of terrestrial water balance using remote sensing data in South America, *Journal of Hydrology*, *575*, 131–147, doi:10.1016/j.jhydrol.2019.05.021, 2019.

Mrozek, D. J., Measurements and interpretation of oxygen isotopes in stratospheric carbon dioxide, Ph.D. thesis, Utrecht University, ISBN: 978-90-393-6824-4, 2017.

Mrozek, D. J., C. van der Veen, M. E. G. Hofmann, H. Chen, R. Kivi, P. Heikkinen, and T. Röckmann, Stratospheric Air Sub-sampler (SAS) and its application to analysis of $\Delta^{17}O(CO_2)$ from small air samples collected with an AirCore, *Atmospheric Measurement Techniques*, *9*(11), 5607–5620, doi:10.5194/amt-9-5607-2016, 2016.

Naus, S., L. G. Domingues, M. Krol, L. V. Gatti, N. Nechita-Banda, S. Basu, G. Koren, I. Luijkx, and W. Peters, Sixteen years of variability and trends in CO emissions from Amazonian fires, in prep.

Nechita-Banda, N., et al., Monitoring emissions from the 2015 Indonesian fires using CO satellite data, *Philosophical Transactions of the Royal Society B: Biological Sciences*, *373*(1760), 20170,307, doi:10.1098/rstb.2017.0307, 2018.

Neigh, C. S. R., J. McCorkel, and E. M. Middleton, Quantifying Libya-4 surface reflectance heterogeneity with WorldView-1, 2 and EO-1 Hyperion, *IEEE Geoscience and Remote Sensing Letters*, *12*(11), 2277–2281, doi:10.1109/LGRS.2015.2468174, 2015.

Nelson, D. D., J. B. McManus, S. C. Herndon, M. S. Zahniser, B. Tuzson, and L. Emmenegger, New method for isotopic ratio measurements of atmospheric carbon dioxide using a 4.3 μm pulsed quantum cascade laser, *Applied Physics B*, *90*(2), 301–309, doi:10.1007/s00340-007-2894-1, 2008.

Ogée, J., J. Sauze, J. Kesselmeier, B. Genty, H. Van Diest, T. Launois, and L. Wingate, A new mechanistic framework to predict OCS fluxes from soils, *Biogeosciences*, *13*(8), 2221–2240, doi:10.5194/bg-13-2221-2016, 2016.

Oliveira, R. S., et al., Embolism resistance drives the distribution of Amazonian rainforest tree species along hydro-topographic gradients, *New Phytologist*, *221*(3), 1457–1465, doi:10.1111/nph.15463, 2019.

Olson, J. S. and Watts, J. A. and Allison, L. J., Major world ecosystem complexes ranked by carbon in live vegetation: A Database (NDP-017), 1985.

Oort, A. H., *Global atmospheric circulation statistics, 1958-1973*, U.S. Department of Commerce, National Oceanic and Atmospheric Administration, 1983.

Ouwersloot, H. G., J. Vilà-Guerau de Arellano, B. J. H. van Stratum, M. C. Krol, and J. Lelieveld, Quantifying the transport of subcloud layer reactants by shallow cumulus clouds over the Amazon, *Journal of Geophysical Research: Atmospheres*, *118*(23), 041–13, doi:10.1002/2013JD020431, 2013.

Ouwersloot, H. G., A. F. Moene, J. J. Attema, and J. Vilà-Guerau de Arellano, Large-eddy simulation comparison of neutral flow over a canopy: Sensitivities to physical and numerical conditions, and similarity to other representations, *Boundary-Layer Meteorology*, *162*(1), 71–89, doi:10.1007/s10546-016-0182-5, 2017.

Palmer, P. I., L. Feng, D. Baker, F. Chevallier, H. Bösch, and P. Somkuti, Net carbon emissions from African biosphere dominate pan-tropical atmospheric CO_2 signal, *Nature Communications*, *10*(1), 3344, doi:10.1038/s41467-019-11097-w, 2019.

Parazoo, N. C., K. Bowman, J. B. Fisher, C. Frankenberg, D. B. A. Jones, A. Cescatti, O. Pérez-Priego, G. Wohlfahrt, and L. Montagnani, Terrestrial gross primary production inferred from satellite fluorescence and vegetation models, *Global Change Biology*, *20*(10), 3103–3121, doi:10.1111/gcb.12652, 2014.

Parazoo, N. C., et al., Interpreting seasonal changes in the carbon balance of southern Amazonia using measurements of XCO_2 and chlorophyll fluorescence from GOSAT, *Geophysical Research Letters*, *40*(11), 2829–2833, doi:10.1002/grl.50452, 2013.

Pastorello, G. Z., D. Papale, H. Chu, C. Trotta, D. A. Agarwal, E. Canfora, D. D. Baldocchi, and M. S. Torn, A new data set monitors land-air exchanges, *Eos*, *August*, 2017.

Paul, D., et al., Evaluation of a field-deployable Nafion-based air-drying system for collecting whole air samples and its application to stable isotope measurements of CO_2, *Atmospheric Measurement Techniques*, *13*, 4051–4064, doi:10.5194/amt-13-4051-2020, 2020.

Pearcy, R. W., and J. Ehleringer, Comparative ecophysiology of C_3 and C_4 plants, *Plant, Cell and Environment*, *7*(1), 1–13, doi:10.1111/j.1365-3040.1984.tb01194.x, 1984.

Peters, W., J. B. Miller, J. Whitaker, A. S. Denning, A. Hirsch, M. C. Krol, D. Zupanski, L. Bruhwiler, and P. P. Tans, An ensemble data assimilation system to estimate CO_2 surface fluxes from atmospheric trace gas observations, *Journal of Geophysical Research*, *110*(D24), D24,304, doi:10.1029/2005JD006157, 2005.

Peters, W., et al., An atmospheric perspective on North American carbon dioxide exchange: CarbonTracker, *Proceedings of the National Academy of Sciences*, *104*(48), 18,925–18,930, doi:10.1073/pnas.0708986104, 2007.

Peters, W., et al., Seven years of recent European net terrestrial carbon dioxide exchange constrained by atmospheric observations, *Global Change Biology*, *16*(4), 1317–1337, doi:10.1111/j.1365-2486.2009.02078.x, 2010.

Peters, W., et al., Increased water-use efficiency and reduced CO_2 uptake by plants during droughts at a continental scale, *Nature Geoscience*, *11*(10), 744–748, doi:10.1038/s41561-018-0212-7, 2018.

Peylin, P., P. Ciais, P. P. Tans, K. Six, J. A. Berry, and A. S. Denning, ^{18}O in atmospheric CO_2 simulated by a 3-D transport model: A sensitivity study to vegetation and soil fractionation factors, *Physics and Chemistry of the Earth*, *21*(5-6), 463–469, doi:10.1016/S0079-1946(97)81143-3, 1997.

Peylin, P., P. Ciais, A. S. Denning, P. P. Tans, J. A. Berry, and J. W. C. White, A 3-dimensional study of $\delta^{18}O$ in atmospheric CO_2: contribution of different land ecosystems, *Tellus B*, *51*(3), 642–667, doi:10.3402/tellusb.v51i3.16452, 1999.

Peylin, P., et al., Global atmospheric carbon budget: results from an ensemble of atmospheric CO_2 inversions, *Biogeosciences*, *10*(10), 6699–6720, doi:10.5194/bg-10-6699-2013, 2013.

Peylin, P., et al., A new stepwise carbon cycle data assimilation system using multiple data streams to constrain the simulated land surface carbon cycle, *Geoscientific Model Development*, *9*(9), 3321–3346, doi:10.5194/gmd-9-3321-2016, 2016.

Phillips, O. L., et al., Drought sensitivity of the Amazon Rainforest, *Science*, *323*(5919), 1344–1347, doi:10.1126/science.1164033, 2009.

Pierchala, A., K. Rozanski, M. Dulinski, Z. Gorczyca, and R. Czub, Triple isotope effects accompanying evaporation of water: New insights from laboratory experiments, doi:10.5194/egusphere-egu2020-6708, EGU General Assembly, Vienna, Austria, 2020.

Potter, C., S. Klooster, C. Hiatt, V. Genovese, and J. C. Castilla-Rubio, Changes in the carbon cycle of Amazon ecosystems during the 2010 drought, *Environmental Research Letters*, *6*(3), doi:10.1088/1748-9326/6/3/034024, 2011.

Potter, C. S., J. T. Randerson, C. B. Field, P. A. Matson, P. M. Vitousek, H. A. Mooney, and S. A. Klooster, Terrestrial ecosystem production: A process model based on global satellite and surface data, *Global Biogeochemical Cycles*, *7*(4), 811–841, doi:10.1029/93GB02725, 1993.

Powell, T. L., et al., Confronting model predictions of carbon fluxes with measurements of Amazon forests subjected to experimental drought, *New Phytologist*, *200*(2), 350–364, doi:10.1111/nph.12390, 2013.

Prather, M. J., Numerical advection by conservation of second-order moments, *Journal of Geophysical Research*, *91*(D6), 6671, doi:10.1029/JD091iD06p06671, 1986.

Raj, R., N. A. S. Hamm, C. v. d. Tol, and A. Stein, Uncertainty analysis of gross primary production partitioned from net ecosystem exchange measurements, *Biogeosciences*, *13*(5), 1409–1422, doi:10.5194/bg-13-1409-2016, 2016.

Rap, A., et al., Fires increase Amazon forest productivity through increases in diffuse radiation, *Geophysical Research Letters*, *42*(11), 4654–4662, doi:10.1002/2015GL063719, 2015.

Rayner, P. J., R. M. Law, and R. Dargaville, The relationship between tropical CO_2 fluxes and the El Niño-Southern Oscillation, *Geophysical Research Letters*, *26*(4), 493–496, doi:10.1029/1999GL900008, 1999.

Rebmann, C., et al., ICOS eddy covariance flux-station site setup: A review, *International Agrophysics*, *32*(4), 471–494, doi:10.1515/intag-2017-0044, 2018.

Reichstein, M., et al., On the separation of net ecosystem exchange into assimilation and ecosystem respiration: Review and improved algorithm, *Global Change Biology*, *11*(9), 1424–1439, doi:10.1111/j.1365-2486.2005.001002.x, 2005.

Restrepo-Coupe, N., et al., What drives the seasonality of photosynthesis across the Amazon basin? A cross-site analysis of eddy flux tower measurements from the Brasil flux network, *Agricultural and Forest Meteorology*, *182-183*, 128–144, doi:10.1016/j.agrformet.2013.04.031, 2013.

Restrepo-Coupe, N., et al., Do dynamic global vegetation models capture the seasonality of carbon fluxes in the Amazon basin? A data-model intercomparison, *Global Change Biology*, *23*(1), 191–208, doi:10.1111/gcb.13442, 2017.

Röckmann, T., C. A. M. Brenninkmeijer, P. Neeb, and P. J. Crutzen, Ozonolysis of nonmethane hydrocarbons as a source of the observed mass independent oxygen isotope enrichment in tropospheric CO, *Journal of Geophysical Research: Atmospheres*, *103*(D1), 1463–1470, doi:10.1029/97JD02929, 1998a.

Röckmann, T., C. A. M. Brenninkmeijer, G. Saueressig, P. Bergamaschi, J. N. Crowley, H. Fischer, and P. J. Crutzen, Mass-independent oxygen isotope fractionation in atmospheric CO as a result of the reaction CO + OH, *Science*, *281*(5376), 544–546, doi:10.1126/science.281.5376.544, 1998b.

Röckmann, T., P. Jöckel, V. Gros, M. Bräunlich, G. Possnert, and C. A. M. Brenninkmeijer, Using ^{14}C, ^{13}C, ^{18}O and ^{17}O isotopic variations to provide insights into the high northern latitude surface CO inventory, *Atmospheric Chemistry and Physics*, *2*(2), 147–159, doi:10.5194/acp-2-147-2002, 2002.

Rödenbeck, C., S. Zaehle, R. Keeling, and M. Heimann, History of El Niño impacts on the global carbon cycle 1957–2017: A quantification from atmospheric CO_2 data, *Philosophical Transactions of the Royal Society B: Biological Sciences*, *373*(1760), 20170,303, doi:10.1098/rstb.2017.0303, 2018a.

Rödenbeck, C., S. Zaehle, R. Keeling, and M. Heimann, How does the terrestrial carbon exchange respond to inter-annual climatic variations? A quantification based on atmospheric CO_2 data, *Biogeosciences*, *15*(8), 2481–2498, doi:10.5194/bg-15-2481-2018, 2018b.

Rowland, L., et al., Death from drought in tropical forests is triggered by hydraulics not carbon starvation, *Nature*, *528*(7580), 119–122, doi:10.1038/nature15539, 2015.

Russell, G. L., and J. A. Lerner, A new finite-differencing scheme for the tracer transport equation, *Journal of Applied Meteorology*, *20*(12), 1483–1498, doi:10.1175/1520-0450(1981)020<1483:ANFDSF>2.0.CO;2, 1981.

Saatchi, S., S. Asefi-Najafabady, Y. Malhi, L. E. O. C. Aragao, L. O. Anderson, R. B. Myneni, and R. Nemani, Persistent effects of a severe drought on Amazonian forest canopy, *Proceedings of the National Academy of Sciences*, *110*(2), 565–570, doi:10.1073/pnas.1204651110, 2013.

Saatchi, S. S., et al., Benchmark map of forest carbon stocks in tropical regions across three continents, *Proceedings of the National Academy of Sciences*, *108*(24), 9899–9904, doi:10.1073/pnas.1019576108, 2011.

Sakschewski, B., W. von Bloh, A. Boit, L. Poorter, M. Peña-Claros, J. Heinke, J. Joshi, and K. Thonicke, Resilience of Amazon forests emerges from plant trait diversity, *Nature Climate Change*, *6*(11), 1032–1036, doi:10.1038/nclimate3109, 2016.

Saleska, S. R., K. Didan, A. R. Huete, and H. R. da Rocha, Amazon forests green-up during 2005 drought, *Science*, *318*(5850), 612–612, doi:10.1126/science.1146663, 2007.

Samanta, A., S. Ganguly, H. Hashimoto, S. Devadiga, E. Vermote, Y. Knyazikhin, R. R. Nemani, and R. B. Myneni, Amazon forests did not green-up during the 2005 drought, *Geophysical Research Letters*, *37*(5), doi:10.1029/2009GL042154, 2010.

Sanders, A., W. Verstraeten, M. Kooreman, T. van Leth, J. Beringer, and J. Joiner, Spaceborne sun-induced vegetation fluorescence time series from 2007 to 2015 evaluated with Australian flux tower measurements, *Remote Sensing*, *8*(12), 895, doi:10.3390/rs8110895, 2016.

Sanhueza, E., Y. Dong, J. M. Lobert, and P. J. Crutzen, Carbon monoxide uptake by temperate forest soils: the effects of leaves and humus layers, *Tellus B*, *50*(1), 51–58, doi:10.3402/tellusb.v50i1.16021, 1998.

Santos, P., and A. J. Negri, A Comparison of the Normalized Difference Vegetation Index and Rainfall for the Amazon and Northeastern Brazil, *Journal of Applied Meteorology*, *36*(7), 958–965, doi:10.1175/1520-0450(1997)036<0958:ACOTND>2.0.CO;2, 1997.

Schaefer, K., G. J. Collatz, P. Tans, A. S. Denning, I. Baker, J. Berry, L. Prihodko, N. Suits, and A. Philpott, Combined Simple Biosphere/Carnegie-Ames-Stanford Approach terrestrial carbon cycle model, *Journal of Geophysical Research*, *113*(G3), G03,034, doi:10.1029/2007JG000603, 2008.

Schneider, L., Simulating the global distribution of $\Delta^{17}O$ in CO_2, Master's thesis, Wageningen University, 2015.

Schoeberl, M. R., A. R. Douglass, R. S. Stolarski, S. Pawson, S. E. Strahan, and W. Read, Comparison of lower stratospheric tropical mean vertical velocities, *Journal of Geophysical Research*, *113*(D24), D24,109, doi:10.1029/2008JD010221, 2008.

Schuh, A. E., et al., Quantifying the impact of atmospheric transport uncertainty on CO_2 surface flux estimates, *Global Biogeochemical Cycles*, *33*(4), 484–500, doi:10.1029/2018GB006086, 2019.

Shaheen, R., C. Janssen, and T. Röckmann, Investigations of the photochemical isotope equilibrium between O_2, CO_2 and O_3, *Atmospheric Chemistry and Physics*, *7*(2), 495–509, doi:10.5194/acp-7-495-2007, 2007.

Siegenthaler, U., and J. L. Sarmiento, Atmospheric carbon dioxide and the ocean, *Nature*, *365*(6442), 119–125, doi:10.1038/365119a0, 1993.

Smith, N. E., et al., Spring enhancement and summer reduction in carbon uptake during the 2018 drought in northwestern Europe, *Philosophical Transactions of the Royal Society B*, 2020.

Snyder, K. A., J. H. Richards, and L. A. Donovan, Night-time conductance in C_3 and C_4 species: do plants lose water at night?, *Journal of Experimental Botany*, *54*(383), 861–865, doi:10.1093/jxb/erg082, 2003.

Solander, K. C., et al., The pantropical response of soil moisture to El Niño, *Hydrology and Earth System Sciences*, *24*(5), 2303–2322, doi:10.5194/hess-24-2303-2020, 2020.

Sperry, J. S., Y. Wang, B. T. Wolfe, D. S. Mackay, W. R. L. Anderegg, N. G. McDowell, and W. T. Pockman, Pragmatic hydraulic theory predicts stomatal responses to climatic water deficits, *New Phytologist*, *212*(3), 577–589, doi:10.1111/nph.14059, 2016.

Spivakovsky, C. M., et al., Three-dimensional climatological distribution of tropospheric OH: Update and evaluation, *Journal of Geophysical Research: Atmospheres*, *105*(D7), 8931–8980, doi:10.1029/1999JD901006, 2000.

Stern, L. A., R. Amundson, and W. T. Baisden, Influence of soils on oxygen isotope ratio of atmospheric CO_2, *Global Biogeochemical Cycles*, *15*(3), 753–759, doi:10.1029/2000GB001373, 2001.

Steur, F., B. Scheeren, G. Adnew, D. Nelson, T. Röckmann, and H. Meijer, Simultaneous measurement of δ^{13}C-CO_2, δ^{18}O-CO_2 and δ^{17}O-CO_2 in atmospheric samples by the Aerodyne Quantum Cascade Dual-Laser Absorption Spectrometer at the Centre for Isotope Research, The 3rd ICOS Science Conference, Prague, Czech Republic, 2018.

Still, C. J., J. A. Berry, G. J. Collatz, and R. S. DeFries, Global distribution of C_3 and C_4 vegetation: Carbon cycle implications, *Global Biogeochemical Cycles*, *17*(1), 1006, doi:10.1029/2001GB001807, 2003.

Still, C. J., et al., Influence of clouds and diffuse radiation on ecosystem-atmosphere CO_2 and $CO^{18}O$ exchanges, *Journal of Geophysical Research*, *114*(G1), G01,018, doi:10.1029/2007JG000675, 2009.

Stoltmann, T., M. Casado, M. Daëron, A. Landais, and S. Kassi, Direct, precise measurements of isotopologue abundance ratios in CO_2 using molecular absorption spectroscopy: Application to Δ^{17}O, *Analytical Chemistry*, *89*(19), 10,129–10,132, doi:10.1021/acs.analchem.7b02853, 2017.

Sullivan, M. J. P., et al., Long-term thermal sensitivity of Earth's tropical forests, *Science*, *368*(6493), 869–874, doi:10.1126/science.aaw7578, 2020.

Sutanudjaja, E. H., et al., PCR-GLOBWB 2: A 5 arcmin global hydrological and water resources model, *Geoscientific Model Development*, *11*(6), 2429–2453, doi:10.5194/gmd-11-2429-2018, 2018.

Swinbank, R., and A. O'Neill, A stratosphere-troposphere data assimilation system, *Monthly Weather Review*, *122*(4), 686–702, doi:10.1175/1520-0493(1994)122<0686:ASTDAS>2.0.CO;2, 1994.

Thiemens, M. H., T. Jackson, E. C. Zipf, P. W. Erdman, and C. van Egmond, Carbon dioxide and oxygen isotope anomalies in the mesosphere and stratosphere, *Science*, *270*(5238), 969–972, doi:10.1126/science.270.5238.969, 1995a.

Thiemens, M. H., T. L. Jackson, and C. A. M. Brenninkmeijer, Observation of a mass independent oxygen isotopic composition in terrestrial stratospheric CO_2, the link to ozone chemistry, and the possible occurrence in the Martian atmosphere, *Geophysical Research Letters*, *22*(3), 255–257, doi:10.1029/94GL02996, 1995b.

Thiemens, M. H., S. Chakraborty, and T. L. Jackson, Decadal $\Delta^{17}O$ record of tropospheric CO_2: Verification of a stratospheric component in the troposphere, *Journal of Geophysical Research: Atmospheres*, *119*(10), 6221–6229, doi:10.1002/2013JD020317, 2014.

Thoning, K. W., P. P. Tans, and W. D. Komhyr, Atmospheric carbon dioxide at Mauna Loa Observatory: 2. Analysis of the NOAA GMCC data, 1974-1985, *Journal of Geophysical Research: Atmospheres*, *94*(D6), 8549–8565, doi:10.1029/JD094iD06p08549, 1989.

Tian, C., and L. Wang, Stable isotope variations of daily precipitation from 2014-2018 in the central United States, *Scientific Data*, *6*, doi:10.1038/sdata.2019.18, 2019.

Tian, C., L. Wang, K. F. Kaseke, and B. W. Bird, Stable isotope compositions (δ^2H, $\delta^{18}O$ and $\delta^{17}O$) of rainfall and snowfall in the central United States, *Scientific Reports*, *8*(1), 6712, doi:10.1038/s41598-018-25102-7, 2018.

Toomey, M., D. A. Roberts, C. Still, M. L. Goulden, and J. P. McFadden, Remotely sensed heat anomalies linked with Amazonian forest biomass declines, *Geophysical Research Letters*, *38*(19), doi:10.1029/2011GL049041, 2011.

Townsend, A. R., G. P. Asner, J. W. C. White, and P. P. Tans, Land use effects on atmospheric ^{13}C imply a sizable terrestrial CO_2 sink in tropical latitudes, *Geophysical Research Letters*, *29*(10), doi:10.1029/2001GL013454, 2002.

Tramontana, G., et al., Predicting carbon dioxide and energy fluxes across global FLUXNET sites with regression algorithms, *Biogeosciences*, *13*(14), 4291–4313, doi:10.5194/bg-13-4291-2016, 2016.

Uemura, R., E. Barkan, O. Abe, and B. Luz, Triple isotope composition of oxygen in atmospheric water vapor, *Geophysical Research Letters*, *37*(4), 1–4, doi:10.1029/2009GL041960, 2010.

van der Laan-Luijkx, I. T., et al., Response of the Amazon carbon balance to the 2010 drought derived with CarbonTracker South America, *Global Biogeochemical Cycles*, *29*(7), 1092–1108, doi:10.1002/2014GB005082, 2015.

van der Laan-Luijkx, I. T., et al., The CarbonTracker Data Assimilation Shell (CTDAS) v1.0: implementation and global carbon balance 2001–2015, *Geoscientific Model Development*, *10*(7), 2785–2800, doi:10.5194/gmd-10-2785-2017, 2017.

van der Sleen, P., P. Groenendijk, M. Vlam, N. P. R. Anten, A. Boom, F. Bongers, T. L. Pons, G. Terburg, and P. A. Zuidema, No growth stimulation of tropical trees by 150 years of CO_2 fertilization but water-use efficiency increased, *Nature Geoscience*, *8*(1), 24–28, doi:10.1038/ngeo2313, 2015.

van der Velde, I. R., J. B. Miller, K. Schaefer, G. R. van der Werf, M. C. Krol, and W. Peters, Terrestrial cycling of $^{13}CO_2$ by photosynthesis, respiration, and biomass burning in SiBCASA, *Biogeosciences*, *11*(23), 6553–6571, doi:10.5194/bg-11-6553-2014, 2014.

van der Werf, G. R., D. C. Morton, R. S. DeFries, L. Giglio, J. T. Randerson, G. J. Collatz, and P. S. Kasibhatla, Estimates of fire emissions from an active deforestation region in the southern Amazon based on satellite data and biogeochemical modelling, *Biogeosciences*, *6*(2), 235–249, doi:10.5194/bg-6-235-2009, 2009.

van der Werf, G. R., et al., Global fire emissions and the contribution of deforestation, savanna, forest, agricultural, and peat fires (1997–2009), *Atmospheric Chemistry and Physics*, *10*(23), 11,707–11,735, doi:10.5194/acp-10-11707-2010, 2010.

van Noije, T. P. C., H. J. Eskes, M. van Weele, and P. F. J. van Velthoven, Implications of the enhanced Brewer-Dobson circulation in European Centre for Medium-Range Weather Forecasts reanalysis ERA-40 for the stratosphere-troposphere exchange of ozone in global chemistry transport models, *Journal of Geophysical Research*, *109*(D19), D19,308, doi:10.1029/2004JD004586, 2004.

van Schaik, E., Retrieving sun-induced fluorescence from the Global Ozone Monitoring Experiment 2, Wageningen University MSc internship report for Royal Netherlands Meteorological Institute (KNMI), https://goo.gl/fgAMG7, 2016.

van Schaik, E., L. Killaars, N. E. Smith, G. Koren, L. P. H. van Beek, W. Peters, and I. T. van der Laan-Luijkx, Changes in surface hydrology, soil moisture and gross primary production in the Amazon during the 2015/2016 El Niño, *Philosophical Transactions of the Royal Society B: Biological Sciences*, *373*(1760), 20180,084, doi:10.1098/rstb.2018.0084, 2018.

van Schaik, E., et al., Improved SIFTER v2 algorithm for long-term GOME-2A satellite retrievals of fluorescence with a correction for instrument degradation, *Atmospheric Measurement Techniques Discussions*, pp. 1–33, doi:10.5194/amt-2019-384, 2020.

Vilà-Guerau de Arellano, J., B. Gioli, F. Miglietta, H. J. J. Jonker, H. Klein Baltink, R. W. A. Hutjes, and A. A. M. Holtslag, Entrainment process of carbon dioxide in the atmospheric boundary layer, *Journal of Geophysical Research*, *109*(D18), D18,110, doi:10.1029/2004JD004725, 2004.

Vilà-Guerau de Arellano, J., C. C. van Heerwaarden, B. J. H. van Stratum, and K. van den Dries, *Atmospheric Boundary Layer*, Cambridge University Press, Cambridge, doi:10.1017/CBO9781316117422, 2015.

Vilà-Guerau de Arellano, J., G. Koren, H. G. Ouwersloot, I. van der Velde, T. Röckmann, and J. B. Miller, Sub-diurnal variability of the carbon dioxide and water vapor isotopologues at the field observational scale, *Agricultural and Forest Meteorology*, *275*, 114–135, doi:10.1016/j.agrformet.2019.05.014, 2019.

Vilà-Guerau de Arellano, J., et al., CloudRoots: Integration of advanced instrumental techniques and process modelling of sub-hourly and sub-kilometre land-atmosphere interactions, *Biogeosciences Discussions*, pp. 1–49, doi:10.5194/bg-2020-132, 2020.

Vogel, J. C., P. M. Grootes, and W. G. Mook, Isotopic fractionation between gaseous and dissolved carbon dioxide, *Zeitschrift für Physik A Hadrons and nuclei*, *230*(3), 225–238, doi:10.1007/BF01394688, 1970.

Volk, C. M., J. W. Elkins, D. W. Fahey, G. S. Dutton, J. M. Gilligan, M. Loewenstein, J. R. Podolske, K. R. Chan, and M. R. Gunson, Evaluation of source gas lifetimes from stratospheric observations, *Journal of Geophysical Research: Atmospheres*, *102*(D21), 25,543–25,564, doi:10.1029/97JD02215, 1997.

Wanninkhof, R., Relationship between wind speed and gas exchange over the ocean, *Journal of Geophysical Research*, *97*(C5), 7373, doi:10.1029/92JC00188, 1992.

Watkins, M. M., D. N. Wiese, D.-N. Yuan, C. Boening, and F. W. Landerer, Improved methods for observing Earth's time variable mass distribution with GRACE using spherical cap mascons, *Journal of Geophysical Research: Solid Earth*, *120*(4), 2648–2671, doi:10.1002/2014JB011547, 2015.

Wehr, R., J. W. Munger, D. D. Nelson, J. B. McManus, M. S. Zahniser, S. C. Wofsy, and S. R. Saleska, Long-term eddy covariance measurements of the isotopic composition

of the ecosystem–atmosphere exchange of CO_2 in a temperate forest, *Agricultural and Forest Meteorology*, *181*, 69–84, doi:10.1016/j.agrformet.2013.07.002, 2013.

Wei, Z., X. Lee, and E. G. Patton, ISOLESC: A coupled isotope-LSM-LES-cloud modeling system to investigate the water budget in the atmospheric boundary layer, *Journal of Advances in Modeling Earth Systems*, *10*(10), 2589–2617, doi:10.1029/2018MS001381, 2018.

Welp, L. R., R. F. Keeling, H. A. J. Meijer, A. F. Bollenbacher, S. C. Piper, K. Yoshimura, R. J. Francey, C. E. Allison, and M. Wahlen, Interannual variability in the oxygen isotopes of atmospheric CO_2 driven by El Niño, *Nature*, *477*(7366), 579–582, doi:10.1038/nature10421, 2011.

Wen, J., and M. H. Thiemens, Multi-isotope study of the $O(^1D)$ + CO_2 exchange and stratospheric consequences, *Journal of Geophysical Research*, *98*(D7), 12,801–12,808, doi:10.1029/93JD00565, 1993.

West, J. B., A. Sobek, and J. R. Ehleringer, A simplified GIS approach to modeling global leaf water isoscapes, *PLoS ONE*, *3*(6), e2447, doi:10.1371/journal.pone.0002447, 2008.

Wiegel, A. A., A. S. Cole, K. J. Hoag, E. L. Atlas, S. M. Schauffler, and K. A. Boering, Unexpected variations in the triple oxygen isotope composition of stratospheric carbon dioxide, *Proceedings of the National Academy of Sciences*, *110*(44), 17,680–17,685, doi:10.1073/pnas.1213082110, 2013.

Wiese, D. N., D.-N. Yuan, C. Boening, F. W. Landerer, and M. M. Watkins, JPL GRACE mascon ocean, ice, and hydrology equivalent water height RL05M.1 CRI filtered version 2, doi:10.5067/TEMSC-2LCR5, 2016.

Wigneron, J.-P., L. Fan, P. Ciais, A. Bastos, M. Brandt, J. Chave, S. Saatchi, A. Baccini, and R. Fensholt, Tropical forests did not recover from the strong 2015-2016 El Niño event, *Science Advances*, *6*(6), 1–10, doi:10.1126/sciadv.aay4603, 2020.

Wingate, L., et al., The impact of soil microorganisms on the global budget of ^{18}O in atmospheric CO_2, *Proceedings of the National Academy of Sciences*, *106*(52), 22,411–22,415, doi:10.1073/pnas.0905210106, 2009.

Wolf, A., W. R. L. Anderegg, and S. W. Pacala, Optimal stomatal behavior with competition for water and risk of hydraulic impairment, *Proceedings of the National Academy of Sciences of the United States of America*, *113*(46), E7222–E7230, doi:10.1073/pnas.1615144113, 2016a.

Wolf, S., et al., Warm spring reduced carbon cycle impact of the 2012 US summer drought, *Proceedings of the National Academy of Sciences*, *113*(21), 5880–5885, doi:10.1073/pnas.1519620113, 2016b.

Yang, J., H. Tian, S. Pan, G. Chen, B. Zhang, and S. Dangal, Amazon drought and forest response: Largely reduced forest photosynthesis but slightly increased canopy greenness during the extreme drought of 2015/2016, *Global Change Biology*, *24*(5), 1919–1934, doi:10.1111/gcb.14056, 2018a.

Yang, Y., et al., Post-drought decline of the Amazon carbon sink, *Nature Communications*, *9*(1), 3172, doi:10.1038/s41467-018-05668-6, 2018b.

Yeung, L. Y., et al., Large and unexpected enrichment in stratospheric $^{16}O^{13}C^{18}O$ and its meridional variation, *Proceedings of the National Academy of Sciences*, *106*(28), 11,496–11,501, doi:10.1073/pnas.0902930106, 2009.

Young, E. D., A. Galy, and H. Nagahara, Kinetic and equilibrium mass-dependent isotope fractionation laws in nature and their geochemical and cosmochemical significance, *Geochimica et Cosmochimica Acta*, *66*(6), 1095–1104, doi:10.1016/S0016-7037(01)00832-8, 2002.

Yuan, W., et al., Increased atmospheric vapor pressure deficit reduces global vegetation growth, *Science Advances*, *5*(8), 1–12, doi:10.1126/sciadv.aax1396, 2019.

Yung, Y. L., W. B. DeMore, and J. P. Pinto, Isotopic exchange between carbon dioxide and ozone via $O(^1D)$ in the stratosphere, *Geophysical Research Letters*, *18*(1), 13–16, doi:10.1029/90GL02478, 1991.

Zeng, Y., G. Badgley, B. Dechant, Y. Ryu, M. Chen, and J. Berry, A practical approach for estimating the escape ratio of near-infrared solar-induced chlorophyll fluorescence, *Remote Sensing of Environment*, *232*, 111,209, doi:10.1016/j.rse.2019.05.028, 2019.

Zhang, Y., L. Guanter, J. A. Berry, J. Joiner, C. van der Tol, A. Huete, A. Gitelson, M. Voigt, and P. Köhler, Estimation of vegetation photosynthetic capacity from space-based measurements of chlorophyll fluorescence for terrestrial biosphere models, *Global Change Biology*, *20*(12), 3727–3742, doi:10.1111/gcb.12664, 2014.

Zhang, Y., J. Joiner, P. Gentine, and S. Zhou, Reduced solar-induced chlorophyll fluorescence from GOME-2 during Amazon drought caused by dataset artifacts, *Global Change Biology*, *24*(6), 2229–2230, doi:10.1111/gcb.14134, 2018.

Zhang, Z., et al., Reduction of structural impacts and distinction of photosynthetic pathways in a global estimation of GPP from space-borne solar-induced chlorophyll fluorescence, *Remote Sensing of Environment*, *240*, doi:10.1016/j.rse.2020.111722, 2020.

Zhou, S., R. A. Duursma, B. E. Medlyn, J. W. G. Kelly, and I. C. Prentice, How should we model plant responses to drought? An analysis of stomatal and non-stomatal responses to water stress, *Agricultural and Forest Meteorology*, *182-183*, 204–214, doi:10.1016/j.agrformet.2013.05.009, 2013.

Summary

In this thesis we study the exchange of CO_2 between the atmosphere and biosphere, with a focus on the Amazon region. The exchange of CO_2 between atmosphere and biosphere occurs through photosynthetic uptake, which we usually refer to as gross primary production (GPP), and through respiratory release, usually referred to as terrestrial ecosystem respiration (TER). The sum of GPP and TER is the net ecosystem exchange (NEE). In this thesis we studied $\Delta^{17}O$ in CO_2, which is a potential tracer for GPP (*Hoag et al.*, 2005). The main source of $\Delta^{17}O$ in CO_2 is in the stratosphere and the main sink is the biosphere. The $\Delta^{17}O$ signature of tropospheric CO_2 reflects the relative strengths of the production and removal processes. Assuming that the stratospheric production is known, the exchange with the biosphere, that is related to GPP, can be estimated from $\Delta^{17}O$ in tropospheric CO_2. In addition, we used remotely sensed sun-induced fluorescence (SIF) and near-infrared reflectance from vegetation (NIRv), that were first introduced as proxies for GPP by *Frankenberg et al.* (2011) and *Badgley et al.* (2017), respectively. Finally, we used inverse modelling to estimate net CO_2 surface fluxes from observations of CO_2 mole fractions. The focus of the thesis is on quantifying exchange of CO_2 between the biosphere and atmosphere, and the control of environmental variables on this exchange. In particular, the effect of drought on CO_2 exchange, and the post-drought recovery, are major themes of this thesis.

Chapter 2 describes the 3-D model that we developed for $\Delta^{17}O$ in atmospheric CO_2. We implemented this tracer in the global atmospheric transport model TM5 (*Krol et al.*, 2005), which is driven by ERA-Interim meteorological fields (*Dee et al.*, 2011) from the European Centre for Medium-Range Weather Forecasts (ECMWF). We parameterized the stratospheric source of $\Delta^{17}O$ in CO_2 by exploiting its observed correlation with stratospheric $[N_2O]$. The exchange between the atmosphere and biosphere is simulated using the terrestrial biosphere model SiBCASA (*Schaefer et al.*, 2008). We also included the contributions of soils, oceans, biomass burning, fossil fuel combustion and the oxidation of

atmospheric CO on $\Delta^{17}O$ in CO_2. For CO_2 in the lowest 500 m of the atmosphere, we simulated a $\Delta^{17}O$ signature of 39.6 per meg, which is ∼20 per meg lower than estimates from existing box models. Our model results show good agreement with a measured stratospheric $\Delta^{17}O$ in CO_2 profile from Sodankylä (Finland). In addition, we compared model simulations with tropospheric measurements of $\Delta^{17}O$ in CO_2 from Göttingen (Germany) and Taipei (Taiwan), where we found some agreement but also substantial discrepancies. Finally, we showed model results for Zotino (Russia), Mauna Loa (United States), Manaus (Brazil) and South Pole, which we proposed as possible locations for future measurements of $\Delta^{17}O$ in tropospheric CO_2 that can help to further increase our understanding of the global budget of $\Delta^{17}O$ in atmospheric CO_2.

In Chapter 3 we studied $\Delta^{17}O$ at the ecosystem level, which is the domain that integrates the contributions from vegetation and soil to the atmospheric signal. We reported for the first time an observed diurnal cycle of $\Delta^{17}O$ in CO_2, measured from air samples collected on 15-16 August 2019 at the mid-latitude pine forest Loobos (FLUXNET site NL-Loo, *Dolman et al.*, 2002; *Elbers et al.*, 2011). Most notable is an observed peak for $\Delta^{17}O$ in CO_2 in the morning (∼140 per meg, around 6:30 am) that we tentatively ascribed to the entrainment of residual air masses. Besides $\Delta^{17}O$ in CO_2, we report observations of $\delta^{13}C$ and $\delta^{18}O$ in CO_2 for flasks collected close to the surface (at 0.5 m height, inside the canopy) and from the top of the tower (1–2 m above the canopy). To support the interpretation of observations, we simulated $\delta^{13}C$, $\delta^{18}O$ and $\Delta^{17}O$ in CO_2 in the atmospheric boundary layer (ABL) during daytime for Loobos using the mixed layer model MXL (*Vilà-Guerau de Arellano et al.*, 2019). Furthermore, we used the MXL model to systematically explore the sensitivity of $\delta^{18}O$ and $\Delta^{17}O$ in CO_2 to the cloud cover, humidity of entrained air and degree of isotopic equilibration inside leaves. Finally, we used the global atmospheric transport model TM5 to (1) quantify the contribution of different sources that affect $\Delta^{17}O$ in CO_2 at Loobos using a 'tracer tagging' method; and (2) extend our analysis of the diurnal cycle to the global scale. Based on these simulations, we expect the largest diurnal cycles for $\Delta^{17}O$ in CO_2 in tropical ecosystems, and we propose to follow-up on this study by sampling air from well-equipped tropical sites, such as the ATTO tower (*Andreae et al.*, 2015) in the Amazon.

In Chapter 4, we study the response of the Amazon forest to the 2015/2016 El Niño, using sun-induced fluorescence (SIF) a proxy for GPP. We developed a new remotely-sensed SIF product with improved signal-to-noise in the tropics (*van Schaik et al.*, 2020), and found that SIF was strongly suppressed over areas with anomalously high temperatures and decreased levels of water in the soil. SIF went below its climatological range starting from the end of the 2015 dry season (October) and returned to normal levels by February 2016

when atmospheric conditions returned to normal, but well before the end of anomalously low precipitation which persisted through June 2016. Impacts were not uniform across the Amazon basin, with the eastern part experiencing much larger (10-15%) SIF reductions than the western part of the basin (2-5%). We estimated that the integrated loss of GPP relative to eight previous years is 0.34–0.48 PgC in the 3-month period Oct-Nov-Dec 2015.

Finally, in Chapter 5 we consider the response to Amazon droughts in the period 2010-2017. We used CO_2 profiles collected by aircraft over the Amazon to quantify the net ecosystem exchange for drought and post-drought years using the CarbonTracker South America (CTSAM) inverse modelling system (*van der Laan-Luijkx et al.*, 2015). In addition, we performed inversions using independent CO_2 column observations from OCO-2 to quantify CO_2 exchange for the years 2015-2017. We estimate that the total Amazon CO_2 emissions for the years 2010 and 2016 are 0.3–0.5 PgC and 0.0–0.3 PgC larger than the subsequent years 2011 and 2017, respectively. Furthermore, we used near-infrared reflectance of terrestrial vegetation (NIRv), from MODIS and MAIAC, to diagnose the direct and delayed response of GPP to the 2015/2016 drought. We find a substantial reduction of NIRv in the 2016 dry season, when precipitation and temperature have returned to normal values, while soil moisture is still anomalously low, suggesting a persistent impact of the preceding 2015/2016 El Niño drought.

This work contributed to a better understanding of the exchange of CO_2 between the biosphere and atmosphere. We have investigated variations of $\Delta^{17}O$ in atmospheric CO_2 and paved the way for new measurements campaigns and the actual application of $\Delta^{17}O$ in CO_2 as a tracer for GPP. We have demonstrated that SIF and NIRv are powerful methods to quantify reductions of GPP during drought and track its post-drought recovery. Finally, our analysis of atmospheric CO_2 inversions showed how the interannual variability of the net exchange of CO_2 over the Amazon is controlled by variations in environmental drivers. Although important challenges remain, the work described in this thesis contributes to better understanding of carbon dioxide exchange over the Amazon.

Acknowledgements

Looking back at the past four years, I can say that I have enjoyed the various activities that are part of this PhD project and I have appreciated the freedom that I experienced to 'make this my own project'. Some people say that working on a PhD project is a heavy and demanding task, but luckily, I do not recognize this feeling. To have a job where you can read interesting papers, try to do something new, and attempt to present this in an appealing way, has always felt as a privilege to me. In the following I acknowledge the people who have contributed to this thesis and the positive atmosphere that stimulates learning and creating.

First of all, I want to address my promotor Wouter. I am grateful that you hired me for the ASICA program, even though I did not fit the typical profile, as I had worked in industry for some years and was also expecting a first child. I appreciate that you respect the work-life balance of your co-workers and it is inspiring for me to see that you always put the bar high for yourself, whether it is a presentation at a big conference, or a one-to-one meeting with a student. I have good memories of our visit to the AGU Fall Meeting in 2018, including the scientific discussions that we had, strolling through the National Mall and our spontaneous visit to an ice hockey match of the Washington Capitals. It was a pleasure to work together and I am happy that we continue to collaborate!

I am also grateful for the collaboration with my second promotor Thomas. I enjoyed our discussions about isotopic processes and have always been impressed by your critical attitude and drive to understand even the smallest details. Back in 2016, I presented the first results of the global $\Delta^{17}O$ model (Chapter 2) in an informal meeting at Utrecht University and to simplify things a bit, I stated that $\Delta^{17}O$ in stratospheric CO_2 is correlated with N_2O because these are both affected by the oxygen radical $O(^1D)$. You immediately interrupted me and mentioned that only $\sim$10% of N_2O is removed by $O(^1D)$, whereas $\sim$90% is removed by photolysis. It impresses me that somebody can know so much about different topics.

Ingrid, it was a pleasure to work with you and I am happy that you are my co-promotor. I appreciate how you helped me get familiar with the CTDAS inverse modeling system and taught me how to tackle all the possible bugs that one may encounter using this software. Also, your input on the analysis for the Amazon CO_2 study (Chapter 5) was very valuable. Besides these scientific contributions, I have also enjoyed our collaboration because of your friendly personality and positive attitude.

Getachew, I am happy that you agreed to be a paranymph at my PhD ceremony. I think it is great that we were able to combine your experimental expertise with my modeling background in the ASICA project. To stay in isotope terminology, I can say that this was certainly an 'enrichment' of my PhD project! Especially, our rather spontaneous 24-hour campaign at the Loobos forest site (that resulted in Chapter 3) was a memorable experience. We started our projects nearly at the same time in 2016 and it is very nice that we both have the opportunity to defend our thesis in 2020!

Stijn, I am also happy that you are a paranymph at my PhD ceremony. I enjoyed working together on our CO and CO_2 inverse modeling projects for the Amazon region (Chapter 5), that we presented together or separately at several meetings. The first time we met, you were still a MSc student at Utrecht University, but soon after that, you became a colleague PhD student in Wageningen. We have shared an office together for four years, that was interrupted by the occasional travel, such as your stay at NOAA in Boulder. I hope I will have the opportunity to make this journey myself and I hope to enjoy it as much as you have done.

There are many more people that I have had the pleasure to work with. Anteneh, Erik, Folkert and Maurits, I enjoyed our discussions about the interpretation and validation of SIF data. John, we had pleasant encounters in Wageningen, Washington DC, Paris and Interlaken and I am looking forward to a closer collaboration with you and Aleya. Jordi, I enjoyed working together with you and hope you were not too offended by the Valencia bottle that I usually brought with me. Lucas and Caio, it was nice to meet you at several occasions and I have good memories of the intense table soccer games that we played in Interlaken. Maarten, the TM5, BBOS and NAC meetings that you (co-)organized were pleasant and useful events for me. Alba, Ara, Auke V., Auke v.d. W., Christoph, Ingrid S., Lars, Laurens, Liesbeth, Linda, Marie, Michiel, Naomi, Peter, Santiago and Thomas M., it was a great pleasure to work together in the air quality team and update each other about our progress in the weekly group meetings. I realize that this is an incomplete list and thank all other members of the MAQ group and the ASICA project team for their contributions.

Finally, I would like to thank all the people that have supported me in my personal life. This includes my parents, brother and sister who have always stimulated me from the elementary and high school in Amsterdam, to my BSc and MSc studies at Delft University of Technology and finally my PhD project at Wageningen University. In more recent years, my parents-in-law have also been very supportive. At home, it has been a busy but cheerful time together with Tessa, Stella and Vera, which will hopefully continue for a long time to come!

List of publications

11 Mengistu, A.G., Mengistu Tsidu, G., **Koren, G.**, Kooreman, M.L., Boersma, K.F., Tagesson, T., Ardö, J., Nouvellon, Y., and Peters, W. (in review). Sun-induced fluorescence and near infrared reflectance of vegetation track the seasonal dynamics of gross primary production over Africa. *Biogeosciences*.

10 Adnew, G.A., Pons, T.L., **Koren, G.**, Peters, W., and Röckmann, T. (in review). Exploring the use of ^{17}O-excess of CO_2 for estimating mesophyll conductance of C_3 and C_4 plants *Plant Physiology*.

9 Buitink, J., Swank, A.M., van der Ploeg, M., Smith, N.E., Benninga, H.-J.F., van der Bolt, F., Carranza, C.D.U., **Koren, G.**, van der Velde, R., and Teuling, A.J. (in review). Anatomy of the 2018 agricultural drought in The Netherlands using in situ soil moisture and canopy near-infrared reflectance satellite imagery. *Hydrology and Earth System Sciences*.

8 Adnew, G.A., Pons, T.L., **Koren, G.**, Peters, W., and Röckmann, T. (2020). Leaf-scale quantification of the effect of photosynthetic gas exchange on Δ^{17}O of atmospheric CO_2. *Biogeosciences*. `https://doi.org/10.5194/bg-17-3903-2020`.

7 Smith, N.E., Kooijmans, L.M.J., **Koren, G.**, van Schaik, E., van der Woude, A.M., Wanders N., Xueref-Remy, I., Siebicke, L., Manca, G., Baker, I.T., Haynes, K.D., Luijkx, I.T., and Peters, W. (2020). Spring enhancement and summer reduction in carbon uptake during the 2018 drought in northwestern Europe. *Phil. Trans. R. Soc. B*. `https://doi.org/10.1098/rstb.2019.0509`.

6 **Koren, G.**, Schneider, L., van der Velde, I.R., van Schaik, E., Gromov, S.S., Adnew, G.A., Mrozek Martino, D.J., Hofmann, M.E.G., Liang, M.-C., Mahata, S., Bergamaschi, P., van der Laan-Luijkx, I.T., Krol, M.C., Röckmann, T., and Peters, W. (2019). Global 3-D simulations of the triple oxygen isotope signa-

ture $\Delta^{17}O$ in atmospheric CO_2. *Journal of Geophysical Research: Atmospheres*. https://doi.org/10.1029/2019JD030387

5 Vilà-Guerau de Arellano, J., **Koren, G.**, Ouwersloot, H.G., van der Velde, I., Röckmann, T., and Miller, J.B. (2019). Sub-diurnal variability of the carbon dioxide and water vapor isotopologues at the field observational scale. *Agricultural and Forest Meteorology*. https://doi.org/10.1016/j.agrformet.2019.05.014.

4 Adnew, G.A., Hofmann, M.E.G., Paul, D., Laskar, A., Surma, J., Albrecht, N., Pack, A., Schwieters, J., **Koren, G.**, Peters, W., and Röckmann, T. (2019). Determination of the triple oxygen and carbon isotopic composition of CO_2 from atomic ion fragments formed in the ion source of the 253 Ultra high-resolution isotope ratio mass spectrometer. *Rapid Communications in Mass Spectrometry*. https://doi.org/10.1002/rcm.8478.

3 van Schaik, E., Killaars, L., Smith, N.E., **Koren, G.**, van Beek, L.P.H., Peters, W., and van der Laan-Luijkx, I.T. (2018). Changes in surface hydrology, soil moisture and gross primary production in the Amazon during the 2015/2016 El Niño, *Phil. Trans. R. Soc. B*. https://doi.org/10.1098/rstb.2018.0084.

2 **Koren, G.**, van Schaik, E., Araújo, A.C., Boersma, K.F., Gärtner, A., Killaars, L., Kooreman, M.L., Kruijt, B., van der Laan-Luijkx, I.T., von Randow, C., Smith, N.E., and Peters, W. (2018). Widespread reduction in sun-induced fluorescence from the Amazon during the 2015/2016 El Niño. *Phil. Trans. R. Soc. B*. https://doi.org/10.1098/rstb.2017.0408.

1 Birvalski, M., **Koren, G.**, and Henkes, R.A.W.M. (2014). Experiments and modelling of liquid accumulation in the low elbow of a gas-liquid pipeline. *Proc. 9th North Amer. Conf. Multiphase Technology*. BHR Group, Banff Canada.

Netherlands Research School for the
Socio-Economic and Natural Sciences of the Environment

D I P L O M A

for specialised PhD training

The Netherlands research school for the
Socio-Economic and Natural Sciences of the Environment
(SENSE) declares that

Gerbrand Koren

born on 17 December 1987 in Amersfoort, The Netherlands

has successfully fulfilled all requirements of the
educational PhD programme of SENSE.

Wageningen, 18 September 2020

Chair of the SENSE board

Prof. dr. Martin Wassen

The SENSE Director

Prof. Philipp Pattberg

The SENSE Research School has been accredited by the Royal Netherlands Academy of Arts and Sciences (KNAW)

KONINKLIJKE NEDERLANDSE
AKADEMIE VAN WETENSCHAPPEN

The SENSE Research School declares that **Gerbrand Koren** has successfully fulfilled all requirements of the educational PhD programme of SENSE with a work load of 45.6 EC, including the following activities:

SENSE PhD Courses

- Environmental research in context (2016)
- Research in context activity: 'Effective communication of scientific results' (2017-2020)

Other PhD and Advanced MSc Courses

- 4th Integrated Carbon Observation System Summer School "Challenges in measurement and interpretation of greenhouse gas concentrations and fluxes", ICOS (2017)
- High Performance Computing, UvA/SURFSARA (2017)
- Navigating Brussels with ELLS (2019)

Management and Didactic Skills Training

- Supervising MSc student with thesis entitled 'A statistical model of the biospheric carbon cycle for CarbonTracker' (2019)
- Teaching in the MSc course 'Earth System Modelling' (2017-2020)
- Teaching in the MSc course 'Interdisciplinary Topics in Earth and Environment' (2017-2020)
- Teaching in the BSc-MSc course 'Chemical Processes in Soil, Water, Atmosphere' (2016-2019)

Selection of Oral Presentations

- *A global 3D model for the triple oxygen isotope signature $\Delta^{17}O$ of atmospheric CO_2 in TM5.* BBOS Autumn Symposium, 25-27 October 2017. Berg en Dal, The Netherlands
- *Global 3D simulations of the triple oxygen isotope signature $\Delta^{17}O$ in atmospheric CO_2.* AGU Fall Meeting, 10-14 December 2018, Washington DC, United States of America
- *Biosphere-atmosphere exchange of CO_2 over the Amazon.* NAC, 14-15 March 2019, Utrecht, The Netherlands
- *Interannual variability and trends of CO_2 exchange over the Amazon from 8 years of aircraft profile measurements.* IG3IS Transcom meeting, 15-18 October 2019, Paris, France

SENSE coordinator PhD education

Dr. ir. Peter Vermeulen

The research described in this thesis was financially supported by the European Research Council (ERC) as part of the 'Airborne Stable Isotopes of CO_2 from the Amazon' (ASICA) project (grant number 649087)

Financial support from Wageningen University for printing this thesis is gratefully acknowledged

Cover design by ProefschriftMaken

Printed by ProefschriftMaken